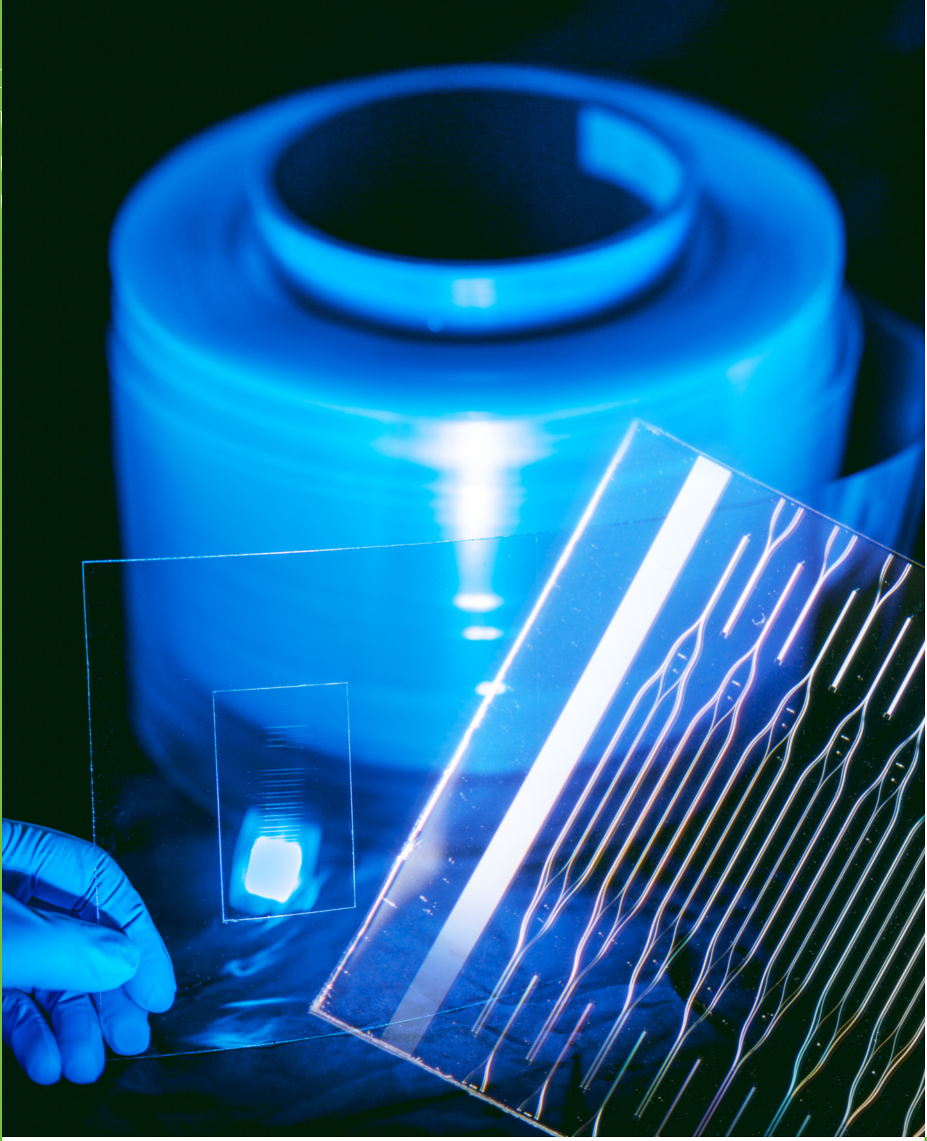

SCIENCE•TECHNOLOGY•RESEARCH HIGHLIGHTS•VISIONS•
Dissertation
136

Improving robustness and disposability of integrated Young interferometer sensors for portable diagnostics

Sanna Aikio

VTT SCIENCE 136

Improving robustness and disposability of integrated Young interferometer sensors for portable diagnostics

Sanna Aikio

VTT Technical Research Centre of Finland Ltd

Thesis for the degree of Doctor of Science in Technology to be presented with due permission for public examination and criticism in Auditorium TS101, at the University of Oulu, on the 18th of November, at 12 o'clock noon.

ISBN 978-951-38-8462-8 (Soft back ed.)
ISBN 978-951-38-8461-1 (URL: http://www.vttresearch.com/impact/publications)

VTT Science 136

ISSN-L 2242-119X
ISSN 2242-119X (Print)
ISSN 2242-1203 (Online)
http://urn.fi/URN:ISBN:978-951-38-8461-1

JULKAISIJA – UTGIVARE – PUBLISHER

Teknologian tutkimuskeskus VTT Oy
PL 1000 (Tekniikantie 4 A, Espoo)
02044 VTT
Puh. 020 722 111, faksi 020 722 7001

Teknologiska forskningscentralen VTT Ab
PB 1000 (Teknikvägen 4 A, Esbo)
FI-02044 VTT
Tfn +358 20 722 111, telefax +358 20 722 7001

VTT Technical Research Centre of Finland Ltd
P.O. Box 1000 (Tekniikantie 4 A, Espoo)
FI-02044 VTT, Finland
Tel. +358 20 722 111, fax +358 20 722 7001

Cover image: Janne Aikio

Juvenes Print, Tampere 2016

Preface

This thesis is based on the research carried out at VTT Technical Research Centre of Finland Ltd. The work was supported in part by the Infotech Oulu Doctoral Program as well as VTT. A major part of the work was carried out in the PHOTOSENS project, which is funded by the European Commission.

First, I would like to express my deep gratitude to my supervisors Professor Emeritus Risto Myllylä (University of Oulu) and Docent Jussi Hiltunen (VTT). I would like to thank Professor Myllylä for his firm support and encouragement during these years, and Docent Hiltunen for his support, guidance and never-fading enthusiasm driving me forward in this work. I would like to express my appreciation to my doctoral training follow-up group, Docent Alexey Popov (University of Oulu) and Research Professor Jukka Hast (VTT), for their guidance. Assistant Professor Kristinn B. Gylfason (Kungliga Tekniska Högskolan) and Dr Erkki Alarousu (King Abdullah University of Science and Technology) are greatly acknowledged for their comprehensive peer-review of the thesis manuscript.

I am most grateful to all my co-authors and co-workers for their expertise and contributions that have made this work possible. I especially wish to thank Dr Marianne Hiltunen, Johanna Hiitola-Keinänen, Jyrki Ollila, Sari Pohjonen, Inka Päkkilä and Hanna Toppila (VTT), Dr Petri Stenberg (University of Eastern Finland), Eva Spieker (University of Vienna) and Dr Jarkko Puustinen (University of Oulu). I am grateful to Professor Peter Lieberzeit and Dr Martin Zeilinger (University of Vienna) as well as Dr Samuli Siitonen and Dr Ville Kontturi (Nanocomp Oy) for their expertise, support and dedication.

I wish to thank Research Professor Pentti Karioja (VTT) for being the initiator of my PhD studies, for enabling this work and for his steadfast support throughout the years. I am also grateful to Dr Leena Hakalahti, Dr Arto Maaninen, Professor Harri Kopola, Research Professor Kristiina Takkinen and Dr Eero Punkka (VTT) for their support that enabled this work and thesis.

Finally, I would like to thank my husband Janne, daughter Aino and son Juho for their patience, encouragement and support during this lengthy journey.

Oulu, August 2016

Sanna Aikio

Academic dissertation

Supervisors
Professor Emeritus Risto Myllylä
University of Oulu
Faculty of Information Technology and Electrical Engineering
P.O. Box 4500
FI-90014 University of Oulu, Finland

Docent Jussi Hiltunen
VTT Technical Research Centre of Finland Ltd
P.O. Box 1100
FI-90571 Oulu, Finland

Reviewers
Assistant Professor Kristinn B. Gylfason
Kungliga Tekniska Högskolan
School of Electrical Engineering, Micro and Nanosystems
Osquldas väg 10
100 44 Stockholm, Sweden

DSc (Tech.) Erkki Alarousu
King Abdullah University of Science and Technology
Solar and Photovoltaics Engineering Research Center
Thuwal 23955-6900, Kingdom of Saudi Arabia

Opponents
Professor Peter Van Daele
Ghent University
Department of Information Technology
Tech Lane Ghent Science Park – Campus A, 15
B-9052 Gent, Belgium

Assistant Professor Kristinn B. Gylfason
Kungliga Tekniska Högskolan
School of Electrical Engineering, Micro and Nanosystems
Osquldas väg 10
100 44 Stockholm, Sweden

List of publications

This thesis is based on the following original publications which are referred to in the text as I–IV. The publications are reproduced by kind permission of the publishers.

I Sanna Aikio, Marianne Hiltunen, and Jussi Hiltunen (2015), *Compensation of drift by using a multichannel integrated Young interferometer*, Applied Optics 54, 4771-4780

II Sanna Aikio, Marianne Hiltunen, Petri Stenberg, and Jussi Hiltunen (2015), *Drift compensation using a multichannel slot waveguide Young interferometer*, Journal of the European Optical Society - Rapid Publications 10, 15053, 7 p.

III Sanna Aikio, Jussi Hiltunen, Johanna Hiitola-Keinänen, Marianne Hiltunen, Ville Kontturi, Samuli Siitonen, Jarkko Puustinen, and Pentti Karioja (2016), *Disposable photonic integrated circuits for evanescent wave sensors by ultra-high volume roll-to-roll method*, Optics Express 24, 2527-2541

IV Sanna Aikio, Martin Zeilinger, Jussi Hiltunen, Leena Hakalahti, Johanna Hiitola-Keinänen, Marianne Hiltunen, Ville Kontturi, Samuli Siitonen, Jarkko Puustinen, Peter Lieberzeit, and Pentti Karioja (2016), *Disposable (bio)chemical integrated optical waveguide sensors implemented on roll-to-roll produced platforms*, RSC Advances 6, 50414-50422

Author's contributions

Paper I: Compensation of drift by using a multichannel integrated Young interferometer

Author derived the theory of the drift compensation method, co-designed sensor configuration, established optical sensor characterization methodology, co-designed and performed sensor measurements, prepared software for sensor data analysis, analysed sensor measurement data, and prepared the manuscript. Co-authors prepared the sensor chips and conducted the waveguide simulations.

Paper II: Drift compensation using a multichannel slot waveguide Young interferometer

Author performed sensor measurements, analysed sensor measurement data, and prepared the manuscript. The work utilised the drift compensation method, the optical sensor characterization methodology and the data analysis software developed in Paper I. Co-authors prepared the sensor chips and conducted the waveguide simulations.

Paper III: Disposable photonic integrated circuits for evanescent wave sensors by ultra-high volume roll-to-roll method

Author co-designed sensor configuration, established optical sensor characterization methodology, designed and performed sensor measurements, prepared software for sensor data analysis, analysed sensor measurement data, and prepared the manuscript with co-authors. Co-authors prepared the sensor chips, performed attenuation measurements and conducted the waveguide simulations.

Paper IV: Disposable (bio)chemical integrated optical waveguide sensors implemented on roll-to-roll produced platforms

Author co-designed the sensor configurations, designed surface functionalization, designed and performed sensor measurements, analysed sensor measurement data, and prepared the manuscript with co-authors. The work utilised the sensor characterization methodology and the sensor data analysis software developed in Paper III. Co-authors prepared the sensor chips, developed the molecularly imprinted polymer material and prepared the surface functionalization.

Contents

List of abbreviations

BSA	Bovine serum albumin
CRP	C-reactive protein
DFT	Discrete Fourier transform
FDM	Finite difference method
FEM	Finite element method
FFT	Fast Fourier transform
hCG	Human chorionic gonadotropin
IgG	Immunoglobulin G
Mab	Monoclonal antibody
MIP	Molecularly imprinted polymer
NIP	Non-imprinted polymer
PBS	Phosphate buffered saline
PBST	Phosphate buffered saline with Tween-20
PM	Polarization maintaining
R2R	Roll-to-roll
RI	Refractive index
RIU	Refractive index unit
SEM	Scanning electron microscope
TE	Transverse electric
TIR	Total internal reflection
TM	Transverse magnetic
UV	Ultraviolet

wt. %	Weight per cent
YI	Young interferometer
YI1	Young interferometer number 1
YI2	Young interferometer number 2

List of symbols

a	Variable, real number
α	Angle
$\boldsymbol{B}$	Magnetic field vector
b	Variable, real number
B_{0i}	Amplitude of the incident magnetic wave
B_{0r}	Amplitude of the reflected magnetic wave
B_{0t}	Amplitude of the refracted magnetic wave
C	Concentration
c	Speed of light in vacuum
d_{ij}	Separation of channels *i* and *j* at the outcoupling end of the chip
Δd_{AL}	Change of the adlayer thickness
$\Delta\phi_0$	Initial phase difference between the channels before the sample exposure
$\Delta\phi$	Phase change induced by the sample
$\Delta\phi_{\mathrm{bulk}}$	Phase change induced by bulk RI change
$\Delta\phi_{\mathrm{diff}}$	Difference in the phase changes
$\Delta\phi_{ij}$	Measured phase change of the sub-interferogram fringes formed by the channel pair *i* and *j*
$\Delta\phi_{ij}^{s}$	Sample induced phase change of the sub-interferogram fringes formed by the channel pair *i* and *j*
$\Delta\phi_{\mathrm{MIP}}$	Phase change of the interferometer functionalized with molecularly imprinted polymer
$\Delta\phi_{\mathrm{NIP}}$	Phase change of the interferometer coated with non-imprinted polymer

Δl_{opt}	Change in the mutual optical path length difference between the measurement and reference channels
$\Delta l_{\mathrm{opt,m}}$	Change in the optical path length of the waveguide within the measurement window
$\Delta l_{\mathrm{opt,r}}$	Change in the optical path length of the waveguide of the reference channel
$\mathit{\Delta} n$	Refractive index difference of sample solution to pure water
Δn_{eff}	Difference in the changes of the effective refractive indices of the measurement and reference channels
$\Delta n_{\mathrm{eff,m}}$	Change in the effective refractive index value of the measurement channel
$\Delta n_{\mathrm{eff,r}}$	Change in the effective refractive index value of the reference channel
Δn_{OC}	Refractive index change of the overcladding
Δs_{ij}	Lateral shift of the interferogram fringes of the sub-interferogram formed by the channel pair *i* and *j*
Δs^{d}	Setup drift induced lateral shift of the interferogram fringes
Δs_{ij}^{d}	Setup drift induced lateral shift of the interferogram fringes of the sub-interferogram formed by the channel pair *i* and *j*
Δs_{ij}^{I}	Chip internal drift induced lateral shift of the interferogram fringes of the sub-interferogram formed by the channel pair *i* and *j*
Δs_{ij}^{s}	Sample induced lateral shift of the interferogram fringes of the sub-interferogram formed by the channel pair *i* and *j*
$\boldsymbol{E}_{0i}$	Amplitude of the incident electric wave (vector)
E_{0i}	Amplitude of the incident electric wave
$\boldsymbol{E}_{0r}$	Amplitude of the reflected electric wave (vector)
E_{0r}	Amplitude of the reflected electric wave
$\boldsymbol{E}_{0t}$	Amplitude of the refracted electric wave (vector)
E_{0t}	Amplitude of the refracted electric wave
$\boldsymbol{E}_{i}$	Incident electric field
$\boldsymbol{E}_{r}$	Reflected electric field
$\boldsymbol{E}_{t}$	Refracted electric field
Φ	Phase shift related to the total internal reflection

Φ_{OC}	Phase shift related to the total internal reflection from the core-overcladding boundary
Φ_{TE}	Phase shift between incident and reflected waves for TE polarization
Φ_{TM}	Phase shift between incident and reflected waves for TM polarization
Φ_{UC}	Phase shift related to the total internal reflection from the core-undercladding boundary
ϕ	Phase
ϕ_{ij}	Phase of channel pair *i* and *j*
φ	Phase difference between the channels caused by the difference in the geometrical optical path lengths between the channel outcoupling point and the observation point at the camera
h	Height of the waveguide
i	Sensor chip channel (imaginary unit in Appendix A)
I	Intensity
I_i	Power of the light beam outcoupling from the channel *i*
I_j	Power of the light beam outcoupling from the channel *j*
I_m	Power of the light beam outcoupling from the measurement channel
I_r	Power of the light beam outcoupling from the reference channel
j	Sensor chip channel
k	Spatial frequency
k_{ij}	Spatial frequency of the sub-interferogram formed by a channel pair *i* and *j*
$\boldsymbol{\kappa}$	Wave vector
κ	Length of wave vector
$\boldsymbol{\kappa}_{+}$	Wave vector of a plane wave
$\kappa_{+\boldsymbol{z}}$	Positive wave vector component in *z*-direction
$\boldsymbol{\kappa}_{-}$	Wave vector of a plane wave
$\kappa_{-\boldsymbol{z}}$	Negative wave vector component in *z*-direction
$\kappa_{\boldsymbol{x}}$	Wave vector component in *x*-direction
$\boldsymbol{\kappa_i}$	Wave vector of incident wave

$\boldsymbol{\kappa_r}$	Wave vector of reflected wave
$\boldsymbol{\kappa_t}$	Wave vector of refracted wave
L	Distance between the chip outcoupling end and camera
l	Length of the measurement window
Λ	Spatial wavelength
λ	Wavelength of light in vacuum
m	Positive integer
n	Refractive index
n_1	Refractive index of medium 1
n_2	Refractive index of medium 2
n_{eff}	Effective refractive index
$n_{\mathrm{eff},1}$	Effective refractive index of channel 1
$n_{\mathrm{eff,m}}$	Effective refractive index of measurement channel
$n_{\mathrm{eff,r}}$	Effective refractive index of reference channel
n_{OC}	Refractive index of the waveguide overcladding material
n_{melamine}	Refractive index of melamine
n_{UC}	Refractive index of the waveguide undercladding material
n_W	Refractive index of the waveguide core material
n_{water}	Refractive index of water
ω	Frequency of the plane wave
ρ_{m}	Density of melamine
$\boldsymbol{r}$	Observation point
S	Sensitivity
S_{OC}	Sensitivity to changes in the overcladding refractive index
S_{AL}	Sensitivity to changes in adlayer thickness
t	Time
t_0	Start time of an experiment
θ	Angle relative to the longitudinal axis of the waveguide
θ_c	Critical angle
$\theta_{c,OC}$	Critical angle of core-overcladding boundary

$\theta_{c,UC}$	Critical angle of core-undercladding boundary
θ_i	Angle of incidence
θ_m	Angle of mth mode
θ_r	Angle of reflection
θ_t	Angle of refraction
u	Position along camera detector
x	Co-ordinate
y	Position along camera detector
z	Co-ordinate

1. Introduction

In this introductory section, the background to the research is discussed in Section 1.1. The objectives and scope of the work, as well as the research questions studied in Papers I-IV, are described in Section 1.2. The dissertation structure is summarized in Section 1.3.

1.1 Background and research environment

To enable laboratory grade analysis at point-of-need, sensitive analytical methods need to be brought out from the laboratory implemented as low-cost, robust, and user-friendly systems.[1-4] Research on micro total analysis systems, lab-on-a-chips, point-of-care diagnostics, and opto-fluidic systems is developing sensors for a wide range of applications, among others medical diagnostics, food safety, environmental monitoring, and public safety.[2, 5-8] The global market for diagnostic biochips is growing fast and is forecast to reach a value of over $10 billion by 2020.[9]

Sensors for the above-mentioned applications can be based on different transduction methods, such as optical, electrical, and mechanical, on labelled or label-free measurement techniques, and on biological or artificial recognition. A great many different sensing concepts thus exists. However, work is continuing on developing portable quantitative sensing systems that are sensitive, reliable, multi-analyte, fast, robust, low-cost, use low sample volumes, are easy to use in variable ambient conditions with real-life samples, and can be operated by non-trained persons.[1, 3, 10]

Optical sensors utilize different properties of light, such as intensity, spectrum, polarization and phase.[4, 7] Optical transducers are based on various phenomena and properties of materials such as colour, fluorescence, luminescence, Raman scattering, and refractive index that is used in this thesis. Refractive index sensor chips can be implemented using various structures such as gratings [11-13], ring resonators [14], photonic crystals [15], and interferometers [1] as well as the surface plasmon resonance phenomenon [16, 17].

Integrated planar waveguide interferometers form a class of optical sensors and are considered to have potential to be developed for portable point-of-need diagnostics.[1, 18] The work discussed in this thesis is related to this group of sensors. Section 1.1.1 briefly describes their properties and Section 1.1.2 focuses on integrated Young interferometers (YIs) being the sensing method utilized in this thesis.

1.1.1 Planar waveguide interferometer chemical sensors

Integrated interferometer chemical sensors are based on waveguides integrated onto a single chip and evanescent wave sensing of refractive index (RI) changes occurring in close proximity to the waveguide surface.[1, 18, 19] The sensing principle is illustrated in Figure 1. When light propagates in the optical waveguide, an evanescent wave of the light extends ~100-150 nm [20] into the liquid sample matrix on top of the waveguide. When the RI changes within the volume probed by the evanescent wave, the light propagation in the waveguide also changes, inducing a phase change $\Delta\phi$, as illustrated in Figure 1. The phase change is directly produced by the analyte-induced RI change, and there is no need to utilize any additional labels to generate the signal, i.e. the sensing method is label-free. The phase change is transduced into a measurable signal by using an additional reference wave, that is inert to the analytes, and letting these two waves interfere. The produced signal depends on the sensor configuration: in Mach-Zehnder interferometers, the light intensity changes; in Young interferometers, the positions of the interferogram fringes shift. A recognition layer applied onto the waveguide selectively binds analytes, i.e. the compounds of interest, onto the waveguide surface, making the sensor react specifically to them. The analyte binding changes the RI since the sample matrix is replaced by the compounds that typically have a higher RI.[19] The recognition layers are based on either biological receptors, such as antibodies, or artificial receptors, such as molecularly imprinted polymers (MIPs).[21-23]

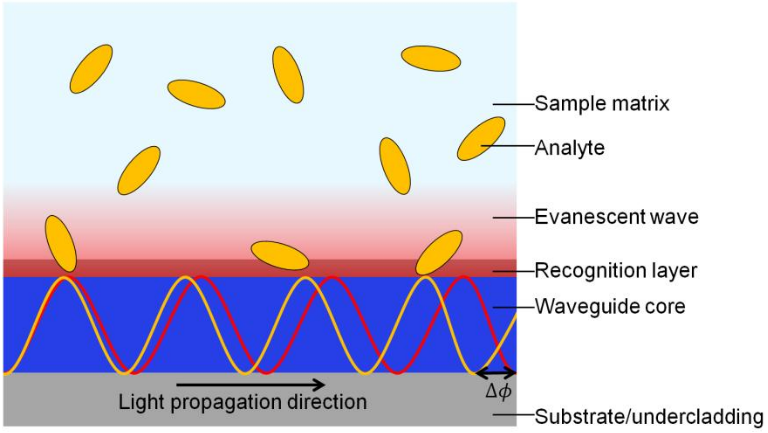

Figure 1 Sensing principle of an integrated interferometer chemical sensor. The red curve and the yellow curve illustrate the light wave before and after the analyte-induced RI change, respectively, and $\Delta\phi$ is the induced phase change. Illustration adapted from Ref. [18].

Integrated interferometer sensors have been shown to be sensitive enough to enable detection of small amounts of analytes although the labelled techniques are even more sensitive and enable single molecules to be detected.[18] However, evanescent wave based label-free sensing methods have advantageous properties over labelled methods: analytes are detected in their natural form without possible interference of labels, such as fluorophores, nanoparticles and plastic beads, and the low power of the evanescent field does not harm the analytes.[18, 20] The simpler assays reduce the complexity and cost of the analysis compared to labelled methods, which is an advantage in cost-critical sensing applications.[18] The integrated interferometer sensors are also capable to real-time and multi-analyte sensing.[18] The compatibility of the sensors for low-cost portable diagnostics is further improved by developing more cost-efficient manufacturing methods, and by miniaturizing the sensor chips leading to lower reagent consumption and faster response times.[18]

Integrated interferometers are implemented using optical waveguides that are structures capable confining light and guiding it by total internal reflections. Waveguides can be implemented using various geometries, as shown in Figure 2. Optical waveguide consist of a core that has a larger refractive index than the surrounding materials. The cross-sectional dimensions of the waveguides used in the sensors are typically about a micrometre or less, and the lengths are a few centimetres. Waveguides for the sensor chips are manufactured in batch-based processes.[18] Waveguide layers are typically applied onto rigid substrates, for example silicon dioxide wafers or polymers, using microfabrication methods such as photolithography, embossing, [1, 18] UV-imprinting, [24] or moulding [25]. Utilization of sensor waveguides manufactured by continuous ultra-high volume roll-to-roll (R2R) manufacturing methods is discussed later in this thesis. (Paper III)

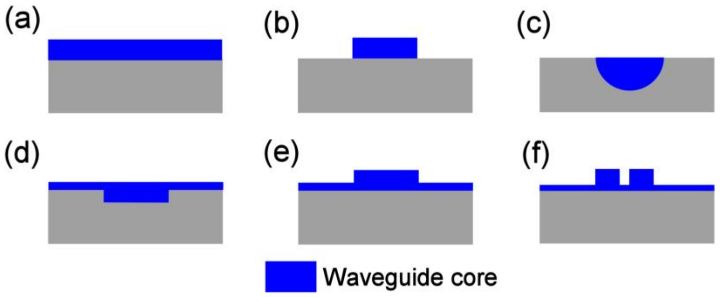

Figure 2 Illustrations of the cross-sections of different waveguide types. a) Slab waveguide, b) strip waveguide, c) diffused waveguide, d) inverted ridge waveguide (Papers I, III, and IV), e) ridge waveguide (Paper II), and f) slot waveguide (Paper II).[18, 26, 27] The paper numbers indicate the waveguide types utilized in them.

Light from an external source, typically a laser, has to be coupled into the waveguides of a sensor chip.[18] Due to the small cross-sectional size of the waveguides, efficient light coupling requires the use of one of the coupling methods illustrated in Figure 3.[18, 26] In the experimental part of this work, the end-fire coupling was utilized using either a focusing lens (Papers I and II) or a tapered fibre (Papers III and IV).

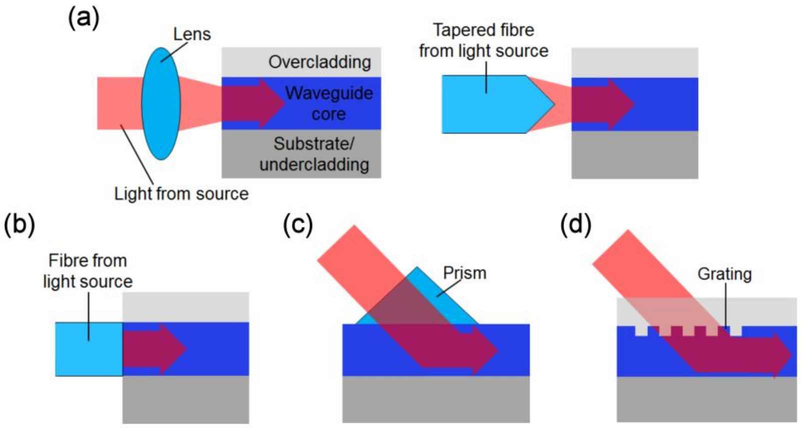

Figure 3 Illustration of light incoupling methods into optical waveguides. a) End-fire coupling using either a lens (Papers I and II) or a tapered fibre (Papers III and IV). b) Butt-coupling. c) Prism coupling. d) Grating coupling. The paper numbers indicate the waveguide types utilized in them.

Among integrated interferometer sensors, YIs have proven to be most sensitive.[1, 18] Up to two orders of magnitude lower limit of detection values have been reached than with integrated Mach-Zehnder interferometers using simpler sensing configurations.[1] The signal analysis of integrated YIs is done from the captured interferogram images, which provide more information for signal processing than the intensity values obtained from Mach-Zehnder interferometers and enable straightforward monitoring of the induced phase changes by using discrete Fourier transform (DFT).[19] Since the sensing method is not sensitive to intensity variations, there is no need to modulate or calibrate the light source intensity.[18] In addition to having these desirable features from a portable diagnostics point of view, there are also inherent drawbacks related to robustness and to the need for a camera, which is a more costly component than the light detectors needed with Mach-Zehnder interferometers.[1, 18]

1.1.2 Integrated Young interferometer sensors

Young interferometers are based on the findings of Thomas Young during the first years of 19th century.[28, 29] In his lectures published in 1807, he describes the double slit, or hole, experiment and the formation of interference fringes. The first integrated YI sensor was reported by Brandenburg and Henninger in 1994.[30] It was based on a Y-junction implemented in glass.

Integrated YI sensor chips are based on waveguides. In the simplest implementation, light from a light source is split into two optical waveguides: one waveguide is inert to the analytes, forming a reference light path, and the other is a sensing waveguide, enabling interaction with the sample. Light beams coupling out from the end facet of the chip diverge, overlap and interfere, forming a fringed interference pattern that can be imaged onto a screen or a camera detector to form an interferogram.

YI sensor chips have been implemented using slab [31-34], diffused [30, 35], strip [36], ridge [37], inverted ridge [24, 38], and slot waveguides [25, 39] (see Figure 2, p. 19) and based on silicon [34, 36, 37], glass [30, 35], tantalum pentoxide [33], and polymers [24, 25, 31, 32, 38, 39]. From now on in this thesis, the term waveguide is used when discussing the photonic light guiding structure itself, and the term channel is used when a waveguide has an assigned role in the YI sensor chip. In addition to the two-channel implementation described in the paragraph above, multichannel and single channel implementations exist. In multichannel sensors, one of the channels is an inert reference channel and the rest of the channels are measurement channels that interact with the sample, enabling multi-analyte detection. Beams emanating from all the channels are allowed to interfere forming a multi-beam interferogram.[37] In single-channel YIs, two polarizations propagate within a single waveguide and are configured to interfere after emanating from the sensor chip.[40]

Integrated YI sensors are shown to be sensitive, having limit of detection values of 10^{-5}-10^{-8} refractive index units (RIU) for bulk RI changes.[24, 33, 37] To enhance the sensor sensitivity, use of tagging antibodies [41] is studied as well as the utilization of high-index coatings with polymeric YIs.[38, 39] Multi-wavelength approaches have been reported enabling adjustment of the probing characteristics of the evanescent wave to differentiate between bulk and surface bound effects, and to reduce temperature sensitivity.[42, 43] Different polarization states have also been used to enable analysis of the layer thicknesses and densities.[34] It has also been demonstrated that the use of slot waveguides reduces the temperature sensitivity of integrated YIs.[25]

As discussed in Section 1.1.1, YIs have to be functionalized with a recognition layer to make them specifically interact with the chosen analytes. Of biological receptors, antibodies have been used with inorganic and polymeric integrated YIs to detect proteins and viruses, including demonstration of multi-analyte sensing and use of a complex sample matrix i.e. serum.[24, 34, 38, 41, 44, 45] However, detection of more than two analytes has not been reported.[1] Of artificial receptors, MIP layers have been applied with silicon-based sensors to detect vapour phase trinitrotoluene and proteins.[46, 47] The MIP-based recognition layers may be advantageous for low-cost sensors since they have the potential to be robust, repeatable, low-cost and mass-manufacturable.[22] Antibody receptor layers are formed by either incubating the antibody solution on the sensor surface or flowing it through a flow cell assembled on top of the chip.[24, 32, 34, 38, 41, 44, 45] The MIP layers are formed either by dip coating the sensor chip or performing the polymerization of the material under a glass plate applied onto the sensor surface to form a thin layer.[46, 47] Although robotic surface functionalization methods have been used to functionalize integrated Mach-Zehnder interferometers,[1] and inkjet printing has been used for multi-analyte functionalization of ring resonators,[48] these methods have not been applied with integrated YI sensors prior to the work discussed in this thesis. As an additive method, inkjet printing enables efficient use of potentially expensive receptor materials and minimizes waste.[49] As a non-contact method, it is suitable for the functionalization of easily damaged surfaces. The method is also considered to be applicable to large-scale manufacturing.

In the work discussed in this thesis, integrated YI sensor chips were functionalized with antibody-based receptors to detect human chorionic gonadotropin (hCG) and C-reactive protein (CRP), whereas MIP recognition layer was utilized to measure melamine. CRP and hCG, shown in Figure 4(a) and Figure 4(b), respectively, are important clinical analytes: CRP is an inflammation marker and an indicator for the assessment of cardiovascular disease,[50, 51] whereas hCG is an early stage pregnancy marker.[52] Melamine, shown in Figure 4(c), is a small molecule that has become an interesting analyte regarding food safety in respect of contaminated dairy products.[53] In addition, glucose (see Figure 4(d)) was used in unspecific ambient RI sensing experiments to modify the bulk RI of the sample solutions.

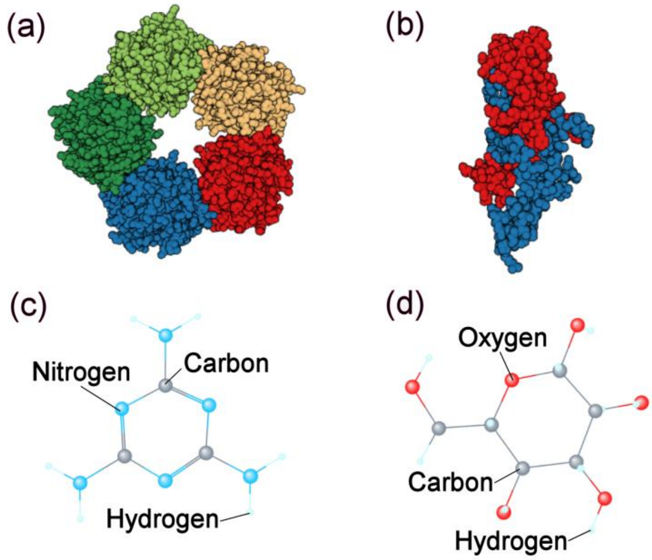

Figure 4 Structure of a) CRP molecule having five repetitive units in a ring formation [54], b) hCG molecule [55], c) melamine molecule [56], and d) glucose molecule [57]

As discussed above, YI sensors have many desirable features and properties for portable diagnostics: they are sensitive, can be manufactured using low-cost polymeric materials, and are capable of multi-analyte detection. Compact reader units are also implemented.[41] However, there are also disadvantages. One of the major issues from the portable diagnostics point of view is that the sensor signal is easily disrupted by ambient mechanical disturbances since they shift the interferogram fringes similarly to the sample-induced phase changes, thus obscuring the readout signal.[1, 18] The sensor readout systems are typically well isolated from the ambient disturbances [18] but this kind of approach is not necessarily easily adaptable to low-cost portable readers.

As an alternative approach to mechanical disturbance management, Ymeti et al. have studied the possibility to compensate drifts by using a multichannel YI chip with two reference channels.[58] In the article, it was assumed that the ratio of the drift-induced phase changes remains constant between different channel pairs. The phase change signal produced by the reference channel pair as a response to system drift can thus be used to compensate the signals produced by other channel pairs. In the article, the phase change ratios between the different channel pairs were first derived from measured phase change curves and then used to calculate the compensated phase change curves of an experiment where an RI change was induced. It was found that the method was working well resulting in about a tenfold reduction in drift. Ymeti et al. provide two possible explanations for the constant phase change ratios: the first explanation is related to different responses of the channels to temperature changes, and the second explanation speculates that the phase change ratios are chip specimen specific parameters. However, the origin of the constant phase change ratios was not looked into further in the article. Also the applicability of the method for RI sensing was demonstrated using one sample solution concentration. The drift compensation method reported by Ymeti et al. is of interest as regards portable readers since it can be implemented using typical optical arrangements of integrated YI readout systems, and it was further studied in the work discussed in this thesis.

One of the key issues with the sensor chips is the requirement for sensor disposability.[59] In many applications, such as in medical diagnostics, sensor chips have to be single-use to avoid cross-contamination between samples. Applications are at the same time cost-critical, making it difficult to realize photonic sensor chips using batch-based manufacturing methods since the footprint of a sensor chip is typically several square centimetres, as required by its easy handling as well as the different functionalities. To enable wide dissemination of photonic sensor chips in cost-critical point-of-need applications, they have to be manufactured using high-volume methods and low-cost materials. Since R2R fabrication methods are capable of ultra-high volume and large-area manufacturing, they provide an interesting alternative to batch-based processing. In this work, the applicability of R2R fabricated polymeric waveguides to integrated YI sensors was studied.

1.2 Objectives and scope

The objective of the work discussed in this thesis was to improve the applicability of integrated YI sensors for portable diagnostics. This was approached by means of two themes: improving the robustness of the sensing method and improving the disposability of the sensor chips. The relationships between the articles are shown in Figure 5. Papers I and II are related to the robustness theme and Papers III and IV to the disposability theme.

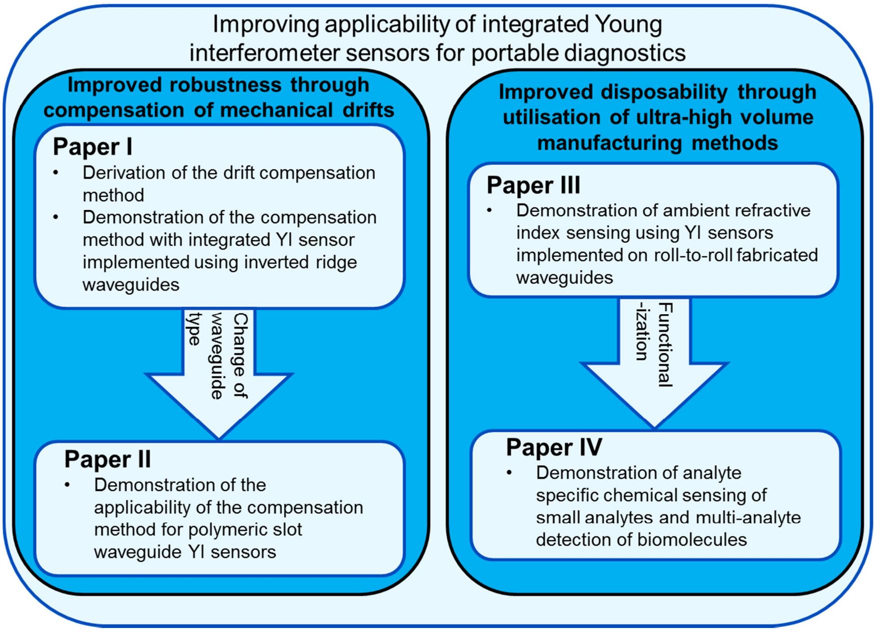

Figure 5 Article relationships and the main content of the articles discussed in this thesis. Paper I and Paper II are related to the robustness theme and Paper III and Paper IV to the disposability theme. The main difference in the research setting between the articles is indicated in the arrow.

In Paper I the research question was “Is it possible to derive a drift compensation method that is based on analysis of the spatial shifts of the interferogram fringes, and that is able to compensate for mechanical drifts when using a multichannel inverted ridge waveguide YI sensor chip having two reference channels?” In Paper II this research question was modified to “Is the derived drift compensation method also applicable for multichannel slot waveguide YI sensors having two reference channels?”

In Paper III the disposability theme was approached by expressing a question “Are roll-to-roll fabricated polymeric waveguides applicable for evanescent wave sensing of ambient refractive index using an integrated YI sensor as a model sensor?” In Article IV the question was augmented as “Is it possible to implement these YI sensors for analyte-specific chemical sensing of small analytes by using an MIP receptor layer, and for multi-analyte detection of biomolecules by using antibody-based receptor layers?”

Each paper provides an answer to a specific research question and these contributions are combined in this summary. The aim is to present the theory of the drift compensation method and the experimental results demonstrating the capability of the compensation method to compensate mechanical drifts, and the applicability of the roll-to-roll manufactured waveguides for evanescent wave sensing. The design and characterization of the waveguides as photonic components *per se* were excluded from the scope of the thesis to limit the discussion the issues directly related to the research questions listed above.

1.3 Dissertation structure

The structure of this thesis is as follows. In Section 2, the sensing principle of integrated YI sensors is reviewed and the theory of the drift compensation method is derived. The related topics of the light propagation in an optical waveguide and the numerical modelling of waveguide properties are discussed in Appendix A. In Section 3, detailed descriptions are given of the five sensor chip embodiments used in the experiments. In addition, the specific sensing principles related to the slot waveguide YI chip and the sensor chips implemented using R2R fabricated waveguides are discussed. In Section 4, the experimental work and results are described, including the cross-talk effects seen in the experiments. Section 5 provides a discussion about the results of the sensing experiments, the theoretical and practical implications of the work together with the reliability and validity of the results. Recommendations for the further research are also given. Section 6 contains a short summary of the thesis.

2. Sensing principle of integrated Young interferometers and the theory of the drift compensation

In this chapter, the sensing principle of integrated YI sensors is reviewed for a 2-channel and multichannel sensor chips. This is followed by a presentation of the theory of the drift compensation calculation. The basic phenomena governing light propagation in an optical fibre and numerical calculations of waveguide properties are discussed in Appendix A (p. 98).

2.1 Sensing principle of integrated Young interferometer sensors

In this section, the sensing principle of integrated YIs is discussed first for a basic 2-channel chip layout, and then extended to cover the specific issues of multi-channel chips.

2.1.1 2-channel integrated Young interferometers

A schematic of an integrated YI sensor chip is shown in Figure 6(a). The input waveguide of the chip has a Y-junction that branches the waveguide into two parallel waveguides. An overcladding layer is patterned onto the chip, leaving an opening, a measurement window, unclad on top of one of the waveguides for sample interaction. The measurement channel is the waveguide having the measurement window and the reference channel is the waveguide covered by the overcladding layer.

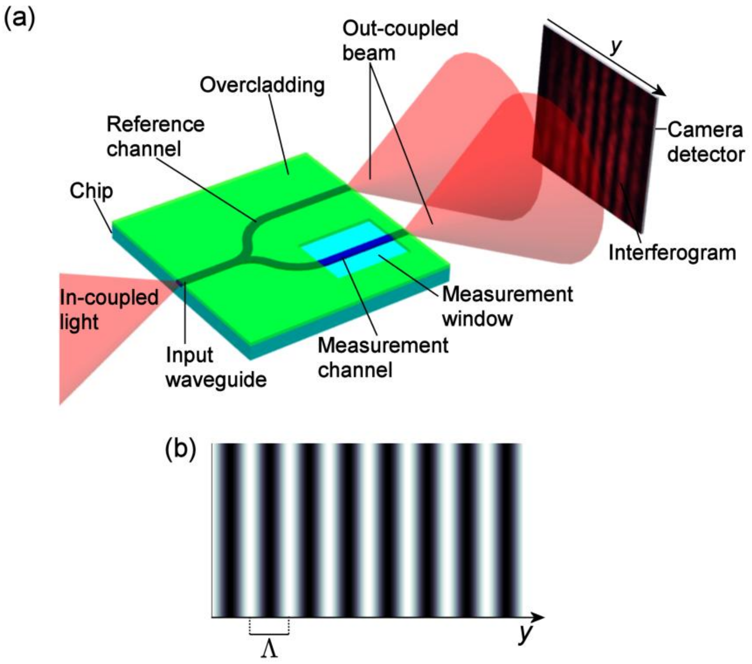

Figure 6 a) Schematic of a 2-channel integrated YI sensor chip and a captured interferogram. b) Theoretically calculated intensity distribution of an interferogram. The spatial wavelength, Λ, is also shown.

When laser light with wavelength λ is coupled into the input waveguide, the Y-branch splits light into the measurement and reference channels. Light is guided through the chip by the waveguides and two beams emanate from the end facet of the chip. The diverging beams overlap and interfere, forming a fringed interference pattern. The interference pattern can be imaged onto a camera detector by means of a microscope objective forming an interferogram.

An example of a captured interferogram is shown in Figure 6(a) and a theoretically calculated interferogram in Figure 6(b). The intensity variation of the interferogram along the *y*-axis can be calculated [19]

$$I(y) \approx I_\mathrm{m} + I_\mathrm{r} + 2\sqrt{(I_\mathrm{m} I_\mathrm{r})}\ \cos(\varphi(y) - \Delta\phi_0 - \Delta\phi), \qquad (1)$$

where I_m and I_r are the powers of the light beams emanating from the measurement and reference channels, respectively, φ the phase difference between the channels caused by the difference in their geometrical path lengths between the outcoupling point from the chip and the observation point at the camera detector, $\Delta\phi_0$ is the initial phase difference between the channels before sample exposure, and $\Delta\phi$ the phase change caused by the sample interaction when applicable.

Here it is assumed that the emanating beams are point sources and that they overlap completely at the camera detector. Eq. (1) does not take into account that the intensity of the diverging beams decreases when the distance between the beam outcoupling point and the observation point at the camera detector increases. The equation is therefore valid only over a limited area where the variation in the beam intensities can be considered to be small.

As indicated by Eq. (1), the intensity of the interferogram varies sinusoidally along the *y*-axis as shown in Figure 6(b). The intensity maxima are located at the positions where the two beams interfere constructively, i.e. the total optical path length difference between the measurement and the reference channels is an integer multiple of λ. The intensity minima are located at the positions where beams interfere destructively. The period of the interferogram fringes defines their spatial wavelength, Λ, and spatial frequency, k, whereas the position of the fringes along the *y*-axis defines their phase, ϕ.

The sensing method is based on the analysis of the sample-induced shifts of the interferogram fringes along the *y*-axis. When RI in the measurement window is changed by the sample, the effective RI of the measurement channel, $n_{\mathrm{eff,m}}$, changes, as discussed in Appendix A (p. 98). Due to the passivation layer, the effective RI of the reference channel, $n_{\mathrm{eff,r}}$, is not directly affected by the sample but can be changed, for example due to temperature variations. Since the effects of the sample are different to the effective refractive indices of the measurement and reference channels, their optical path lengths also change differently. This changes their mutual optical path length difference that again changes the value of $\Delta\phi$ in Eq. (1) and induces a shift in the position of the interferogram fringes. An example of the shift of the fringes is shown in Figure 7. It is worth noticing that the initial absolute optical path lengths of the channels do not have any impact on the sensor readout but just define the initial position of the interferogram fringes. There is thus no need to match the optical lengths of the waveguides, relaxing the manufacturing tolerances of the sensor chips. However, since the actual fringe order of the fringes is not known, the track of the phase change is lost if a phase change larger than 2π is induced between two consecutive captured interferograms. The fringe order ambiguity can be avoided by using an incoherent light source.[30]

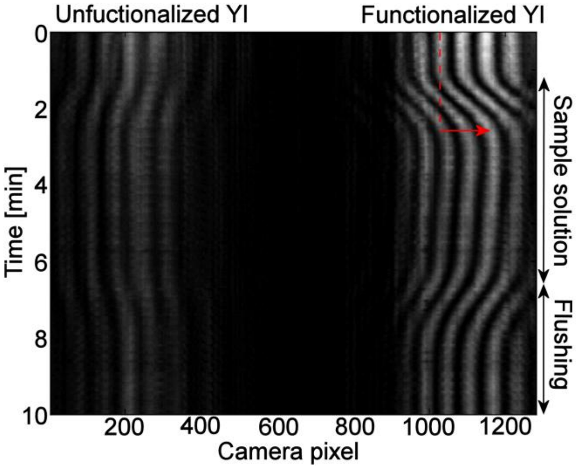

Figure 7 Example of the shift of the interferogram fringes during a sensing experiment conducted with a chip having two parallel 2-channel YIs. The red arrow shows the shift of a fringe when an MIP-functionalized YI was exposed to sample solution containing 1.0 g/l melamine in water. The image was constructed by selecting a same 5-pixel section across each of the interferograms captured during the experiment and combining them. The chip configuration is discussed in Section 3.2.2 and the experiment in Section 4.2.3.

The chip shown in Figure 8 is used to derive the mathematical formulation for the calculation of the shifts of the interferogram fringes. The measurement channel is coated with an overcladding layer except at the measurement window with length l, whereas the reference channel is passivated with an overcladding layer. Now the channels are similar everywhere else except within length l. It can be assumed that within the similar sections of the channels the changes in the effective RIs are identical, and thus these sections do not contribute to the change in the mutual optical path length difference. It is thus sufficient to study the changes within length l.

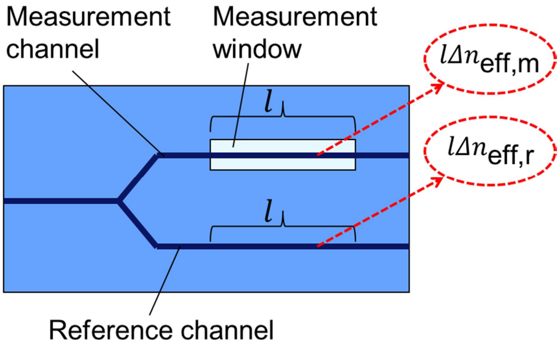

Figure 8 Illustration for the calculation of the phase changes of the fringes.

When the effective RI of the measurement channel is changed by an amount $\Delta n_{\mathrm{eff,m}}$ within the measurement window, the optical path length of the waveguide is changed by an amount $\Delta l_{\mathrm{opt,m}} = \Delta n_{\mathrm{eff,m}} l$, as illustrated in Figure 8. Similarly, the optical path length of the reference channel waveguide is changed by $\Delta l_{\mathrm{opt,r}} = \Delta n_{\mathrm{eff,r}} l$, where $\Delta n_{\mathrm{eff,r}}$ is the change in the effective RI of the reference channel. This is also illustrated in Figure 8. Now the change in the mutual optical path length difference between the channels is $\Delta l_{\mathrm{opt}} = l(\Delta n_{\mathrm{eff,m}} - \Delta n_{\mathrm{eff,r}})$. By dividing Δl_{opt} by λ, the number of wavelength periods that Δl_{opt} equals can be calculated. The positions of the fringes at the camera detector are shifted an equal number of periods in the function of the spatial wavelength Λ since the positions of the fringes at the camera detector are directly related to the optical path length difference between the channels, i.e. if Δl_{opt} equals one λ the fringes are shifted by one Λ.

The shifts in wavelength periods can be converted into phase changes $\Delta\phi$ by multiplying with 2π, i.e. the phase change corresponding to a shift of one period. Now the sample-induced phase change, $\Delta\phi$, of the interferogram fringes can be calculated [19]

$$\Delta\phi = 2\pi \frac{l\Delta n_{\mathrm{eff,m}} - l\Delta n_{\mathrm{eff,r}}}{\lambda} = \frac{2\pi}{\lambda} l\Delta n_{\mathrm{eff}}, \qquad (2)$$

where Δn_{eff} is the difference in the changes in the effective refractive indices of the measurement and the reference channels. It can be seen that the phase changes are linearly proportional to the length of the measurement window and the change in Δn_{eff}, and inversely proportional to the wavelength of the light.

The sensitivity of the sensor, S, represents the rate of the interferogram fringe shift in relation to the sample-induced RI change. The sample can either change the RI of the overcladding, Δn_{OC}, or change the thickness of the adlayer, Δd_{AL}, on top of the waveguide, for example due to analyte molecules binding to the receptors.[18] The analyte binding changes the RI since the sample matrix is replaced by compounds having a different RI.[19] The sample-induced phase change can be calculated [18]

$$\Delta\phi = \underbrace{\frac{2\pi}{\lambda} l \frac{\partial \Delta n_{\mathrm{eff}}}{\partial n_{OC}}}_{S_{OC}} \Delta n_{OC} + \underbrace{\frac{2\pi}{\lambda} l \frac{\partial \Delta n_{\mathrm{eff}}}{\partial d_{AL}}}_{S_{AL}} \Delta d_{AL}, \qquad (3)$$

where S_{OC} and S_{AL} are the sensor sensitivities to the changes in the overcladding RI and in the adlayer thickness, respectively.

To analyse the sample-induced phase changes in the experiments, the interferograms are captured during the experiments as time lapse images. Interferograms can be analysed using discrete Fourier transform, for example fast Fourier transform (FFT) algorithm in commercial software. The spatial frequency, *k*, of the interferogram fringes is seen as a peak in the amplitude spectrum, as shown in Figure 9. Phase changes can be calculated by analysing the phase values related to the spatial frequency *k* at different time points in the experiments. The phase change of the interferogram fringes at time *t*, $\Delta\phi(t)$, can be calculated

$$\Delta\phi(t) = \phi(t) - \phi(t_0), \qquad (4)$$

where $\phi(t)$ and $\phi(t_0)$ are the phase values related to spatial frequency *k* at time *t*, and at the beginning of the experiment at time t_0, respectively. A phase change curve in an experiment is obtained by analysing the phase changes of the interferograms captured during the experiment and plotting them as a function of time.

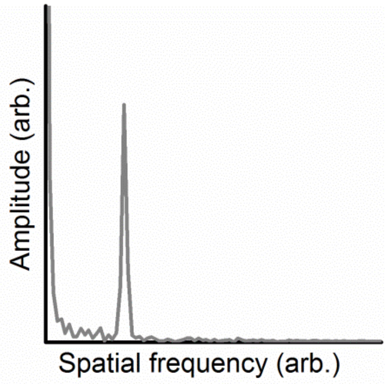

Figure 9 Amplitude spectrum where the spatial frequency *k* of the interferogram fringes is seen as a well-defined spike

2.1.2 Multichannel integrated Young interferometers

An example of a multichannel YI chip with 3-channels is illustrated in Figure 10(a) with channel numbering. In the illustrated chip, channels 1 and 2 are measurement channels and channel 3 is a reference channel. An interferogram of a multichannel YI is a superposition [19] of the two beam sub-interferograms formed by all the possible channel pairs, i.e. channel pairs 1&2, 1&3, and 2&3 in the example discussed here, as illustrated in Figure 10(b). The intensity distribution I of a multichannel YI interferogram along the *y*-axis (shown in Figure 6) is [19]

$$I(y) \approx \sum_{i=1}^{N} I_i + 2 \sum_{i,j=1;i<j}^{N} \left(I_\mathrm{i} I_\mathrm{j}\right)^{1/2} \cos(\varphi(y) - \Delta\phi_0 - \Delta\phi), \qquad (5)$$

where I_i and I_j are the powers of the light beams emanating from the channels *i* and *j*, respectively.

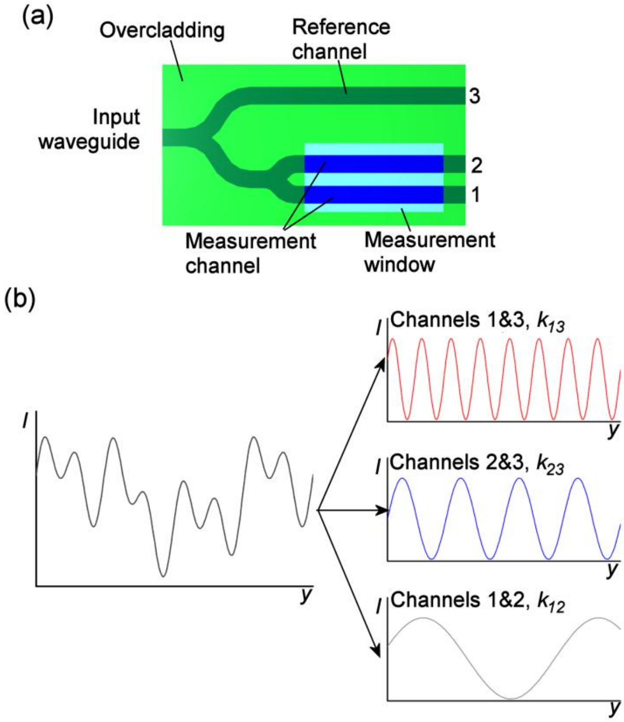

Figure 10 a) Schematic illustration of a 3-channel YI sensor chip. b) Left, schematic illustration of a 3-channel interferogram intensity (*I*) distribution across the fringes. Intensity distribution is a superposition of the sub-interferograms shown on the right.

The phase changes of the channel pairs are analysed in a similar way to that in the 2-channel YI case discussed above. In order to be able to analyse the sub-interferograms individually, they must all have their own spatial frequency i.e. the separations of the channel pairs at the outcoupling end have to be unique. This is since the spatial frequency, k_{ij}, of the sub-interferogram fringes formed by the channel pair *i&j* is dependent on their separation, d_{ij}, at the outcoupling end of the chip as

$$k_{ij} = \frac{d_{ij}}{\lambda L}, \tag{6}$$

where L is the distance between the end of the chip and the camera and $L \gg d_{ij}$.[19] In addition, the channel separations have to be chosen so that they are not integer multiples of the separation of some other channel pair, to reduce the cross-talk between the sub-interferograms in DFT analysis. [19]

2.2 Theory of the drift compensation with multichannel Young interferometers

The theory of the drift compensation calculation is presented in this section. The method enables the sample-induced phase changes to be calculated despite mechanical disturbances. Calculation is based on the analysis of the spatial shifts of the sub-interferogram fringes of a multichannel YI with two reference channels. The discussion here follows the discussion in Paper I.

The 3-channel YI sensor chip shown in Figure 11(a) is used to derive the calculation of the drift-compensated phase changes. Channel 1 is the measurement channel with the measurement window for sample interaction and channels 2 and 3 are reference channels.

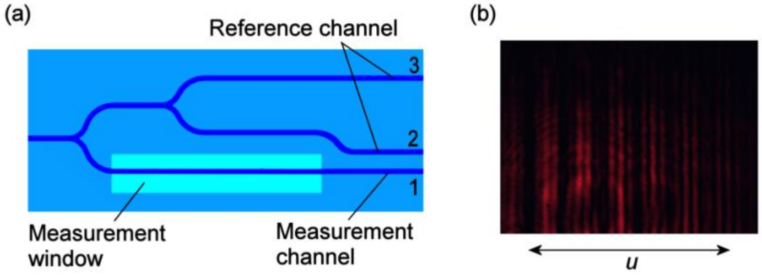

Figure 11 a) Illustration of a 3-channel YI sensor chip showing numbering of the measurement and reference channels used in the derivation of the theory. b) Captured interferogram with an arrow showing the *u*-direction discussed in the derivation.

When the YI chip is used to measure RI changes within the measurement window, the measured phase shift is a combination of the phase change components induced by:

1. Sample solutions
2. Internal drift of the chip (e.g. caused by temperature fluctuations)
3. Mechanical drift of the setup (e.g. caused by the movement of components).

The first two of the listed phase change components are related to changes occurring at or within the chip. If they affect in a similar way to channel pairs, they induce the same phase change to corresponding sub-interferograms. The effect of the mechanical drift of the setup, however, is different: if the mechanical drift of the setup moves the fringes of the sub-interferograms along the u-direction in Figure 11(b), the same mechanical displacement induces different phase changes to the sub-interferograms. This is illustrated in Figure 12 where the grey rectangle over the sub-interferograms shows the same spatial shift caused, for example, by the movement of the camera. Although the rectangle spans the same spatial distance in all the sub-interferograms, it spans a different number of fringe periods in each of them. The analysis of the effect of the mechanical drift between channel pairs thus has to be made by analysing the spatial shifts of the sub-interferogram fringes instead of the phase changes.

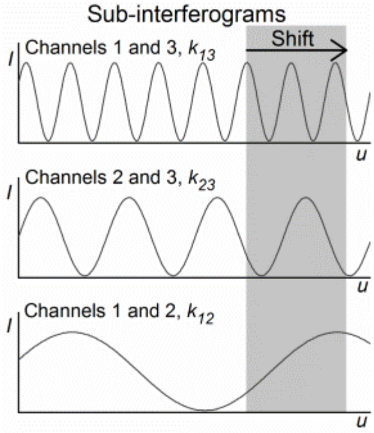

Figure 12 Illustration of how the same lateral shift (grey rectangle) induces different phase changes between the sub-interferograms. (Paper I)

The calculation of the drift compensation is initiated by using DFT to analyse the captured interferograms yielding the spatial frequency k_{ij} and phases $\phi_{ij}(t)$ of the sub-interferogram formed by channel pair *i&j*. These are analysed for all the channel pairs, i.e. 1&2, 1&3, and 2&3. This is Stage 1 in Figure 13.

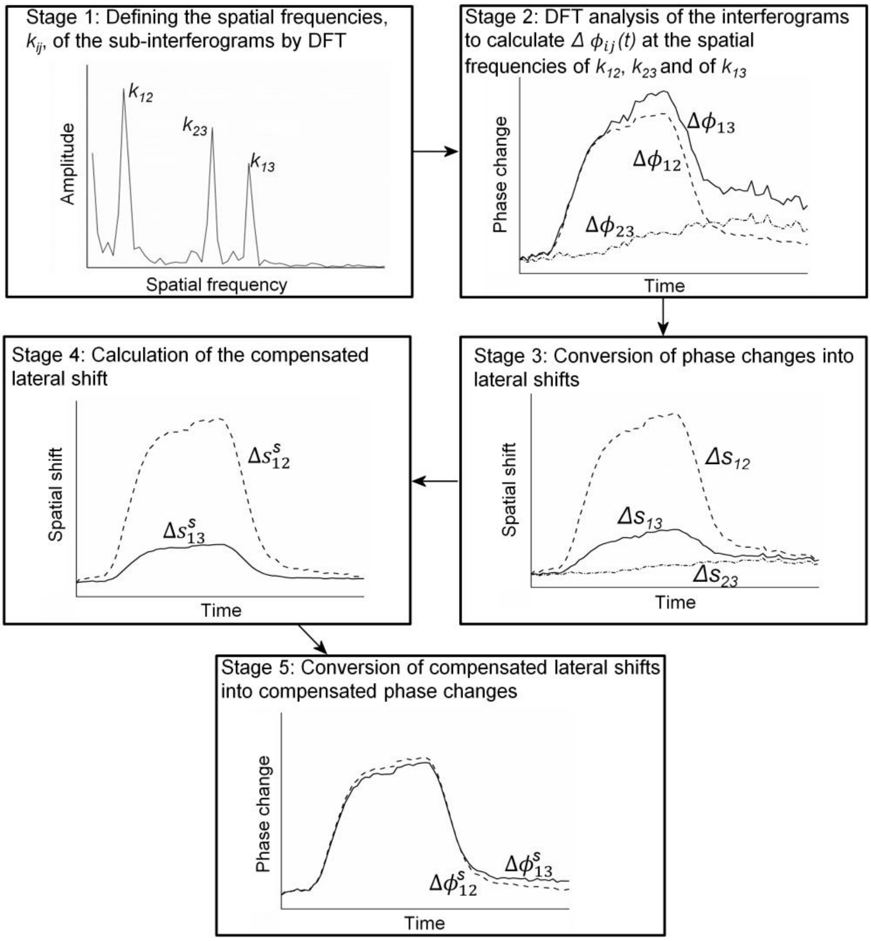

Figure 13 Stages in the calculation of the compensated signals. Curves are calculated using the data from an experiment measured with the 3-channel inverted ridge waveguide YI with undisturbed setup and 0.05 wt. % glucose solutions as samples. The experiment is discussed in Section 4.1.3.1.

Phases ϕ_{ij} are used to calculate the phase changes $\Delta\phi_{ij}(t)$ for all possible channel pairs *i&j*, using Eq. (4) (p. 31). This is shown as Stage 2 in Figure 13. The phase changes are converted into lateral shifts Δs_{ij} of channel pair *i&j* using relationship

$$\Delta s_{ij}(t) = \frac{\Delta\phi_{ij}(t)}{2\pi}\Lambda_{ij} = \frac{\Delta\phi_{ij}(t)}{2\pi k_{ij}} \qquad (7)$$

where Λ_{ij} is the spatial wavelength of the sub-interferogram fringes formed by channel pair *i&j*. This is Stage 3 in Figure 13.

As listed, the measured phase changes are caused by three factors and the lateral shift of channel pair *i&j*, Δs_{ij}, can thus also be expressed as a sum of the same factors,

$$\Delta s_{ij}(t) = \Delta s_{ij}^{s}(t) + \Delta s_{ij}^{d}(t) + \Delta s_{ij}^{I}(t), \tag{8}$$

where Δs_{ij}^{s} is the lateral shift caused by the interaction of the sample, Δs_{ij}^{d} the lateral shift caused by the drift of the setup, and $\Delta s_{ij}^{I}$the lateral shift caused by the internal drifts of the chip.

Since the channels share the components of the optical setup and are integrated into a single chip, it can be assumed that Δs_{ij}^{d} is the same for all channel pairs and we can rewrite Eq. (8)

$$\Delta s_{ij}(t) = \Delta s_{ij}^{s}(t) + \Delta s^{d}(t) + \Delta s_{ij}^{I}(t), \tag{9}$$

where Δs^{d} is the lateral shift caused by the drift of the setup.

Eq. (9) can now be written for channel pairs 1&3 and 2&3

$$\Delta s_{13}(t) = \Delta s_{13}^{s}(t) + \Delta s^{d}(t) + \Delta s_{13}^{I}(t) \tag{10}$$

$$\Delta s_{23}(t) = \Delta s_{23}^{s}(t) + \Delta s^{d}(t) + \Delta s_{23}^{I}(t). \tag{11}$$

Since channels 2 and 3 are reference channels, they do not interact with the sample and thus

$$\Delta s_{23}^{s}(t) = 0. \tag{12}$$

Now we can substitute Eq. (12) for Eq. (11) and solve Δs^{d}

$$\Delta s^{d}(t) = \Delta s_{23}(t) - \Delta s_{23}^{I}(t). \tag{13}$$

The sample-induced spatial shift of channel pair 1&3, Δs_{13}^{s}, can be solved from Eq. (10)

$$\Delta s_{13}^{s}(t) = \Delta s_{13}(t) - \Delta s^{d}(t) - \Delta s_{13}^{I}(t), \tag{14}$$

and by substituting Δs^{d} from Eq. (13) into Eq. (14) we get

$$\Delta s_{13}^{s}\,(t) = \Delta s_{13}(t) - \Delta s_{23}(t) + \Delta s_{23}^{I}(t) - \Delta s_{13}^{I}(t) \qquad (15)$$

that is the drift-compensated sample-induced lateral shift of channel pair 1&3.

The internal drifts of the chip, Δs_{23}^{I} and Δs_{13}^{I}, in Eq. (15) are unknown in the experiments discussed in this thesis and the exact value of Δs_{13}^{s} therefore cannot be calculated. However, it can be assumed that the internal drifts are small, since the waveguides are located near each other at a single sensor chip and are exposed to similar temperature fluctuations, and Eq. (15) can thus be approximated

$$\Delta s_{13}^{s}\,(t) \approx \Delta s_{13}(t) - \Delta s_{23}(t), \qquad (16)$$

which is the sample-induced lateral shift used in the calculations in this thesis. This is Stage 4 in Figure 13.

The lateral shift of Eq. (16) can be converted back into a phase change by using the relationship in Eq. (7). If the conversion is done by using the initial spatial frequency, k_{13}, of the sub-interferogram of channel pair 1&3, the calculated phase change values can be compared with the initial measured values. The sample-induced drift-compensated phase change of channel pair 1&3, $\Delta\phi_{13}^{s}$, can now be written

$$\Delta\phi_{13}^{s}(t) = 2\pi k_{13} \mathit{\Delta} s_{13}^{s}(t). \qquad (17)$$

This is Stage 5 in Figure 13 and completes the calculation of the compensated phase change signal.

A compact expression for $\Delta\phi_{13}^{s}$ can be derived by first substituting Eq. (16) into Eq. (17) to obtain

$$\Delta\phi_{13}^{s}(t) = 2\pi k_{13}\big(\Delta s_{13}(t) - \Delta s_{23}(t)\big), \qquad (18)$$

and then using the relationship in Eq. (7) to write

$$\begin{aligned}\Delta\phi_{13}^{s}(t) &= 2\pi k_{13}\left(\frac{\Delta\phi_{13}(t)}{2\pi k_{13}} - \frac{\Delta\phi_{23}(t)}{2\pi k_{23}}\right)\\ &= \Delta\phi_{13}(t) - \frac{k_{13}}{k_{23}}\Delta\phi_{23}(t) \qquad (19)\\ &= \Delta\phi_{13}(t) - \frac{d_{13}}{d_{23}}\Delta\phi_{23}(t). \qquad (20)\end{aligned}$$

The two latter forms of Eq. (20) are similar to the relationship given by Ymeti et al. in Ref. [58] for the calculation of the drift-compensated signal. The form presented in Eq. (20) was derived using the relationship of Eq. (6) (p. 33) and is thus valid only when the separation of the camera and the chip is much larger than the separation of the channel pair. In this thesis, the compensated phase change curves are calculated by applying Eqs. (16) and (17) or equivalently Eq. (19).

The drift-compensated phase changes of channel pair 1&2 can be analysed in a similar way. The calculation of the drift compensation can be applied to YI chips having more than one measurement channel by analysing every measurement channel individually.

Looking at the last form of Eq. (20) it can be seen that the multiplier for $\Delta\phi_{23}$can be defined based on the chip geometry and there is no need to define it from the experimental data. However, in the experiments the multiplier obtained using the ratio of channel separations may differ from the ratio of the spatial frequencies if the DFT analysis is unable to identify the spatial frequencies of the sub-interferograms exactly. This can occur, for example, when the spatial frequency of a sub-interferogram falls in-between two discrete spatial frequencies defined by the DFT analysis. In this thesis, the compensated phase changes are calculated using the spatial frequencies.

3. Young interferometer sensor chip embodiments

In this chapter, the five chip embodiments used in the experiments are introduced: two sensor layouts were used in the drift compensation experiments and three sensor embodiments were used to study the applicability of the R2R fabricated waveguides for integrated YI sensor chips. The discussion of the chip types includes short descriptions of the chip manufacturing methods, and chip specific sensing principles with the slot waveguide YI and R2R fabricated sensor platforms.

3.1 Young interferometer sensor chips for drift compensation experiments

This section discusses 3-channel chip layouts used in the drift compensation experiments. The chips have two reference channels and one measurement channel. The 3-channel inverted ridge waveguide YI sensor layout is described first followed by a discussion of the slot waveguide YI sensor. The differences in the sensing principle of the slot waveguide YI compared to the sensing principle of the basic 2-channel YI are pointed out. The chips' fabrication steps are also briefly described.

3.1.1 3-channel inverted ridge waveguide Young interferometer chip

A schematic of a 3-channel inverted ridge waveguide YI sensor chip is shown in Figure 14(a) with dimensions and channel numbering. The input waveguide has two Y-junctions branching it into three waveguides. The middle channel, i.e. reference channel number 2, crosses over the chip, enabling patterning of the measurement window with loose tolerances and improving the outcome of the drift compensation method by enhancing the similarity between the drifts of channels 1 and 2. The separations of the waveguides at the outcoupling end of the chip were chosen such that every channel pair, i.e. channel pairs 1&2, 1&3 and 2&3, had a unique separation, ensuring that the phase changes of the sub-interferograms could be monitored individually. In addition, the channel pair separations are not integer multiples of each other to reduce cross-talk in DFT analysis.

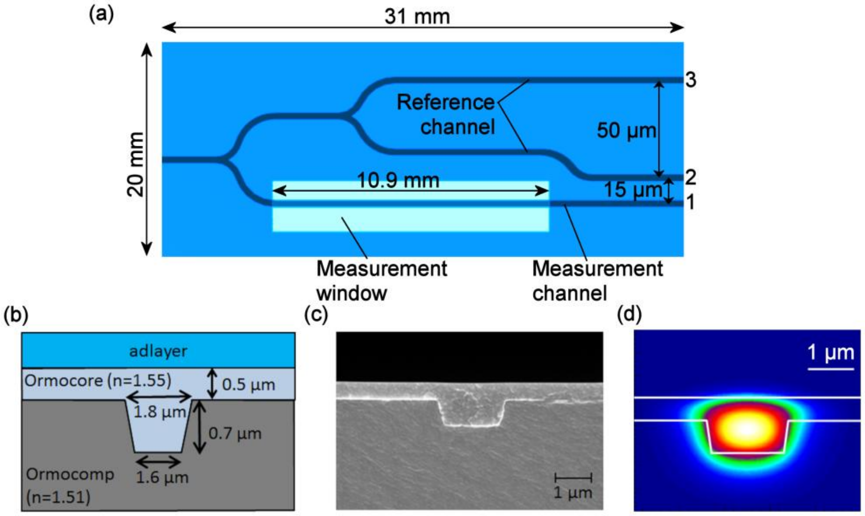

Figure 14 a) Schematic layout and chip dimensions of the 3-channel inverted ridge waveguide YI sensor chip. b) Cross-section of the inverted ridge waveguide showing the materials and their refractive indices. c) SEM image of the waveguide cross-section. d) Simulated TM-mode field profile. (Figure (b) and (c) from Paper I)

The sensor layout was realized using polymeric single-mode inverted ridge waveguides designed to work at a wavelength of 633 nm. The dimensions of the waveguides, used polymers and their RIs are shown in Figure 14(b), and a scanning electron microscope (SEM) image of the waveguide cross-section in Figure 14(c). The simulated transverse magnetic mode (TM-mode) field profile is shown in Figure 14(d). Optical field intensity distribution was modelled when the waveguide was covered with water. According to simulations, 0.4% of the optical field intensity was confined in water.

Waveguides were fabricated using the UV-imprinting method.[60, 61] The fabrication steps are illustrated in Figure 15. UV-curable undercladding material (Ormocomp, Micro resist technology) was first dispensed onto a silicon wafer that was used as a mechanical support having no role in the optical operation of the waveguides. Waveguide grooves were fabricated by pressing a mould with ridge structures into uncured undercladding material and curing the undercladding material with UV-light through the transparent mould. The mould was fabricated using a combination of UV-lithography and UV-nanoimprinting techniques.[61] The grooves were filled with the waveguide core material (Ormocore, Micro resist technology) by means of spin coating and the layer was cured by UV-exposure.

The UV-curable overcladding layer (Ormoclad, Micro resist technology) was spin coated onto the structure, and the measurement window was patterned lithographically on the measurement channel.

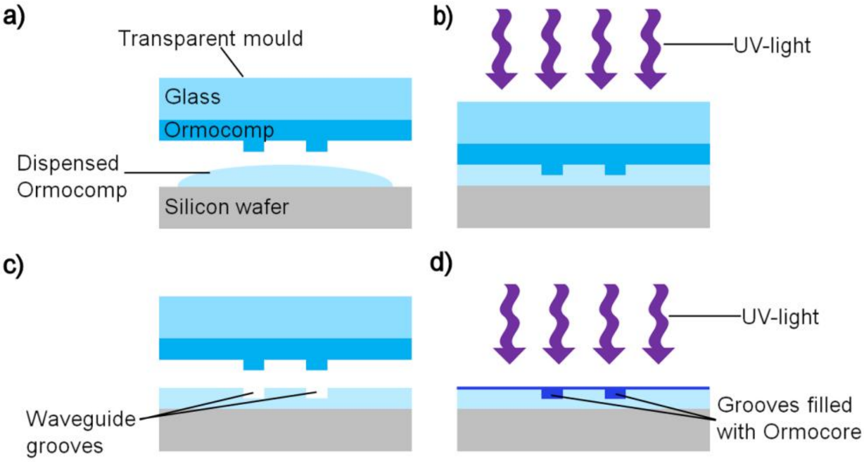

Figure 15 Fabrication steps of inverted ridge waveguides. a) Undercladding material (Ormocomp) is dispensed onto a silicon wafer. b) The mould is pressed against the undercladding material, which is then cured by UV-light exposure through the transparent mould. c) The mould is detached from the cured undercladding material that now has waveguide grooves. c) The grooves are filled with the waveguide core material (Ormocore) by spin coating and the material is cured by UV-light exposure.

An image of the beams emanating from the outcoupling end of the sensor chip is shown in Figure 16(a), example of a 3-channel YI interferogram in Figure 16(b), and the amplitude spectrum in Figure 16(c). The amplitude spectrum shows three well-defined peaks that indicate the spatial frequencies of the three sub-interferograms formed by channel pairs 1&2, 2&3, and 1&3.

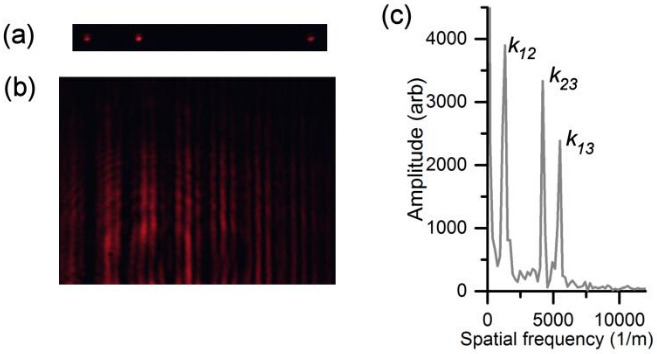

Figure 16 a) Image of beams emanating from the outcoupling end of the chip. b) Captured 3-channel interferogram. c) Amplitude spectrum of the 3-channel cross-over YI chip.

3.1.2 3-channel slot waveguide Young interferometer chip

A schematic illustration of the multichannel slot waveguide YI chip is shown in Figure 17(a) with dimensions and channel numbering. The input ridge waveguide has two Y-junctions splitting it into three parallel waveguides. Channel 1 is the measurement channel, which has a slot structure, i.e. a narrow groove with a length of 7.5 mm and a width of about 150 nm. Channels 2 and 3 are reference channels formed by ridge waveguides without slot structures. The ridge and slot waveguide regions of channel 1 change abruptly without any tapered interconnection section and thus mode mismatch losses occur at these two abrupt slot-ridge waveguide interfaces. According to simulations, the mode mismatch loss of these two interfaces is 1 dB. (Paper II) Due to the higher losses of the measurement channel it was placed in channel 1, enabling coupling of higher optical power to the slot structure. In principle, the slot structure could have been placed in any one of the channels. The channel separations were designed such that the spatial frequencies of the sub-interferograms differ in DFT analysis. Figure 17(b) is a top view microscope image showing part of the chip. SEM images of the cross-sections of the slot and inverted ridge waveguides are shown in Figure 17(c) and simulated transverse electric -mode (TE-mode) field profiles of the slot and ridge waveguides in Figure 17(d).

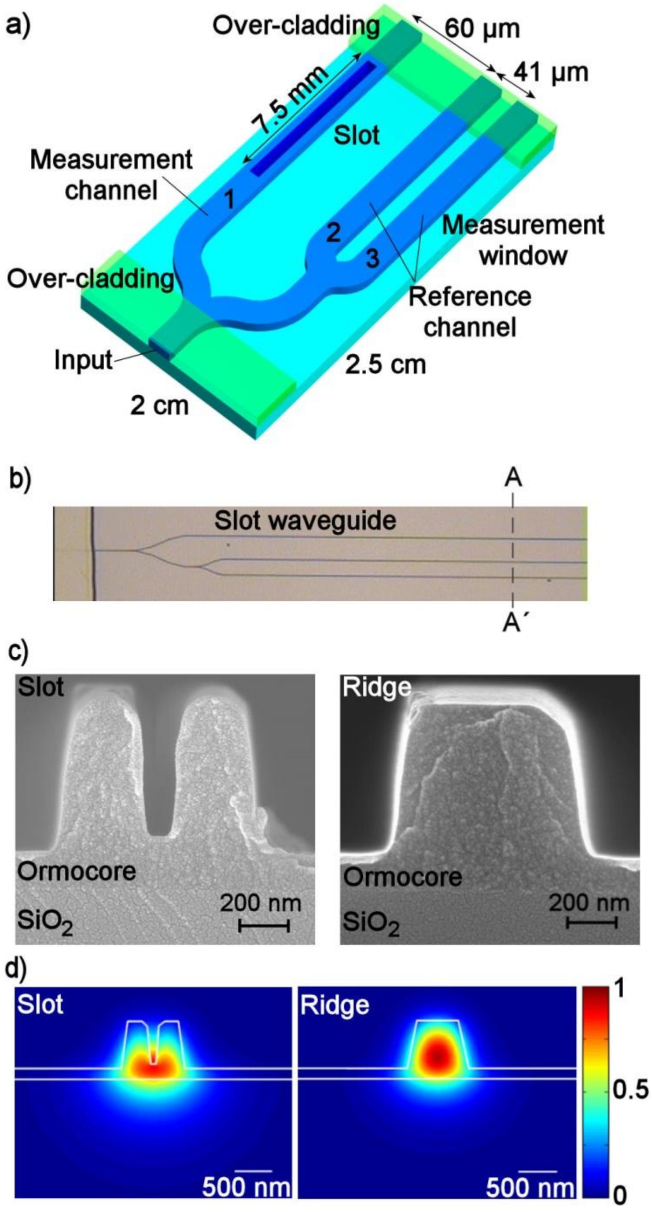

Figure 17 a) Schematic of slot waveguide YI with chip dimensions and channel numbering, b) top view microscope image of sensor waveguides, c) SEM images of the cross-sections of slot and ridge waveguides taken approximately along line A-A’ in figure b, and d) simulated TE-mode field profiles of slot and ridge waveguides. (Paper II)

The ends of the chip were protected by an overcladding layer that also defines the measurement window for the sample interaction. It is worth noting that the reference channels are not covered by the overcladding layer, contrary to the basic 2-channel case discussed in Section 2.1, but all the channels are exposed similarly to the samples in the measurement window. Although the measurement window is defined by the overcladding layer, the sensing length of the sensor is defined by the length of the slot structure since it is the only part where the measurement and reference channels differ significantly and react differently to the sample-induced RI changes. Since the sensing length is defined by the slot structure, the patterning of the measurement window can be done with loose tolerances. Since the Y-junctions are within the measurement window, the measurement and reference channels also differ due to the Y-junction branching reference channels 2 and 3. However, the length of the differing part of the measurement and reference channels is only 100 µm being thus much shorter than the sensing length (7.5 mm), and has little impact on the sensor responses.

The sensing principle of the slot waveguide YI sensor is based on the difference between the changes in the effective RIs of the slot and ridge waveguides when exposed to sample-induced RI changes. It has been shown that the same RI change within the measurement window induces a larger effective RI change of the slot structure than of the ridge waveguide.[25] According to simulations, the effective RI change of the slot and ridge waveguides was 11% and 7%, respectively, of the ambient RI change. When the RI within the measurement window is modified by the sample, the mutual optical path length difference between the measurement and reference channels therefore changes again shifting the interferogram fringes. The larger effective RI change in the slot structure is caused by the electric field confined in the narrow gap, as shown in the simulated TE-mode field profile in Figure 17(d). The change in the effective RI of the slot structure is larger because a larger share of the electric field is confined in the covering medium than with the ridge waveguide, as shown in the simulated TE-mode field profiles in Figure 17(d). Simulations showed that when the slot structure is covered with water, 5.4% of the optical field intensity is confined in the groove and a total of 10.4% in water. Similarly, 5.4% of the optical field intensity was confined in water with the ridge waveguide geometry. The difference in the changes of the effective refractive indices between the slot and ridge waveguides enables a sensor layout where all the channels are exposed similarly to the samples.

The manufacturing steps [25] of the ridge waveguides with and without the slot structures are shown in Figure 18. The transparent polymeric (Ormocomp) mold is fabricated by UV-nanoimprinting from the silicon master fabricated by electron beam lithography. The sensor waveguide is moulded by first spin coating UV-curable waveguide core polymer (Ormocore, RI 1.553) onto a silicon oxide wafer. The mould is pressed into the waveguide core material, which is then cured by UV-light through the mould. The mould is detached from the waveguide structures and the waveguide fabrication is finalized by hard-baking on a hotplate. The protective overcladding layer is patterned using lithography. UV-curable overcladding polymer (Ormostamp, Micro resist technology) is spin coated onto the sensor waveguides and cured by UV-exposure through a shadow mask, leaving the region of the measurement window uncured. The overcladding layer is developed to remove the uncured material, forming the opening for the measurement window. The polymer mould can be used to fabricate several sensor chips, enabling simple low-cost fabrication of replicas.

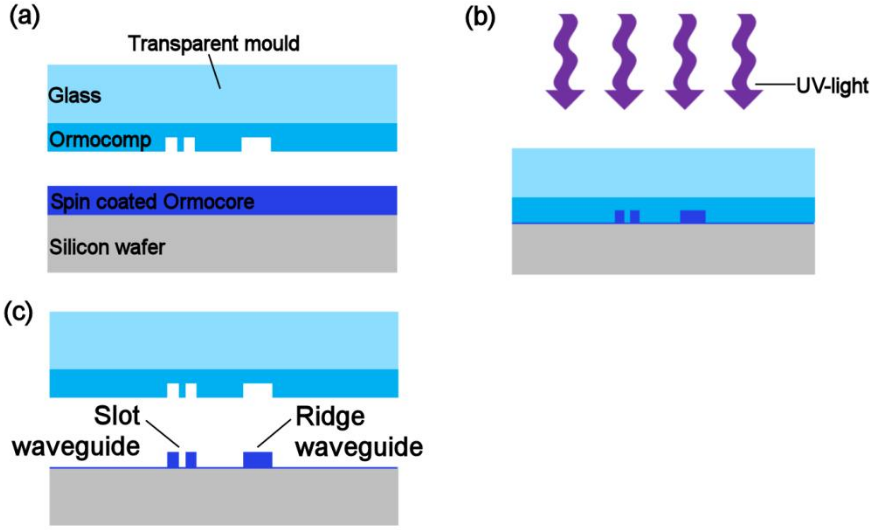

Figure 18 Fabrication steps of ridge waveguides and slot structures. a) The waveguide core material (Ormocore) is dispensed onto a silicon wafer. b) The mould is pressed into the core material and cured with UV-light exposure through the transparent mould. c) The mould is detached after curing and the waveguides are formed.

An image of the beams emanating from the outcoupling end of the sensor chip is shown in Figure 19(a), example of a captured interferogram in Figure 19(b), and the amplitude spectrum in Figure 19(c). The amplitude spectrum shows three well-defined peaks that indicate the spatial frequencies of the three sub-interferograms formed by channel pairs 1&2, 2&3, and 1&3.

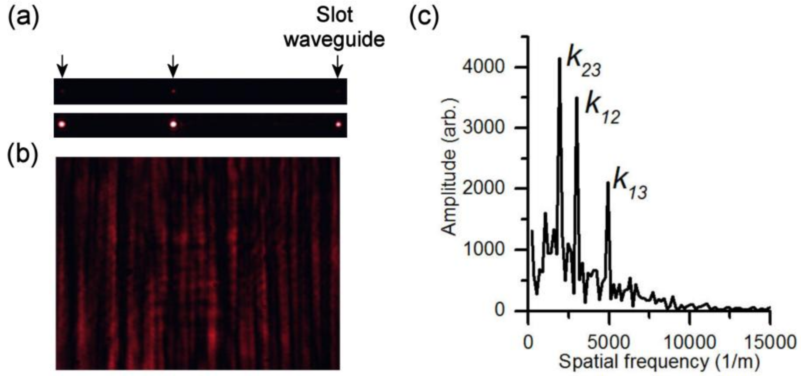

Figure 19 a) Image of the beams emanating from the outcoupling end of the sensor chip. The arrows indicate the beam locations. The upper figure is filtered so that beams are not overexposed. Lower picture is taken without filtering and clearly shows the three outcoupling beams. b) Captured interferogram of a 3-channel slot waveguide YI. c) Amplitude spectrum showing three well-defined spikes at the frequencies corresponding to the spatial frequencies of the sub-interferograms. (Figures (b) and (c) from Paper II)

3.2 Young interferometer sensor chips based on roll-to-roll fabricated waveguides

A schematic of the sensor waveguide platform fabricated by R2R processing is shown in Figure 20(a). The input waveguide has three Y-junctions branching it into four waveguides. These form two parallel 2-channel YIs named YI1 and YI2, each of which has a measurement channel and a reference channel. The separation between the reference and measurement channels is increased within the sensing area, enabling patterning of overcladding and receptor layers with loose positional tolerances.

In the experiments, laser light was end-fire coupled into the input waveguide and split into the interferometer channels. When light couples out from the chip, the beams diverge and overlap. If the imaging is done sufficiently close to the outcoupling end of the chip, the beams overlap and interfere only with the nearest beam and thus two separate 2-channel interferograms are formed. In addition, the setup can be configured so that the interferograms are imaged simultaneously onto a single camera detector, as shown in Figure 20(a), enabling both interferometers to be monitored. The optical setup is described in detail in Section 4.2.1 (p. 70).

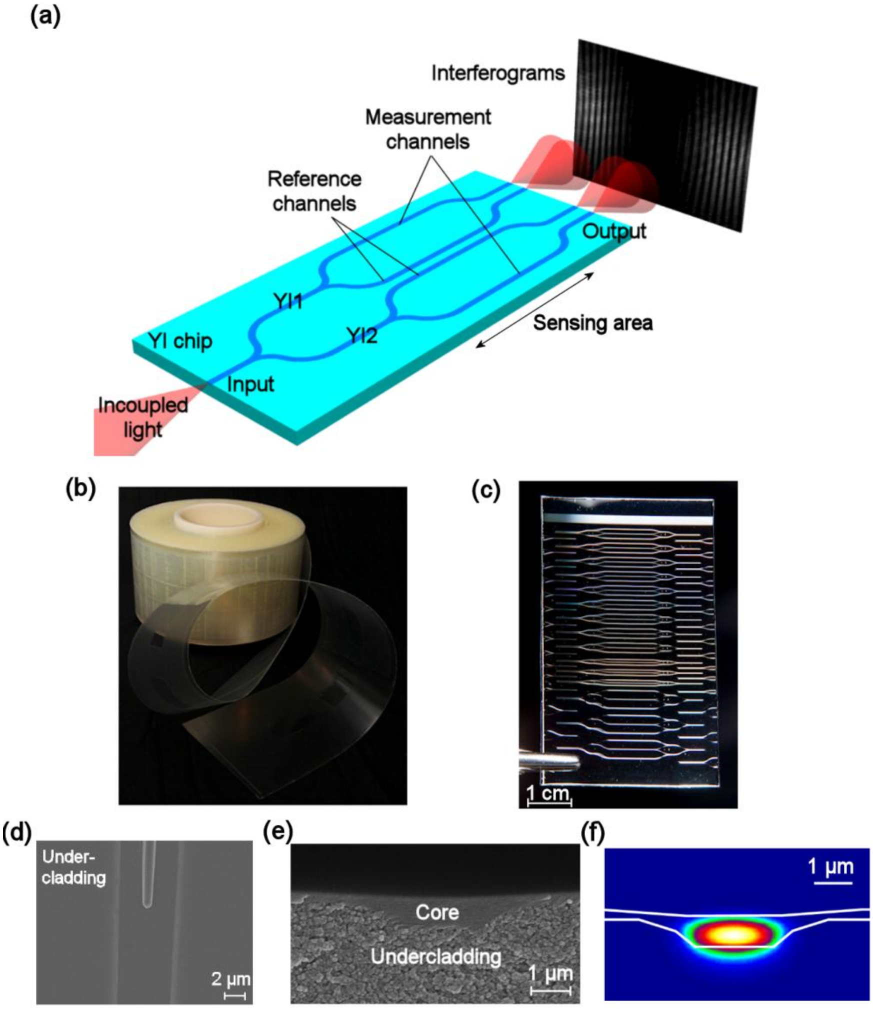

Figure 20 a) Schematic illustration of the sensor chip layout with two parallel 2-channel YIs. The embedded image shows two 2-channel interferograms captured simultaneously onto a single camera detector. b) Roll of sensor waveguides. c) Sensor waveguides cut from the roll. d) Top view image of the waveguide groove, showing a Y-junction. e) SEM image of the waveguide cross-section. f) Simulated TM-mode field profile. (Paper III)

Single-mode inverted ridge waveguides for the sensor chips were manufactured by R2R processing in two phases. A roll of waveguide platforms is shown in Figure 20(b). In the first phase, the waveguide grooves were manufactured into the undercladding layer and in the second phase the grooves were filled. A waveguide groove is shown in Figure 20(d) and a cross-section of the waveguide in Figure 20(e). A simulated TM-mode field profile is shown in Figure 20(f). Optical field intensity distribution was modelled when the waveguide was covered with water. According to simulations, 2.1% of the optical field intensity was confined in water.

The R2R units for the waveguide groove fabrication and for the groove filling are shown in Figure 21(a) and Figure 21(b), respectively, with manufacturing steps. The waveguide grooves were manufactured using the UV-nanoimprinting method. The UV-curable acrylate-based undercladding material (Nalax2, RI 1.508, Nanocomp) was applied onto polycarbonate carrier foil using the gravure coating method.[62] In the gravure coating method, the coating material is deposited onto the substrate using a printing roll that has small pits. The container below the printing roll contains the solution to be coated. The lower edge of the printing roll is submerged in the solution. When the roll traverses through the container, the pits are filled with the solution, and when the roll touches the carrier the pits are emptied and the coating material is transferred onto the carrier. In the second fabrication phase, the waveguide grooves were filled with the epoxy-based waveguide core material (Epocore, RI 1.583, Micro resist technology) using the gravure coating method. The length of the processed roll was about 200 m and the width 15 cm.

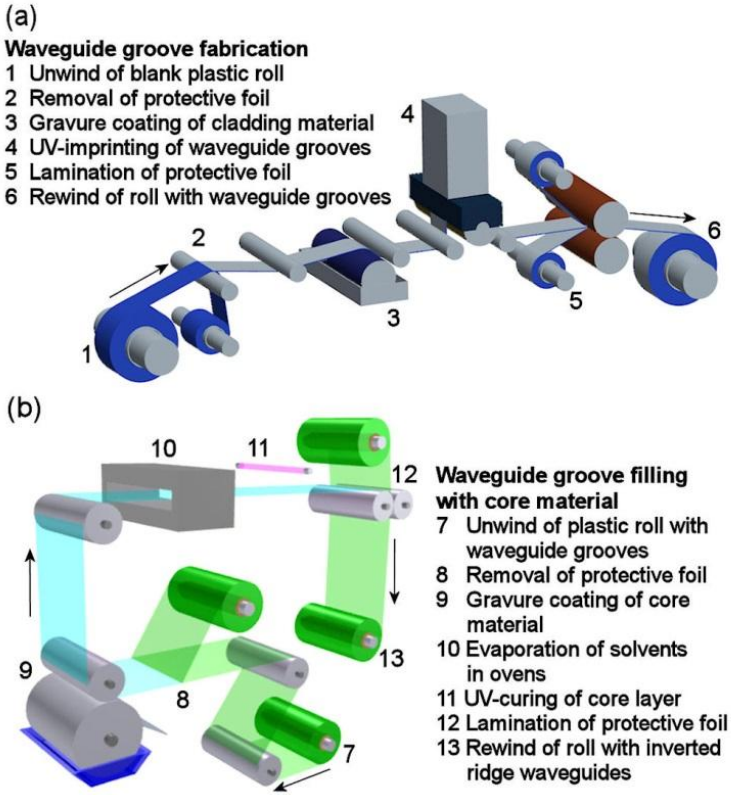

Figure 21 Schematic of the R2R units and the fabrication steps in a) waveguide groove manufacturing and b) waveguide groove filling. (Paper III)

Sensor chips were cut from the roll for post-processing, as shown in Figure 20(c). Three different sensor schemas were designed: one for sensing of ambient RI changes, one for chemical sensing, and one for multi-analyte biochemical sensing. Cross-sections of the sensor embodiments within the sensing area are shown in Figure 22(a)-(c), and the chip dimensions in Figure 22(d). An optical adhesive (OP-4-20632, Dymax) based overcladding layer was applied onto the sensor chips, defining the measurement window for sample interaction and acting as a passivation layer on top of the waveguides when required by the sensor embodiment. The overcladding layer was also required by the single-mode operation of the waveguides. (Paper III) Sensor schemas are discussed in detail in Sections 3.2.1-3.2.3 below.

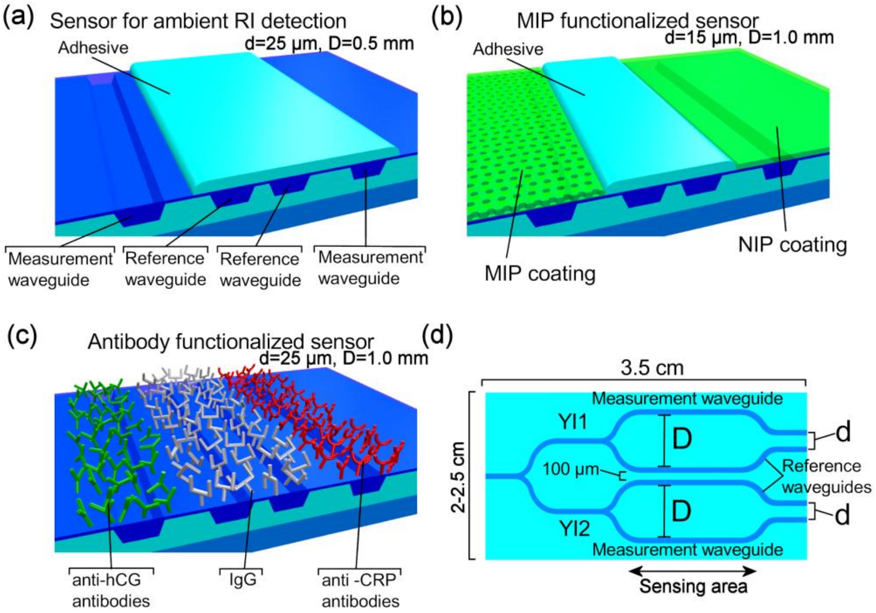

Figure 22 Illustration of cross-sections of the sensor chip schemas within the sensing area. a) Non-functionalized sensor chip for ambient RI sensing, b) chip functionalized with MIP receptor layer and non-imprinted polymer (NIP) reference layer for chemical sensing, and c) antibody-functionalized chip for multi-analyte detection of biomolecules. d) Sensor chip dimensions. Separation of the measurement and reference waveguides, D, within the sensing area, and centre-to-centre separation of the waveguides at the outcoupling end of the chip, d, are shown next to the illustrations in sub-figures (a)-(c). (Figures (b) and (c) from Paper IV)

3.2.1 Chip for sensing ambient refractive index

An illustration of the chip layout for ambient RI sensing is shown in Figure 23 with dimensions. Two chips were post-processed by applying an overcladding layer on the waveguides. The measurement channel of YI2 was left uncoated for a length of 10 mm, forming a measurement window for sample interaction. YI1 was completely passivated with an adhesive layer and did not interact with the samples. YI1 thus measured only the drift of the setup. In the experiments, chips were exposed to aqueous glucose solutions to measure ambient RI changes.

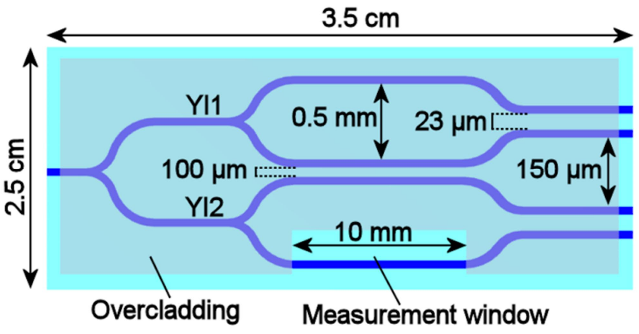

Figure 23 Sensor chip layout for ambient RI sensing. (Paper III)

3.2.2 MIP/NIP-functionalized chip for chemical sensing

An illustration of the YI chip for chemical sensing is shown in Figure 24. The reference waveguides of both YIs were passivated with an overcladding layer. The measurement windows were formed by leaving a length of 10 mm of the measurement waveguides without the overcladding layer. The MIP receptor layer was applied in the measurement window of YI1, and the reference NIP layer in the measurement window of YI2.

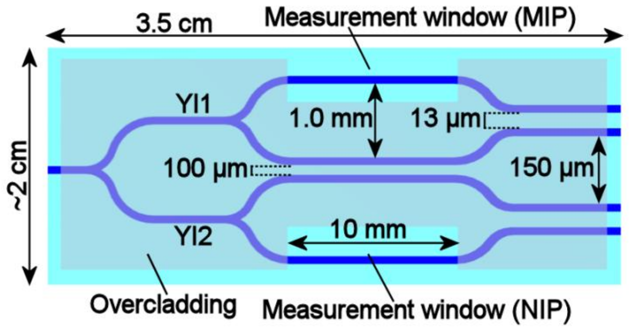

Figure 24 Sensor chip layout for chemical sensing of small molecules.

A schematic of the fabrication of the MIP and NIP layers is shown in Figure 25. The solution for the MIP layer was prepared by dissolving monomer, cross linker, and melamine in de-ionized water. The solution was heated and radical initiator was added. The solution was allowed to polymerize until it turned slightly turbid. The solution for the NIP layer was prepared similarly but for melamine. The solutions were applied onto the respective measurement channels using spin-coating and layers were polymerized. The length of the coatings on the measurement channels was 10 mm, defined by an opening in the adhesive layer. The melamine molecules were removed from the MIP layer by immersing the chip in water and shaking it overnight, leaving empty cavities in the MIP layer in the shape of the melamine molecule. The MIP recognition layer binds molecules selectively due to the specific shape of these cavities and interactions (e.g. Van der Waals and electrostatic) between the analyte molecules and the polymer material.[23] It is worth noting that the binding of the melamine molecules to the cavities is reversible, and one sensor chip can thus be used to perform several measurements.

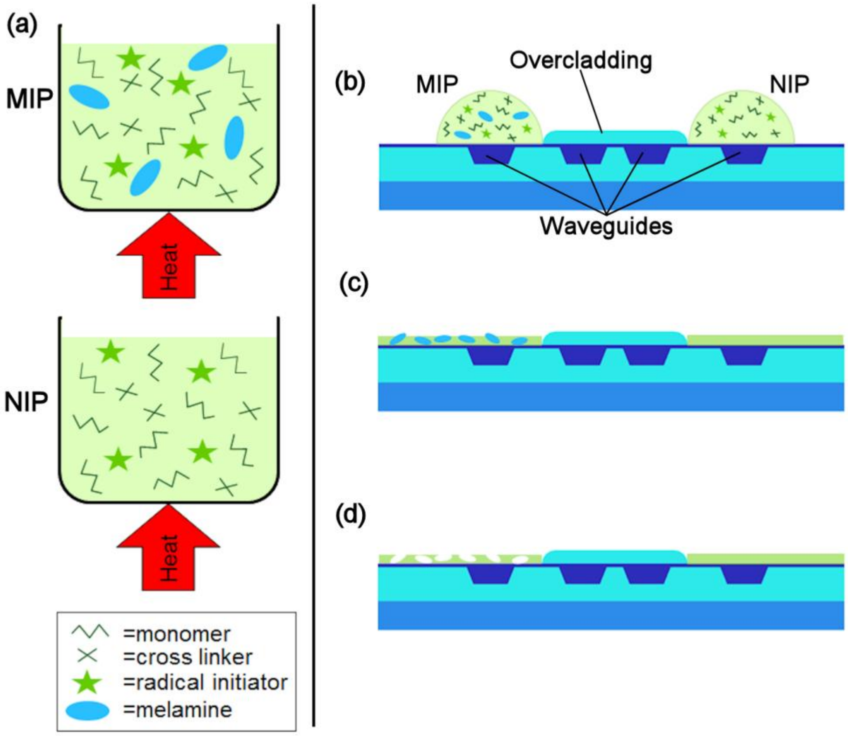

Figure 25 MIP/NIP functionalization. a) The MIP and NIP solutions are prepared. b) MIP and NIP solutions are applied onto the respective waveguides of the YI chip. c) Solutions are spin-coated onto the sensor chip to form layers that are polymerized. d) Analyte template molecules are removed from the MIP layer by rinsing in water, leaving imprinted cavities.

During the measurements, YI1 and YI2 are monitored separately and their phase changes $\Delta\phi_{\mathrm{MIP}}$ and $\Delta\phi_{\mathrm{NIP}}$, respectively, are analysed separately. Due to the MIP coating, YI1 measures the specific binding of melamine to the sensor surface. However, molecules can also bind surfaces unspecifically and the phase change caused by this unspecific binding is measured by the NIP-coated YI2. Both interferometers also measured the bulk effects of the sample solutions through the applied coatings.

To analyse the phase changes caused by the specific binding of the melamine to the sensor surface, the difference in the phase changes, $\Delta\phi_{\mathrm{diff}}$, between YI1 and YI2 is calculated as $\Delta\phi_{\mathrm{diff}}(t) = \Delta\phi_{\mathrm{MIP}}(t) - \Delta\phi_{\mathrm{NIP}}(t)$ to exclude the effects of the unspecific binding to the sensor surface and ambient RI changes within the measurement window. Calculation of $\Delta\phi_{\mathrm{diff}}$ eliminates also phase changes related to internal changes at the chip that both YIs see similarly. These could be induced, for example, by temperature variations.

3.2.3 Antibody-functionalized chip for multi-analyte detection

An illustration of the chip layout for multi-analyte detection is shown in Figure 26. The chip was functionalized with biological receptor layers using antibodies patterned onto the waveguides. Antibodies are biomolecules that are related to the immunological responses.[63] A single antibody binds to a certain surface structure of their target analyte in a similar manner to how a key fits a certain lock, enabling specific binding of the analyte molecules onto the sensor surface.[64] The measurement waveguide of YI1 was coated with anti-hCG antibodies that bind hCG molecules. Similarly, the anti-CRP antibody coating on the measurement waveguide of YI2 selectively binds CRP molecules. The reference waveguides were coated with mouse immunoglobulin G (IgG) antibodies to act as a reference layer taking into account the unspecific binding (i.e. the tendency of the proteins to attach onto surfaces unspecifically) of the analytes to the antibody coatings. It is worth noting that all the antibodies used here were of IgG type.

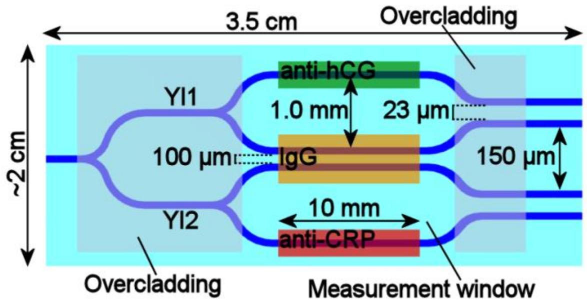

Figure 26 Sensor chip layout for multi-analyte detection of biomolecules.

With this chip layout, the overcladding layer was used to define the measurement window but the sensing length was defined by the length of the antibody areas along the waveguides. It is worth noting that during the experiments all the channels are exposed in a similar fashion to the solutions within the measurement window. YI1 and YI2 thus measure the specific binding of the analytes directly since, in theory, the effects of ambient RI changes and the unspecific binding are inherently cancelled out. The similarity of the channels also makes them react in a similar way to temperature variations that reduces the sensor’s temperature sensitivity.

The antibody layers were patterned onto waveguides using a table-top piezoelectric inkjet printer (Dimatix DMP-2800, Fujifilm Dimatix). In the printer, ink is contained in a cartridge that is connected to a printhead. The printhead has a small orifice and a piezoelectric transducer that is used to generate waves that push the ink through the orifice to form small ink droplets that fall onto the surface.[65] Patterning is done by moving the printhead over the surface, enabling droplets to be positioned.

Bio-inks were prepared containing either anti-human CRP antibodies (monoclonal antibody (Mab) 6404, Medix Biochemica), anti-hCG antibodies (Mab 5006, Medix Biochemica) or mouse IgG (Chrompure, Jackson ImmunoResearch Laboratories). Each ink contained the respective antibody and was prepared in a buffer solution containing solvent and surfactant. To enhance the printing quality, the chips were oxygen plasma treated prior to printing to make the surfaces more hydrophilic. Printed rectangular antibody patterns measuring 0.6×10 mm^2 on the waveguides are shown in Figure 27. The antibodies were attached to the sensor’s surface by means of physisorption and their orientation was random. Looking at the microscope images, it can be seen that the printed coatings do not look even that most likely have an impact on the sensor responses. This is discussed further in Section 4.2.4 (p. 77).

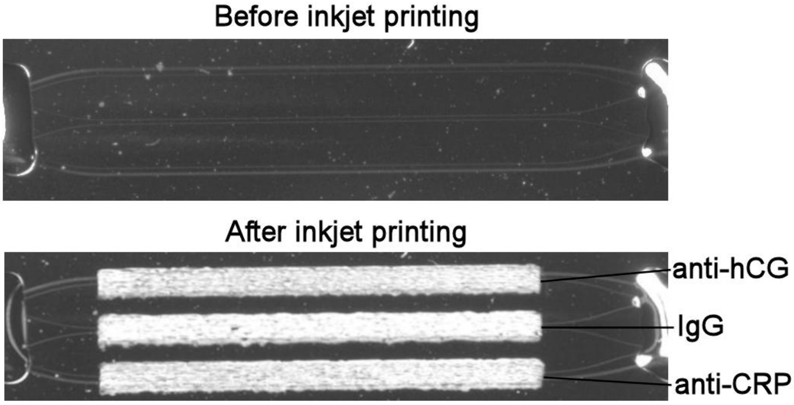

Figure 27 Top view microscope image of the chip before (above) and after (below) inkjet printing of the antibody coatings.

The chip’s surface was blocked after printing. In the blocking the uncoated surface of the sensor is coated with a protein layer that reduces the unspecific binding of the biomolecules to the sensor’s surface during the interferometric measurements. Blocking was done using bovine serum albumin (BSA) that is a protein found in cow blood. During the blocking step, the salts in the bio-inks that make the printed areas visible in Figure 27 were also washed away.

4. Experiments and results

This section describes the experiments and results. Section 4.1 includes the experiments conducted with 3-channel YI chips to study the applicability of the drift compensation method. Section 4.2 contains the experiments conducted with chips having R2R fabricated waveguides. In Section 4.3, the cross-talk effects observed during the experiments are discussed.

4.1 Drift compensation with 3-channel Young interferometers

The aim of the experiments conducted with the 3-channel YIs was to study the applicability of the drift compensation method, described in Section 2.2 (p. 33), to compensate small intrinsic drifts of the setup and large mechanical disturbances that were induced deliberately. The compensation method was first studied with an inverted ridge waveguide YI chip but the method was also demonstrated to be applicable with slot waveguide YI sensors.

An experimental setup (Section 4.1.1) was built to enable undisturbed and mechanically disturbed measurements as well as the modification of the ambient RI on top of the sensor chip by different sample solutions, i.e. aqueous glucose solutions (Section 4.1.2). Sensor chip responses to ambient RI changes were determined from the undisturbed and disturbed experiments and values were compared to study the capability of the compensation method to extract the sample-induced responses under mechanical disturbances (Section 4.1.3). Finally, the residual phase changes were studied to further analyse the capability of the compensation method (Section 4.1.4). Residual phase changes were used to gauge the ability of the phase change values to return to their initial value at the end of the experiment when the RI difference was also returned to its initial value.

4.1.1 Experimental setup

A schematic of the optical setup is shown in Figure 28. Laser light from a frequency-stabilized laser source (HRS015, Thorlabs) emitting at 633 nm was used in the experiments. This was followed by an optical isolator that prevented backreflections into the laser. A quarter wave plate and a polarizer were used to modify the laser light and select the polarization state. TM-polarization was used in the experiments with the inverted ridge waveguide YI due to its higher sensitivity [24] and TE-polarization with the slot waveguide YI experiments to enable enhancement of the electric field in the slot structure.[25] A beam expander (5×) was used to reduce the spot size generated by the focusing lens (C230TM-B, Thorlabs) to improve the incoupling efficiency and reduce stray light. Laser light was end-fire coupled into the chip.

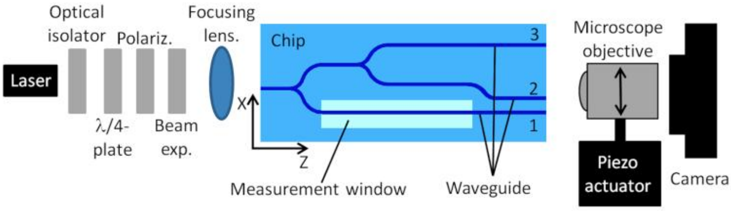

Figure 28 Setup for drift compensation measurements (Paper I)

A 40× microscope objective (Micro Plan, numerical aperture 0.65, Edmund optics) was used to image the outcoupled diverging beams onto the camera detector (PL-E425CU, PixeLink). The imaging was done at a distance of 0.5 mm from the output facet in the inverted ridge waveguide YI experiments and at a distance of 0.8 mm in the slot waveguide YI experiments. The interval between the captured interferograms was 10 s. The exposure time was chosen such that the image was not overexposed: ~1 ms in the experiments with the inverted ridge YI and varying from 3 to 13 ms in the experiments with the slot waveguide YI.

In the mechanically disturbed experiments, the microscope objective was mounted onto a piezo-actuated XYZ-translation stage that was manually controlled during the experiments. The microscope objective was moved in the *x*-direction shown in Figure 28. The direction of the movement was changed around the midpoint at each of measurements but the rate of the movement as well as the maximum displacement varied between measurements. The maximum displacement of the microscope objective varied in the inverted ridge waveguide YI experiments from ~7 to ~19 µm and in the slot waveguide YI experiments from ~6 to ~11 µm.

For the actuation of the solutions, a flow cell was assembled onto the YI chips and sealed with a silicone seal. The inlet of the flow cell was connected to the sample vial and the outlet to a syringe pump (Nexus 3000, Chemyx) by a tube. The syringe pump was driven in a withdraw mode at a constant flow rate of 100 µl/min. The flow cell was assembled onto the chips and filled with water at least a day before to reduce the effect of water absorption into the waveguides during the experiments.[32, 38]

4.1.2 Sample solutions

Aqueous glucose solutions were prepared by dissolving D-glucose (Sigma-Aldrich) into ultrapure water (MilliQ Academic, Merck Millipore). The concentrations and the RI differences of the glucose solutions to pure water, Δn, are shown in Table 1 for the experiments with the inverted ridge and slot waveguide YIs. The RI differences to pure water were calculated using a polynomial (Paper I):

$$\Delta n = 6 \times 10^{-6} C^2 + 0.0014C, \qquad (21)$$

where C is the glucose concentration in weight % (wt. %). The polynomial was fitted to the empirical tabulated RI values given for aqueous glucose solutions in Ref. [66] measured at a wavelength of 589 nm and at 20°C. Here it was assumed that Δn values are the same at the wavelength of 633 nm used in the experiments as at their characterization wavelength of 589 nm although the absolute RI values vary in the function of wavelength due to dispersion.

Table 1 Concentrations of the aqueous glucose sample solutions and their RI differences to pure water, Δn.

Glucose concentration [wt. %]	**Δn [RIU]×10^{-4}**
0.01	0.14
0.02	0.28
0.05	0.70
0.1	1.40
0.2	2.80
0.5	7.02
0.7	9.83

4.1.3 Phase change curves and responses

Responses of the inverted ridge and slot waveguide YI sensor chips to the bulk RI changes were determined with the undisturbed and with the disturbed setup by exposing the sensor chips to 500 µl pulses glucose solutions followed by flushing with water. The approximate timing of the glucose solutions in the flow cell is indicated by the background colour in Figure 29 for the inverted ridge waveguide YI experiments, and in Figure 32 for the slot waveguide YI experiments.

The phase change curves were first analysed from the captured interferograms by using FFT algorithm of commercial software (MATLAB, MathWorks) to yield the phases of the sub-interferograms, as discussed in Section 2.1. As indicated by the chip descriptions of the 3-channel inverted ridge waveguide YI (Section 3.1.1, p. 39) and the 3-channel slot waveguide YI (Section 3.1.2, p. 42), channel 1 was the measurement channel in both chip types and channels 2 and 3 were the reference channels. The uncompensated phase chance curves were calculated for all the channel pairs and the compensated phase change curves for channel pairs 1&3, and 1&2 using the phase changes of channel pair 2&3. The sensor responses were determined from the phase change curves by calculating the height of the phase change step induced by the sample solutions. The phase change curves and responses of the inverted ridge waveguide YI are described in Section 4.1.3.1, and for the slot waveguide YI in Section 4.1.3.2.

4.1.3.1 3-channel inverted ridge waveguide Young interferometer

The measured and compensated phase change curves of the experiments with the 3-channel inverted ridge waveguide YI obtained with an undisturbed and with a mechanically disturbed setup are shown in Figure 29(a) and Figure 29(b), respectively. With the undisturbed setup, the concentrations of 0.05 and 0.1 wt.% were measured three times, concentrations of 0.2 and 0.5 wt.% twice, and concentration of 0.7 wt.% once. With the mechanically disturbed setup, all the concentrations were measured once. For the undisturbed measurements, only one set of curves per concentration is shown in the figures for clarity.

Looking the undisturbed phase change curves $\Delta\phi_{13}$ and $\Delta\phi_{12}$ in Figure 29(a), it can be seen that the phase changes follow the sample-induced bulk RI changes, as expected, indicating that the measurement setup and the interferogram analysis were working properly. It can be seen that the compensated $\Delta\phi_{13}^{s}$ and $\Delta\phi_{12}^{s}$ curves are practically overlapping although the differences in the measured $\Delta\phi_{13}$ and $\Delta\phi_{12}$ phase change curves are more noticeable. Since the compensated curves are more similar, this indicates that the spatial frequency dependent part of the phase changes is almost eliminated and the curves are reflecting the changes related to the chip.

The intrinsic drift of the measurement system is shown by $\Delta\phi_{23}$ curves from undisturbed experiments in Figure 29(a). It can be seen that during the 0.5 wt. % experiment there is a distinctive linear drift that is also reflected onto the measured $\Delta\phi_{13}$ and $\Delta\phi_{12}$ curves. However, this drift is almost completely eliminated from the compensated $\Delta\phi_{13}^{s}$ and $\Delta\phi_{12}^{s}$ curves showing the capability of the compensation method to reduce the effects of intrinsic drifts of the setup. In addition, the phase change curve of the reference channel pair, $\Delta\phi_{23}$, in 0.7 wt. % experiment seems to have a minor response to bulk RI change as shown in Figure 30. Nonetheless, this reaction is caused by cross-talk between the channel pairs that is a known phenomenon in multichannel YIs.[67] Cross-talk effects seen in the experiments are discussed further in Section 4.3 (p. 81).

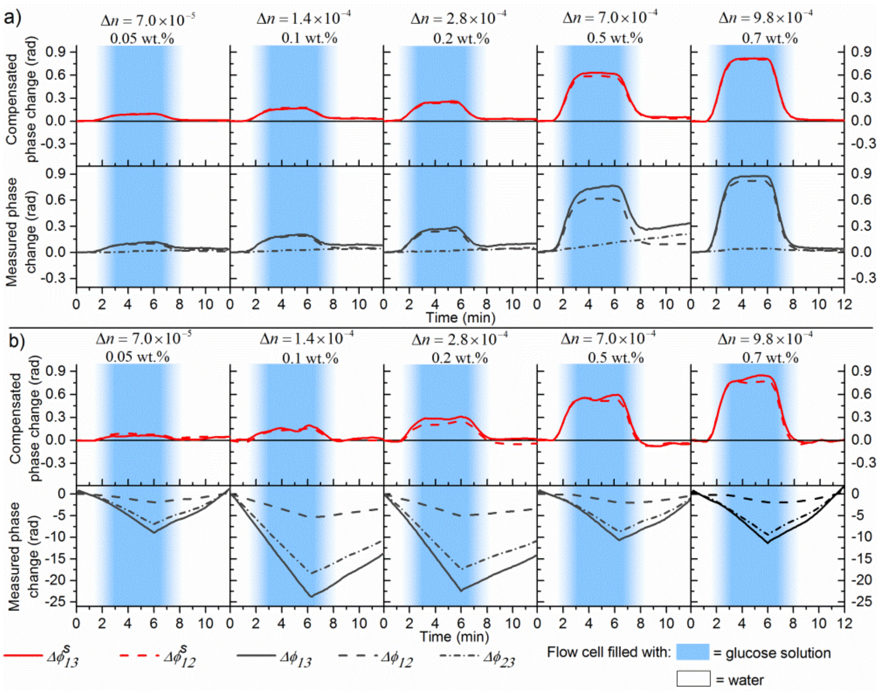

Figure 29 Phase change curves measured with the 3-channel inverted ridge waveguide YI of a) undisturbed experiments, and b) disturbed experiments.

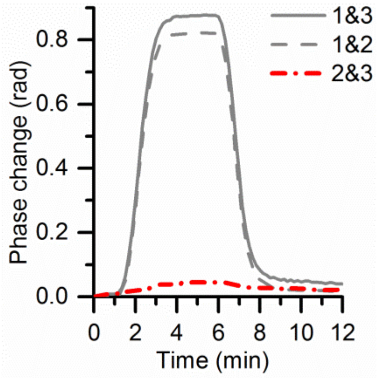

Figure 30 Phase change curves measured at the glucose concentration of 0.7 wt. % with the undisturbed setup. The phase change signal of reference channel pair is drawn with red colour and shows cross-talk induced phase changes. (These are the same curves as in Figure 29(a) and are redrawn here for enhanced visibility of cross-talk related phase changes.)

The phase change curves of the disturbed experiments are shown in Figure 29(b). The measured phase change curves are shown in the lower row of the figure and the compensated $\Delta\phi_{13}^{s}$ and $\Delta\phi_{12}^{s}$ curves in the upper row. The mechanical disturbance of the setup is shown by $\Delta\phi_{23}$ curves showing the direction of the mechanical disturbance and its magnitude. By comparing the shapes of $\Delta\phi_{13}^{s}$ and $\Delta\phi_{12}^{s}$ curves between the undisturbed and disturbed experiments, it can be seen that the curves have a similar shape and timing, confirming that the compensation method is able to extract the phase changes induced by bulk RI changes from the much larger measured phase changes.

Sensor responses were determined by calculating the sample-induced phase change step height by taking the average of the phase change values between 3.5 and 6.0 minutes. Responses were calculated from the $\Delta\phi_{13}$, $\Delta\phi_{12}$, $\Delta\phi_{13}^{s}$ and $\Delta\phi_{12}^{s}$ curves of the undisturbed experiments and from the $\Delta\phi_{13}^{s}$ and $\Delta\phi_{12}^{s}$ curves of the disturbed experiments and are shown in Figure 31. It can be seen that the response values as expected increase with increasing glucose concentration. It can be also seen that the response values calculated from the disturbed experiments are in good agreement with the undisturbed response values. The similarity between the response values calculated from the phase change curves of the undisturbed and from the compensated phase change curves of disturbed experiments demonstrate that the compensation method is able to extract the sample-induced phase changes from the much larger measured phase changes. The largest ratio of the maximum value of $|\varDelta\boldsymbol{\phi}_{\mathbf{13}}|$ to response value calculated from $\Delta\phi_{13}^{s}$ curves was 161, which was measured at the concentration of 0.1 wt. %.

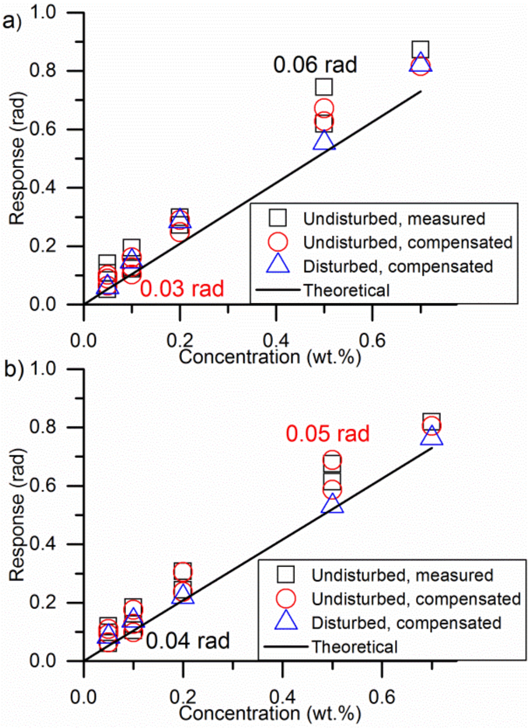

Figure 31 Responses calculated from uncompensated and compensated phase change curves of the undisturbed experiments, and from the compensated curves of the disturbed experiments: a) channel pair 1&3, and b) channel pair 1&2. The theoretical response is shown by the line. Half of the maximum range values for the data sets are shown as text next to the related data points: black lettering = undisturbed, measured data set, and red lettering = undisturbed, compensated data set.

Theoretical sensor responses were calculated by using film mode matching method (Fimmwave, Photon Design). The effective RIs, $n_{\mathrm{eff},1}$, of the waveguide modes of the channel 1, i.e. the measurement channel, were calculated with various ambient RI values corresponding the RIs of the sample solutions and water. The effective RI values of the reference channels were assumed to be constant. The effective RI values of the measurement channel were used to calculate the effective refractive index differences, Δn_{eff}, between the measurement and reference channels. These were again applied to Eq. (2) (p. 30) to calculate the theoretical phase change responses.

4.1.3.2 3-channel slot waveguide Young interferometer

The measured and compensated phase change curves of the experiments with 3-channel slot waveguide YI are shown in Figure 32. The measured phase change curves for all the channel pairs are shown in the lower row of Figure 32(a) and Figure 32(b), and the compensated phase change curves of the channel pairs 1&3, and 1&2 in the upper row. With the undisturbed setup the concentrations of 0.01, 0.05 and 0.2 wt. % were measured once, and the concentrations of 0.02, and 0.1 wt. % three times. With the disturbed setup the concentration of 0.05 wt. % was measured twice and the concentrations of 0.1 and 0.2 wt. % once. Only one set of curves per concentration of the undisturbed experiments is shown for clarity.

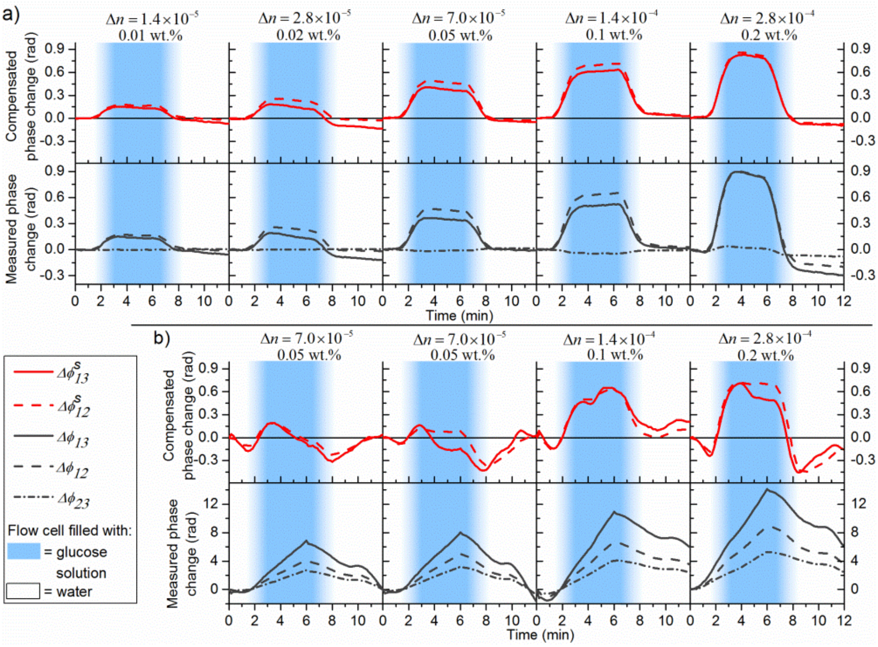

Figure 32 Phase change curves of the slot waveguide experiments of a) undisturbed experiments, and b) mechanically disturbed experiments. (Paper II)

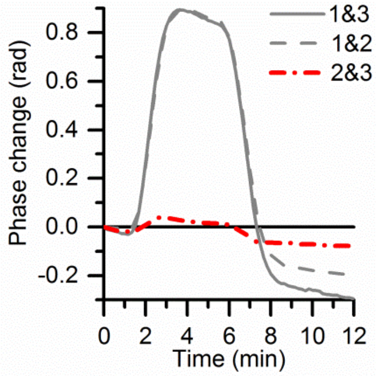

Figure 33 Phase change curves of undisturbed experiment measured at the glucose concentration of 0.2 wt. %. The phase change signal of the reference channel pair is drawn with red colour and shows cross-talk induced phase changes. (These are the same curves as in Figure 32(a) and are redrawn here for enhanced visibility of cross-talk related phase changes.)

Looking at the $\Delta\phi_{13}^{s}$ and $\Delta\phi_{12}^{s}$ curves of the undisturbed experiments in Figure 32(a), it can be seen that the sensor shows clear phase change responses to the sample-induced bulk RI changes at all the glucose concentrations. The shape and timing of the phase change curves also confirm that the measurement system and the phase change analysis were working properly. It can also be seen that the $\Delta\phi_{23}$ curve seems to react to the sample-induced bulk RI changes at the two highest concentrations (0.1 and 0.2 wt. %), showing small negative and positive phase change responses. The curves of 0.2 wt % experiment are redrawn in Figure 33 for clarity. Since channels 2 and 3 are reference channels, and also due to the different signs of the induced phase change responses, these were not considered to be direct responses to the sample-induced RI changes but caused by cross-talk [67] between the channel pairs. Cross-talk issues with multichannel YI sensors are discussed in more detail in Section 4.3 (p. 81).

The lower row in Figure 32(b) shows the measured phase change curves of mechanically disturbed experiments for all the channel pairs. Here again, the $\Delta\phi_{23}$ curve shows the direction of the mechanical disturbance for all the channel pairs and its magnitude for the sub-interferogram of the channel pair 2&3. It can be seen that the direction of the microscope objective movement was reversed at the midpoint of the measurement and that the magnitude of the disturbance varied between the measurements. The compensated $\Delta\phi_{13}^{s}$ and $\Delta\phi_{12}^{s}$ curves are shown in the upper row. By comparing the $\Delta\phi_{13}^{s}$ and $\Delta\phi_{12}^{s}$ curves between Figure 32(a) and Figure 32(b) it can be seen that the shape and timing of the curves of the disturbed experiments are similar but that the fluctuations in the disturbed experiments are much larger. At the two highest concentrations the sample-induced phase changes are discernible, and thus the compensation method can be considered to be able to extract the bulk RI changes from the larger measured phase changes. At the lowest concentration, i.e. at the RI difference of 7.0×10^{-5} RIU, the phase change curve fluctuations and the sample-induced phase changes are within the same range, as shown by the two sets of phase change curves in Figure 32(b), and the compensation method therefore cannot be considered to be able to extract the sample-induced RI changes at this RI difference level. The fluctuations were attributed to cross-talk between the channel pairs, which was also seen in the undisturbed experiments.

Sensor responses were calculated by determining the phase change step height by subtracting the mean value within 1.2-1.5 min from the mean value within 4.8-5.2 min from the $\Delta\phi_{13}$, $\Delta\phi_{12}$, $\Delta\phi_{13}^{s}$ and $\Delta\phi_{12}^{s}$ curves of the undisturbed experiments and from the compensated $\Delta\phi_{13}^{s}$ and $\Delta\phi_{12}^{s}$ curves of the disturbed experiments. The responses for channel pair 1&3 are shown in Figure 34(a) and for channel pair 1&2 in Figure 34(b). It can be seen that overall the responses as expected increase with increasing glucose concentration. It can also be seen that the response values calculated from the $\Delta\phi_{13}^{s}$ and $\Delta\phi_{12}^{s}$ curves of the disturbed experiments are in agreement with the values of the undisturbed experiments proving that the compensation method is compatible with slot waveguide YI sensors. The similarity between the response values shows that the compensation method was able to extract the phase change responses induced by an RI difference of 1.4×10^{-4} RIU from 18 times larger measured phase changes. However, some response values of the undisturbed experiments defined at different glucose concentrations overlap, and the sensor readout is therefore not quantitative but resemble semi-quantitative. To indicate the variation in the measurements, the maximum ranges of the response values for the undisturbed data sets were calculated and are shown next to the related data points in Figure 34. Based on these data sets, the compensation method reduces the range of the response values.

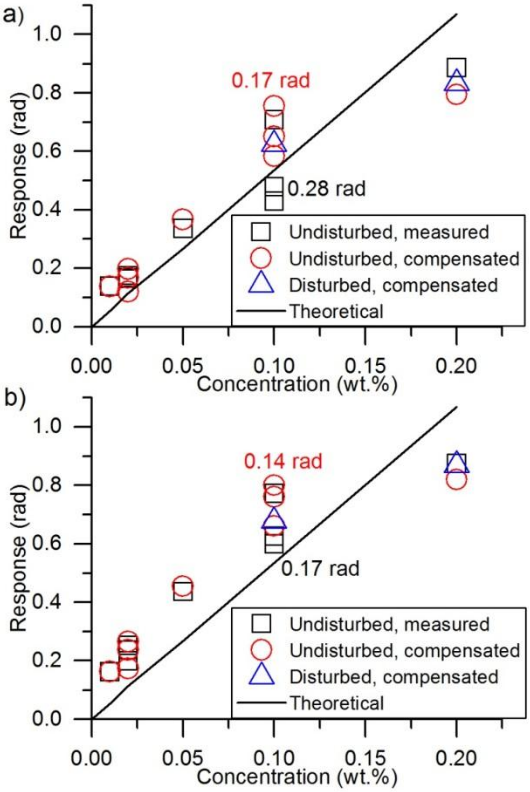

Figure 34 Responses calculated from uncompensated and compensated phase change curves of the undisturbed experiments and from compensated curves of the disturbed experiments. a) Channel pair 1&3, and b) channel pair 1&2. The theoretical response is shown by the line. The maximum ranges of the undisturbed data sets are shown next to the related data points: black lettering, undisturbed measured; and red lettering, undisturbed compensated. (Paper II)

Theoretical sensor responses were determined using a finite-element method of commercial software (Fimmwave, Photon Design). The waveguide dimensions were first determined from the SEM images in Figure 17(c) (p. 43) and the waveguide effective RI indices $n_{\mathrm{eff,1}}$ and $n_{\mathrm{eff,r}}$ of slot and ridge waveguides, respectively, were then calculated with various ambient RI index values corresponding to the RIs of the glucose solutions. These effective RI values were used to determine the difference in the effective RI changes between the measurement and reference channels, Δn_{eff}, and this value was substituted into Eq. (2) (p. 30) to calculate the theoretical sample-induced phase changes at various glucose concentrations. These theoretical phase change values are included in Figure 34, and it can be seen that the experimental response values are in good agreement with the theoretical values. The theoretical phase change values show a linear trend but the experimental responses seem to saturate at the highest concentration. This was attributed to the flow and diffusion dynamics of the glucose molecules within the slot structure, which was not studied further in this work. It is worth noting that the saturation effect was not seen in the experiments with the inverted ridge waveguide YI sensor although sample solutions having higher glucose concentrations were measured.

4.1.4 Residual phase changes

The efficacy of the compensation method to compensate the drifts of the setup was studied by analysing the phase change values within the last two minutes of the measurements with 3-channel inverted ridge and slot waveguide YIs. Since the ambient RI in the measurement window was restored to its initial value during the last two minutes of the measurements, the phase change curves should also return to zero.

The residual phase changes were determined by calculating the average of the phase change values between 10-12 min for the uncompensated and compensated phase change curves of the undisturbed experiments, and for the compensated phase change curves of the disturbed experiments for channel pairs 1&3 and 1&2. The average values and maximum ranges of the data sets were also calculated. Calculated values for the inverted ridge YI are shown in Figure 35 and for the slot waveguide YI in Figure 36.

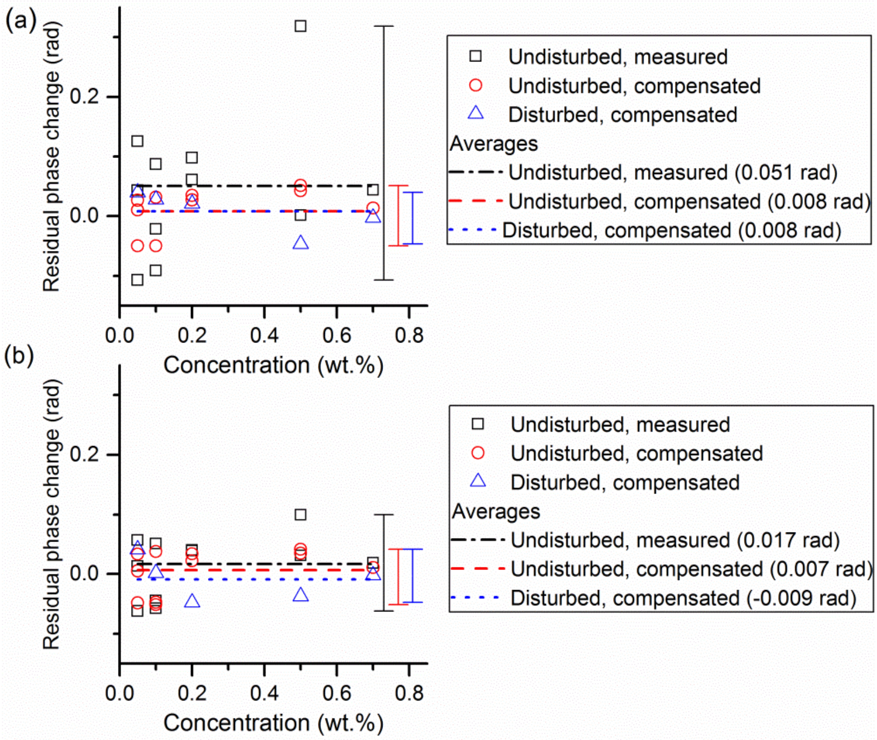

Figure 35 Residual phase changes of inverted ridge waveguide YI. Values are calculated from the measured and compensated phase change curves of the undisturbed experiments, and from the compensated curves of the disturbed experiments: a) channel pair 1&3, and b) channel pair 1&2. The average values for each data set are shown by the line and the value is given in the legend. The range of each data set is displayed by the bars on the right: black undisturbed measured, red undisturbed compensated and blue disturbed compensated.

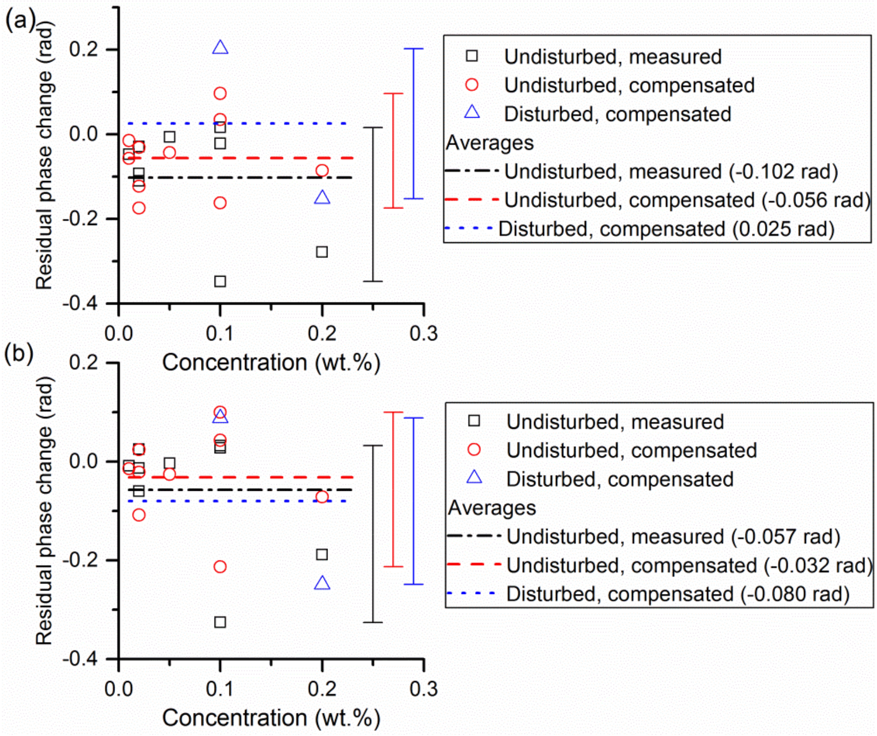

Figure 36 Residual phase changes of slot waveguide YI. Values are calculated from the measured and compensated phase change curves of the undisturbed experiments, and from the compensated curves of the disturbed experiments: a) channel pair 1&3, and b) channel pair 1&2. The average values for each data set are shown by the line and the value is given in the legend. The range of each data set is displayed by the bars on the right: black undisturbed measured, red undisturbed compensated and blue disturbed compensated.

Looking at the residual phase change values of inverted ridge waveguide YI, it can be seen that the averages calculated from the compensated phase change curves of the undisturbed experiments for channel pairs 1&3 and 1&2 are practically the same although the averages of the uncompensated curves clearly differ. The similarity between the compensated values indicates that the compensation method was able to reduce the effect of the drift of the optical setup. The average value calculated from the compensated phase change curves for channel pair 1&3 is 84% smaller than the values calculated from the uncompensated curves. For channel pair 1&2, the reduction is 61%. The reduction in the case of channel pair 1&3 is similar to the value, ~10 times, reported in Ref. [58]. The average values and ranges calculated from the disturbed data sets are similar to the values of in the undisturbed cases, providing further proof of the capability of the method to compensated mechanical drifts.

The residual phase changes calculated from the experiments with the slot waveguide YI show larger values than the inverted ridge waveguide YI due to the larger fluctuations in the phase change curves. The averages of the undisturbed compensated data sets are about half the values in the corresponding uncompensated cases. The residual values of the disturbed compensated data sets also show a similar kind of values to the undisturbed cases indicating that the compensation method also works properly with the slot waveguide YI with large mechanical drifts.

4.2 Young interferometer sensor chips based on roll-to-roll fabricated waveguides

To study the applicability of the R2R fabricated waveguide platform for sensing, the experiments were conducted with the three chip types described in Section 3.2 (p. 46) for ambient RI, chemical and multi-analyte biochemical sensing. In Section 4.2.1 the optical setup and the actuation of the solutions are discussed. The experiments and the results of the ambient RI sensing are discussed in Section 4.2.2, of the chemical sensing in Section 4.2.3, and of the biochemical sensing in Section 4.2.4.

4.2.1 Experimental setup

A schematic of the optical setup is shown in Figure 37. Coherent light from a laser source (QFBGLD-980-5, QPhotonics) emitting at 975 nm was coupled to polarization-maintaining fibre with a tapered outcoupling end. An optical isolator was used to prevent reflections back into the laser. TM-polarized light was used in the measurements due to its higher sensitivity than TE-polarization.[24] The polarization state was confirmed with an external polarizer. The tapered end of the incoupling fibre formed a spot with a diameter of ~2.8 µm. Light was end-fire coupled from the fibre into the chip's input waveguide.

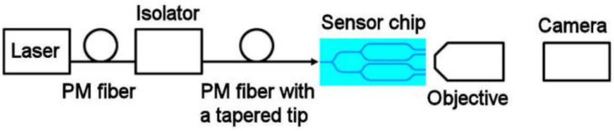

Figure 37 Optical setup for experiments with chips having R2R fabricated waveguides. PM=polarization-maintaining. (Paper III)

The interference patterns were imaged onto the camera (UI-3240CP-NIR-GL, IDS Imaging Development Systems) using a 40× microscope objective (E Plan, numerical aperture 0.65, BaySpec). The imaging was done at a distance of ~250 µm for ambient RI measurements and at a distance of ~200 µm for the chemical sensing and biochemical sensing experiments. The imaging was done at an interval of

2 s in the ambient RI and chemical sensing experiments and at an interval of 10 s in the biochemical sensing experiments. The distance between the camera detector and the outcoupling end of the chip was 17 cm.

The part of the captured interferograms used in FFT analysis was selected independently for both interferometers and for each measurement. The area contained 4-5 fringe periods depending on the visibility of the fringes. The phase change curves of YI1 and YI2 were calculated separately as discussed in Section 2.1 for 2-channel YIs.

A flow cell was assembled onto the chips in a similar manner to the drift compensation experiments described in Section 4.1.1 to enable the actuation of the sample and flushing solutions. The flow rate of 100 µl/min was used in the ambient RI and chemical sensing experiments and 20 µl/min in the biochemical sensing experiments.

4.2.2 Ambient refractive index sensing experiments

The capability of the sensor chip configuration described in Section 3.2.1 (p. 50) to sense ambient RI differences was studied with two chips. Aqueous glucose solutions were prepared in ultrapure water to modify the ambient RI within the measurement window. The concentrations of the solutions and their RI differences to water are shown in Table 2. The RI differences were calculated using Eq. (21) (p. 58). The solutions were stored at room temperature before the experiments to avoid temperature differences between the solutions and the setup that might affect the results.

Table 2 Concentration of the aqueous glucose solutions and their RI differences, Δn, to pure water.

Glucose concentration [wt. %]	**Δn [RIU]$\times 10^{-5}$**
0.006	0.8
0.01	1.4
0.03	4.2
0.1	14
0.5	70

Each glucose concentration was measured four times. During each measurement, the measurement channel of YI2 was exposed to 500 µl glucose solution, leading to 5 minutes' sample exposure followed by flushing with water until the end of the measurement. The approximate timing of the glucose solutions and water in the flow cell is indicated by the background colour in Figure 38. Due to the passivation layer, YI1 was not exposed to the samples.

The phase change curves of YI1 and YI2 were calculated and were baseline corrected based on the values of 0-1.1 min. The phase change curves of YI2 are shown in Figure 38(a) and it can be seen that the phase change responses were obtained for all the glucose concentrations showing that ambient RI changes were detected at a level of 10^{-6} RIU. The phase change curves of the passivated YI1 in Figure 38(b) show the drift-induced signals during the measurements. The apparent responses in the 0.5 wt. % experiments to ambient RI differences were attributed to cross-talk between the interferograms of YI1 and YI2, which is further discussed in Section 4.3 (p. 81).

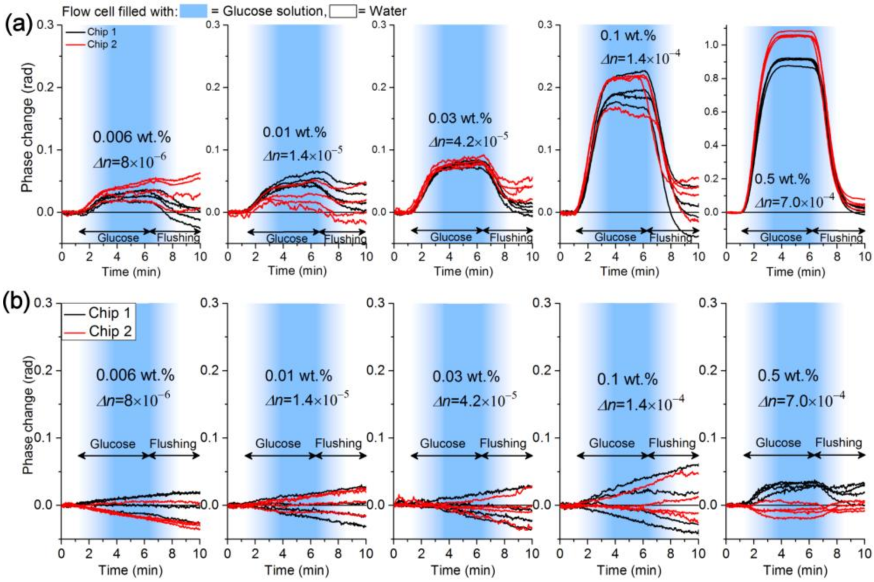

Figure 38 Phase change curves of ambient RI sensing experiments of a) YI2, and b) YI1. (Figure (a) from Paper III)

The responses were calculated from the phase change curves of YI2 using two methods. In the first method, the height of the phase change step was calculated by taking the average of the phase change values within 5.0-5.3 min. In the second method, the slope of the phase change curves was determined by fitting a line to the phase change values within 2.0-2.8 min. The response values are shown in Figure 39, including a line fitted to the data points. It can be seen that overall the responses as expected increase with increasing glucose concentration. However, at the two lowest concentrations (0.006 and 0.01 wt. %) the responses overlap and measurement cannot be considered to be quantitative below the RI difference of 1.4×10^{-5} RIU. The slope-based method enables faster quantification of the signal after induction of the sample than the step height method, which is an advantage from a rapid diagnostics point of view.

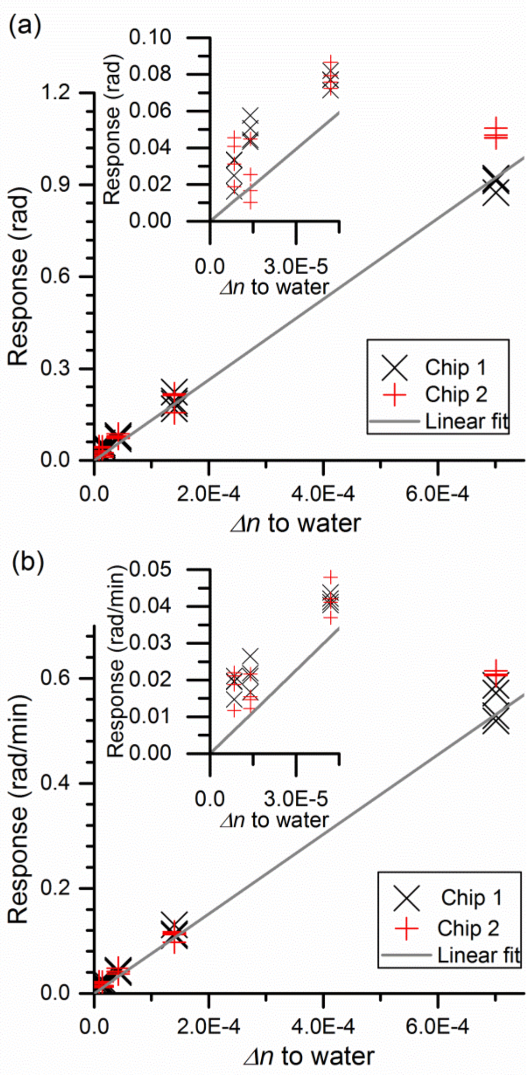

Figure 39 Responses calculated from the phase change curves of YI2 based on a) phase change step height, and b) the slope of the rising edge of the phase change curves. The responses for the three lowest concentrations are shown in the inset.

4.2.3 Chemical sensing with an MIP/NIP functionalized sensor chip

To demonstrate the applicability of the MIP/NIP-functionalized sensor configuration described in Section 3.2.2 (p. 51) for chemical sensing, a chip was exposed to aqueous melamine solutions. Sample solutions were prepared by dissolving melamine (Alfa Aesar) in ultrapure water at the concentrations shown in Table 3. Each concentration was measured three times by exposing the sensor's surface to 500 µl melamine solution leading to 5 minutes' sample exposure followed by flushing with water until the end of the measurement. The approximate timing of the melamine solutions and water in the flow cell is indicated by the background colour in Figure 40.

Table 3 Concentrations of the melamine solutions and approximate RI differences of the solutions to pure water.

Melamine concentration [g/l]	**Δn [RIU]×10^{-4}**
0.1	0.3
0.25	0.9
0.5	1.7
1.0	3.4

Refractive index differences of the sample solutions to pure water, Δn, were calculated in order to evaluate the phase changes induced by mere bulk RI changes later in this section. RI values were calculated by assuming that the RI of the aqueous melamine solution is dependent on the volume fraction of melamine.[68] The RI differences to water, Δn, were calculated using the formula:

$$\Delta n = \underbrace{\frac{C}{\rho_\mathrm{m}} n_\mathrm{melamine} + \left(1 - \frac{C}{\rho_\mathrm{m}}\right) n_\mathrm{water}}_{\text{RI of melamine solution}} - n_\mathrm{water}, \qquad (22)$$

where C is the concentration of melamine in g/cm^3 and n_melamine and n_water the RI values of melamine and water, respectively, and ρ_m the density of melamine in g/cm^3. In the calculations, an RI value of 1.872 was used for melamine [66] and 1.333 for water [66]. The density of melamine is 1.573 g/cm^3.[66]

As discussed in Section 3.2.2, the MIP-functionalized YI1 bound the melamine molecules selectively onto the sensor's surface whereas YI2 was coated with the reference NIP layer to measure the non-specific binding of melamine to the polymer layer. In addition to the surface-bound reactions, the interferometers also measure the bulk RI changes though the MIP or NIP coatings. The phase change curves of both interferometers were analysed from the captured interferograms and were baseline corrected based on the values between 0-1.1 min. The phase change curves for MIP-coated YI1, $\Delta\phi_\mathrm{MIP}$, and for NIP coated YI2, $\Delta\phi_\mathrm{NIP}$ are shown in Figure 40(a). It can be seen that during the melamine exposure the phase changes of YI1 are about four times larger than the phase changes of YI2. This is attributed to the incorporation of the melamine molecules into the MIP layer. Since this is reversible, the melamine molecules dissociate from the layer during the flushing step, which is seen as reducing phase change values. It was also seen that the phase change responses of $\Delta\phi_\mathrm{MIP}$ and $\Delta\phi_\mathrm{NIP}$ curves decreased with time. This was attributed to swelling and a loss of a few per cent of the MIP and NIP layers during the measurements. The loss of RI during the first two rounds of measurements, i.e. the phase change curves have negative values at the end of the measurements, was also attributed to these effects.

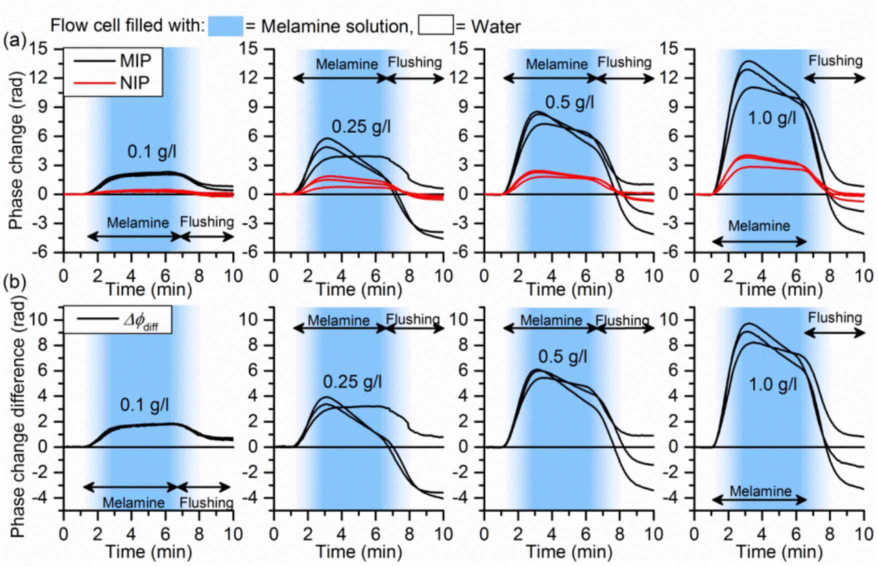

Figure 40 a) Phase change curves of the chemical sensing experiments of MIP-functionalized YI1 and NIP-coated YI2. b) $\Delta\phi_{\mathrm{diff}}$ curves showing the difference in the measured phase changes between YI1 and YI2. The timing of the solutions in the flow cell is shown by the arrows and the background colour. (Paper IV)

To analyse the phase changes induced by the specific interaction of the melamine molecules with the MIP layer, the net differences in the induced phase changes between YI1 and YI2, $\Delta\phi_{\mathrm{diff}}(t) = \Delta\phi_{\mathrm{MIP}}(t) - \Delta\phi_{\mathrm{NIP}}(t)$, were calculated. The $\Delta\phi_{\mathrm{diff}}$ curves in Figure 40(b) show distinctive phase change responses depending on the melamine concentration. The phase change step height and slope based responses in Figure 41(a) and Figure 41(b) were calculated from $\Delta\phi_{\mathrm{diff}}$ curves in a similar way to the ambient RI experiments discussed above. It can be seen that the responses increase with the increasing melamine concentration, demonstrating the applicability of the sensor chip to chemical sensing. Nonetheless, it can also be seen that responses begin to saturate at a concentration of 1.0 g/l, which is coherent with the findings of an earlier paper about detection of small molecules.[69] Due to the saturation, a second order polynomial was fitted to the response values. Based on the experiments, the slope-based method seems more capable of differentiating between small concentrations but the saturation effect is more distinctive than in the step height method. The slope-based method here also enables faster quantification than the step height method.

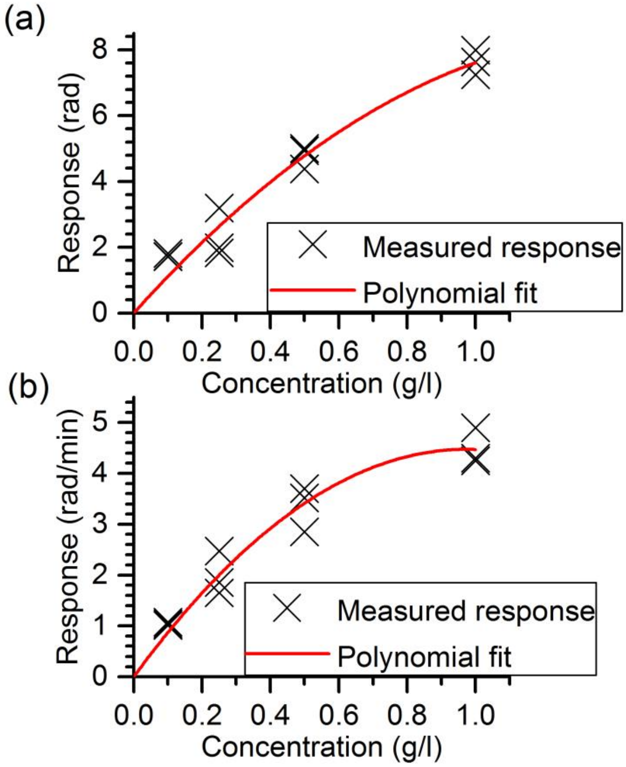

Figure 41 Responses calculated using a) the phase change step height, and b) the slope of the rising edge of the phase change curves. (Paper IV)

It was also found that the measured phase changes shown in Figure 40(a) clearly exceed the values that would have been produced by the mere bulk RI differences of the melamine solutions to pure water. The bulk RI change induced phase changes, $\Delta\phi_{\mathrm{bulk}}$, were evaluated using the Δn values in Table 3 (p. 74) and the sensor sensitivity of 1251 rad/RIU obtained from the line fitted to the data points in Figure 39(a) (p. 73) measured for ambient RI changes. The bulk RI change induced phase changes can be calculated as

$$\Delta\phi_{\mathrm{bulk}} = 1251\,\mathrm{rad/RIU}\,\Delta n. \qquad (23)$$

For the melamine concentration of 1.0 g/l, $\Delta\phi_{\mathrm{bulk}}$ was calculated to be 0.4 rad. However, this is only an indicative value due to the uncertainty of the RI value estimation for the melamine solutions and the uncertainty of the sensor chip's response to bulk RI changes through the MIP and NIP layers. Since the measured phase changes in Figure 40(a) for this concentration are roughly a magnitude larger, it is evident that the phase changes are enhanced by specific surface reactions of YI1, but also by non-specific interactions of YI2.

4.2.4 Multi-analyte biochemical sensing with antibody-functionalized sensor chips

To study the applicability of the antibody-functionalized sensor schema described in Section 3.2.3 (p. 53) for the multi-analyte biochemical sensing, three sensor chips were exposed to sample solutions containing hCG and CRP analytes that are shown in Figure 4 (p. 22). After the analyte-specific measurements, the chips were exposed to a glucose solution to study sensor responses to ambient RI differences.

The sample solutions were prepared in the sample matrix containing 1% BSA (Sigma-Aldrich) in phosphate buffered saline (PBS). The purpose of the chosen sample matrix is to provide benign conditions for the biomolecules by providing the proper salinity and adjusting the pH of the solutions. The BSA in the sample matrix prevents unspecific binding of the analytes into the tubes and flow cell. Sample solutions contained either 2.0 µg/ml human-CRP antigen (BBI Solutions) or 0.9 µg/ml hCG antigen (Scripps Laboratories). For ambient RI change measurements, a solution containing 0.5 wt. % glucose in the sample matrix was prepared.

During the measurements, the chips were sequentially exposed to sample solutions separated by flushing with the sample matrix. Solutions were passed through the flow cell in the following order: sample matrix, 400 µl hCG solution, 300 µl sample matrix, 400 µl CRP solution, 300 µl sample matrix, 400 µl glucose solution, and sample matrix. This led to 20 minutes' sample exposure followed by 15 minutes' flushing, as indicated by the background colour in Figure 42(a). All the channels were simultaneously and similarly exposed to the solutions in the flow cell.

The anti-hCG and anti-CRP antibody coatings of the measurement channels of YI1 and YI2, respectively, caused them to specifically bind their target molecules whereas the IgG coating of the reference channels took into account the unspecific binding. Since all the channels were exposed to the solutions in the flow cell similarly, in theory the ambient RI change does not induce any phase change between the measurement and reference channels. The interferometers can therefore be assumed to measure the difference between the binding of the analyte molecules to the measurement and reference channels directly in real-time and there is no need to calculate the difference signal as with the MIP/NIP-functionalized sensor chips.

The phase change curves shown in Figure 42 were analysed from the captured interferograms and were baseline corrected based on the values between 0 and 5.7 min. The phase change curves of YI1 show clear responses when the sensor chips were exposed to hCG sample solutions whereas the curves of YI2 remain almost constant. This indicates that hCG molecules bound specifically to the measurement channel of YI1. The phase change curves of YI1 level off during the following flushing step, indicating that no more analyte molecules bound to the surface. In contrast to the MIP/NIP-functionalized chip, the phase change curves do not return to the initial value during the following flushing step. This is because the antibodies bind the analyte molecules more strongly than the MIP layer and analyte molecules thus do not dissociate from the receptor layer as readily. When the sensor chips were exposed to CRP sample solutions, the phase change curves of YI2 show clear phase change responses whereas the curves of YI1 do not show responses, again indicating that CRP analytes were specifically bound to the measurement channel of YI2.

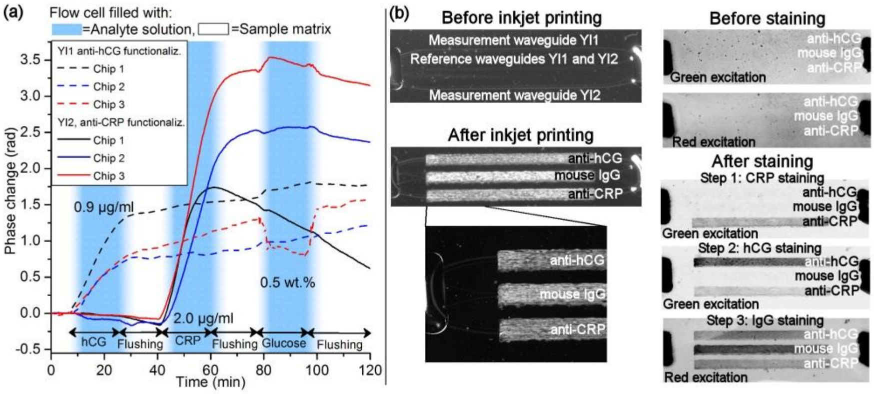

Figure 42 a) Phase change curves of multi-analyte biochemical sensing experiments. The phase change curves of YI1 and YI2 show clear analyte-specific phase change responses to hCG and CRP sample solutions, respectively. Responses to glucose solutions demonstrate the sensor's sensitivity to ambient RI changes. b) Verification of the interferometric results by fluorescent staining. Left: microscope images show the inkjet-printed antibody coatings on the waveguides. Right: the inkjet-printed areas do not fluoresce after the interferometric measurements but before the fluorescent staining. During each of the fluorescent staining steps, the corresponding inkjet-printed area became fluorescent (the darker the area the higher the fluorescence intensity), showing the localized presence of the analyte molecules and IgG and thus verifying the interferometric results. (Paper IV)

Responses were determined from the phase change curves by calculating the average value of the phase change values during the flushing step following the analyte exposure. The response of YI1 to hCG was calculated from the phase change values within 35-38 min, and YI2 to CRP from the values within 68-71 min. The average response of YI1 to hCG was 1.0 rad and the range of the response values was 0.6 rad. The average response of YI2 to CRP was 2.5 rad and the range 1.7 rad. Since the responses vary greatly between chips, the measurement only indicates the presence or absence of the analytes in the sample solution and no quantitative responses were obtained in these experiments. The large variation in the responses was attributed to the variations in the printed antibody layer thicknesses and to the number of binding antibodies on the waveguides, indication of which was already given by the non-uniformity of the inkjet-printed antibody areas as discussed in Section 3.2.3 (p. 53).

The sensitivity of the sensor layout to ambient RI changes was studied by exposing the chips to 400 µl glucose solutions. As discussed above, the sensor should be insensitive to ambient RI changes. By studying the phase change curves during the glucose exposure, it can be seen that five out of the six curves show only minor responses to ambient RI changes, and one of the curves shows a response of about 0.5 rad. By comparison, the sensor layout designed for ambient RI sensing shows responses of about 1 rad in Section 4.2.2 (p. 71) with the aqueous glucose solution having the same concentration in weight per cent. The larger phase change was attributed to the differences in the receptor layer thicknesses of the measurement and reference channels causing a different penetration of the evanescent wave to the sample volume and also different changes in the effective RIs of the waveguides. Although the sensor schema could not render the sensor completely insensitive to the ambient RI changes, the responses were nonetheless suppressed.

After the interferometric measurements, the results were verified by fluorescent staining and imaging. The goal was to confirm the specific binding of the analyte molecules to the correspondingly functionalized areas and the presence of IgG at the reference channels. The CRP and hCG analyte molecules were stained selectively using fluorescently labelled secondary antibodies (Mab 6450 and Mab 5014, respectively, Medix Biochemica) as illustrated in Figure 43. The secondary antibodies were labelled with Alexa Fluor 546 (Thermo Fisher Scientific) fluorophore that is a fluorescent label excitable by green light and emitting orange light. The fluorescence imaging is based on the difference in the excitation and emission wavelengths of the fluorophores. IgG was stained with antibodies (goat anti-mouse IgG, Thermo Fischer Scientific) that were labelled with Alexa Fluor 647 (Thermo Fisher Scientific) fluorophore excitable by red light and emitting red light with longer wavelengths. The antibody for IgG staining non-specifically bound to all the other antibodies present at the chip.

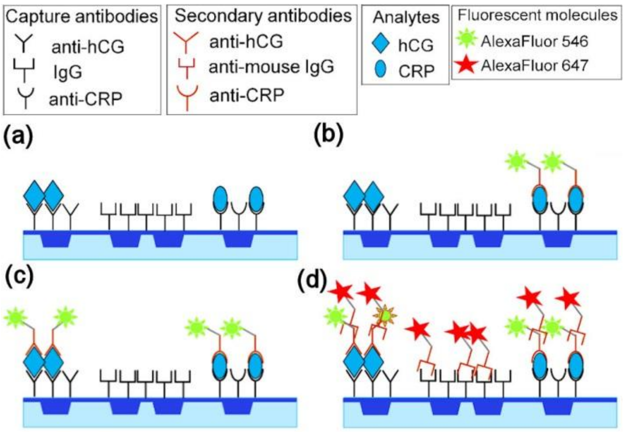

Figure 43 Illustration of the fluorescent staining steps. a) After the interferometric measurement chip has the inkjet-printed capture antibodies as well as the analyte molecules that were bound to the respective capture antibodies during the interferometric experiment. These are not fluorescing. b) In the first staining step, the secondary antibodies with a fluorescent label were specifically bound to CRP analyte molecules. Due to the fluorescent label, the areas containing CRP molecules became fluorescent. c) In the second staining step, the secondary antibodies for hCG were specifically bound to hCG analytes, rendering the corresponding area fluorescent. d) In the third staining step, all the antibodies present at the chip were stained, rendering these areas fluorescent. The inkjet-printed capture antibodies for CRP and hCG were also stained, but this is not shown for the sake of clarity.

The fluorescent staining was done in three sequential steps in the following order: CRP analyte molecules, hCG analyte molecules, and mouse IgG. These steps are illustrated in Figure 43. Before the fluorescent staining, the inkjet-printed areas did not fluoresce at green or red excitation as can be seen from the image in Figure 42(b). During the first staining step, the CRP analyte molecules were stained by applying 500 µl of the solution containing labelled secondary antibodies for CRP onto the chip and shaking for 10 min. This was followed by washing with PBS with Tween-20 (PBST) solution to wash all the unbound secondary antibodies from the chip. After this staining step the correspondingly anti-CRP functionalized area became fluorescent, as can be seen from the image in Figure 42(b), verifying that the CRP analyte molecules were present at this area in accordance with the interferometric results. The hCG staining was done in a similar way to CRP and the area functionalized with anti-hCG antibodies became fluorescent during this staining step, as shown in Figure 42(b). This verifies the presence of hCG analyte molecules at this area as well as the interferometric results of specific binding of analytes. During the third staining step the reference mouse-IgG and all the other antibodies already present at the chip were stained since they all belong to the IgG class of antibodies and thus all fluoresced in the fluorescence image taken with the red excitation in Figure 42(b). Since the area where the reference mouse-

IgG coating was inkjet-printed became fluorescent, the presence of IgG was confirmed at this area. It can be seen that the fluorescence signal from the inkjet-printed areas is also non-uniform, further verifying that the number of captured analyte molecules is non-uniform over the functionalized areas, which affects the repeatability of the sensor responses. The fluorescent imaging was done using a fluorescence scanner (Typhoon Trio, General Electric).

4.3 Cross-talk

This section discusses in more detail the cross-talk effects that were briefly mentioned earlier when discussing the experimental results. Cross-talk induced phase change responses were seen in the phase change curves of the reference channel pairs of 3-channel inverted ridge and slot waveguide YIs as well as in the ambient RI measurements with the chips having R2R fabricated waveguides. Although the effect of the cross-talk on the phase change curves was the same in all three cases, the origin of the cross-talk with 3-channel YIs is different to that in the R2R fabricated sensor chips: with 3-channel YIs, cross-talk is generated as a by-product of the FFT-analysis whereas with the R2R fabricated chip layout, the cross-talk is induced by the interaction of the two interferograms imaged onto a single camera detector.

4.3.1 3-channel Young interferometers

Cross-talk between the sub-interferograms is a known phenomenon with multi-channel YIs that disturbs the analysis of the phase changes by leaking the phase change occurring at one spatial frequency to other spatial frequencies.[67] The amount of cross-talk undulates based on the phase difference between the channels. Suppression of the cross-talk can rely on the dimensions of the chip and the measurement setup or computational signal analysis methods as well as the combination of these two.[67]

In the experiments, it was seen that phase change responses were induced into the sub-interferograms formed by two reference channels as discussed in Section 4.1.3 (p. 58). Although cross-talk effects were seen in the experiments done with inverted ridge and slot waveguide YIs, these were studied more closely with the inverted ridge YI chip.

The cross-talk suppression starts with proper design of the multichannel chip layout. As discussed in Section 2.1.2 (p. 31), the chip has to be designed such that the separations of the channel pairs at the out-coupling end of the chip are mutually different enabling individual monitoring of the sub-interferograms by separating the spatial frequencies of the sub-interferograms. The layouts of the inverted ridge and slot waveguide YIs were designed according to this rule.

Cross-talk could also be reduced by adjusting the optical setup so that the captured interferogram contains integer multiples of the fringe periods of all the sub-interferograms.[67] Adjustment of the setup was not studied in this thesis since the effect is strongly dependent on the absolute distances between the chip, microscope objective and camera detector that were not known with required precision.

The signal analysis based methods are related either to the matching of the spatial frequency of the sub-interferogram fringes and the discrete set of frequencies available in the FFT analysis, or to the application of a windowing technique that modifies the intensity distribution of the captured interferograms. Different methods can also be combined in the analysis. The effect of the cross-talk is reduced if one of the spatial frequencies of the FFT analysis is coincident with the spatial frequency of the sub-interferogram fringes.[67] The spatial frequencies of the FFT analysis are again determined by the image width (i.e. the number of pixels along the *y*-direction in Figure 6(a) p. 27) chosen for the analysis. The number of the available frequencies can also be increased by augmenting the original interferogram image with "pixels" having an intensity of zero before calculating the FFT. [67] Window functions, such as Hamming and Hanning, can be applied to the captured interferograms before FFT analysis. The window function modifies the intensity of the fringes at the sides of the images, which suppresses the leaking of the phase changes to other spatial frequencies. It has been reported that the Hamming window is the most efficient of the windowing techniques for reducing cross-talk in the multichannel YIs.[67]

In this work, the effect of the chosen image width and the Hamming window on the cross-talk was studied using the captured interferograms of the 0.7 wt. % undisturbed experiment measured with the inverted ridge waveguide YI chip (Section 4.1.3.1, p. 59). The phase change curves, $\Delta\phi_{23}$, of the sub-interferogram formed by reference channel pair 2&3 were calculated with different image widths and with and without the Hamming window. The image width was varied from 992 to 2592 (=full width) pixels in 10 pixel intervals, i.e. changing the width of the image from both sides by 5 pixels. The obtained $\Delta\phi_{23}$ curves were baseline corrected based on the values between 0-1.3 min. Curves are shown in Figure 44(a) and Figure 44(b) without and with the Hamming window, respectively. In theory, these phase change curves should be flat but they display both negative and positive phase change responses to sample-induced RI changes that are dependent on the chosen image width, indicating the presence of cross-talk.

To analyse the induced phase changes, the responses of $\Delta\phi_{23}$ curves were calculated by subtracting the mean phase change value within 1.5-1.7 from the mean phase change value between 4.2-4.5 minutes for all the measured curves. Responses calculated with different image widths are shown in Figure 44(c) and Figure 44(e) without and with the Hamming window, respectively. It can be seen that when the Hamming window is applied, the induced cross-talk responses are smaller than without the windowing technique and the variation is more systematic. However, the smallest absolute response value, 0.8×10^{-4} rad, was obtained without the Hamming window at an image width of 2392 pixels. The smallest response with the Hamming window was 1.0×10^{-4} rad, obtained an image width of 1842 pixels.

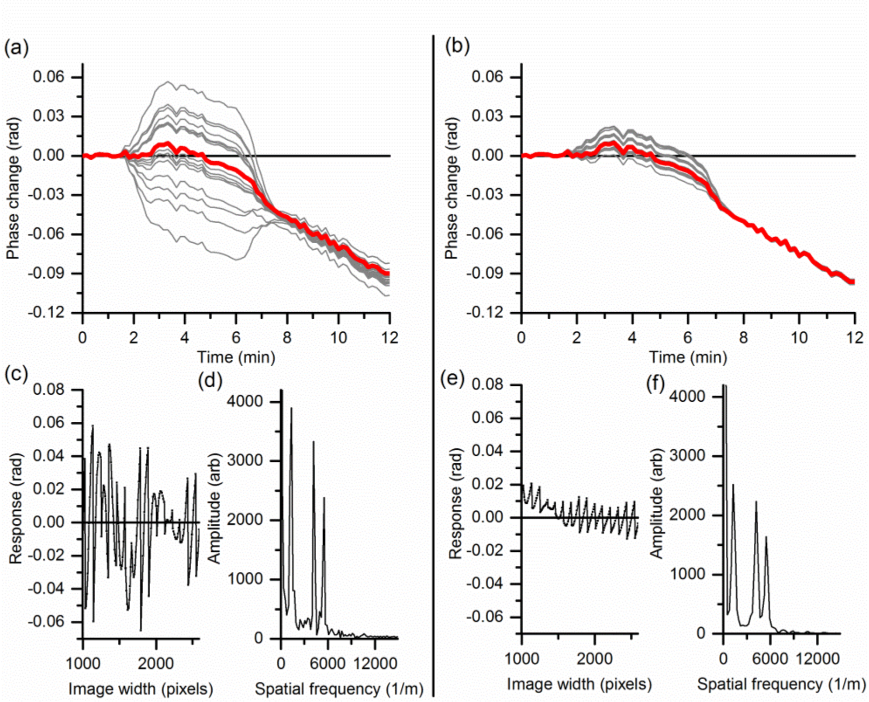

Figure 44 Cross-talk analysis of inverted ridge waveguide YI with different image widths a) without the Hamming window, and b) with the Hamming window. Calculated cross-talk responses at various image widths c) without the Hamming window, and e) with the Hamming window. Amplitude spectra of d) with an image width of 2392 pixels without the Hamming window, and f) with an image width of 1842 pixels with the Hamming window.

Amplitude spectra were calculated at the image widths with the smallest cross-talk responses without and with the Hamming window to verify that the small responses were not a result of a poor match between the spatial frequencies of the sub-interferogram fringes and the FFT analysis. The amplitude spectra in Figure 44(d) and Figure 44(f) calculated without and with the Hamming window, respectively, show well-defined peaks, indicating that the spatial frequencies are coincident, and that these image widths are suitable for the phase change analysis.

Since the smallest cross-talk response was obtained without the Hamming window, the phase change curves of the undisturbed experiments measured with the inverted ridge waveguide YI were analysed without the Hamming window, using an image width of 2392 pixels. The disturbed measurements were analysed using the full image width of 2592 pixels since in these experiments the image width of 2392 displayed a poorer match of the spatial frequencies of the sub-interferogram fringes and the FFT analysis than the full image width, as shown in Figure 45. The compensated phase change curves also had much larger fluctuations if analysed with an image width of 2392, as can be seen by comparing the curves in Figure 46 and in Figure 29(b) (p. 60).

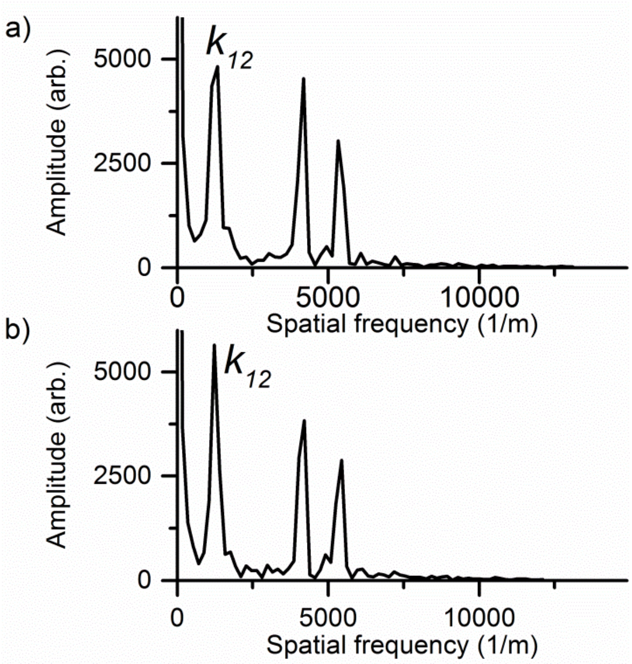

Figure 45 Amplitude spectra calculated from the captured interferogram of 0.7 wt. % disturbed experiment measured with inverted ridge waveguide YI at an image width of a) 2392 and b) 2592 pixels. The spike at the sub-interferogram spatial frequency k_{12} is clearly truncated with an image width of 2392 pixels, indicating a poor match between the spatial frequency of the sub-interferogram and the frequencies available in the FFT analysis.

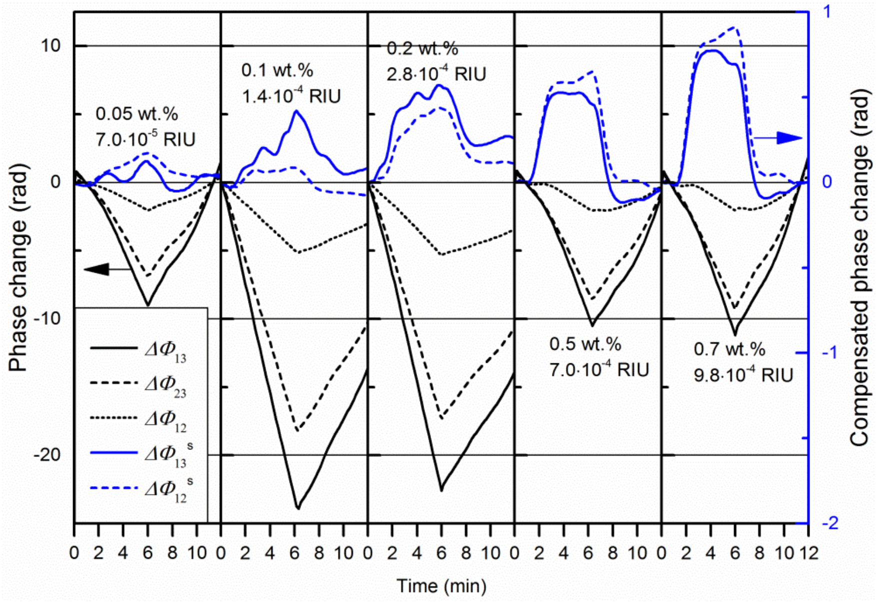

Figure 46 Measured and compensated phase change curves calculated from the disturbed experiments with inverted ridge waveguide YI using an image width of 2392 pixels.

The same approach was used to find the optimal image width for the calculation of the phase change curves in slot waveguide YI experiments. An image width of 1202 pixels displayed the smallest cross-talk response when analysed in a similar way to the inverted ridge case using the captured interferograms of the 0.2 wt. % undisturbed experiment. However, it turned out that despite 1202 pixels being the optimal image width from a cross-talk analysis point of view in one experiment, the amplitude spectra from some other experiments were severely distorted as can be seen from the amplitude spectra in Figure 47(a) and (b) calculated for the 0.1 wt. % and 0.2 wt. % experiments, respectively. This was attributed to the narrow width of the found optimal image width having fewer data points and spatial frequencies for analysis, making the phase change analysis vulnerable to small variations. The visibility of the interference fringes also varied between the sub-interferograms due to the differences in the powers of the outcoupling beams between the channels. This affects the accuracy of the FFT analysis since the sub-interferograms with lower intensity are presented with a smaller number of intensity levels and thus having coarser presentation. Since the amplitude spectra analysed using the full image width displayed clear spikes in all the experiments, an example of which is shown in Figure 19(c) (p. 46), the phase change curves of slot waveguide experiments were analysed using the full image width although this was not optimal from a cross-talk point of view. Use of a larger number of pixels also increases the amount of information for the FFT analysis, which improves the analysis of the lower intensity fringes.

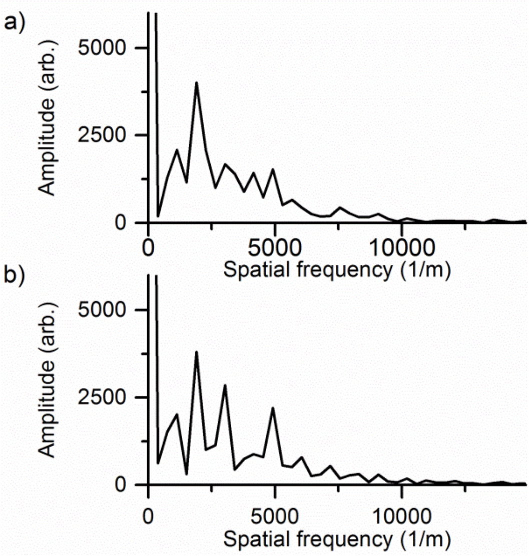

Figure 47 Amplitude spectra analysed from the undisturbed 3-channel slot waveguide YI experiments at an imaged width of 1202 pixels and at a glucose concentration of a) 0.1 wt. % and b) 0.2 wt. %. It can be seen that the frequencies corresponding to the sub-interferogram spatial frequencies are discernible in figure (b) as spikes, but not distinguishable in figure (a).

4.3.2 Chips with roll-to-roll manufactured waveguides

Cross-talk was observed in the ambient RI sensing experiments conducted with the R2R fabricated chip layout as discussed in Section 4.2.2 (p. 71) where phase change responses were seen in the phase change curves of the passivated YI2.

In the experiments with the chips having R2R fabricated waveguides, the interferograms of YI1 and YI2 were imaged onto a single camera detector. The two 2-channel interferograms seem to be well localized onto the respective sides of the camera detector, as shown in Figure 20(a) (p. 47). However, the edge of the interference pattern is not sharp but the intensity of the interference fringes decreases when the distance between the observation point on the detector and the outcoupling point of the diverging beams increases. The interferogram of YI1 is thus overlapping the interferogram of YI2 although the intensity of the fringes is small and vice versa, as shown in Figure 48. Since the interferometers have the same separation at the outcoupling end between the reference and measurement channels, the interferograms also have the same spatial frequency and thus the overlapping of the interferograms is seen as cross-talk. Since the intensity of the fringes overlapping with the adjacent interferogram is small, the effect on the intensity distribution of the actual interferogram fringes is also small. By studying the phase change curves of the ambient RI experiments with the glucose concentration of 0.7 wt. % in Figure 38 (p. 72), it can be seen that the cross-talk induced responses of the passivated YI1 are at most a few per cent of the responses measured by the YI2. It can also be seen that the amount and direction of the cross-talk induced responses vary between measurements. This was attributed to the changes in the measurement system, such as differences in the drift between YI1 and YI2, and to the differences between the areas chosen from the captured interferograms for FFT analysis.

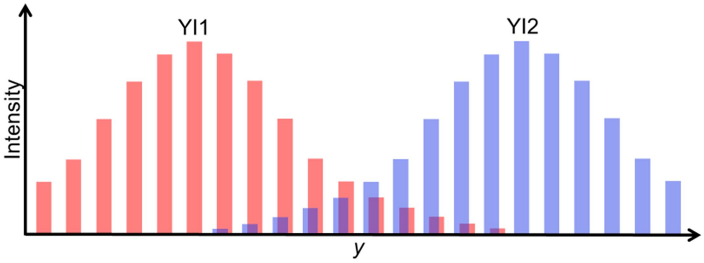

Figure 48 Schematic illustration of the overlapping interferograms along the *y*-axis of the camera detector.

5. Discussion

This section discusses the results of the experiments, the theoretical and practical implications of the work and the reliability and validity of the results. Recommendations for further research can be found in the final subsection.

5.1 Results of the experiments

In this section, the results of the drift compensation experiments and experiments with sensors chips with R2R fabricated waveguides are discussed.

The capability of the drift compensation method, introduced in Section 2.2 (p. 33), was studied with 3-channel YI chip layouts having two reference channels implemented using either inverted ridge or slot waveguides. Measurements to sense ambient RI changes were conducted with undisturbed and mechanically disturbed setups. Phase change responses were compared between these two experiment types and the compensation method was found to be capable of extract the sample-induced RI changes under large induced mechanical disturbances. Sample-induced phase changes were extracted from 161 and 18 times larger measured phase changes with the inverted ridge and slot waveguide YI layout, respectively.

Analysis of the residual phase changes showed that similar values were obtained from both undisturbed and mechanically disturbed experiments, providing a further proof that the compensation method was able to compensate for the large mechanical drifts. The compensation method was more effective at reducing of the residual phase changes of the inverted ridge waveguide YI than the slot waveguide YI. This was attributed to the differences in the chip layouts: the cross-over chip layout of the inverted ridge waveguide YI was designed to enhance the similarity of the drifts seen by the measurement channel and reference channel number 2, and also had smaller separations of the channel pairs than the slot waveguide YI, reducing the differences in the drifts between the channels. The larger signal fluctuations of the slot waveguide YI, attributed to the cross-talk, also impaired the outcome of analysis.

The applicability of the R2R fabricated waveguides for sensing was studied with three different sensor schemas: sensor for ambient RI sensing, MIP/NIP-functionalized sensor for chemical sensing, and antibody functionalized chip for multi-analyte detection of biomolecules. The ambient RI sensing was demonstrated with three chips by using glucose solutions of various concentrations to modify the ambient RI on the sensor. Phase change responses showed an increasing trend with increasing glucose concentration, demonstrating the sensor's compatibility for sensing of ambient RI changes that were detected down to the level of 10^{-6} RIU. Sensors showed thus rather comparable performance than reported earlier for polymeric integrated YI sensors.[24, 25]

With the MIP/NIP-functionalized sensor, the sensing of small molecules was demonstrated by using melamine as a model analyte. The sensor was exposed to aqueous melamine solutions of various concentrations and the net differences between the phase change curves of MIP-coated YI1 and NIP-coated YI2 were calculated to determine the analyte-specific responses. Responses increased with increasing melamine concentrations but began to saturate at the highest concentration, which was in line with earlier findings. Experiments demonstrated the applicability of the sensor embodiment for the chemical sensing of small analytes, which is the first demonstration of MIP-receptor on a polymeric integrated YI sensor chip for direct RI sensing.

Antibody-functionalized YI sensors were used for multi-analyte detection of biomolecules using hCG and CRP as model analytes. The receptor layers were patterned onto the waveguides by means of inkjet printing and the chosen sensor schema enabled direct measurement of the specific binding of the analytes to the sensor's surface. Three sensor chips were exposed to analyte solutions, inducing analyte-specific phase change responses. Calculated response values varied substantially from chip to chip and the measurements thus indicated the presence or absence of the analytes but no quantitative measurements were made. The variation in the response values was attributed to the variations in the receptor layers. The interferometric results indicating analyte-specific binding onto measurement channels were verified by fluorescent staining. Experiments demonstrated the applicability of the sensor chips for multi-analyte detection of biomolecules as well as the compatibility of the inkjet-printed receptor layers with polymeric YI sensor waveguides.

Cross-talk effects were seen in the experiments conducted with the 3-channel YIs and the sensor chips with R2R fabricated waveguides. The origin of the cross-talk in the experiments with 3-channel layouts is in the FFT analysis, whereas with the YI chips with R2R fabricated waveguides cross-talk arises out of the chosen measurement arrangement. To reduce the cross-talk with the 3-channel inverted ridge waveguide YI, the effect of the chosen image width for the FFT analysis and the use of the Hamming window to reduce the cross-talk were analysed. Based on the cross-talk analysis, an optimal image width was found and chosen for the calculation of the phase change curves in the inverted ridge waveguide YI experiments. The windowing technique was not applied since it did not reduce cross-talk in this particular case.

In the analysis of the slot waveguide YI measurements, the effect of the image width on the cross-talk was analysed in a similar way to the inverted ridge waveguide YI case. The optimal image width found was narrow and thus had a limited number of spatial frequencies in the FFT analysis and was therefore vulnerable to small changes in the setup, leading to distorted amplitude spectra in some experiments. Since the full image width with more data points for the FFT analysis provided adequate amplitude spectra in all the experiments, it was used in the analysis despite the increased cross-talk. The full image width also had more data points, which improved the outcome of the FFT analysis of the interferogram that also had low-intensity fringes. The fluctuations of the phase change curves with slot waveguide YI were attributed to the cross-talk between the channels limiting the applicability to measure small concentrations.

Cross-talk in the R2R fabricated chip layouts was mediated between the interferometers by overlapping of the interferograms formed by YI1 and YI2. The largest cross-talk induced phase change response of the passivated YI1 was a few per cents of the phase change of YI2 measured in the ambient RI sensing experiments.

5.2 Theoretical implications

Theoretical implications of the work are related to the drift compensation method derived in Section 2.2 (p. 33). It enables calculation of the sample-induced phase changes from mechanically disturbed experiments when using a multichannel integrated YI chip with two reference channels. The method is based on analysis of the spatial shifts of the sub-interferograms of a multichannel interferogram. The calculation is made by converting the analysed phase changes into spatial shifts. This is done by utilizing the spatial frequencies of the sub-interferograms in the conversion. The method also enables the drift compensated signal to be calculated based on the chip geometry in experimental configurations where the distance between the camera and the sensor chip is large.

The derived compensation method also explains the findings in an earlier article by Ymeti et al. [58] related to signal compensation with multichannel integrated YIs. In the article, it was assumed and experimentally shown that the ratio of the phase changes between different sub-interferograms remains constant and that this ratio can be used to compensate for the drifts. The origin of the constant phase change ratio is speculated in the article, and two possible explanations are given, however no definitive cause is identified. The stability of the phase change ratios between sub-interferograms becomes evident in the compensation method derived here since they are based on the spatial frequencies of the sub-interferograms that again depend on the separations of the waveguides at the outcoupling end of the chip.

5.3 Practical implications

The practical implications of the work are related to the derived compensation method and the use of R2R fabricated waveguides in evanescent wave sensors.

The demonstrated compensation of mechanical drifts with multichannel integrated YI sensors improves the robustness of the interferometric measurements. This opens up new possibilities to implement measurements in noisy environments and improves the compatibility of the measurement technique with low-cost portable reader devices where the implementation of efficient suppression of the ambient disturbances is not easily implementable. It is also worth noting that the compensation method does not require any special optical components or arrangements of the optical setup, beyond the use of a multichannel sensor chip, and the method is thus easily exploitable.

The demonstrated applicability of the R2R fabricated waveguides for evanescent wave sensors presents a new ultra-high volume manufacturing method for disposable polymeric sensor chips. The use of low-cost materials and manufacturing methods enables sensors to be used in cost-critical applications despite the typically large footprints of sensor chips (several square centimetres) required for easy handling of the chip, integration of sample handling features and sample actuation. With disposable sensor chips, both regeneration of the sensor's surface and cross-contamination between samples are avoided. The demonstrated compatibility of the receptor layers with polymeric single-mode waveguides is an important step towards the implementation of analyte-specific sensors for various analytical applications.

5.4 Reliability and validity

The factors affecting the reliability and validity of the results are related to the number of chips used in the experiments, the number of repeated experiments, the properties of the sample solutions and the experimental setups, the quality of the phase change analysis, drift of the experimental setup and the applied baseline correction.

All the experiments were conducted with small numbers of chips. Drift compensation experiments were conducted using two different chip layouts based on two different waveguide types. One chip per chip type was used in the drift compensation experiments and the repeatability of the results was therefore unassessed in this work. Although the results demonstrate that the drift compensation method was able to extract the sample-induced phase changes in the mechanically disturbed experiments with both chip types, the influence of the chip layout and the waveguide type on the compensated phase change curves cannot be fully assessed since they both varied between the chips. In the experiments, the mechanical drift was induced in the direction perpendicular to the interferogram fringes and the direction of the drift was changed once in every experiment. The capability of the compensation method to compensate for drifts in other directions, rotations and rapid undulations was beyond the scope of this study.

A total of six chips having R2R manufactured waveguides were used in the experiments with three different sensor waveguide layouts. The layouts varied with regard to the separation of the waveguides within the sensing region and at the outcoupling end of the chip. Two unfunctionalized sensors were used in the ambient RI sensing experiments, one sensor chip was functionalized with an MIP receptor coating for chemical sensing experiments, and three sensor chips were functionalized with antibodies for biochemical sensing experiments. It was demonstrated that all of these sensor configurations could be utilized as integrated YI sensor chips. Due to the limited number of chips, however, it was not feasible to statistically assess repeatability in the present study. Measurements conducted with a sample solution were repeated up to four times with one chip to give an indication of the repeatability of the measurement and the quantitativity of the sensor response.

The compensation and chemical sensing experiments were conducted with aqueous sample solutions prepared in ultra-pure water with a minimum of interfering factors. The biochemical sensing experiments were conducted using buffered saline solutions containing protein as a sample matrix, thus having interfering factors. However, this sample matrix is less complex than physiological samples such as blood serum. Demonstration of the sensors with natural sample matrices that may have a large number of interfering factors was beyond the scope of this work.

One experimental bench-top setup was used for drift compensation experiments and one for the experiments with chips having R2R fabricated waveguides. The setups were implemented using a fixed configuration. How the properties of the individual components, their positioning and alignment affected the system's performance was therefore not assessed in this work.

The ability of the self-written DFT-based analysis code to extract the phase changes from the captured interferograms was the foundation for the analysis of the phase change curves and the sensor responses. The validity of the self-written code was evaluated by comparing the sensor responses obtained using the self-written code and the numerical simulations of the waveguides. Since the responses obtained with these two separate methods were in relatively good agreement, as shown in Figure 31 (p. 62) and Figure 34 (p. 66), the self-written code seems to work adequately.

As discussed in Section 4.3, the outcome of the analysis is sensitive to the chosen image width, affecting the match between the spatial frequencies of the interferogram fringes and the available spatial frequencies in the analysis. When the phase change curves were analysed, the analysis area was first chosen from the interferogram and the amplitude spectrum was calculated. If the spatial frequencies corresponding to the interferogram fringes were seen as well-formed spikes in the amplitude spectrum, the analysis area was used to analyse all the interferograms from that experiment. If spikes were truncated, the analysis area was adjusted until a proper amplitude spectrum was obtained. In this work, the focus was on demonstration of the sensor concepts, and the complexity of interferogram analysis was therefore kept relatively simple. However, the use of more sophisticated signal processing approaches would most likely have reduced the cross-talk effects seen in the phase change curves.

Drift that was not deliberately induced was observed in the measured phase change curves. This may be caused by mechanical instability of the readout systems, changes in the ambient temperature and absorption of water into the polymeric waveguides. The last is a phenomenon known to cause drift by changing the RI of the sensor waveguides. It has been reported by Wang et al. that drift of polymeric YI sensors flattens after a couple of hours of water exposure.[32] In this work, the chips were exposed to water at least a day before the measurements to reduce the effect of water absorption. However, this aspect was not studied *per se* with the materials and sensor embodiments used in this work, and thus the role of water absorption in the observed drift is unknown. Due to long exposure of sensor chips to water, the effect on drift was most likely small during the measurements. With the multi-analyte biosensor embodiment, the effect is further alleviated since the measurement and reference channels were similarly exposed to water and, in theory, no additional RI difference between the channels was induced. During the water exposure the chip and the flow-cell were mounted into the optical setup. This enabled the relaxation of the mounting-related mechanical stresses before the experiments. YI sensor chips based on R2R fabricated waveguides were especially susceptible to mechanical stresses since they were implemented without a rigid carrier and were thus flexible and deformable. The temperature of the setups was not controlled and all the experiments were conducted at ambient room temperature. The temperature of the sample and flushing solutions was allowed to equalize with the optical setup by letting them sit on the laboratory table for at least several hours. Phase change drift related to ambient room temperature changes was considered to be slow compared to sample-induced phase changes and was therefore assumed to have a minor influence on the demonstration of the sensor concepts.

Linear baseline correction was applied to phase change curves of experiments done with chips based on R2R manufactured waveguides. This method was chosen since it was observed in the experiments that the phase change curves typically approached a linear trend within few hours after the initiation of the pumping and incoupling of laser light as shown in Paper IV. The phase change drift trend was monitored before initiation of the experiments. Linear correction was done separately for each of the phase change curves based on the data points within the first few minutes of the experiment, i.e. before the sample solution entered the flow cell. The applied method is therefore vulnerable to changes in the trend of the phase change drift during an experiment related to e.g. ambient temperature change rate. The method was considered to work decently in the analysis of the measured phase change curves although it was not able to eliminate all of the phase change drift. From Figure 38 (p. 72), it can be seen that for the baseline corrected phase change curves of ambient RI experiments the maximum deviation from the baseline, i.e. *x*-axis, is below 0.08 rad at the end of the experiments. On the other hand, the baseline corrected phase change curves of chemical sensing experiments, shown in Figure 40(a) (p. 75), have much larger deviations from the baseline at the end of the experiments, up to several radians. Since the functional coatings applied onto the chemical sensor surface are the only major difference between these two experiments, it seems more plausible that the functional coatings are the factor behind this outcome, as discussed in Section 4.2.3 (p. 73), than the baseline correction method. In the biochemical sensing experiments, the baseline correction seems to work adequately: All the phase change curves shown in Figure 42(a) (p. 78) were baseline corrected based on the data points within the first 5.7 min and the deviation of the phase change curves of YI2 from the baseline is less than -0.16 rad at the time point of 40 min, i.e. just before the corresponding analyte exposure. The phase change curves however show different phase change drift trends at the end of the experiment. This was attributed to the differences in the applied antibody layers but may also be related to the baseline correction method. Due to the low number of repeated experiments, however, the definitive cause could not be identified. The baseline correction method affects the sensor response and the response range values but it was not considered to have a major impact in the demonstration of the feasibility of the sensor concepts.

5.5 Recommendations for further research

The work discussed in this thesis demonstrated several sensor concepts, but their implementation in real-life portable diagnostics requires further research. This section provides a short discussion of recommended topics for further research.

For efficient utilization of the drift compensation method, the cross-talk between the different channel pairs needs to be minimized. Different chip layouts and implementations should therefore be studied as well as the use of sophisticated signal analysis methods. Other topics for study include how the compensation method copes with different combinations of movements and rotations and with rapidly varying disturbances. The method should be tested with a portable reader in noisy ambient conditions to demonstrate its viability for portable diagnostics.

This work has shown that single-mode waveguides for an evanescent wave sensor can be fabricated using ultra-high volume manufacturing methods. In the future, the goal is to demonstrate that the entire sensor structure can be implemented using ultra-high volume methods to enable widespread utilization of evanescent wave sensors in cost-critical applications. The sensor chips used in the experiments contained photonic and transducing functionalities. The sample actuation, however, was implemented using a flow cell and an external pump. For a self-contained easy-to-use sensor chip, the fluid actuation and sample handling functionalities need to be integrated with the sensor platform. A robust, low-cost and simple-to-use method to couple light into the sensor chip needs to be developed to enable easy insertion of the sensor chips into the reader even by non-trained persons

Implementation of fully integrated sensor chips requires further manufacturing steps in addition to the fabrication of photonic waveguide platforms. These steps include, for example, patterning of functional analyte binding surfaces, blocking of sensor surfaces to prevent unspecific binding, integration of microfluidic structures with the photonic platform for sample actuation and handling, integration of a sampling device such as a needle, integration of reagent reservoirs into the chip, cutting the chips from the roll, and packing them. To realize this cost-effectively, combinations of various mass-manufacturing methods need to be applied. These methods may include printing and dispensing for patterning layers, hot-embossing and imprinting of microfluidic structures, lamination of layers, sawing, laser and die cutting, as well as use of pick-and-place machines for assembling components. Finally, fully integrated sensor chips containing all the necessary optical, sample handling, and actuation functionalities should be developed and demonstrated using low-cost materials and manufacturing methods, real samples, realistic conditions and low-cost portable readers.

Reliability and reproducibility of the sensor chips and sensor responses is one of the main topics for future work. The sensing experiments discussed in this thesis should be repeated with large numbers of chips and with real sample matrices to characterize the sensor properties and to identify the main factors affecting sensor reliability and repeatability. The large number of repeated experiments would enable determination of the limit of detection and limit of quantification that should be established with various kinds of analytes, sample matrices and experimental setups. The methods to implement signal enhancement, e.g. high index coatings, with the drift compensation method and R2R fabricated waveguides should be studied to enhance their applicability to diagnostic applications with high sensitivity requirements. The effect of water absorption into the R2R fabricated waveguides with the demonstrated sensor embodiments should be studied.

6. Summary

The aim of the work discussed in this thesis was to develop integrated YI sensors for portable diagnostics by improving the robustness of the sensing method and the disposability of the sensor chips.

The robustness of the sensing method was improved by deriving and demonstrating a method of compensating for mechanical drifts that is applicable for multichannel integrated YI sensors with two reference channels. The method was shown to be able to extract the sample-induced phase change responses from the phase change curves measured under mechanical disturbances using inverted ridge and slot waveguide based sensor chips. The sample induced phase change responses were extracted from up to 161 times larger phase changes measured with deliberately mechanically disturbed setup. The compensation method is readily adaptable to integrated YI readers since it is based on the properties of the multichannel sensor chips and analysis of the interferograms and does not require any additional special optical components or arrangements from the reader. The compensation method opens up new possibilities to utilize YI sensors in noisy environments and improves the compatibility of the measurement technique with low-cost portable readers by alleviating the requirements for suppression of ambient disturbances.

Sensor chip disposability was enhanced by demonstrating that all-polymeric single-mode waveguides fabricated using ultra-high volume manufacturing methods can be utilized as a photonic platform for an evanescent wave sensor. This enables cost-efficient production methods to be used for integrated YI sensors, rendering them inherently disposable and enabling their wide-spread use in cost-critical applications. Sensors were shown to be able to detect ambient RI changes at a level of 10^{-6} RIU and to quantify them at a level of 10^{-5} RIU. They thus showed fairly comparable performance than reported earlier for polymeric integrated YI sensors.[24, 25] A lower state-of-the-art limit of detection values at a level of 10^{-8} RIU has been reported for silicon based integrated YI sensors as well as for surface plasmon resonance sensors that are commercialized and widely used in research laboratories.[17, 33, 37] It was also demonstrated that polymeric YI sensor chips could be functionalized with an MIP layer for chemical sensing of small molecules and with inkjet-printed antibody layers for multi-analyte detection of biomolecules. These sensor concepts were demonstrated using application relevant analyte molecule concentrations. Artificial MIP receptor layers may be advantageous for low-cost sensors since they have the potential to be low-cost, robust, repeatable, and mass-manufacturable. The demonstration of the functionalization of a polymeric integrated YI sensor by inkjet printing opens up new implementation possibilities for low-cost sensors since, as an additive method, inkjet printing minimizes the consumption of potentially expensive receptor materials and is also considered to be compatible with mass-production methods.

The results discussed in this thesis form one of the stepping-stones on the path towards the use of integrated YI sensors in portable diagnostics. Since the development of low-cost sensor solutions is one of the main challenges in the sensor field, the demonstrated concepts of disposable, low-cost photonic sensor chips and the developed drift compensation method open up both scientifically and economically interesting opportunities for exploiting portable low-cost diagnostics in various application areas, including point-of-need and home diagnostics, environmental monitoring, security, and food safety.

Appendix A: Light propagation in an optical waveguide

In this section, the basic principles defining the light propagation in the waveguides are discussed using a slab waveguide as an example. The topics discussed are critical angle of refraction, formation of an evanescent wave, total internal reflection (TIR) at the material boundary, phase shift associated with TIR, formation of modes in waveguides, and numerical calculations of waveguide properties. The theoretical discussion is adapted from Ref. [70], [71] and [72]. A slab waveguide is used here due to its simplicity. The same phenomena are present in other waveguide types but the formalism is more complex or no analytical expressions exist.

A.1 Critical angle, evanescent wave and total internal reflection

Electromagnetic plane wave incidents an interface between two materials as illustrated in Figure 49. The refractive indices of the materials are n_1 and n_2, and $n_2 > n_1$. At the interface, the incident wave is reflected and refracted. The waves travel in the direction shown by their wave vectors, $\boldsymbol{\kappa}$. The electric fields of the waves are:

$$\begin{aligned} \text{Incident: } \mathrm{E}_i &= \mathrm{E}_{0i} e^{i\boldsymbol{\kappa}_i \cdot \mathrm{r} - i\omega t} \\ \text{Reflected: } \mathrm{E}_r &= \mathrm{E}_{0r} e^{i\boldsymbol{\kappa}_r \cdot \mathrm{r} - i\omega t} \\ \text{Refracted: } \mathrm{E}_t &= \mathrm{E}_{0t} e^{i\boldsymbol{\kappa}_t \cdot \mathbf{r} - i\omega t} = \mathrm{E}_{0t} \underbrace{e^{i\boldsymbol{\kappa}_t \cdot \mathrm{r}}}_{\text{propag. factor}} e^{-i\omega t}, \end{aligned} \tag{24}$$

where ω is the frequency of the plane wave, t is time, and $\boldsymbol{r}$ an observation point. $\boldsymbol{E}_{0i}$, $\boldsymbol{E}_{0r}$ and $\boldsymbol{E}_{0t}$ are the amplitudes, and $\boldsymbol{\kappa}_i$, $\boldsymbol{\kappa}_r$ and $\boldsymbol{\kappa}_t$ the wave vectors of the incident, reflected, and refracted waves, respectively. The length of the wavevector $|\boldsymbol{\kappa}| = 2\pi/\lambda$, where λ is the wavelength of the wave. Analysis of an electromagnetic wave is typically divided into two orthogonal polarizations called transverse magnetic (TM) and transverse electric (TE) polarization states. In the TE polarization state, electric field vectors are perpendicular and magnetic field vectors, $\boldsymbol{B}$, parallel to the plane of incidence, as shown in Figure 49(a). For the TM polarization state, electric field vectors are parallel to the plane of incidence and magnetic field vectors are perpendicular, as shown in Figure 49(b).

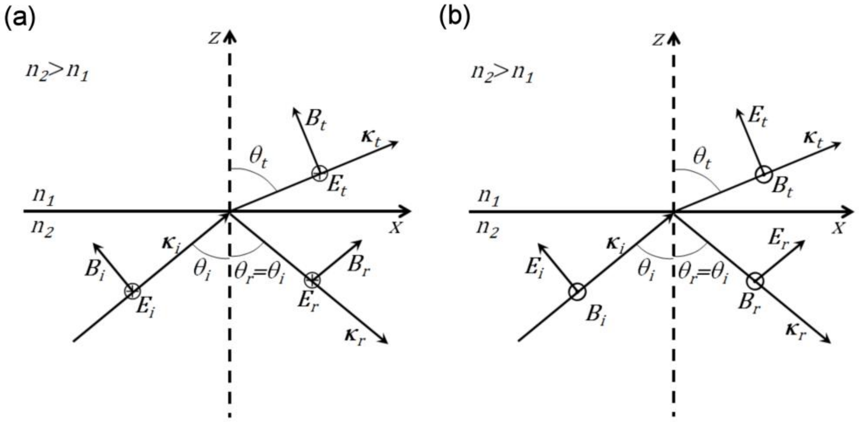

Figure 49 Wave vectors, electric and magnetic fields, and angles of incidence, reflection and refraction for a plane wave hitting a material boundary for a) TE polarization, and b) TM polarization. In the figure the electric field vectors of TE polarization are directed away from and the magnetic field vectors of TM polarization towards the reader.

According to the law of reflection, the angle of incidence, θ_i, and angle of reflection, θ_r, are equal, i.e. $\theta_r = \theta_i$. The angle of refraction, θ_t, of the refracted wave can be calculated using Snell's law:

$$n_1 \sin\theta_t = n_2 \sin\theta_i \Leftrightarrow \sin\theta_t = \frac{n_2}{n_1}\sin\theta_i. \qquad (25)$$

When light approaches the material interface from the media having higher RI, it follows from Eq. (25) that $\theta_t > \theta_i$. Thus, at some specific angle of incidence $\theta_t = 90°$ and the refracted ray propagates along the material interface. This angle of incidence is called *critical angle*, θ_C, and can be calculated using Eq. (25):

$$\sin\theta_C = \frac{n_1}{n_2} \Leftrightarrow \theta_C = \arcsin\frac{n_1}{n_2}. \qquad (26)$$

When $\theta_i > \theta_C$, it follows from Eq. (26) that $\sin\theta_i > n_1/n_2$ and from the latter form of Eq. (25) that $\sin\theta_t > 1$, meaning that θ_t is a complex angle. From the trigonometrical identity $\sqrt{\sin^2\alpha + \cos^2\alpha} = 1$ it follows that $\cos\theta_t$ is now imaginary. The value of $\cos\theta_t$ can be calculated using the trigonometrical identity, Eqs. (25) and (26)

$$\begin{aligned}\cos\theta_t &= \sqrt{1-\sin^2\theta_t} = i\sqrt{\sin^2\theta_t - 1} \\ &= i\sqrt{\left(\frac{n_2}{n_1}\sin\theta_i\right)^2 - 1} = i\sqrt{\left(\frac{\sin\theta_i}{\sin\theta_C}\right)^2 - 1}.\end{aligned} \qquad (27)$$

Now the propagation factor of the refracted field of Eq. (24) at point $\boldsymbol{r}(x, z > 0)$ can be expressed by using the second form for $\cos\theta_t$ in Eq. (27)

$$e^{i\boldsymbol{\kappa}_t\cdot\mathrm{r}} = e^{i|\boldsymbol{\kappa}_t|(x\sin\theta_t + z\cos\theta_t)} = \underbrace{e^{i|\boldsymbol{\kappa}_t|x\sin\theta_t}}_{\text{wave along interface}}\ \underbrace{e^{-|\boldsymbol{\kappa}_t|z\sqrt{\sin^2\theta_t - 1}}}_{\text{exponentially decaying part}}. \qquad (28)$$

The propagation factor separates into two parts: the first part represents a wave propagating in the *x*-direction and the second part decays exponentially when moving away from the material interface. When $\theta_i > \theta_C$ the refracted wave thus propagates parallel to the material interface and decays exponentially in the *z*-direction ($z > 0$). The exponentially decaying part of the refracted wave forms the *evanescent wave* that attenuates rapidly within a few wavelengths. Although part of the refracted wave exists above the material interface, there is no energy transfer through the boundary. This can be verified by studying the time averaged normal component of the Poynting vector just above the material interface. Since the energy is conserved, the intensities of the incident and reflected waves have to be equal when $\theta_i > \theta_C$, and the wave is *totally internally reflected* within the material having higher RI.

A.2 Phase shift associated with total internal reflection

At total internal reflection a phase shift, Φ, occurs between the incident and reflected rays. This follows from the boundary condition requiring that the tangential components of electric and magnetic fields be continuous across the material interface. Phase shift also depends on the polarization state of the light. In this section the phase shift for TE polarization, Φ_{TE}, is derived first followed by the derivation of the phase shift for TM polarization, Φ_{TM}.

In the case of TE polarization, the tangential components of the electric field are perpendicular to the plane of incidence, as illustrated in Figure 49(a), and the boundary condition can be written

$$E_{0i} + E_{0r} = E_{0t}, \qquad (29)$$

where E_{0i}, E_{0r} and E_{0t} are the amplitudes of incident, reflected and refracted electric fields, respectively. The magnetic field vectors are parallel to the plane of incidence and the boundary condition can be written

$$\begin{aligned} -B_{0i}\cos\theta_i + B_{0r}\cos\theta_i &= -B_{0t}\cos\theta_t \\ \Leftrightarrow n_2 E_{0i}\cos\theta_i - n_2 E_{0r}\cos\theta_i &= n_1 E_{0t}\cos\theta_t , \end{aligned} \qquad (30)$$

where B_{0i}, B_{0r} and B_{0t} are the amplitudes of incident, reflected and refracted magnetic fields, respectively. The latter form is obtained using the relationship $B = (n/c)E$, where n is the refractive index of the material and c the speed of light, and multiplying by -1.

Ratio of the amplitudes between the incident and reflected waves can be calculated by first solving E_{0t} from the latter form of Eq. (30), and then substituting it into Eq. (29) yielding

$$\frac{E_{0r}}{E_{0i}} = \frac{n_2\cos\theta_i - n_1\cos\theta_t}{n_2\cos\theta_i + n_1\cos\theta_t} \qquad (31)$$

If $\theta_i > \theta_C$, the amplitude ratio for TE polarization can be written

$$\frac{E_{0r}}{E_{0i}} = \frac{n_2\cos\theta_i - i\sqrt{\left(n_2\sin\theta_i\right)^2 - n_1^2}}{n_2\cos\theta_i + i\sqrt{\left(n_2\sin\theta_i\right)^2 - n_1^2}} \qquad (32)$$

that is obtained by substituting the third form for $\cos\theta_t$ in Eq. (27) into Eq. (31). The amplitude ratio is now a complex number. The phase shift between the incident and reflected waves, Φ_{TE}, can be calculated by setting

$$\frac{E_{0r}}{E_{0i}} = \frac{a - ib}{a + ib} = \frac{e^{-i\alpha}}{e^{i\alpha}} = e^{i\Phi_{\mathrm{TE}}} , \qquad (33)$$

where $\alpha = -\frac{\Phi_{\mathrm{TE}}}{2}$, and a and b are real numbers. By using the relationship $\tan\alpha = \frac{b}{a}$, the phase change Φ_{TE} is

$$\Phi_{\mathrm{TE}} = -2\alpha = -2\arctan\frac{\sqrt{\left(n_2\sin\theta_i\right)^2 - n_1^2}}{n_2\cos\theta_i}. \qquad (34)$$

The phase shift, Φ_{TM}, of TM polarised wave at total internal reflection can be calculated using the same procedure as for TE polarization. The directions of electric and magnetic fields for TM polarization are shown in Figure 49(b). The boundary condition for an electric field is

$$E_{0i}\cos\theta_i - E_{0r}\cos\theta_i = E_{0t}\cos\theta_t, \tag{35}$$

and for a magnetic field

$$\begin{aligned} &B_{0i} + B_{0r} = B_{0t} \\ \Leftrightarrow\ & n_2 E_{0i} + n_2 E_{0r} = n_1 E_{0t}. \end{aligned} \tag{36}$$

In the case of TM polarization the ratio of the amplitudes of reflected and incident waves is calculated by first solving E_{0t} from the latter form of Eq. (36), and then substituting it into Eq. (35) yielding

$$\frac{E_{0r}}{E_{0i}} = \frac{n_1\cos\theta_i - n_2\cos\theta_t}{n_1\cos\theta_i + n_2\cos\theta_t}. \tag{37}$$

If $\theta_i > \theta_C$, the amplitude ratio is

$$\frac{E_{0r}}{E_{0i}} = \frac{\left(\frac{n_1}{n_2}\right)^2\cos\theta_i - i\sqrt{\sin^2\theta_i - \left(\frac{n_1}{n_2}\right)^2}}{\left(\frac{n_1}{n_2}\right)^2\cos\theta_i + i\sqrt{\sin^2\theta_i - \left(\frac{n_1}{n_2}\right)^2}}. \tag{38}$$

that is obtained by substituting the third form for $\cos\theta_t$ in Eq. (27) into Eq. (37). The amplitude ratio is again a complex number and the phase change Φ_{TM} is

$$\Phi_{TM} = -2\arctan\frac{\sqrt{\sin^2\theta_i - \left(\frac{n_1}{n_2}\right)^2}}{\left(\frac{n_1}{n_2}\right)^2\cos\theta_i} \tag{39}$$

that is obtained in a similar way to TE polarization.

As shown by Eqs. (34) and (39), the phase change depends on the refractive indices at both sides of the material boundary. This is utilized in waveguide-based evanescent wave sensors since it enables the sensing of refractive index changes outside the waveguide, which is discussed in the next section.

A.3 Modes in optical waveguide and effective refractive index

A schematic illustration of a three-layer slab waveguide structure is shown in Figure 50. The core and the undercladding and overcladding layers have RIs n_W, n_{UC}

and n_{OC}, respectively, and $\{n_{UC}, n_{OC}\} < n_W$. As illustrated in Figure 50, light propagates within the waveguide core along zigzag paths by means of consecutive total internal reflections from the material boundaries, when the incidence angle θ_i is larger than the critical angle of the core-undercladding, $\theta_{c,UC}$, and the critical angle of the core-overcladding, $\theta_{c,OC}$, boundaries. The total internal reflections enable lossless propagation over large distances. Light having an incidence angle of θ_i < max$\{\theta_{c,UC}, \theta_{c,OC}\}$ is only partially reflected and is radiated out of the core forming radiation modes.[18, 73]

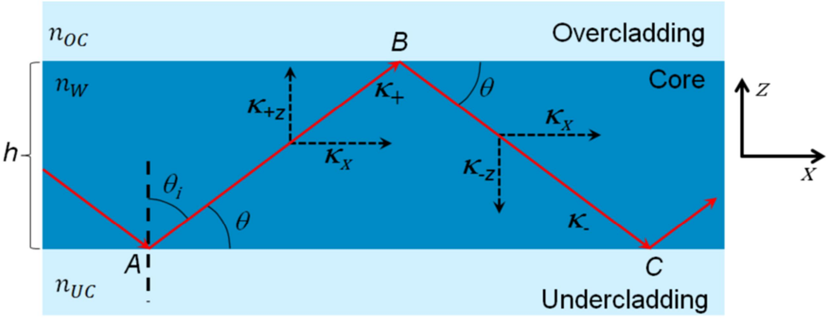

Figure 50 Schematic illustration of the light propagation within a waveguide. The red arrows show the path of the light within the waveguide core.

Although the critical angle defines the smallest incidence angle for total internal reflection, light with arbitrary incidence angles θ_i > max$\{\theta_{c,UC}, \theta_{c,OC}\}$ cannot propagate over large distances in waveguides. Only light with certain discrete incident angles propagates long distances within the waveguide. These light paths are called *modes* and are related to specific transverse field profiles that are constant in the longitudinal direction of the waveguide. With optical waveguides, the angles are typically defined with reference to the longitudinal axis of the waveguide instead to the normal of the material interfaces, and the angle θ shown in Figure 50 is therefore used here in the discussion of the waveguide modes.

The path shown by red arrows in Figure 50 can be considered to present a plane wave reflecting back and forth from the material boundaries or two plane waves, one having a positive, $\kappa_{+\mathbf{z}} = |\boldsymbol{\kappa}_+| \sin\theta$, and one having a negative, $\kappa_{-\mathbf{z}} = -|\boldsymbol{\kappa}_-| \sin\theta$, wave vector component in the *z*-direction and $|\boldsymbol{\kappa}_+| = |\boldsymbol{\kappa}_-| \equiv \kappa$. The vector component in the *x*-direction, $\kappa_{\mathbf{x}} = \kappa \cos\theta$, is the same for both of the waves and is the propagation factor. The *effective refractive index*, n_{eff}, is

$$n_{\text{eff}} = \frac{\kappa_x}{\kappa / n_{\text{w}}} = n_{\text{w}} \cos\theta \qquad (40)$$

that is a ratio of the propagation factor and the length of the wave vector in the core material, giving an apparent refractive index for the wave in *x*-direction, *i.e.* along the length of the waveguide.

The plane wave can be presented as a superposition of two perpendicular plane waves one propagating in *x*-direction along the longitudinal axis of the waveguide core, and one propagating in the *z*-direction. To have a stable transverse field profile as required for the modes, the two plane waves propagating in the transverse *z*-direction have to interfere constructively, i.e. the accumulated phase of the transverse roundtrip in the *z*-direction has to be an integer multiple of 2π. The accumulated phase is formed by the propagated distance in the *z*-direction and by the phase shifts related to the total internal reflections at the two material boundaries, as discussed in the previous section. Now the condition for the *modes* can be written

$$2h\kappa\sin\theta+\Phi_{\mathrm{OC}}+\Phi_{\mathrm{UC}}=2m\pi, \qquad (41)$$

where h is the height of the waveguide, Φ_{OC} and Φ_{UC} the phase shifts related to the total internal reflections at the core-overcladding and core-undercladding boundaries, respectively, and m = 0,1,2 ... a positive integer. Now angle θ_m, the angle θ related to the m^{th} mode, is

$$\theta_m=\arcsin\frac{2m\pi-\Phi_{\mathrm{OC}}-\Phi_{\mathrm{UC}}}{2h\kappa}. \qquad (42)$$

In the evanescent wave sensors, the overcladding layer is formed by the sample media at the sensor sensing area. When analyte molecules induce a refractive index change at the sensing area, it follows from Eqs. (34) and (39) that the phase shift Φ_{OC} at the core-overcladding boundary changes, which again changes θ_m calculated from Eq. (42). Since θ_m is changed, the propagation factor $\kappa_{\mathbf{x}}$ and effective refractive index n_{eff} for the wave are also changed, affecting the apparent optical length of the waveguide in the longitudinal direction.

A.4 Numerical calculation of waveguide properties

In the preceding discussion, a slab waveguide was used as an example to introduce the key phenomena in optical waveguides. Although analytical expressions can be derived for simple structures, numerical methods, e.g. the finite element method (FEM) or the finite difference method (FDM), have to be used with more complex waveguide geometries.[72, 74]

The mode field profiles and effective refractive indices of the waveguides used in the YI sensor chips were modelled by means of FEM or FDM using commercial software (Fimmwave, Photon Design). The waveguide geometries were first derived from the scanning electron microscope (SEM) images taken from the waveguide cross-sections. The effective refractive index values were calculated with various overcladding values corresponding the sample solutions, enabling calculation of the change of n_{eff} in the function of the change in n_{OC}, yielding the theoretical sensitivity of the sensor.

References

1. E. Makarona, P. Petrou, S. Kakabakos, K. Misiakos, and I. Raptis, "Point-of-need bioanalytics based on planar optical interferometry," Biotechnol. Adv. 34, 209-233 (2016).

2. X. Fan and I. M. White, "Optofluidic microsystems for chemical and biological analysis," Nature Photon. **5,** 591-597 (2011).

3. A. Gebauer, S. Schmidt, and W. Hoffmann, "Status and perspective of lab-on-a-chip systems for common diseases: a systematic review from 2003 to 2013," Personal. Med. **13,** 71-91 (2016).

4. P. B. Luppa, A. Bietenbeck, C. Beaudoin, and A. Giannetti, "Clinically relevant analytical techniques, organizational concepts for application and future perspectives of point-of-care testing," Biotechnol. Adv. **34,** 139-160 (2016).

5. D. E. W. Patabadige, S. Jia, J. Sibbitts, J. Sadeghi, K. Sellens, and C. T. Culbertson, "Micro total analysis systems: Fundamental advances and applications," Anal. Chem. **88,** 320-338 (2016).

6. Y. Chen, L. Jiang, M. Mancuso, A. Jain, V. Oncescu, and D. Erickson, "Optofluidic opportunities in global health, food, water and energy," Nanoscale **4,** 4839-4857 (2012).

7. H. O. Fatoyinbo and M. P. Hughes, "Biosensors," in *Encyclopedia of Nanotechnology,* B. Bhushan, ed. (Springer, 2012), pp. 329-345.

8. J. L. Garcia-Cordero and A. J. Ricco, "Lab-on-a-chip (General philosophy)," in *Encyclopedia of Microfluidics and Nanofluidics,* D. Li, ed. (Springer, 2015), pp. 1501-1511.

9. J. Evans, "Biochips markets," in *Global Biochip Markets: Microarrays and Lab-On-A-Chip,* Anonymous (BCC Research, 2016), pp. 204-249.

10. X. Fan, I. M. White, S. I. Shopova, H. Zhu, J. D. Suter, and Y. Sun, "Sensitive optical biosensors for unlabeled targets: A review," Anal. Chim. Acta **620,** 8-26 (2008).

11. F. Kehl and S. Follonier, "Self-referenced waveguide grating sensor," Opt. Lett. **41,** 1447-1450 (2016).

12. I. J. G. Sparrow, P. G. R. Smith, G. D. Emmerson, S. P. Watts, and C. Riziotis, "Planar Bragg grating sensors-Fabrication and applications: A Review," J. of Sensors **2009,** 607647 (2009).

13. C. Lv, Z. Jia, Y. Liu, J. Mo, P. Li, and X. Lv, "Angle-resolved diffraction grating biosensor based on porous silicon," J. Appl. Phys. **119,** 094502 (2016).

14. K. A. Wilson and F. Vollmer, "Optical ring resonator biosensor," in *Encyclopedia of Nanotechnology,* B. Bhushan, ed. (Springer, 2012), pp. 2837-2849.

15. Y. Zhang, Y. Zhao, and R. Lv, "A review for optical sensors based on photonic crystal cavities," Sens. Actuator A-Phys. **233,** 374-389 (2015).

16. A. Abbas, M. J. Linman, and Q. Cheng, "New trends in instrumental design for surface plasmon resonance-based biosensors," Biosens. Bioelectron. **26,** 1815-1824 (2011).

17. D. Erickson, "Surface plasmon resonance sensors," in *Encyclopedia of Microfluidics and Nanofluidics,* D. Li, ed. (Springer, 2015), pp. 3123-3131.

18. P. Kozma, F. Kehl, E. Ehrentreich-Förster, C. Stamm, and F. F. Bier, "Integrated planar optical waveguide interferometer biosensors: A comparative review," Biosens. Bioelectron. **58,** 287-307 (2014).

19. J. S. Kanger, V. Subramaniam, P. H. J. Nederkoorn, and A. Ymeti, "A Fast and sensitive integrated Young interferometer biosensor," in *Advanced Photonic Structures for Biological and Chemical Detection,* X. Fan, ed. (Springer, 2009), pp. 270-295.

20. M. A. Cooper, ed., *Label-Free Biosensors* (Cambridge University Press, 2009).

21. J. P. Chambers, B. P. Arulanandam, L. L. Matta, A. Weis, and J. J. Valdes, "Biosensor recognition elements," Curr. Issues Mol. Biol. **10,** 1-12 (2008).

22. L. Uzun and A. P. F. Turner, "Molecularly-imprinted polymer sensors: realising their potential," Biosens. Bioelectron. **76,** 131-144 (2016).

23. S. A. Piletsky and A. P. F. Turner, "Imprinted polymers and their application in optical sensors," in *Optical Biosensors: Today and Tomorrow,* F. S. Ligler and C. R. Taitt, eds. (Elsevier, 2008), pp. 543-581.

24. M. Wang, J. Hiltunen, C. Liedert, L. Hakalahti, and R. Myllylä, "An integrated Young interferometer based on UV-imprinted polymer waveguides for label-free biosensing applications," J. Eur. Opt. Soc, Rapid Publ. **7,** 12019 (2012).

25. M. Hiltunen, J. Hiltunen, P. Stenberg, S. Aikio, L. Kurki, P. Vahimaa, and P. Karioja, "Polymeric slot waveguide interferometer for sensor applications," Opt. Express **22,** 7229-7237 (2014).

26. B. E. A. Saleh and M. C. Teich, *Fundamentals of photonics* (Wiley, 1991).

27. V. R. Almeida, Q. Xu, C. A. Barrios, and M. Lipson, "Guiding and confining light in void nanostructure," Opt. Lett. **29,** 1209-1211 (2004).

28. T. Young, "The Bakerian lecture: Experiments and calculations relative to physical optics," Philosophical Transactions of the Royal Society of London **94,** 1-16 (1804).

29. T. Young, *A course of lectures on natural philosophy and the mechanical arts, vol. 1* (Johnson, 1807).

30. A. Brandenburg and R. Henninger, "Integrated optical Young interferometer," Appl. Opt. **33,** 5941-5947 (1994).

31. G. H. Cross, Y. Ren, and N. J. Freeman, "Young's fringes from vertically integrated slab waveguides: Applications to humidity sensing," J. Appl. Phys. **86,** 6483-6488 (1999).

32. M. Wang, S. Uusitalo, C. Liedert, J. Hiltunen, L. Hakalahti, and R. Myllylä, "Polymeric dual-slab waveguide interferometer for biochemical sensing applications," Appl. Opt. **51,** 1886-1893 (2012).

33. K. Schmitt, B. Schirmer, C. Hoffmann, A. Brandenburg, and P. Meyrueis, "Interferometric biosensor based on planar optical waveguide sensor chips for label-free detection of surface bound bioreactions," Biosens. Bioelectron. **22,** 2591-2597 (2007).

34. G. H. Cross, A. A. Reeves, S. Brand, J. F. Popplewell, L. L. Peel, M. J. Swann, and N. J. Freeman, "A new quantitative optical biosensor for protein characterisation," Biosens. Bioelectron. **19,** 383-390 (2003).

35. A. Schimpf, D. Bucci, M. Nannini, A. Magnaldo, L. Couston, and J.-E. Broquin, "Photothermal microfluidic sensor based on an integrated Young interferometer made by ion exchange in glass," Sens. Actuator B-Chem. **163,** 29-37 (2012).

36. E. Brynda, M. Houska, A. Brandenburg, and A. Wikerstål, "Optical biosensors for real-time measurement of analytes in blood plasma," Biosens. Bioelectron. **17,** 665-675 (2002).

37. A. Ymeti, J. S. Kanger, R. Wijn, P. V. Lambeck, and J. Greve, "Development of a multichannel integrated interferometer immunosensor," Sens. Actuator B-Chem. **83,** 1-7 (2002).

38. M. Wang, J. Hiltunen, C. Liedert, S. Pearce, M. Charlton, L. Hakalahti, P. Karioja, and R. Myllylä, "Highly sensitive biosensor based on UV-imprinted layered polymeric–inorganic composite waveguides," Opt. Express **20,** 20309-20317 (2012).

39. L. Ahmadi, M. Hiltunen, P. Stenberg, J. Hiltunen, S. Aikio, M. Roussey, J. Saarinen, and S. Honkanen, "Hybrid layered polymer slot waveguide Young interferometer," Opt. Express **24,** 10275-10285 (2016).

40. W. Lukosz, C. Stamm, H. R. Moser, R. Ryf, and J. Dübendorfer, "Difference interferometer with new phase-measurement method as integrated-optical refractometer, humidity sensor and biosensor," Sens. Actuator B-Chem. **39,** 316-323 (1997).

41. J. Xu, D. Suarez, and D. S. Gottfried, "Detection of avian influenza virus using an interferometric biosensor," Anal. Bioanal. Chem. **389,** 1193-1199 (2007).

42. H. K. P. Mulder, A. Ymeti, V. Subramaniam, and J. S. Kanger, "Size-selective detection in integrated optical interferometric biosensors," Opt. Express **20,** 20934-20950 (2012).

43. C. Stamm, R. Dangel, and W. Lukosz, "Biosensing with the integrated-optical difference interferometer: dual-wavelength operation," Opt. Commun. **153,** 347-359 (1998).

44. A. Ymeti, J. S. Kanger, J. Greve, G. A. J. Besselink, P. V. Lambeck, R. Wijn, and R. G. Heideman, "Integration of microfluidics with a four-channel integrated optical Young interferometer immunosensor," Biosens. Bioelectron. **20,** 1417-1421 (2005).

45. A. Ymeti, J. Greve, P. V. Lambeck, T. Wink, S. W. F. M. van Hövell, T. A. M. Beumer, R. R. Wijn, R. G. Heideman, V. Subramaniam, and J. S. Kanger, "Fast, ultrasensitive virus detection using a Young interferometer sensor," Nano Lett. **7,** 394-397 (2007).

46. P. L. Edmiston, D. P. Campbell, D. S. Gottfried, J. Baughman, and M. M. Timmers, "Detection of vapor phase trinitrotoluene in the parts-per-trillion range using waveguide interferometry," Sens. Actuator B-Chem. **143,** 574-582 (2010).

47. S. M. Reddy, D. M. Hawkins, Q. T. Phan, D. Stevenson, and K. Warriner, "Protein detection using hydrogel-based molecularly imprinted polymers integrated with dual polarisation interferometry," Sens. Actuator B-Chem. **176,** 190-197 (2013).

48. J. T. Kirk, G. E. Fridley, J. W. Chamberlain, E. D. Christensen, M. Hochberg, and D. M. Ratner, "Multiplexed inkjet functionalization of silicon photonic biosensors," Lab Chip **11,** 1372-1377 (2011).

49. N. Komuro, S. Takaki, K. Suzuki, and D. Citterio, "Inkjet printed (bio)chemical sensing devices," Anal. Bioanal. Chem. **405,** 5785-5805 (2013).

50. K. D. McClatchey, S. Alkan, and E. Hackel, "Section 3 Clinical Chemistry," in *Clinical Laboratory Medicine,* 2nd ed*.,* (LWW, 2001).

51. P. M. Ridker, "C-Reactive Protein, Inflammation, and Cardiovascular Disease: Clinical Update," Tex. Heart Inst. J. **32,** 384-386 (2005).

52. M. Montagnana, T. Trenti, R. Aloe, G. Cervellin, and G. Lippi, "Human chorionic gonadotropin in pregnancy diagnostics," Clin. Chim. Acta **412,** 1515-1520 (2011).

53. J. Liu, A. Ren, L. Yang, J. Gao, L. Pei, R. Ye, Q. Qu, and X. Zheng, "Urinary tract abnormalities in Chinese rural children who consumed melamine-contaminated dairy products: a population-based screening and follow-up study," Can. Med. Assoc. J. **182,** 439-443 (2010).

54. CRP, Image from the RCSB PDB (www.rcsb.org) of PDB ID 1B09 created with Protein Viewer (D. Thompson, M.B. Pepys, S.P. Wood (1999) "The physiological structure of human C-reactive protein and its complex with phosphocholine" Structure Fold.Des. **7**: 169-177).

55. hCG, Image from the RCSB PDB (www.rcsb.org) of PDB ID 1HRP created with Protein Viewer (A.J. Lapthorn, D.C. Harris, A. Littlejohn, J.W. Lustbader, R.E. Canfield, K.J. Machin, F.J. Morgan, N.W. Isaacs (1994) "Crystal structure of human chorionic gonadotropin" Nature **369**: 455-461).

56. Melamine, National Center for Biotechnology Information. PubChem Compound Database; CID=7955, https://pubchem.ncbi.nlm.nih.gov/compound/7955 (accessed Nov. 10, 2015).

57. Glucose, National Center for Biotechnology Information. PubChem Compound Database; CID=5793, https://pubchem.ncbi.nlm.nih.gov/compound/5793 (accessed Nov. 10, 2015).

58. A. Ymeti, J. Greve, P. V. Lambeck, R. Wijn, R. G. Heideman, and J. S. Kanger, "Drift correction in a multichannel integrated optical Young interferometer," Appl. Opt. **44,** 3409-3412 (2005).

59. A. Ymeti, V. Subramaniam, T. A. M. Beumer, and J. S. Kanger, "An ultrasensitive Young interferometer handheld sensor for rapid virus detection," Expert Rev. Med. Devices **4,** 447-454 (2007).

60. J. Hiltunen, A. Kokkonen, J. Puustinen, M. Hiltunen, and J. Lappalainen, "UV-imprinted single-mode waveguides with low loss at visible wavelength," IEEE Photon. Technol. Lett. **25,** 996-998 (2013).

61. M. Wang, J. Hiltunen, S. Uusitalo, J. Puustinen, J. Lappalainen, P. Karioja, and R. Myllylä, "Fabrication of optical inverted-rib waveguides using UV-imprinting," Microelectron. Eng. **88,** 175-178 (2011).

62. H. Kipphan, ed., *Handbook of Print Media* (Springer-Verlag, 2001).

63. "Antibody," in Encyclopedia of Microfluidics and Nanofluidics, D. Li, ed. (Springer, 2015), p. 74.

64. D. Sugumar and L. Kong, "Lab-on-chip devices for immunoassays," in *Encyclopedia of Microfluidics and Nanofluidics,* D. Li, ed. (Springer, 2015), pp. 1557-1561.

65. J. G. Korvink, *Advanced Micro and Nanosystems : Inkjet-Based Micromanufacturing* (Wiley-VCH, 2012).

66. D. R. Lide, ed., *CRC Handbook of Chemistry and Physics. 83rd Edition* (CRC, 2002).

67. A. Ymeti, J. S. Kanger, J. Greve, P. V. Lambeck, R. Wijn, and R. G. Heideman, "Realization of a multichannel integrated Young interferometer chemical sensor," Appl. Opt. **42,** 5649-5660 (2003).

68. W. Heller, "Remarks on refractive index mixture rules," J. Phys. Chem. **69,** 1123-1129 (1965).

69. R. Suedee, W. Intakong, P. A. Lieberzeit, P. Wanichapichart, P. Chooto, and F. L. Dickert, "Trichloroacetic acid-imprinted polypyrrole film and its property in piezoelectric quartz crystal microbalance and electrochemical sensors to application for determination of haloacetic acids disinfection by-product in drinking water," J. Appl. Polym. Sci. **106,** 3861-3871 (2007).

70. J. D. Jackson, *Classical electrodynamics* (John Wiley & Sons, 1998).

71. T. Yoshizawa, ed., *Handbook of Optical Metrology : Principles and Applications* (CRC Press, 2009).

72. K. Okamoto, *Fundamentals of optical waveguides* (Academic Press, 2000).

73. P. K. Tien, "Integrated optics and new wave phenomena in optical waveguides," Rev. Mod. Phys. **49,** 361-420 (1977).

74. P. Lüsse, P. Stuwe, J. Schüle, and H. G. Unger, "Analysis of vectorial mode fields in optical waveguides by a new finite difference method," J. Lightw. Technol. **12,** 487-494 (1994).

PAPER I

Compensation of drift by using a multichannel integrated Young interferometer

Applied Optics 54, 4771–4780.

applied optics

Compensation of drift by using a multichannel integrated Young interferometer

SANNA AIKIO,* MARIANNE HILTUNEN, AND JUSSI HILTUNEN

VTT Technical Research Centre of Finland, Kaitoväylä 1, FI-90571 Oulu, Finland
**Corresponding author: sanna.aikio@vtt.fi*

Received 18 December 2014; revised 20 April 2015; accepted 21 April 2015; posted 21 April 2015 (Doc. ID 231085); published 15 May 2015

Polymer-based integrated Young interferometer (YI) sensor chips have proven to be sensitive and have potential to be mass-manufactured. The sensing method is however, disturbed by the mechanical drifts, thus requiring well stabilized and isolated measurement setups that limit its applicability to low-cost readers for rapid diagnostics. In this paper we derive a method for the compensation of mechanical drift by using a multichannel integrated YI chip having two reference channels. The compensation method was demonstrated by quantitative measurements with a three-channel integrated polymeric YI sensor chip using an undisturbed and a mechanically disturbed setup. By applying the compensation method, the intrinsic drift of the undisturbed setup was reduced up to 84%. With the mechanically disturbed setup, the sample-induced phase-change responses were separated up to a 161 times larger disturbed signal.

OCIS codes: (120.3180) Interferometry; (120.2650) Fringe analysis; (130.6010) Sensors.

http://dx.doi.org/10.1364/AO.54.004771

1. INTRODUCTION

Robust measurement techniques are needed for rapid diagnostic applications such as point-of-care and environmental diagnostics. In many applications, sensitive, quantitative, real-time measurements need to be done outside well-controlled laboratories in noisy ambient conditions. In addition, low-cost readers and sensor chips are preferred, as well as simple sample handling and capability for multi-analytic detection.

Integrated Young interferometers (YIs) have many features that make them compatible with the above listed qualities. Glass [1] and SiON [2] sensor chips are discussed in the literature as well as polymer-based sensor-chips that have potential to be mass-manufactured at low cost [3]. Measurement technique is very sensitive, and it is able to detect bulk refractive-index differences down to 10^{-8} refractive-index units (RIU) [2,4]. Sensor chips are functionalized with antibodies, and are able to detect biomolecules [3] and viruses even from a complex sample matrix like serum [5]. Multi-analyte detection is demonstrated with a multi-channel YI [5]. The label-free detection technique enables simpler sample handling compared to the labelled techniques.

Although YIs have many desired features, the readout method is inherently sensitive to mechanical drifts that disturb the signal quantification. Usually the readout systems are well stabilized and isolated from the surroundings to reduce the mechanical disturbances [6]. This approach however, is not readily adaptable with low-cost compact readers. Also, a drift correction method is described in the literature where a multichannel YI with two reference channels is used for the drift correction [7].

In this paper we derive a compensation method for a multichannel YI having two reference channels based on the analysis of the spatial shifts of the fringes of the interferograms. To study the capability of the compensation method, a three-channel polymer-based YI sensor chip was designed and manufactured, and two sets of quantitative measurements were done: one with an undisturbed setup and one with a mechanically disturbed setup. The compensation method was applied to the measured results. It was found to be effective in reducing the intrinsic mechanical drifts of the undisturbed setup, and able to compensate the large induced mechanical drifts of the disturbed setup.

2. SENSOR CHIP LAYOUT AND DETECTION PRINCIPLE

The schematic of the three-channel YI chip discussed in this paper is shown in Fig. 1 as well as the measurement setup. In our YI sensor layout, the waveguide splits twice forming three parallel waveguides called channels. Channels 2 and 3 are reference channels that are covered by over cladding and are not interacting with the samples, e.g., solutions having various refractive indices. Channel 1 is a measurement channel having an opening, a measurement window, patterned into the over cladding layer where the sample interacts with the evanescent wave of the light propagating in the waveguide. A chip layout, where channel 2 crosses over the interferometer chip,

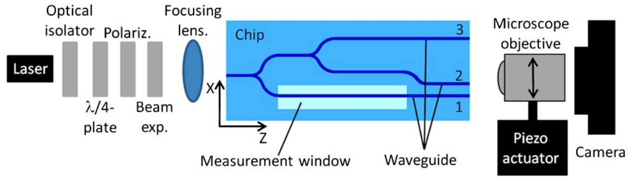

Fig. 1. Schematic of the chip layout and the measurement setup. The microscope objective was mounted onto a piezo actuated translation stage for mechanically disturbed experiments. The channel numbering is shown next to the waveguides.

was chosen to enable easy patterning of the measurement window, and to expose channels 1 and 2 to similar drifts to improve the effectiveness of the compensation. Design principles of a multichannel YI are discussed in [8] and [9].

In the measurements, laser light was end-fire coupled into the waveguide and split into the three waveguides. When the light couples out, the beams diverge, overlap, and interfere forming an interferogram. A three-channel YI interferogram is shown in Fig 2(a). In the case of a multichannel YI, the interferogram is a superposition of the sub-interferograms formed by all the possible channel pairs [9] as illustrated in Fig 2(b). The interferogram was imaged by a microscope objective onto the camera detector, and the image was recorded.

When the refractive index is changed by the sample at the measurement window of the chip, the effective refractive index $N_{\mathrm{eff},1}$ of the measurement channel 1 changes. This again changes the optical path difference between channel 1 and a reference channel, which is seen as a phase change, $\Delta\Phi_{1,\mathrm{ref}}$, of the sub-interferogram formed by these channels. The phase change can be calculated [8]

$$\Delta\Phi_{1,\mathrm{ref}} = \frac{2\pi}{\lambda} l(\Delta N_{\mathrm{eff},1} - \Delta N_{\mathrm{eff,ref}}) = \frac{2\pi}{\lambda} l\Delta N_{\mathrm{eff,1ref}}, \quad (1)$$

where λ is the vacuum wavelength of the light, l is the length of the measurement window, $\Delta N_{\mathrm{eff},1}$ and $\Delta N_{\mathrm{eff,ref}}$ are the changes of the effective refractive indices of channel 1 and the reference channel, respectively, and $\Delta N_{\mathrm{eff,1ref}}$ is the difference in the changes of the effective refractive indices of the measurement and the reference channels. The effective refractive index of the reference channel is only changed if the refractive index of the waveguide material changes, e.g., due to temperature.

3. CALCULATION OF DRIFT COMPENSATED PHASE CHANGES

Discrete Fourier transform (DFT) can be used to analyze captured interferograms yielding the phase Φ and spatial frequency k of the fringes. The analysis method is discussed in detail in [8].

Let k_{ij} be the spatial frequency of a sub-interferogram formed by channels i and j. Spatial frequency is dependent on the separation d_{ij} of the channels, and thus if all channel pairs have a unique separation, their corresponding spatial frequencies can be identified as peaks in the amplitude spectrum of the interferogram. This again enables the monitoring of their phases simultaneously during the measurements. An example of an amplitude spectrum of a three-channel YI is shown in stage 1 in Fig. 3.

If $\Phi_{ij}(t)$ is the phase of the fringes of a sub-interferogram formed by channels i and j at the time t, then the phase change, $\Delta\Phi_{ij}(t)$, for the channel pair is

$$\Delta\Phi_{ij}(t) = \Phi_{ij}(t) - \Phi_{ij}(t_0), \quad (2)$$

where t_0 is the chosen reference time point. In this paper $t_0 = 0$ s. This is stage 2 in Fig 3.

The measured phase change is a sum of the changes caused by (1) the interaction of the sample, when applicable; (2) the internal drift of the chip; and (3) the mechanical drift of the setup, e.g., shift of the camera. The first two are related to the changes at the chip, and if their effect is the same to the channel pairs, they induce the same phase change to the corresponding sub-interferograms. The influence of the mechanical drift to the sub-interferograms is different anyway. If channel pairs are influenced by the same lateral shift caused by the drift

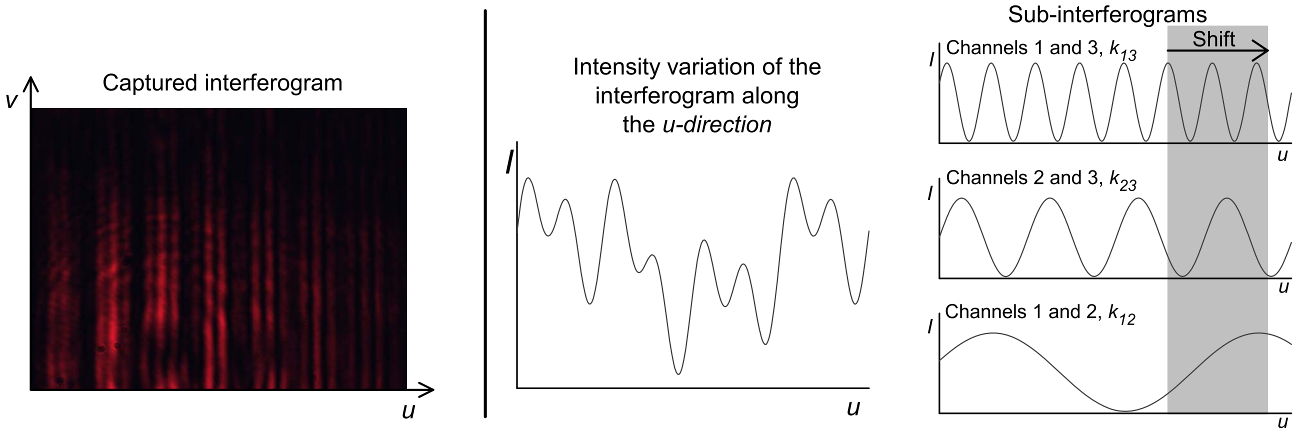

(a) (b)

Fig. 2. (a) Three-channel YI interferogram captured by a camera. (b) Left, schematic illustration of intensity (I) variation of a three-channel YI interferogram formed as a superposition of the sub-interferograms shown on the right. The grey rectangle illustrates that the same lateral shift spans over a different number of waves at each of the sub-interferograms and thus induces different phase changes.

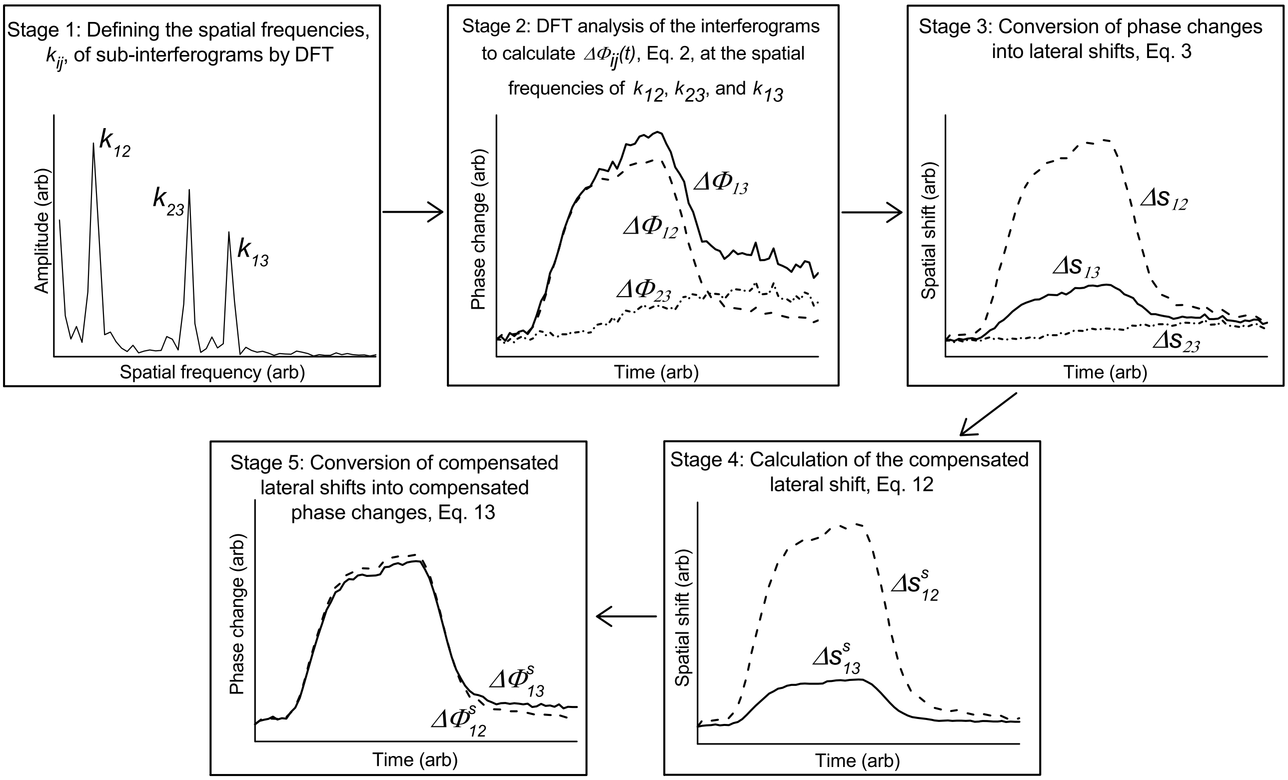

Fig. 3. Stages of the calculation of the compensated signals. The example curves are calculated by using the data of the 0.05 wt. % undisturbed experiment discussed in Section 7.B.

of the setup, value in the phase-change domain varies between channel pairs due to the different spatial frequencies. The value in the lateral shift domain, however, would naturally be the same as illustrated in Fig. 2. Thus, in order to compare the mechanical drift induced effects between different channel pairs, the phase changes have to be converted into lateral shifts Δs_{ij}:

$$\Delta s_{ij}(t) = \frac{\Delta\Phi_{ij}(t)}{2\pi}\Lambda_{ij} = \frac{\Delta\Phi_{ij}(t)}{2\pi k_{ij}}, \tag{3}$$

where Λ_{ij} is the spatial wavelength of the sub-interferogram formed by channels i and j. This is stage 3 in Fig. 3.

Now the lateral shift of channel pair i and j can be expressed as a sum

$$\Delta s_{ij}(t) = \Delta s^s_{ij}(t) + \Delta s^d_{ij}(t) + \Delta s^I_{ij}(t), \tag{4}$$

where Δs^s_{ij} is the lateral shift caused by the interaction of the sample, Δs^d_{ij} the lateral shift caused by the drift of the setup, and Δs^I_{ij} the lateral shift caused by the internal drifts of the chip such as a temperature drift between the waveguides. Since all channels are integrated into a single chip and share the mechanical and optical components of the setup, an assumption can be made that Δs^d_{ij} is the same for all channel pairs, and we can rewrite

$$\Delta s_{ij}(t) = \Delta s^s_{ij}(t) + \Delta s^d(t) + \Delta s^I_{ij}(t), \tag{5}$$

where Δs^d is the lateral shift caused by the drift of the setup.

Let Δs_{13} and Δs_{23} be the lateral shifts of the sub-interferograms formed by channels 1 and 3, and 2 and 3, respectively. Now Eq. (5) can be written for these channel pairs

$$\Delta s_{13}(t) = \Delta s^s_{13}(t) + \Delta s^d(t) + \Delta s^I_{13}(t), \tag{6}$$

$$\Delta s_{23}(t) = \Delta s^s_{23}(t) + \Delta s^d(t) + \Delta s^I_{23}(t). \tag{7}$$

Since channels 2 and 3 are reference channels, they are not interacting with the sample, and thus

$$\Delta s^s_{23}(t) = 0. \tag{8}$$

By substituting Eq. (8) into Eq. (7) we can solve Δs^d,

$$\Delta s^d(t) = \Delta s_{23}(t) - \Delta s^I_{23}(t). \tag{9}$$

Now Δs^s_{13} can be solved from Eq. (6),

$$\Delta s^s_{13}(t) = \Delta s_{13}(t) - \Delta s^d(t) - \Delta s^I_{13}(t), \tag{10}$$

and substituting Δs^d from Eq. (9) into Eq. (10) we get

$$\Delta s^s_{13}(t) = \Delta s_{13}(t) - \Delta s_{23}(t) + \Delta s^I_{23}(t) - \Delta s^I_{13}(t), \tag{11}$$

which is the drift-compensated sample-induced lateral shift of channel pairs 1 and 3.

The internal drifts of the chip in Eq. (11) are unknown in our experiments, and thus the exact value cannot be calculated. Therefore, it can be assumed that $\Delta s^I_{23}(t)$ and $\Delta s^I_{13}(t)$ are small, since the waveguides are located near each other at a single sensor chip and are exposed to similar temperature fluctuations. Thus, we can approximate Eq. (11),

$$\Delta s^s_{13}(t) \approx \Delta s_{13}(t) - \Delta s_{23}(t), \tag{12}$$

which is the form used to calculate the compensated lateral shifts in this paper. This is stage 4 in Fig. 3.

The compensated lateral shift of Eq. (12) can be converted into the compensated phase change $\Delta\Phi^s_{13}(t)$ at the spatial frequency of k_{13} by using the relation shown in Eq. (3):

$$\Delta\Phi^s_{13}(t) = 2\pi\frac{\Delta s^s_{13}(t)}{\Lambda_{13}} = 2\pi k_{13}\Delta s^s_{13}(t), \tag{13}$$

which is the sample induced drift compensated phase change of channel pair 1 and 3. These phase-change values can be compared with the measured values. This is stage 5 shown in Fig. 3 and completes the calculation of the compensated phase-change signal.

A compact expression for the $\Delta\Phi^s_{13}(t)$ can be derived by substituting Eq. (12) into Eq. (13) to obtain

$$\Delta\Phi^s_{13}(t) = 2\pi k_{13}(\Delta s_{13}(t) - \Delta s_{23}(t)). \tag{14}$$

Then, using the relation of Eq. (3), we can write

$$\begin{aligned}\Delta\Phi^s_{13}(t) &= 2\pi k_{13}\left(\frac{\Delta\Phi_{13}(t)}{2\pi k_{13}} - \frac{\Delta\Phi_{23}(t)}{2\pi k_{23}}\right)\\ &= \Delta\Phi_{13}(t) - \frac{k_{13}}{k_{23}}\Delta\Phi_{23}(t)\\ &= \Delta\Phi_{13}(t) - \frac{d_{13}}{d_{23}}\Delta\Phi_{23}(t). \end{aligned} \tag{15}$$

The two latter forms of the Eq. (15) are similar to the relation derived in [7] for the calculation of drift compensated signal. The last form of Eq. (15) was derived by using a relation $k_{ij} = d_{ij}/(\lambda L)$ where L is the distance between the end of the chip and the camera, and $L \gg d_{ij}$ [8].

The last form of Eq. (15) shows that the calculation of the compensated signal can be directly related to the layout of the chip, and there is no need to define the multiplier of $\Delta\Phi_{23}$ from the phase-change measurements. In the experiments the multiplier calculated based on the spatial frequencies may differ from the multiplier obtained for channel distances, if the interferogram analysis method is unable to identify exactly the spatial frequencies of the sub-interferograms, for example when the spatial frequency of a sub-interferogram is located between the discrete spatial frequencies of fast Fourier transform analysis. In this paper the compensated signal was calculated based on the spatial frequencies.

The sample-induced phase change can also be analyzed from the sub-interferogram formed by channels 1 and 2. The compensated phase change $\Delta\Phi^s_{12}(t)$ can be calculated similarly for channel pair 1 and 3. Although a three-channel YI is used in this paper, the compensation method can be applied to YIs having more channels by analyzing every measurement channel individually.

4. INTEGRATED INTERFEROMETER CHIP

The dimensions of the sensor chip are shown in Fig. 4(a). The sensor layout was realized as an inverted ridge polymeric single-mode waveguide working at the wavelength of 633 nm. Figure 4(b) shows a schematic of the waveguide structure with dimensions and refractive indices of the materials. A scanning electron microscope image of a waveguide cross section is shown in Fig. 4(c).

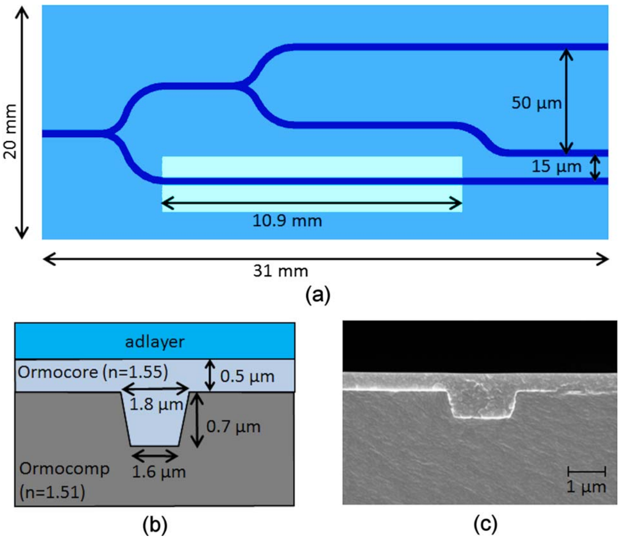

Fig. 4. (a) Schematic of the chip layout with dimensions. (b) Schematic of the waveguide cross section with dimensions, polymer materials, and their refractive indices. (c) Scanning electron microscope image of the waveguide cross section.

Waveguides were fabricated by using a UV-imprinting method, which is described in detail in [10]. In short, a mould, having a ridge structure was pressed into the soft UV-curable under-cladding material (Ormocomp), that was cured by UV light to form grooves. The grooves were filled with the waveguide core material (Ormocore) by spin coating, and the layer was cured by UV light. The over-cladding layer (Ormoclad) was spin coated, and the measurement window was patterned on top of the measurement channel by UV lithography.

Theoretical response of the sensor chip was simulated by using the film-mode matching method [11]. The effective refractive indices, $N_{\mathrm{eff},1}$, of the waveguide modes of channel 1 were calculated with various ad layers having corresponding refractive indices as the sample glucose solutions and water. The $N_{\mathrm{eff},1}$ values were used to calculate the effective refractive index differences, $\Delta N_{\mathrm{eff},1}$, of the sample solutions to water. These were again applied to Eq. (1) to calculate the theoretical phase-change response rate of the chip 68 rad/RIU/mm.

5. MEASUREMENT SETUP

Schematic of the measurement setup is shown in Fig. 1. The light source was a frequency stabilized HeNe laser emitting at 632.991 nm (@ vacuum) (HRS015, Thorlabs Inc.) followed by an optical isolator to prevent the back reflections into the laser, a quarter-wave plate for polarization circularization, a polarizer to select the polarization stage of the incoupled light, a 5× beam expander to improve the performance of the coupling lens (C230TM-B, Thorlabs Inc.) used to end-fire couple light into the YI chip. The beam expander was used to increase the diameter of the laser beam so that it filled a larger part of the aperture of the coupling lens. This leads to a smaller focused spot size, which again improves the light coupling efficiency into the waveguide, and reduces the stray light. TM polarization was used in the measurements due to its higher sensitivity [3].

After, the chip, a 40× microscope objective (Micro Plan, Edmund Optics Inc.), was used to image the interferograms onto a camera (PL-E425CU, PixeLink) having 2592 by 1944 pixels. The camera was connected to a computer to record the images. For the mechanically disturbed experiments, the microscope objective was mounted onto a piezo actuated XYZ-translation stage (Picomotor Multi-Axis, New Focus Inc.) enabling objective movement during the experiments.

In the undisturbed and mechanically disturbed experiments, the interferograms were formed by first imaging the ends of the waveguides onto the camera, and then moving the microscope objective ~0.5 mm further from the chip. The interval between the recorded interferograms was 10 s.

6. SAMPLES AND SAMPLE HANDLING

Glucose-water solutions were used to change the bulk refractive index at the measurement window of the YI chip. The refractive-index differences Δn of the glucose solutions to pure water were calculated by fitting a polynomial to the empirical values tabulated in [12] defined at the wavelength of 589 nm and at 20°C:

$$\Delta n = 6 \times 10^{-6} C^2 + 0.0014C, \tag{16}$$

where C is the glucose concentration in weight percent (wt. %).

The following D-Glucose (Sigma-Aldrich) solutions in ultrapure water (MilliQ Academic, Merk Millipore) by weight percent were prepared: 0.05, 0.1, 0.2, 0.5 and 0.7 wt. % having the following RIU differences to water 7.0×10^{-5}, 1.4×10^{-4}, 2.8×10^{-4}, 7.0×10^{-4}, and 9.8×10^{-4}, respectively. Samples were kept at room temperature before measurement in order to stabilize them into the same temperature as the measurement setup.

A flow cell was attached on top of the waveguide chip to enable sample handling, and it was sealed by using a silicone seal. The flow cell was filled with water on the day before the first experiments to reduce the effect of water absorption to the polymer waveguides [13]. A tube from a sample vial was attached to the inlet of the flow cell, and a tube to syringe pump was attached to the outlet. A syringe pump (Nexus 3000, Chemyx Inc.) in withdrawal mode was used to pump the samples through the flow cell at the flow rate of 100 μl/min.

The following sample sequence was used in all the measurements. A glucose solution of 500 μl was pipetted into the sample vial at the beginning of the measurement. There was approximately a two minute delay until it reached the flow cell. Water was pipetted into the sample vial after the glucose solution at approximately five minutes, and it reached the flow cell at approximately seven minutes. Water was pumped through the flow cell until the end of the measurement.

7. EXPERIMENTS AND ANALYSIS

Two sets of experiments were conducted to study the capability of the compensation method. A set of quantitative measurements was done with an undisturbed setup to test the capability of the compensation method to compensate the intrinsic drifts of the setup. Another set was done with a mechanically disturbed setup to test the capability of the method to compensate large mechanical drifts.

During the experiments the interferograms were recorded while the bulk refractive index in the measurement window was varied by the glucose solutions. With the undisturbed setup, the measurement was repeated three times for the concentrations of 0.05 and 0.1 wt. %, and two times for the concentrations of 0.2 and 0.5 wt. %. The concentration of 0.7 wt. % was measured once. With the mechanically disturbed setup, the same concentrations were measured once.

A. Image Analysis and Cross Talk

The DFT analysis of the captured interferograms was done by using a two-dimensional (2D) fast-Fourier transform (FFT) algorithm of commercial software (MATLAB). The use of a 2D image for the analysis instead of a one-dimensional cross section provides more data points to the analysis and averages out the effects of local imperfections of the interferograms caused, for example, by dust particles on the camera detector.

When analyzing multichannel YIs, it is known that cross talk may occur between the sub-interferograms [9]. Cross talk disturbs the analysis of the phase changes by leaking the phase change of one sub-interferogram into the other sub-interferograms. The effect of the cross talk is reduced when the spatial frequencies of the sub-interferograms are coincident with the spatial frequencies of the FFT analysis [9]. The spatial frequencies of the FFT analysis are again determined by the image width, i.e., the number of pixels chosen along the u direction [Fig. 2(a)] of the camera detector. Also window functions can be used to reduce the cross talk. Efficacy of various windows, including Hamming, Hanning, and Blackman, to reduce the cross talk of a multichannel YI is studied in [9] where the Hamming window was found to be the most effective.

To determine the method for the phase-change analysis, the cross-talk induced signal to channel pair 2 and 3 was studied by analyzing the interferograms of the 0.7 wt. % undisturbed experiment with different image widths and with and without the Hamming window. This concentration was chosen because it most likely has the largest cross talk in our experiments. The $\Delta\Phi_{23}$ curves were calculated while the image width was varied from 992 to 2592 pixels in 10 pixel intervals. The $\Delta\Phi_{23}$ curves were baseline corrected based on the phase-change values between 0 and 1.3 min and are shown in Figs. 5(a) and 5(b) without and with the Hamming window, respectively. In theory, the $\Delta\Phi_{23}$ curves should be flat since channels 2 and 3 are reference channels. The analyzed curves, however, show phase-change responses that are dependent on the chosen image width, indicating the presence of cross talk.

The responses of the baseline corrected $\Delta\Phi_{23}$ curves were calculated by subtracting the mean phase-change value between 1.5 and 1.7 min from the mean phase-change value between 4.2 and 4.5 min. Responses are shown in Figs. 5(c) and 5(e) without and with the Hamming window, respectively. It can be seen that the use of the Hamming window reduces the variation of the cross-talk induced responses. The smallest absolute response value, 0.8×10^{-4} rad, was obtained with the image

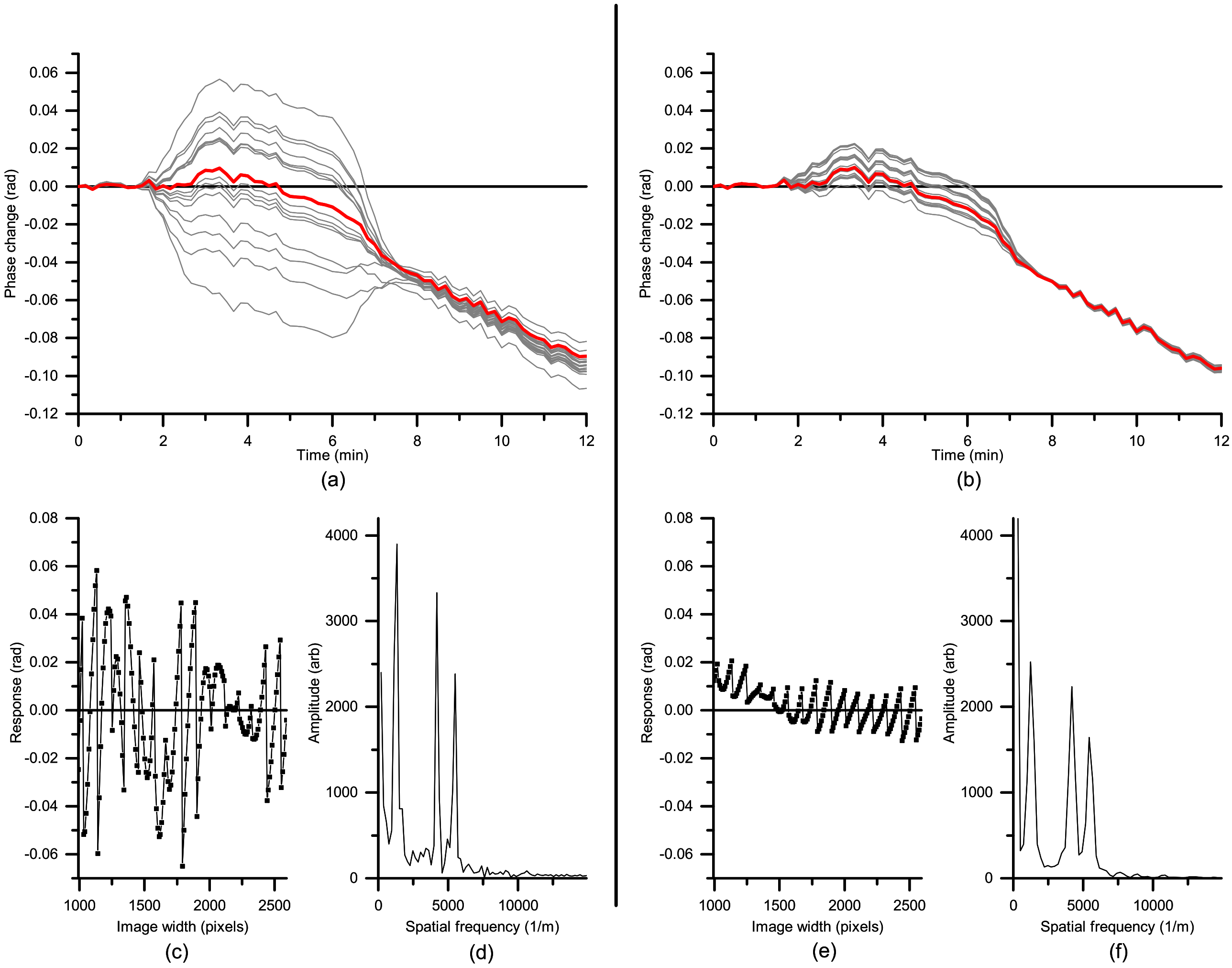

Fig. 5. Baseline corrected $\Delta\Phi_{23}$ curves calculated with the image widths of 992–2592 pixels in 100 pixel intervals; (a) without the Hamming window and (b) with the Hamming window. Curves with the smallest cross-talk responses are drawn with the bold red line: (a) at the image width of 2392 pixels and (b) at the image width of 1842 pixels. Calculated responses of $\Delta\Phi_{23}$ curves with different image widths; (c) without the Hamming window and (e) with the Hamming window. Part of the amplitude spectrum of the interferogram calculated; (d) with the image width of 2392 pixels without the Hamming window and (f) with the image width of 1842 pixels with the Hamming window.

width of 2392 pixels without the Hamming window. With the Hamming window, the smallest response value, 1.0×10^{-4} rad, was obtained with the image width of 1842 pixels.

The amplitude spectrums of the image widths with the smallest cross-talk responses are shown in Figs. 5(d) and 5(f) without and with the Hamming window, respectively. Amplitude spectrums show well defined peaks indicating that the spatial frequencies of the sub-interferograms are coincident with the spatial frequencies of the FFT analysis. This is further proof of suitable image widths for the analysis.

Based on the cross-talk response values and the amplitude spectrum analysis, the use of the image width of 2392 pixels without the Hamming window was chosen to be used for the phase-change analysis of the undisturbed experiments. A detailed analysis of the reasons explaining why the smallest cross -talk response was occurring without the Hamming window in this particular experiment has not been conducted.

B. Undisturbed Experiments

1. Phase-Change Curves

The phase-change curves $\Delta\Phi_{ij}$ were calculated from the recorded interferograms with the image width of 2392 pixels and are shown in Fig. 6. The compensated phase-change curves $\Delta\Phi^{s}_{13}$ and $\Delta\Phi^{s}_{12}$ were calculated by using the method described in Section 3 and are included in Fig. 6. For clarity, the phase-change curves of only one experiment per concentration are shown. The overall shapes of the $\Delta\Phi_{13}$ and $\Delta\Phi_{12}$ curves, and the timing of the phase changes are as expected for the used sample sequence, indicating that the sample handling, interferogram recording, and the phase-change analysis work properly.

By looking at the uncompensated $\Delta\Phi_{13}$ and $\Delta\Phi_{12}$ curves and the compensated $\Delta\Phi^{s}_{13}$ and $\Delta\Phi^{s}_{12}$ curves of a single concentration in Fig. 6, it can be seen that the compensated curves are nearly overlapping, whereas the uncompensated curves are separated by a much greater amount. The overlapping of the

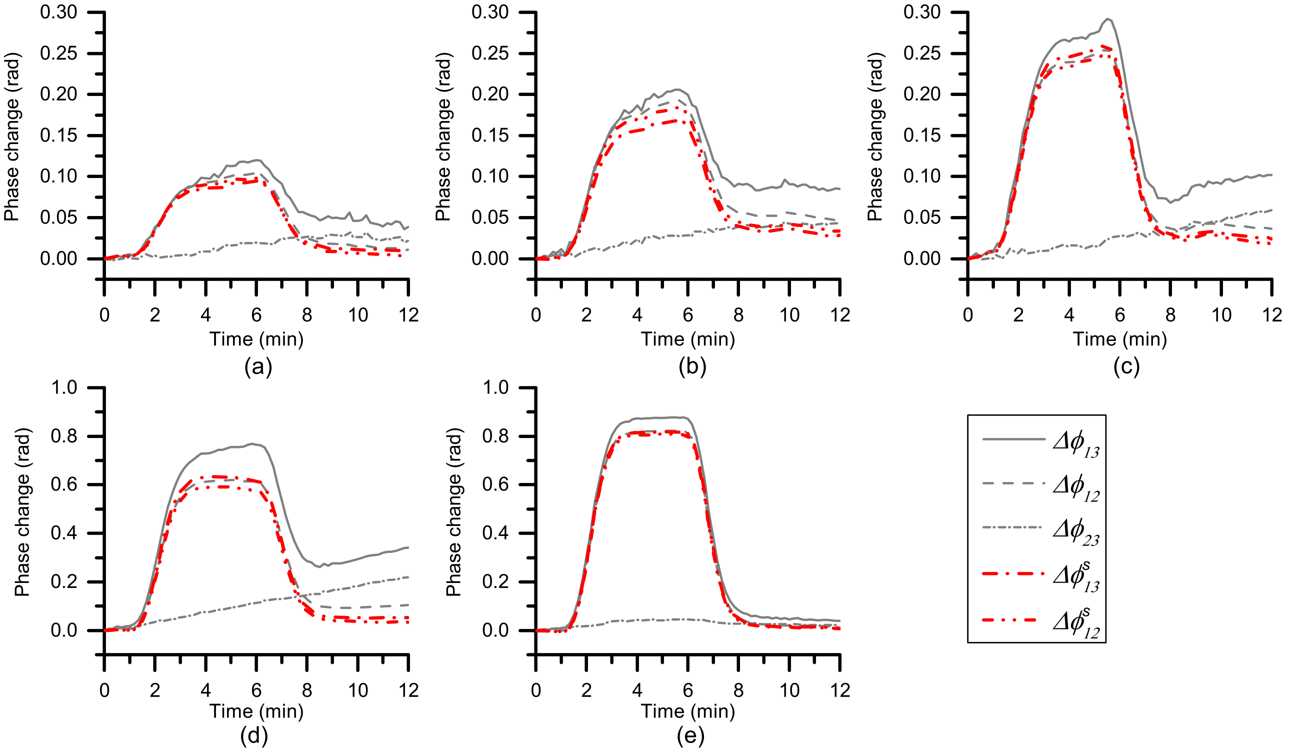

Fig. 6. Measured and compensated phase-change curves of undisturbed experiments at various glucose concentrations; (a) 0.05 wt. %, (b) 0.1 wt. %, (c) 0.2 wt. %, (d) 0.5 wt. %, and (e) 0.7 wt. %.

compensated phase-change curves indicates that the compensation method has almost eliminated the spatial frequency dependent phase changes from the curves, i.e., the changes related to the mechanical drift and the compensated curves are dominated by the changes at the chip. The differences of the compensated curves between the approximately three to seven minutes were assumed to be caused by the remaining cross talk between the sub-interferograms.

2. Responses

Sensor responses were calculated from the uncompensated and compensated phase-change curves. The height of the sample-induced phase-change step was determined by taking the average of the phase-change values between 3.5 and 6.0 min. The calculated responses are shown in Fig. 7 with lines fitted to the data points. The quadratic term of the refractive-index relation of Eq. (16) was ignored in the fitting due to its negligible

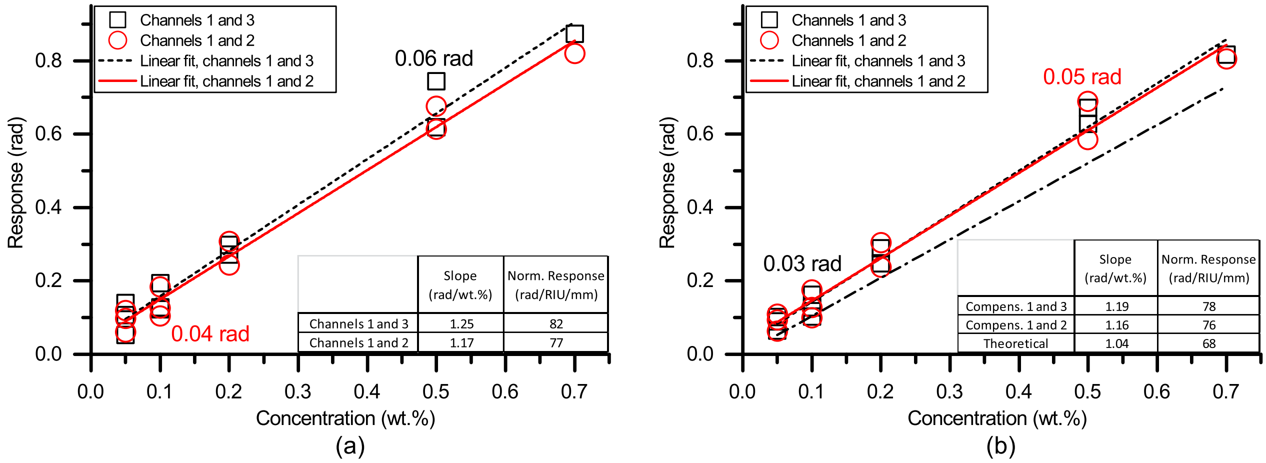

	Slope (rad/wt.%)	Norm. Response (rad/RIU/mm)
Channels 1 and 3	1.25	82
Channels 1 and 2	1.17	77

	Slope (rad/wt.%)	Norm. Response (rad/RIU/mm)
Compens. 1 and 3	1.19	78
Compens. 1 and 2	1.16	76
Theoretical	1.04	68

Fig. 7. Responses and lines fitted to the data points of the undisturbed experiments; (a) from the measured phase-change curves and (b) from the compensated phase-change curves. Also the theoretical response of the sensor chip is included. The slope values and the normalized responses are shown in the inset tables. The maximum range of the response values for channel pair 1 and 3 (black) and for channel pair 1 and 2 (red) is indicated next to the related data points.

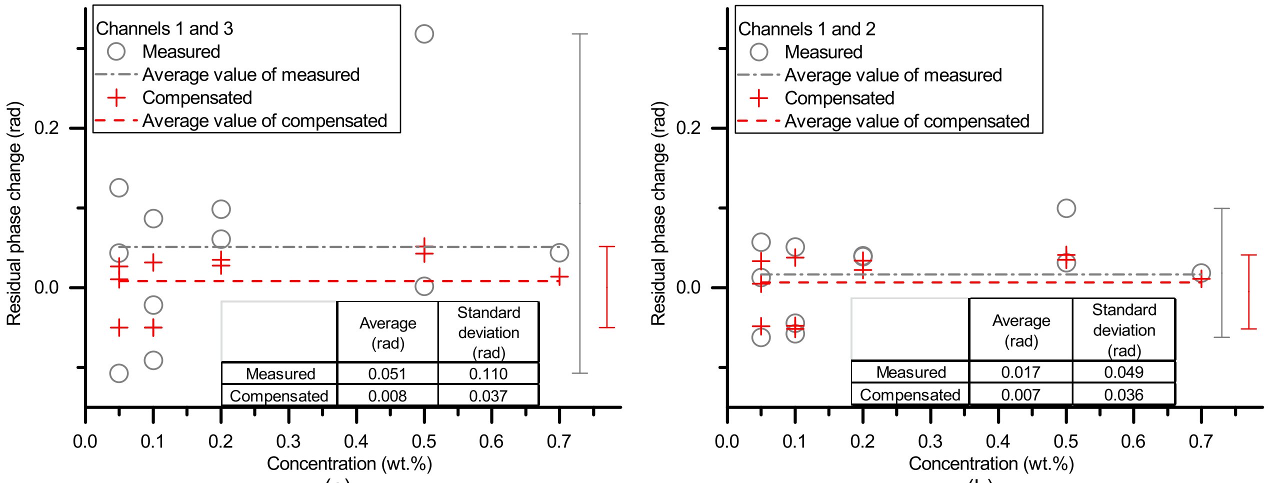

(a) (b)

Fig. 8. Residual phase changes of the measured and compensated phase-change curves, their average values and standard deviations of the undisturbed experiments of (a) channel pair 1 and 3 and (b) channel pair 1 and 2. The error bars show the range of the measured (left bar) and the compensated (right bar) residual phase-change values.

impact at the used glucose concentrations. The normalized responses were calculated, and are shown with the slope values in the inset tables of Fig. 7.

From Fig. 7 it can be seen that the fitted response lines of $\Delta\Phi_{12}$ and $\Delta\Phi_{13}$ differ more than the corresponding lines of $\Delta\Phi^s_{13}$ and $\Delta\Phi^s_{12}$, which are practically overlapping. The similarity of the compensated response values indicates that the quantification of the compensated signals is more consistent between the channel pairs than without the compensation. In addition, the slopes of the fitted lines are in reasonably good agreement with the theoretical response value being 11% and 14% larger.

3. Residual Phase Changes

The effectiveness of the compensation was also gauged by calculating the average value of the residual phase change between 10 and 12 min. In theory, the phase-change values should have returned to zero at the end of the measurements because the refractive index was restored to the initial value, and the deviation from zero is caused by the drift of the system and the changes at the chip.

Figure 8 shows the residual phase-change values, their average values, and standard deviations for $\Delta\Phi_{13}$, $\Delta\Phi_{12}$, $\Delta\Phi^s_{13}$, and $\Delta\Phi^s_{12}$. The mean values of the residual phase changes of $\Delta\Phi^s_{13}$ and $\Delta\Phi^s_{12}$ are practically the same although the mean values of the uncompensated cases differ. This indicates that the intrinsic drift is effectively reduced from the compensated phase-change curves. It can be also seen that the compensation works more effectively for channel pair 1 and 3 by reducing the average residual phase-change value by 84% compared to the uncompensated value. The corresponding reduction for channel pair 1 and 2 is 61%. The calculated reduction for channel pair 1 and 3 is similar to the value, ~10 times, reported in [7].

The standard deviations of the compensated residual phase-change values were reduced, being 66% and 27% smaller than the corresponding uncompensated values for channel pair 1 and 3 and channel pair 1 and 2, respectively.

C. Mechanically Disturbed Experiments

During the disturbed experiments the setup was deliberately mechanically disturbed by moving the microscope objective back and forth in the *x*-direction shown in Fig. 1 while the glucose solutions were used to change the bulk refractive index at the measurement window. The *x*-direction of the movement was chosen because it causes maximal disturbance by shifting the fringes along the *u*-axis (Fig. 2) on the camera detector. The microscope objective was moved by manually controlling the piezo actuated translation stage, and the direction of the movement was reversed at the mid-point, approximately six minutes, of each experiment. The amplitude of the microscope objective movement varied between the experiments from ~7 µm to ~19 µm of 0.05 wt. % and 0.1 wt. % experiments, respectively.

Based on the amplitude-spectrum analysis of the recorded interferograms, the full image width of 2592 pixels was used in the analysis. This was done because it provided a better match of the spatial frequencies of the sub-interferograms and the FFT analysis than the image width of 2359 pixels used in the analysis of undisturbed experiments. The analysis of the mechanically disturbed experiments was done without the Hamming window.

1. Phase-Change Curves

Measured phase-change curves $\Delta\Phi_{13}$, $\Delta\Phi_{12}$, and $\Delta\Phi_{23}$ of the disturbed experiments are shown in Fig. 9. The compensated phase-change curves $\Delta\Phi^s_{13}$ and $\Delta\Phi^s_{12}$ are included in the upper part of the same figure. The shapes of the compensated phase-change curves are similar to the measured curves of the undisturbed experiments. This proves that the compensation method is able to separate the sample-induced bulk refractive-index changes from the much larger measured disturbed-phase changes.

2. Responses

The compensated phase-change curves of Fig. 9 show a quantitative trend. The sensor responses were calculated from

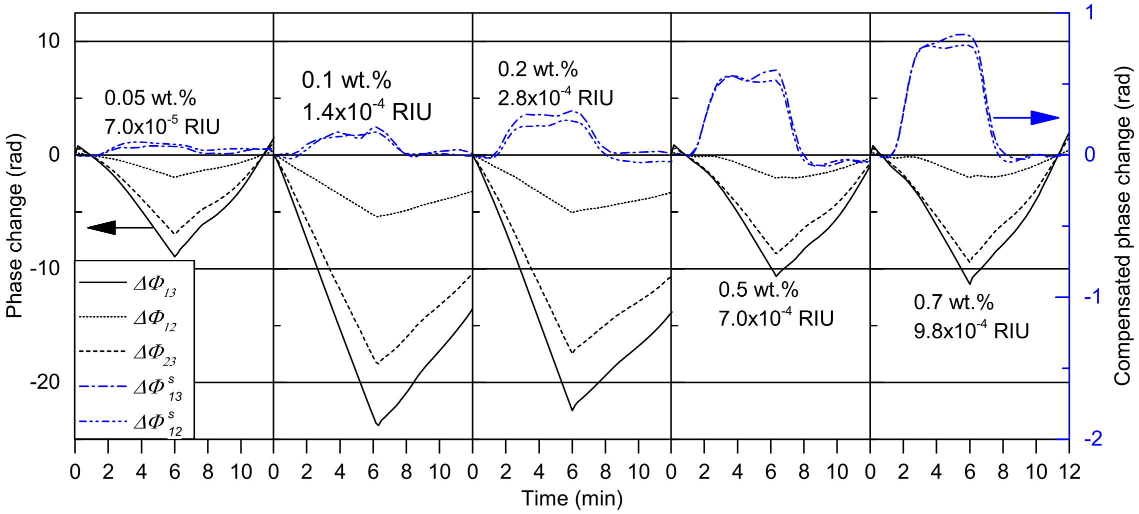

Fig. 9. Measured and compensated phase-change curves of the disturbed experiments at the glucose concentrations of 0.05, 0.1, 0.2, 0.5, and 0.7 wt. % from left to right. The measured phase-change curves are drawn with black lines and refer to the *y*-axis on the left. The compensated curves are drawn with the blue lines and refer to the *y*-axis on the right.

---

the compensated curves similar to those described in Section 7.B for the undisturbed experiments, which enable comparison of the values.

Responses and the lines fitted to the data points are shown in Fig. 10. It can be seen that the responses have a linear trend with the glucose concentration. The slope of the fitted line of $\Delta\Phi^{s}_{13}$ is 6% smaller and of $\Delta\Phi^{s}_{12}$ 11% smaller than the values of the corresponding undisturbed compensated cases. Also the slope values and the normalized responses are shown in the inset table of Fig. 10.

The similarity of the response values between the compensated undisturbed and disturbed cases indicates that the compensation method is capable to quantitatively separate the bulk refractive-index changes from the measured phase-change values under large mechanical drift. The largest ratio of the maximum value of $|\Delta\Phi_{13}|$ to the response of $\Delta\Phi^{s}_{13}$ was 161, which was measured for the glucose concentration of 0.1 wt. %.

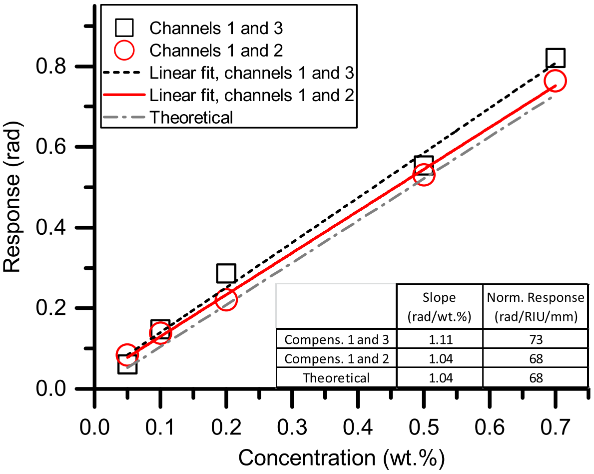

	Slope (rad/wt.%)	Norm. Response (rad/RIU/mm)
Compens. 1 and 3	1.11	73
Compens. 1 and 2	1.04	68
Theoretical	1.04	68

Fig. 10. Responses and lines fitted to the data points of the compensated phase-change curves of the disturbed experiment Also the theoretical response of the sensor chip is included. The slope values and the normalized responses are shown in the inset table.

3. *Residual Phase Changes*

The residual phase-change values of $\Delta\Phi^{s}_{13}$ and $\Delta\Phi^{s}_{12}$ were calculated similarly for the undisturbed experiments. The average value for $\Delta\Phi^{s}_{13}$ was 0.008 rad, and for $\Delta\Phi^{s}_{12}$ – 0.009 rad. Values are similar to those calculated for the compensated undisturbed curves shown in Fig. 8. The negative residual phase-change value of disturbed $\Delta\Phi^{s}_{12}$ indicates that the compensation method over compensates the drift, but its absolute value is similar to the undisturbed compensated case. The similarity of the values between compensated disturbed and compensated undisturbed cases provides further proof of the efficacy of the compensation method to compensate large mechanical drifts.

8. DISCUSSION

Based on the analysis of the phase-change curves, responses and residual phase changes, the compensation method was found to be effective in reducing the drifts of the undisturbed and mechanically disturbed experiments.

With the undisturbed experiments, we have demonstrated that the compensation method converts the compensated phase-change curves mutually more similar than the measured ones, and that the residual phase-change values were reduced. In addition, the compensation method improved the similarity of the responses between the channel pairs. It was also seen that the compensation method was more effective in reducing the drift of channel pair 1 and 3 than of channel pair 1 and 2. The different outcome of the compensation between the channel pairs is attributed to the cross-over chip layout, which was designed on purpose to maximize the similarity of the drift induced signal of the measurement channel pair 1 and 3 and the compensation channel pair 2 and 3. Based on these results, the cross-over chip layout seems beneficial from the compensation point of view.

The mechanically disturbed experiments demonstrated that the compensation method was able to separate the sample-induced phase changes up to 161 times larger measured phase changes, proving the ability of the method to compensate for large mechanical drifts. Responses had a linear trend with the sample-induced bulk refractive-index changes, and the values were similar to calculated undisturbed experiments, indicating that the compensation method is suitable for quantitative measurements even under mechanical disturbances. The responses and the residual phase changes of channel pair 1 and 3 were more similar to the results of the undisturbed experiments than the results of channel pair 1 and 2; further proving the benefit of the cross-over chip layout.

9. CONCLUSIONS

In this paper we derived a compensation method for a multichannel YI having two reference channels. The method is based on the analysis of the spatial shifts of the interferogram fringes.

The capability of the compensation method was demonstrated by an analysis of quantitative measurements done with a three-channel polymeric YI chip manufactured with a UV-imprinting method. The measurements were done with an undisturbed and mechanically disturbed setup. Based on the analysis of the experiments, the compensation method was found to be effective in compensating the intrinsic drifts of the undisturbed measurements and the large induced mechanical drifts of the disturbed experiments.

The derived compensation method can be readily utilized with YI readers since it is based on the properties of a multichannel YI chip and signal analysis, and no specific optical readout arrangements or components are needed. The discussed compensation method improves the robustness of the integrated multi-channel YI sensors to mechanical drifts, making them more compatible with the measurements in noisy environments. Improved robustness again makes YI sensor chips a more feasible platform for low-cost readers for rapid testing and point-of-care diagnostics.

European Commission Seventh Framework Programme (263382); Jenny ja Antti Wihurin Rahasto.

The authors want to thank Professor Emeritus Risto Myllylä, University of Oulu, for his valuable guidance during this work, and the Infotech Oulu Doctoral Program. The authors want to acknowledge the support of Jenny ja Antti Wihurin Rahasto, and the PHOTOSENS project.

REFERENCES

1. A. Brandenburg and R. Henninger, “Integrated optical Young interferometer,” Appl. Opt. **33**, 5941–5947 (1994).
2. A. Ymeti, J. S. Kanger, R. Wijn, P. V. Lambeck, and J. Greve, “Development of a multichannel integrated interferometer immunosensor,” Sensors Actuators B **83**, 1–7 (2002).
3. M. Wang, J. Hiltunen, C. Liedert, L. Hakalahti, and R. Myllylä, “An integrated Young interferometer based on UV-imprinted polymer waveguides for label-free biosensing applications,” J. Eur. Opt. Soc. **7**, 12019 (2012).
4. K. Schmitt, B. Schirmer, C. Hoffmann, A. Brandenburg, and P. Meyrueis, “Interferometric biosensor based on planar optical waveguide sensor chips for label-free detection of surface bound bioreactions,” Biosens. Bioelectron. **22**, 2591–2597 (2007).
5. A. Ymeti, J. Greve, P. V. Lambeck, T. Wink, S. W. F. M. van Hövell, T. A. M. Beumer, R. R. Wijn, R. G. Heideman, V. Subramaniam, and J. S. Kanger, “Fast, ultrasensitive virus detection using a young interferometer sensor,” Nano Lett. **7**, 394–397 (2007).
6. P. Kozma, F. Kehl, E. Ehrentreich-Förster, C. Stamm, and F. F. Bier, “Integrated planar optical waveguide interferometer biosensors: a comparative review,” Biosens. Bioelectron. **58**, 287–307 (2014).
7. A. Ymeti, J. Greve, P. V. Lambeck, R. Wijn, R. G. Heideman, and J. S. Kanger, “Drift correction in a multichannel integrated optical Young interferometer,” Appl. Opt. **44**, 3409–3412 (2005).
8. J. S. Kanger, V. Subramaniam, P. H. J. Nederkoorn, and A. Ymeti, “A fast and sensitive integrated young interferometer biosensor,” in *Advanced Photonic Structures for Biological and Chemical Detection*, X. Fan, ed. (Springer, 2009), pp. 270–273.
9. A. Ymeti, J. S. Kanger, J. Greve, P. V. Lambeck, R. Wijn, and R. G. Heideman, “Realization of a multichannel integrated Young interferometer chemical sensor,” Appl. Opt. **42**, 5649–5660 (2003).
10. J. Hiltunen, A. Kokkonen, J. Puustinen, M. Hiltunen, and J. Lappalainen, “UV-imprinted single-mode waveguides with low loss at visible wavelength,” Photon. Technol. Lett. **25**, 996–998 (2013).
11. Photon Design Ltdm Oxford, U.K., FimmWave software.
12. D. R. Lide, ed., *CRC Handbook of Chemistry and Physics*, 83rd ed. (CRC Press, 2002).
13. M. Wang, S. Uusitalo, C. Liedert, J. Hiltunen, L. Hakalahti, and R. Myllylä, “Polymeric dual-slab waveguide interferometer for biochemical sensing applications,” Appl. Opt. **51**, 1886–1893 (2012).

PAPER II

Drift compensation using a multichannel slot waveguide Young interferometer

Journal of the European Optical Society
– Rapid Publications 10, 15053, 7 p.

J. Eur. Opt. Soc.-Rapid **10**, 15053 (2015)

Drift compensation using a multichannel slot waveguide Young interferometer

S. Aikio VTT Technical Research Centre of Finland, Kaitoväylä 1, FI-90590 Oulu, Finland
sanna.aikio@vtt.fi
M. Hiltunen VTT Technical Research Centre of Finland, Kaitoväylä 1, FI-90590 Oulu, Finland
marianne.hiltunen@vtt.fi
P. Stenberg Institute of Photonics, University of Eastern Finland, P.O. Box 111, FI-80101 Joensuu, Finland
stenberg.p@gmail.com
J. Hiltunen VTT Technical Research Centre of Finland, Kaitoväylä 1, FI-90590 Oulu, Finland
jussi.hiltunen@vtt.fi

Polymeric integrated Young interferometer sensor chips utilizing a slot waveguide have demonstrated to be sensitive, to work at visible wavelengths, to be manufacturable by simple process, and to have a reduced sensitivity to temperature fluctuations. Although slot waveguide Young interferometers have these desirable features for low-cost rapid diagnostics, the sensor readout is disturbed by mechanical drifts of the sensing system. In this paper we demonstrate that mechanical drifts of the readout system can be compensated by using a multichannel slot waveguide Young interferometer having two reference waveguides and applying a drift compensation method based on the analysis of the spatial shifts of the interferogram fringes. The applicability of the drift compensation method was studied by conducting experiments with undisturbed and with mechanically disturbed setup to measure the phase changes induced by the changes of the bulk refractive index. By applying the drift compensation method, the sample induced phase change responses were extracted from up to 18 times larger measured phase changes in the disturbed experiments proving the applicability of the method with multichannel slot waveguide Young interferometers.

[DOI: http://dx.doi.org/10.2971/jeos.2015.15053]

Keywords: Slot waveguide, integrated Young interferometer, drift compensation, interferometry, polymer waveguides

1 INTRODUCTION

Integrated Young interferometers (YI) have been demonstrated to be a sensitive label free sensor platform being able to detect bulk refractive index (RI) differences in the level of 10^{-5}–10^{-8} refractive index units (RIU) [1]–[3]. Sensor chips have been implemented as silicon, glass, TaO_5 and polymeric devices based on slab, planar, ridge, inverted ridge and slot waveguides [1]–[7]. Integrated YI sensors have been demonstrated to be compatible with multi-analyte sensing and detection from complex sample matrices [8]. The label free detection technique enables simpler assays reducing the complexity and cost of the analysis.

Polymeric integrated YI sensor chips utilizing a slot waveguide have been demonstrated to work at visible wavelengths and to measure bulk RI differences down to level of 10^{-6} RIU [7]. Slot waveguide enables a sensor layout where measurement and reference waveguides are similarly exposed to samples, which has been shown to significantly reduce the sensor sensitivity to temperature fluctuations [7]. These properties make the slot waveguide YI sensor platform interesting for rapid diagnostic applications where low-cost and sensor disposability are key properties as well as the robustness of the measurement.

Although slot waveguide based YI chips have many desirable features, the interferometric sensing method is disturbed by the mechanical drifts of the readout system. One solution is to isolate the readout system from external disturbances [9], but this is not easily implementable with low-cost portable readers. Another approach is based on multichannel chip layouts where two reference waveguides provide signal for the calculation of the drift compensated signal. Idea has been introduced and demonstrated to be applicable for the compensation of intrinsic drifts of the measurement system [10]. Authors have presented a theory for this approach where spatial shifts of the interferogram fringes are used to calculate the drift compensation [11]. It was also demonstrated by using a polymeric multichannel inverted ridge waveguide YI chip that the compensation method is capable to quantitatively extract sample induced bulk RI changes even though the measurement setup was deliberately mechanically disturbed.

In this paper we study whether mechanical drifts of the readout system can be compensated by using a multichannel slot waveguide Young interferometer having two reference waveguides and the drift compensation method based on the analysis of the spatial shifts of the interferogram fringes. For this purpose, two sets of measurements were done: the first set was conducted with an undisturbed setup, and the second set with a mechanically disturbed setup. During the measure-

Received October 02, 2015; Ms. accepted October 22, 2015; published November 20, 2015 ISSN 1990-2573

ments, the chip was exposed to sample solutions, *i.e.*, aqueous glucose solutions with various concentrations, to modify the bulk RI and induce phase change responses. The responses were calculated from the phase change curves of the undisturbed measurements and from the drift compensated phase change curves of the disturbed measurements. The obtained response values of the undisturbed and disturbed experiments were compared to analyse the applicability of the compensation method.

2 SENSOR CHIP

The layout of the multichannel slot waveguide YI sensor chip is shown in Figure 1(a) with dimensions, and a microscope image of part of the waveguides in Figure 1(b). The input ridge waveguide has two Y-junctions splitting it into three parallel waveguides called channels. The channel numbering is shown on the waveguides in Figure 1(a). Channel 1 is the measurement channel containing a slot structure, *i.e.* a narrow groove with the width of about 150 nm and the length of 7.5 mm. Channels 2 and 3 are reference channels implemented as ridge waveguides without slots. Scanning electron microscope (SEM) images of the cross-sections of both waveguide types are shown in Figure 1(c). The ridge and slot waveguide regions of channel 1 change abruptly without any taper structure leading to mode mismatch loss of 1 dB of the two interfaces. Due to the larger losses of the measurement channel, it was designed to have only one Y-junction enabling the coupling of a larger optical power to the slot structure. In principle, the slot structure could have been placed to any one of the channels.

The ends of the waveguides were protected by an overcladding layer leaving the measurement window open for the interaction with the sample solutions. Although the overcladding layer defines the length of the measurement window, the sensing length is defined by the length of the slot structure since it is the only part where the measurement and reference waveguides differ significantly and react differently to the samples. The measurement and reference channels also differ within the measurement window due to the second Y-junction branching the two reference channels. Anyhow the length where the measurement and reference channels differ due to the branching of the channels 2 and 3 is only 100 μm, which is much smaller than the sensing length, and thus does not have a significant impact to the sensor chip responses here.

The waveguides were fabricated from UV-curable hybrid polymer (Ormocore, RI 1.553, Micro resist technology). First, thinned Ormocore (Ormocore : Ma-T1050, weight ratio 1:7) was spin coated on a silicon wafer with 2 μm thick thermal oxide layer acting as an undercladding layer for the waveguides. Thinner (Ma-T1050) was evaporated at 130 °C for 10 minutes on a hot plate. For the waveguide replication, the transparent mold was stacked up in contact with the Ormocore coated wafer and pressed together in a nanoimprint equipment (Eitre 6, Obducat) with 10 bar pressure followed by 2 min UV-exposure. After the patterned waveguides were released from the mold they were hardened by post baking for one hour at 130 °C on a hot plate. In order to protect the waveguides from the contact with the flow cell, an overcladding layer (Ormostamp, RI 1.515, Micro resist technology) having a thickness of 10 μm was processed by using photolithography. The patterning of the over-cladding layer can be done with loose positional tolerances, since the sensing length is defined by the length of the slot structure. The manufacturing of the chip structures is described in detail in Ref. [7], where a two-channel slot waveguide YI sensor was analysed.

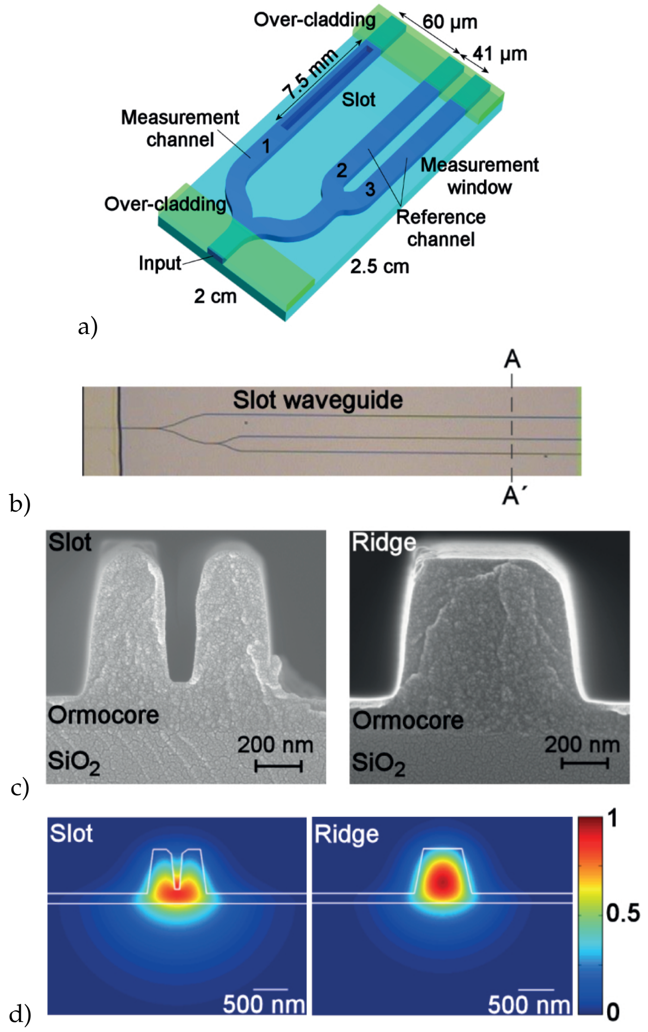

FIG. 1 a) Schematic of YI sensor structure with dimensions and channel numbering; b) Top view microscope image of part of the sensor waveguides; c) Scanning electron microscope images of the cross-sections of slot and ridge waveguides taken approximately along the line A-A´shown in b; d) Theoretical TE-mode field profiles of slot and ridge waveguides.

3 DETECTION PRINCIPLE AND SETUP

In the experiments, laser light was end-fire coupled into the input waveguide and split into the measurement and reference channels. In the measurement window, sample interacts with the evanescent wave of the light propagating in the waveguides, and thus a change of the RI in the measurement window changes the effective RIs of the waveguides. It has been shown that the same bulk RI change induces a larger effective RI change of the slot structure than of the ridge waveguide, which changes their mutual optical path length difference [7]. The change of the effective RI of the slot structure is larger because the electric field is confined into the slot, as shown by the simulated TE-mode field profiles of Figure 1(d), enhancing the light–sample interaction. Based on the simulations of the slot waveguide geometry covered with water, 5.4% of the optical field intensity is confined into the groove and in total of 10.4% into the water. With the ridge waveguide geometry, 5.4% of the optical field intensity is confined into the surrounding water. Light-sample interaction can be further enhanced by applying a high index coating, such as TaO_5, on the waveguide moving the mode outwards and increasing the confinement of the optical field intensity in the overlying medium [12, 13]. The difference in the change of the effective RIs enables a YI sensor chip layout where all the waveguides are exposed to sample solutions similarly.

When light couples out from the chip, the diverging beams overlap and interfere forming an interferogram that is a superposition of the three two-beam sub-interferograms formed by all the possible channel pairs, *i.e.* channel pairs 1 and 2, 1 and 3, and 2 and 3. An example of an interferogram is shown in Figure 2(b). The interferogram fringes shift when the mutual optical path length difference between the measurement and the reference channels changes due to the sample solutions.

Schematic of the measurement setup is shown in Figure 2(a). In the experiments, frequency stabilized laser light (wavelength 633 nm, HRS015, Thorlabs) was coupled into the input waveguide by using a focusing lens (C230TM-B, Thorlabs). In addition, an optical isolator was used to prevent the backreflections into the laser, and a quarter wave plate and a polarizer to select the TE-polarization state of the incoupled light. A beam expander was used to reduce the spot size produced by the focusing lens to enhance the in-coupling efficiency and to reduce the stray light. Interferogram was imaged onto a camera detector (PL-E425CU, PixeLink) by using a 40× microscope objective (NA 0.65, Micro Plan, Edmund Optics) with the image interval of 10 s. To form the interferogram, the microscope objective was mounted onto a translational stage equipped with a micrometer drive enabling the controlled adjustment of the separation between the microscope objective and the chip. The interferogram was formed by first imaging the out-coupling end of the chip to the camera and then moving the microscope objective ~800 μm away from the chip. For the mechanically disturbed experiments, the microscope objective was mounted onto a piezo actuated XYZ-translation stage and the microscope objective was moved in the direction shown by the arrow in Figure 2(a). The direction of the microscope objective movement was chosen to maximise the induced disturbance by mechanically moving the fringes on the camera detector along the same direction as they are shifted by the sample induced RI changes.

4 CALCULATION OF THE DRIFT COMPENSATED SIGNAL

Discrete Fourier transform was used to analyze the captured interferograms yielding the phases and the spatial frequencies of the sub-interferogram fringes. Since all the channel pairs had a unique separation at the outcoupling end, every sub-interferogram had an own spatial frequency, as shown in Figure 2(c), and thus their phases could be monitored separately in the experiments. If the separation of any two channel pairs would be same, then their spatial frequencies would be co-located in the amplitude spectrum and their phase changes could not be monitored separately. The phase change of the channel pair i and j, $\Delta\phi_{ij}$, at time t was calculated as a difference of the phase value ϕ_{ij} at time t and at the beginning of the experiment, t_0, *i.e.* $\Delta\phi_{ij}(t) = \phi_{ij}(t) - \phi_{ij}(t_0)$.

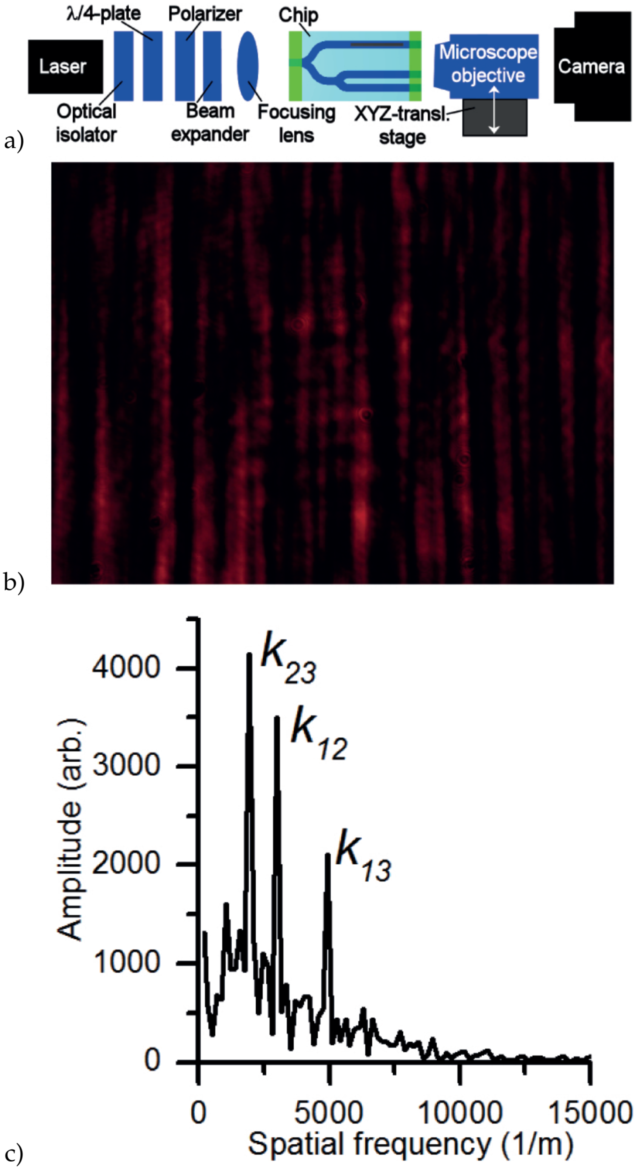

FIG. 2 a) Schematic of the optical setup. In the disturbed measurements, the microscope objective was moved in the direction indicated by the arrow; b) Captured interferogram; c) Amplitude spectrum of an interferogram. The spatial frequencies, k_{ij}, related to the sub-interferogram of channel pair i and j, stand out as a spikes.

Phase changes are a combination of the phase changes caused by the RI changes in the measurement window of the chip and the drifts of the system. Drifts are related either to the internal changes of the chip, caused for example by temperature variations, or to changes of the measurement setup, such as the mechanical movement of the components. Phase changes caused by the chip internal drifts can be assumed to be small since all the channels are integrated into a single chip and are exposed similarly to the samples. It can be also assumed that all the channels see the changes of the measurement setup similarly since they are sharing the optical components.

Since channels 2 and 3 are both reference channels, RI change in the measurement window does not induce any phase change into their sub-interferogram, and thus the phase changes are caused by the drifts that are dominated by the changes of the setup. Based on this, the phase changes of the channel pair 2 and 3 can be used to calculate the drift compensated phase changes of the channel pairs 1 and 2, and 1 and 3. Anyhow, the phase changes of the channel pair 2 and 3 cannot be directly subtracted from the phase changes of the channel pairs 1 and 2, and 1 and 3 since a change of the setup induces a different phase change between different channel pairs. Instead the drift compensation has to be calculated from the spatial shifts of the interferogram fringes since a change of the setup induces the same spatial shift of the fringes in all the sub-interferograms.

Now, the drift compensated sample induced spatial shift of the channel pair 1 and 3, Δs_{13}^{s}, can be calculated as

$$\Delta s_{13}^{s}(t) \approx \Delta s_{13}(t) - \Delta s_{23}(t), \tag{1}$$

where Δs_{13} and Δs_{23} are the spatial shifts of the sub-interferogram fringes of the channel pairs 1 and 3, and 2 and 3, respectively. Eq. (1) is an approximation since the internal changes of the chip are not taken into account and are ignored in this paper. The spatial shift of the channel pair i and j can be calculated from the phase change by using a relation

$$\Delta s_{ij}(t) = \frac{\Delta \phi_{ij}(t)}{2\pi k_{ij}}, \tag{2}$$

where k_{ij} is the spatial frequency of the sub-interferogram of the channel pair.

By using the relation of Eq. (2), the drift compensated sample induced phase change of the channel pair 1 and 3, $\Delta\phi_{13}^{s}$, can be calculated as

$$\Delta \phi_{13}^{s}(t) = 2\pi k_{13} \Delta s_{13}^{s}(t) \tag{3}$$

By substituting Eq. (1) into Eq. (3) and using the relation of Eq. (2), a compact expression for $\Delta\phi_{13}^{s}$ is obtained:

$$\Delta \phi_{13}^{s}(t) = \Delta \phi_{13}(t) - \frac{k_{13}}{k_{23}} \Delta \phi_{23}(t), \tag{4}$$

which is the form used in this paper to calculate the drift compensation.

The drift compensated sample induced phase change of the channel pair 1 and 2 can be calculated similarly. This approach can be applied to chips with more than one measurement channel by analysing each measurement channel separately. A more detailed discussion of the calculation of the drift compensation is presented in Ref. [11].

5 SAMPLE SOLUTIONS

To modify the bulk RI in the measurement window, aqueous glucose solutions with the concentrations of 0.01, 0.02, 0.05, 0.1 and 0.2 weight percent (wt. %) were prepared in ultra-pure water (MilliQ Academic, Merck Millipore). The RI differences of the solutions to pure water were calculated by using a polynomial [11] fitted to the tabulated values [14] yielding the following values from smallest to highest glucose concentration: 1.4×10^{-5}, 2.8×10^{-5}, 7.0×10^{-5}, 1.4×10^{-4} and 2.8×10^{-4} RIU. Glucose solutions were stored in the room temperature to equalize their temperature with the setup.

A flow cell was assembled onto the YI chip to enable actuation of solutions. The inlet of the flow cell was connected to the sample vial and the outlet to a syringe pump (Nexus 3000, Chemyx), which was driven in withdraw mode with the constant flow rate of 100 µl/min. The flow cell was assembled onto the chip and filled with water at least a day before the experiments to reduce the effect of water absorption into the polymeric waveguides during the measurements [6].

6 RESULTS

To study the applicability of the drift compensation with multichannel slot waveguide YI, experiments to sense bulk RI changes were conducted with undisturbed and with mechanically disturbed setup. In this section, the results of the undisturbed experiments are discussed first followed by the discussion of the mechanically disturbed experiments. To facilitate the comparison of the results between these two experiment types, the phase change curves and sensor responses of undisturbed and disturbed experiments are presented side by side in Figure 3 and Figure 4.

6.1 Undisturbed experiments

Responses of the sensor chip to the bulk RI changes were first determined with an undisturbed setup by exposing the sensor chip to 500 µl pulses of glucose solutions followed by flushing with water. The concentrations of 0.01, 0.05 and 0.2 wt. % were measured once, and the concentrations of 0.02, and 0.1 wt. % three times. The approximate timing of the glucose solutions in the flow cell is indicated in Figure 3(a).

The measured phase change curves of all the channel pairs are shown in the lower row of Figure 3(a), and the compensated phase change curves of the channel pairs 1 and 3, and 1 and 2 in the upper row. For clarity, only one set of curves per concentration is shown. It can be seen, that the phase change curves show clear responses to the bulk RI changes at all glucose concentrations. It can be also seen that the phase change curves of the reference channels, $\Delta\phi_{23}$, seem to react to the glucose solutions at the concentrations of 0.1 and 0.2 wt.% showing small negative and positive phase changes, respectively. These phase changes are not anyhow direct reactions to RI changes, but caused by the cross-talk between the channel pairs which is a known phenomenon in multichannel YI sensors [15]. Also the different signs of these phase changes provide a further proof of the cross-talk induced phase changes instead of real sensor responses.

Sensor responses were determined from the phase change curves by subtracting the mean value within 1.2-1.5 min from

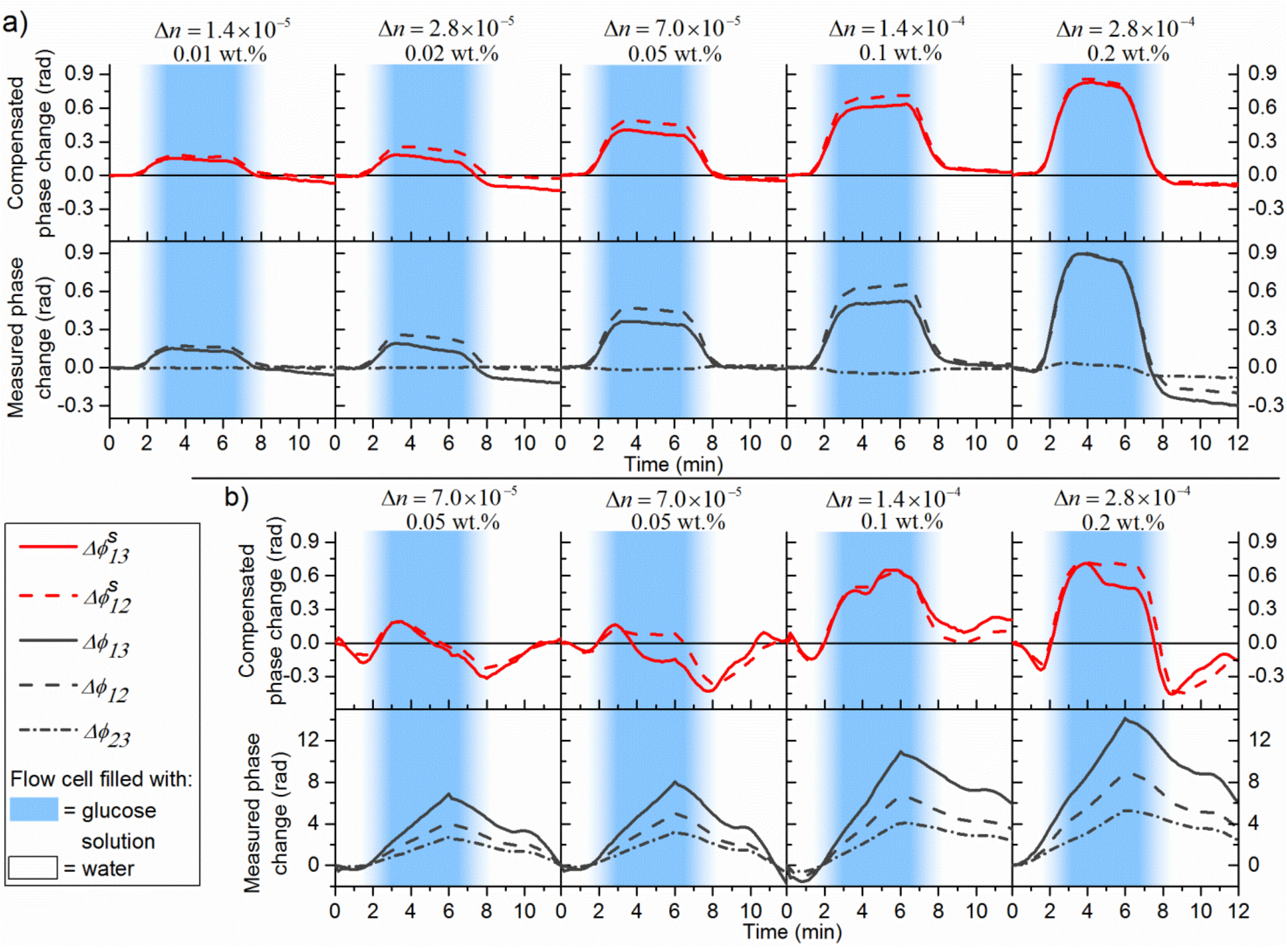

FIG. 3 Phase change curves of a) undisturbed experiments; and b) disturbed experiments. The upper row in the figures shows the compensated and the lower row the measured phase change curves. RI differences, Δn, to pure water and the concentrations of the glucose solutions are displayed above the curves. The background colour indicates the timing of the solutions in the flow cell.

the mean value within 4.8-5.2 min. The sensor responses are shown in Figure 4(a) and Figure 4(b) for the channel pair 1 and 3, and 1 and 2, respectively, with and without the compensation. It can be seen that, in overall, the responses increase with the increasing glucose concentration in all of the cases, as expected. Anyhow, it can be also seen that there is some ambiguity in the quantification since some of the response values of different concentrations are overlapping or are very close to each other, and thus the sensor readout is closer to semi-quantitative than quantitative.

Theoretical sensor responses were calculated by using a finite-element method of commercial software (Fimmwave, Photon Design). Simulations were conducted by first determining the waveguide dimensions from the SEM images (Figure 1(c)) and then calculating the effective RIs of the waveguides with various ambient RI values corresponding to the glucose solutions yielding the theoretical sensitivity of the sensor chip. The theoretical response is shown in Figure 4(a) and Figure 4(b), and is in good agreement with the measured values. Anyhow, the sensor response seems to saturate at the highest concentration that is attributed to the flow and diffusion dynamics of the glucose molecules within the narrow slot structure.

6.2 Disturbed experiments

During the mechanically disturbed experiments, the microscope objective was moved while the glucose solutions were used to change the bulk RI in the measurement window similarly as in the undisturbed experiments. The microscope objective was moved by manually controlling the piezo actuator, and the direction of the movement was reversed during each measurement. The rate of the movement varied between measurements, as well as the maximum displacement of the microscope objective being within 6-11 μm. The concentration of 0.05 wt. % was measured twice and the concentrations of 0.1 and 0.2 wt. % once.

The measured phase change curves of all the channel pairs are shown in the lower row of Figure 3(b) and the compensated phase change curves of channel pairs 1 and 3, and 1 and 2 in the upper row. The shapes of the drift compensated phase change curves of the two highest concentrations (*i.e.* 0.1 and 0.2 wt. %,) are similar than the ones obtained in the undisturbed experiments although they show more fluctuations. At the smallest concentration (0.05 wt. %), the sample induced phase changes and the signal fluctuations are at the same range, and thus the method cannot be considered to be able to extract the bulk RI changes at this level (7.0×10^{-5} RIU) anymore. The fluctuations of the compensated signal are at-

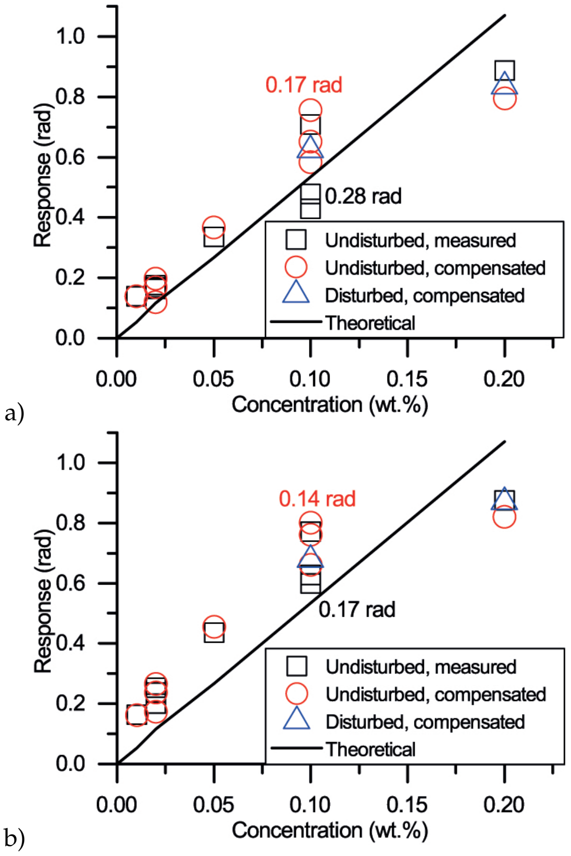

FIG. 4 Responses calculated from undisturbed measured, undisturbed compensated and disturbed compensated phase change curves of a) channel pair 1 and 3; and b) channel pair 1 and 2. The maximum range of the response values of undisturbed measured (black text) and of undisturbed compensated (red text) data sets are indicated next to the related data points.

tributed to the cross-talk between the channel pairs, which was already seen with the undisturbed experiments.

The responses of the compensated phase change curves for the concentrations of 0.1 and 0.2 wt. % were calculated similarly as in the undisturbed measurements and are included into Figure 4(a) and Figure 4(b). The calculated responses are in agreement with the values of the undisturbed experiments for both channel pairs proving the applicability of the drift compensation method with the multichannel slot waveguide YI sensor. The drift compensation method was thus capable to extract sample induced phase change responses from 18 times larger measured phase changes with the bulk RI difference of 1.4×10^{-4} RIU.

7 CONCLUSIONS

In this work we demonstrated that mechanical drifts of the measurement setup can be compensated by using a polymeric multichannel slot waveguide YI sensor having two reference channels and the analysis of the spatial shifts of the interferogram fringes. Experiments were conducted with an undisturbed and with a mechanically disturbed measurement setup while the bulk RI in the measurement window was modified by aqueous glucose solutions with various concentrations.

The sensor responses calculated from the phase change curves of the undisturbed measurements and from the compensated phase change curves of disturbed measurements were in good agreement. This demonstrates the applicability of the drift compensation method with the multichannel slot waveguide YI sensor. Based on the mechanically disturbed experiments, the drift compensation method was able to extract the sample induced phase changes caused by the bulk RI difference of 1.4×10^{-4} RIU from 18 times larger measured phase change signal. At the smaller bulk RI difference, the drift compensation method was not capable to differentiate the sample induced phase change from the overall signal fluctuations. The fluctuations were attributed to the cross-talk between the channel pairs limiting the utilization of the drift compensation method. The applicability of the drift compensation method further improves the compatibility of the polymer slot waveguide YI sensors for low-cost rapid diagnostic applications by enhancing the robustness of the platform.

8 ACKNOWLEDGEMENTS

Authors acknowledge financial support by the European Commission via the Seventh Framework Programme under the grant agreement No. 263382 “PHOTOSENS”, and by Academy of Finland grant No. 284907. S.A. acknowledges the valuable guidance of professor emeritus Risto Myllylä, University of Oulu, during this work.

References

[1] A. Ymeti, J. S. Kanger, R. Wijn, P. V. Lambeck, and J. Greve, “Development of a multichannel integrated interferometer immunosensor,” Sens. Actuator B-Chem. **83**, 1–7 (2002).

[2] K. Schmitt, B. Schirmer, C. Hoffmann, A. Brandenburg, and P. Meyrueis, "Interferometric biosensor based on planar optical waveguide sensor chips for label-free detection of surface bound bioreactions,” Biosens. Bioelectron. **22**, 2591–2597 (2007).

[3] M. Wang, J. Hiltunen, C. Liedert, L. Hakalahti, and R. Myllylä, “An integrated Young interferometer based on UV-imprinted polymer waveguides for label-free biosensing applications,” J. Eur. Opt. Soc.-Rapid **7**, 12019 (2012).

[4] Z. Qi, S. Zhao, F. Chen, and S. Xia, “Integrated Young interferometer sensor with a channel-planar composite waveguide sensing arm,” Opt. Lett. **34**, 2213–2215 (2009).

[5] A. Brandenburg, and R. Henninger, “Integrated optical Young interferometer,” Appl. Optics **33**, 5941–5947 (1994).

[6] M. Wang, S. Uusitalo, C. Liedert, J. Hiltunen, L. Hakalahti, and R. Myllylä, “Polymeric dual-slab waveguide interferometer for biochemical sensing applications,” Appl. Optics **51**, 1886–1893 (2012).

[7] M. Hiltunen, J. Hiltunen, P. Stenberg, S. Aikio, L. Kurki, P. Vahimaa, and P. Karioja, “Polymeric slot waveguide interferometer for sensor applications,” Opt. Express **22**, 7229–7237 (2014).

[8] A. Ymeti, J. Greve, P. V. Lambeck, T. Wink, S. W. F. M. van Hövell, T. A. M. Beumer, R. R. Wijn, et al., “Fast, Ultrasensitive Virus Detection Using a Young Interferometer Sensor,” Nano Lett. **7**, 394–397 (2007).

[9] P. Kozma, F. Kehl, E. Ehrentreich-Förster, C. Stamm, and F. F. Bier, “Integrated planar optical waveguide interferometer biosensors: A comparative review,” Biosens. Bioelectron. **58**, 287–307 (2014).

[10] A. Ymeti, J. Greve, P. V. Lambeck, R. Wijn, R. G. Heideman, and J. S. Kanger, “Drift correction in a multichannel integrated optical Young interferometer,” Appl. Optics **44**, 3409–3412 (2005).

[11] S. Aikio, M. Hiltunen, and J. Hiltunen, “Compensation of drift by using a multichannel integrated Young interferometer,” Appl. Optics **54**, 4771–4780 (2015).

[12] M. Wang, J. Hiltunen, C. Liedert, S. Pearce, M. Charlton, L. Hakalahti, P. Karioja, et al., “Highly sensitive biosensor based on UV-imprinted layered polymeric-inorganic composite waveguides,” Opt. Express **20**, 20309–20317 (2012).

[13] L. Ahmadi, J. Tervo, J. Saarinen, and S. Honkanen, “Enhanced sensitivity in polymer slot waveguides by atomic layer deposited bilayer coatings,” Appl. Optics **52**, 8089–8094 (2013).

[14] D. R. Lide, *CRC Handbook of Chemistry and Physics* (83rd Edition. CRC Press, Boca Raton, 2002).

[15] A. Ymeti, J. S. Kanger, J. Greve, P. V. Lambeck, R. Wijn, and R. G. Heideman, “Realization of a multichannel integrated Young interferometer chemical sensor,” Appl. Optics **42**, 5649–5660 (2003).

PAPER III

Disposable photonic integrated circuits for evanescent wave sensors by ultra-high volume roll-to-roll method

Optics Express 24, 2527–2541.

Disposable photonic integrated circuits for evanescent wave sensors by ultra-high volume roll-to-roll method

Sanna Aikio,[1,*] Jussi Hiltunen,[1] Johanna Hiitola-Keinänen,[1] Marianne Hiltunen,[1] Ville Kontturi,[2] Samuli Siitonen,[2] Jarkko Puustinen,[3] and Pentti Karioja,[1]

[1]VTT Technical Research Centre of Finland, Oulu, FI-90590, Finland
[2]Nanocomp Oy Ltd, Lehmo, FI-80710, Finland
[3]University of Oulu, Faculty of Information Technology and Electrical Engineering, Department of Electrical Engineering, Microelectronics and Materials Physics Laboratories, Oulu, FI-90014, Finland
[*]sanna.aikio@vtt.fi

Abstract: Flexible photonic integrated circuit technology is an emerging field expanding the usage possibilities of photonics, particularly in sensor applications, by enabling the realization of conformable devices and introduction of new alternative production methods. Here, we demonstrate that disposable polymeric photonic integrated circuit devices can be produced in lengths of hundreds of meters by ultra-high volume roll-to-roll methods on a flexible carrier. Attenuation properties of hundreds of individual devices were measured confirming that waveguides with good and repeatable performance were fabricated. We also demonstrate the applicability of the devices for the evanescent wave sensing of ambient refractive index. The production of integrated photonic devices using ultra-high volume fabrication, in a similar manner as paper is produced, may inherently expand methods of manufacturing low-cost disposable photonic integrated circuits for a wide range of sensor applications.

OCIS codes: (130.3120) Integrated optics devices; (230.4000) Microstructure fabrication; (130.5460) Polymer waveguides; (130.6010) Sensors; (120.3180) Interferometry.

References and links

1. P. Dong, Y. Chen, G. Duan, and D. Neilson, "Silicon photonic devices and integrated circuits," Nanophotonics **3**(4-5), 215–228 (2014).
2. P. Dong, L. Xiang, S. Chandrasekhar, L. L. Buhl, R. Aroca, and Y.-K. Chen, "Monolithic silicon photonic integrated circuits for compact 100 Gb/s coherent optical receivers and transmitters," IEEE J. Sel. Top. Quantum Electron. **20**(4), 150–157 (2014).
3. G.-H. Duan, C. Jany, A. Le Liepvre, A. Accard, M. Lamponi, D. Make, P. Kaspar, G. Levaufre, N. Girard, F. Lelarge, J.-M. Fedeli, A. Descos, B. Ben Bakir, S. Messaoudene, D. Bordel, S. Menezo, G. de Valicourt, S. Keyvaninia, G. Roelkens, D. Van Thourhout, D. J. Thomson, F. Y. Gardes, and G. T. Reed, "Hybrid III–V on silicon lasers for photonic integrated circuits on silicon," IEEE J. Sel. Top. Quantum Electron. **20**(4), 158–170 (2014).
4. X. Fan and I. M. White, "Optofluidic microsystems for chemical and biological analysis," Nat. Photonics **5**(10), 591–597 (2011).
5. V. M. Passaro, C. de Tullio, B. Troia, M. La Notte, G. Giannoccaro, and F. De Leonardis, "Recent advances in integrated photonic sensors," Sensors (Basel) **12**(11), 15558–15598 (2012).
6. L. A. Coldren, S. C. Nicholes, L. Johansson, S. Ristic, R. S. Guzzon, E. J. Norberg, and U. Krishnamachari, "High performance InP-based photonic ICs—A tutorial," J. Lightwave Technol. **29**(4), 554–570 (2011).
7. R. Nagarajan, C. H. Joyner, R. P. Schneider, J. S. Bostak, T. Butrie, A. G. Dentai, V. G. Dominic, P. W. Evans, M. Kato, M. Kauffman, D. J. H. Lambert, S. K. Mathis, A. Mathur, R. H. Miles, M. L. Mitchell, M. J. Missey, S. Murthy, A. C. Nilsson, F. H. Peters, S. C. Pennypacker, J. L. Pleumeekers, R. A. Salvatore, R. K. Schlenker, R. B. Taylor, M. F. Huan-Shang Tsai, M. F. Van Leeuwen, J. Webjorn, M. Ziari, D. Perkins, J. Singh, S. G. Grubb, M. S. Reffle, D. G. Mehuys, F. A. Kish, and D. F. Welch, "Large-scale photonic integrated circuits," IEEE J. Sel. Top. Quantum Electron. **11**(1), 50–65 (2005).
8. M. Ferrera, L. Razzari, D. Duchesne, R. Morandotti, Z. Yang, M. Liscidini, J. E. Sipe, S. Chu, B. E. Little, and D. J. Moss, "Low-power continuous-wave nonlinear optics in doped silica glass integrated waveguide structures," Nat. Photonics **2**(12), 737–740 (2008).

#255397 Received 11 Dec 2015; revised 21 Jan 2016; accepted 23 Jan 2016; published 1 Feb 2016

9. H. Jin, F. M. Liu, P. Xu, J. L. Xia, M. L. Zhong, Y. Yuan, J. W. Zhou, Y. X. Gong, W. Wang, and S. N. Zhu, "On-chip generation and manipulation of entangled photons based on reconfigurable lithium-niobate waveguide circuits," Phys. Rev. Lett. **113**(10), 103601 (2014).
10. L. Chen and R. M. Reano, "Compact electric field sensors based on indirect bonding of lithium niobate to silicon microrings," Opt. Express **20**(4), 4032–4038 (2012).
11. M. Schumann, T. Buckmann, N. Gruhler, M. Wegener, and W. Pernice, "Hybrid 2D-3D optical devices for integrated optics by direct laser writing," Light Sci. Appl. **3**(6), e175 (2014).
12. C. Zhang, S. Srinivasan, Y. Tang, M. J. R. Heck, M. L. Davenport, and J. E. Bowers, "Low threshold and high speed short cavity distributed feedback hybrid silicon lasers," Opt. Express **22**(9), 10202–10209 (2014).
13. J. K. Jang, M. J. Erkintalo, J. Schroeder, B. J. Eggleton, S. G. Murdoch, and S. Coen, High-fidelity optical buffer based on temporal cavity solitons" in *CLEO: 2014,* OSA Technical Digest (online) (Optical Society of America, 2014), paper STu3N.7.
14. J. Missinne, S. Kalathimekkad, B. Van Hoe, E. Bosman, J. Vanfleteren, and G. Van Steenberge, "Stretchable optical waveguides," Opt. Express **22**(4), 4168–4179 (2014).
15. S. I. Park, Y. Xiong, R. H. Kim, P. Elvikis, M. Meitl, D. H. Kim, J. Wu, J. Yoon, C. J. Yu, Z. Liu, Y. Huang, K. C. Hwang, P. Ferreira, X. Li, K. Choquette, and J. A. Rogers, "Printed assemblies of inorganic light-emitting diodes for deformable and semitransparent displays," Science **325**(5943), 977–981 (2009).
16. L. Li, H. Lin, S. Qiao, Y. Zou, S. Danto, K. Richardson, J. D. Musgraves, N. Lu, and J. Hu, "Integrated flexible chalcogenide glass photonic devices," Nat. Photonics **8**(8), 643–649 (2014).
17. M. Vosgueritchian, J. B.-H. Tok, and Z. Bao, "Stretchable LEDs: Light-emitting electronic skin," Nat. Photonics **7**(10), 769–771 (2013).
18. D. Liu and T. L. Kelly, "Perovskite solar cells with a planar heterojunction structure prepared using room-temperature solution processing techniques," Nat. Photonics **8**(2), 133–138 (2013).
19. J. Hu, L. Li, H. Lin, P. Zhang, W. Zhou, and Z. Ma, "Flexible integrated photonics: where materials, mechanics and optics meet [Invited]," Opt. Mater. Express **3**(9), 1313–1331 (2013).
20. Y. Chen, H. Li, and M. Li, "Flexible and tunable silicon photonic circuits on plastic substrates," Sci. Rep. **2**, 622 (2012).
21. C. L. Yu, H. Kim, N. de Leon, I. W. Frank, J. T. Robinson, M. McCutcheon, M. Liu, M. D. Lukin, M. Loncar, and H. Park, "Stretchable photonic crystal cavity with wide frequency tunability," Nano Lett. **13**(1), 248–252 (2013).
22. C. W. Tang and S. A. VanSlyke, "Organic electroluminescent diodes," Appl. Phys. Lett. **51**(12), 913–915 (1987).
23. T. W. Kelley, P. F. Baude, C. Gerlach, D. E. Ender, D. Muyres, M. A. Haase, D. E. Vogel, and S. D. Theiss, "Recent progress in organic electronics: Materials, devices, and processes," Chem. Mater. **16**(23), 4413–4422 (2004).
24. H. Shirakawa, E. J. Louis, A. G. MacDiarmid, C. K. Chiang, and A. J. Heeger, "Synthesis of electrically conducting organic polymers: halogen derivatives of polyacetylene, $(CH)_x$," J. Chem. Soc. Chem. Commun. **1977**(16), 578–580 (1977).
25. H. C. Ko, M. P. Stoykovich, J. Song, V. Malyarchuk, W. M. Choi, C. J. Yu, J. B. Geddes 3rd, J. Xiao, S. Wang, Y. Huang, and J. A. Rogers, "A hemispherical electronic eye camera based on compressible silicon optoelectronics," Nature **454**(7205), 748–753 (2008).
26. L. Zhou, A. Wanga, S. Wu, J. Sun, S. Park, and T. N. Jackson, "All-organic active matrix flexible display," Appl. Phys. Lett. **88**(8), 083502 (2006).
27. K. Cherenack, K. V. Os, and L. V. Pieterson, "Smart photonic textiles begin to weave their magic," Laser Focus World **48**, 63–66 (2012).
28. J. Yoon, L. Li, A. V. Semichaevsky, J. H. Ryu, H. T. Johnson, R. G. Nuzzo, and J. A. Rogers, "Flexible concentrator photovoltaics based on microscale silicon solar cells embedded in luminescent waveguides," Nat. Commun. **2**, 343 (2011).
29. J. Liang, L. Li, X. Niu, Z. Yu, and Q. Pei, "Elastomeric polymer light-emitting devices and displays," Nat. Photonics **7**(10), 817–824 (2013).
30. M. S. White, M. Kaltenbrunner, E. D. Glowacki, K. Gutnichenko, G. Kettlgruber, I. Graz, S. Aazou, C. Ulbricht, D. A. M. Egbe, M. C. Miron, Z. Major, M. C. Scharber, T. Sekitani, T. Someya, S. Bauer, and N. S. Sariciftci, "Ultrathin, highly flexible and stretchable PLEDs," Nat. Photonics **7**(10), 811–816 (2013).
31. G. Li, R. Zhu, and Y. Yang, "Polymer solar cells," Nat. Photonics **6**(3), 153–161 (2012).
32. J. J. Dumond and H. Yee Low, "Recent developments and design challenges in continuous roller micro- and nanoimprinting," J. Vac. Sci. Technol. B **30**(1), 010801 (2012).
33. L. Peng, Y. Deng, P. Yi, and X. Lai, "Micro hot embossing of thermoplastic polymers: a review," J. Micromech. Microeng. **24**(1), 013001 (2014).
34. J. H. Hsu, C. H. Lee, and R. Chen, "An integrated optical pickup with roll-to-roll fabricated diffractive components," Opt. Express **19**(14), 13257–13267 (2011).
35. R. Bruck, P. Muellner, N. Kataeva, A. Koeck, S. Trassl, V. Rinnerbauer, K. Schmidegg, and R. Hainberger, "Flexible thin-film polymer waveguides fabricated in an industrial roll-to-roll process," Appl. Opt. **52**(19), 4510–4514 (2013).
36. S. Z. Oo, R. Y. Chen, S. Siitonen, V. Kontturi, D. A. Eustace, J. Tuominen, S. Aikio, and M. D. B. Charlton, "Disposable plasmonic plastic SERS sensor," Opt. Express **21**(15), 18484–18491 (2013).
37. S. F. Leung, L. Gu, Q. Zhang, K. H. Tsui, J. M. Shieh, C. H. Shen, T. H. Hsiao, C. H. Hsu, L. Lu, D. Li, Q. Lin, and Z. Fan, "Roll-to-roll fabrication of large scale and regular arrays of three-dimensional nanospikes for high efficiency and flexible photovoltaics," Sci. Rep. **4**, 4243 (2014).

#255397 Received 11 Dec 2015; revised 21 Jan 2016; accepted 23 Jan 2016; published 1 Feb 2016

38. P. Apilo, J. Hiltunen, M. Välimäki, S. Heinilehto, R. Sliz, and J. Hast, “Roll-to-roll gravure printing of organic photovoltaic modules-insulation of processing defects by an interfacial layer,” Prog. Photovolt. Res. Appl. **23**(7), 918–928 (2015).
39. S. Y. Chou, P. R. Krauss, and P. J. Renstrom, “Imprint of sub-25 nm vias and trenches in polymers,” Appl. Phys. Lett. **67**(21), 3114–3116 (1995).
40. N. Kooy, K. Mohamed, L. T. Pin, and O. S. Guan, “A review of roll-to-roll nanoimprint lithography,” Nanoscale Res. Lett. **9**(1), 320 (2014).
41. J. John, Y. Tang, J. P. Rothstein, J. J. Watkins, and K. R. Carter, “Large-area, continuous roll-to-roll nanoimprinting with PFPE composite molds,” Nanotechnology **24**(50), 505307 (2013).
42. J. Hiltunen, M. Hiltunen, J. Puustinen, J. Lappalainen, and P. Karioja, “Fabrication of optical waveguides by imprinting: usage of positive tone resist as a mould for UV-curable polymer,” Opt. Express **17**(25), 22813–22822 (2009).
43. M. Wang, J. Hiltunen, S. Uusitalo, J. Puustinen, J. Lappalainen, P. Karioja, and R. Myllylä, “Fabrication of optical inverted-rib waveguides using UV-imprinting,” Microelectron. Eng. **88**(2), 175–178 (2011).
44. J. Hiltunen, A. Kokkonen, J. Puustinen, M. Hiltunen, and J. Lappalainen, “UV-imprinted single-mode waveguides with low loss at visible wavelength,” IEEE Photonics Technol. Lett. **25**(10), 996–998 (2013).
45. P. Kozma, F. Kehl, E. Ehrentreich-Förster, C. Stamm, and F. F. Bier, “Integrated planar optical waveguide interferometer biosensors: a comparative review,” Biosens. Bioelectron. **58**, 287–307 (2014).
46. A. Ymeti, J. S. Kanger, R. Wijn, P. V. Lambeck, and J. Greve, “Development of a multichannel integrated interferometer immunosensor,” Sens. Actuators B Chem. **83**(1-3), 1–7 (2002).
47. A. Brandenburg and R. Henninger, “Integrated optical Young interferometer,” Appl. Opt. **33**(25), 5941–5947 (1994).
48. A. Schimpf, D. Bucci, M. Nannini, A. Magnaldo, L. Couston, and J.-E. Broquin, “Photothermal microfluidic sensor based on an integrated Young interferometer made by ion exchange in glass,” Sens. Actuators B Chem. **163**(1), 29–37 (2012).
49. K. Schmitt, B. Schirmer, C. Hoffmann, A. Brandenburg, and P. Meyrueis, “Interferometric biosensor based on planar optical waveguide sensor chips for label-free detection of surface bound bioreactions,” Biosens. Bioelectron. **22**(11), 2591–2597 (2007).
50. M. Wang, S. Uusitalo, C. Liedert, J. Hiltunen, L. Hakalahti, and R. Myllylä, “Polymeric dual-slab waveguide interferometer for biochemical sensing applications,” Appl. Opt. **51**(12), 1886–1893 (2012).
51. M. Wang, J. Hiltunen, C. Liedert, L. Hakalahti, and R. Myllylä, “An integrated Young interferometer based on UV-imprinted polymer waveguides for label-free biosensing applications,” J. Eur. Opt. Soc **7**, 12019 (2012).
52. M. Hiltunen, J. Hiltunen, P. Stenberg, S. Aikio, L. Kurki, P. Vahimaa, and P. Karioja, “Polymeric slot waveguide interferometer for sensor applications,” Opt. Express **22**(6), 7229–7237 (2014).
53. J. S. Kanger, V. Subramaniam, P. H. J. Nederkoorn, and A. Ymeti, “A Fast and Sensitive Integrated Young Interferometer Biosensor,” in *Advanced Photonic Structures for Biological and Chemical Detection*, X. Fan, ed. (Springer, 2009).
54. A. Ymeti, J. S. Kanger, J. Greve, P. V. Lambeck, R. Wijn, and R. G. Heideman, “Realization of a multichannel integrated Young interferometer chemical sensor,” Appl. Opt. **42**(28), 5649–5660 (2003).
55. S. Aikio, M. Hiltunen, and J. Hiltunen, “Compensation of drift by using a multichannel integrated Young interferometer,” Appl. Opt. **54**(15), 4771–4780 (2015).
56. D. R. Lide, ed., *CRC Handbook of Chemistry and Physics. 83rd Edition* (CRC, 2002).
57. H. Kipphan, ed., *Handbook of Print Media* (Springer-Verlag, 2001).
58. P. Kopola, T. Aernouts, S. Guillerez, H. Jin, M. Tuomikoski, A. Maaninen, and J. Hast, “High efficient plastic solar cells fabricated with a high-throughput gravure printing method,” Sol. Energy Mater. Sol. Cells **94**(10), 1673–1680 (2010).
59. R. Hunsperger, “Losses in Optical Waveguides,” in *Integrated Optics*, (Springer-Verlag, 2009).
60. M. Oh, W. Chu, J. Shin, J. Kim, K. Kim, J. Seo, H. Lee, Y. Noh, and H. Lee, “Polymeric optical waveguide devices exploiting special properties of polymer materials,” Opt. Commun. **362**, 3–12 (2016).

1. Introduction

Photonic integrated circuits (PICs) are an optical counterpart for integrated electrical circuits, where several functionalities are integrated onto a single platform to perform a wide variety of optical functions. The research on PICs has been mostly motivated by telecommunication and short-range interconnection applications [1–3]. PICs are also highly applicable in sensor usage, since they enable convenient implementation of waveguide-based signal routing between a light source, sensing area and detection point, as well as multiparameter sensing [4,5]. Silicon-based PICs have become particularly popular due to their compatibility with mature complementary metal–oxide–semiconductor (CMOS) technologies [1]. Due to the diversity of the implemented functionalities, a large variety of other materials has also been used to realize PICs including indium phosphide [6,7], glass [8] and ceramics [9,10]. On the other hand, polymeric materials are also used in PICs and as interconnection busses between PICs due to their versatile processing [11–13].

#255397 Received 11 Dec 2015; revised 21 Jan 2016; accepted 23 Jan 2016; published 1 Feb 2016

Polymers are dominant in flexible photonic platforms [14]. Flexible photonics is an emerging field expanding the usage possibilities of photonics in several applications, such as displays, interconnections, solar cells and sensors [15–19]. This is because flexibility allows the realization of conformable and diverse-shaped photonic devices and systems. To date, flexible photonics has been mostly produced in batches by fabricating functional devices on rigid substrates and assembling separately produced devices on a deformable carrier typically made of plastic [20]. For example, photonic crystals [21], light-emitting diodes (LEDs) [15] and PICs [16] have been integrated on deformable platforms using the device transfer based method. In order to decrease the complexity and the cost of the manufacture, the additional assembly step is preferably avoided. Therefore, flexible photonic devices and systems have been produced also by fabricating functional parts in batches directly on deformable carriers. Particularly, the development of organic light emitting diodes (OLEDs) [22] initiated the vast field of research on flexible organic electronics [23,24] and photonics [20,25–28] resulting in the monolithic fabrication of active and passive devices directly on deformable substrates including light emitting devices [29,30], polymer solar cells [31] and waveguide devices [17].

To date, independent of the choice of material, realization of PICs has relied on batch processing, however. The increasing need to minimize the production costs of photonics has, however, initiated the researchers to seek alternative methods for batch-based fabrication. Especially disposable photonics, such as optical sensors for point-of-care diagnostics, are very difficult to realize by wafer or sheet-level processing due to the large footprint, typically several square centimeters, required for different functionalities and handling as well as due to cost strains. To offer an alternative for traditional batch production, roll-to-roll (R2R) processing has been introduced to produce photonics and electronics in a similar manner as paper is produced [32,33]. In R2R processing, different surface structures and materials are patterned onto a continuously moving carrier. Diffractive optics [34], slab light guiding [35], surface enhanced Raman spectroscopy (SERS) sensor structures [36], and solar cells [37,38] have already been demonstrated in the roll format. However, PICs with signal routing and transducing functionalities have not been produced by ultra-high volume R2R processing.

Micro- and nanoscale replication methods suitable for high-throughput production have attracted significant research and development efforts since the introduction of nanoimprint lithography (NIL) [39,40]. The operation principle of NIL is simple where a mould with a surface pattern is replicated to another surface by stamping and curing the material to be replicated. Depending on the curing method, NIL or imprinting can be divided into thermal embossing and UV-imprinting. In thermal embossing the replication tool is heated above the glass transition temperature of the thermoplastic polymer to be replicated. During the stamping, thermoplastic material softens and the surface pattern of the mould is replicated due to applied pressure. In UV-imprinting, resin to be replicated is in liquid phase when the stamping tool is brought into the contact. By applying UV-light, the resin is cured and the surface structure is replicated. Both, thermal and UV-based methods have been successfully transferred from static wafer- or sheet-level processing to continuous R2R processing with demonstrations to produce sub-µm structures [33,40,41]. As our previous work has shown, sheet-level UV-imprint method can be used to fabricate optical single-mode waveguides [42–44], the UV-curing method was chosen in this work to investigate whether R2R scale processing can be also applied in production of single-mode waveguides.

PICs can be used to implement evanescent wave sensors, such as Young interferometers (YIs) [45]. Integrated YIs are based on waveguides and they utilize an evanescent wave field to sense refractive index (RI) changes at or near the waveguide surface. Sensor chips have been realized by using inorganic materials such as silicon [46], glass [47,48], and tantalum pentoxide [49]. More recently, polymeric YI sensor chips have been implemented based on slab [50], inverted ridge [51] and slot [52] waveguides. Polymeric YIs have been reported to have limit of detections (LODs) 10^{-5}-10^{-6} RIU [51,52] whereas inorganic YIs have achieved LODs 10^{-6}-10^{-8} RIU [46,48,49] placing them among the most sensitive ones among integrated interferometric sensors [45].

#255397 Received 11 Dec 2015; revised 21 Jan 2016; accepted 23 Jan 2016; published 1 Feb 2016

In this paper, we demonstrate that polymeric single-modal PICs for disposable sensors can be manufactured on rolls at lengths of hundreds of meters by R2R processing. This opens a new avenue for the utilization of PICs by enabling their wide spread usage as disposable platforms. We assess the single-modal operation of the waveguides, and analyze attenuation properties of hundreds of individual waveguide samples. The results show that waveguide devices with good and repeatable performance were fabricated. Then we demonstrate the applicability of the PICs for evanescent wave sensing of ambient RI changes utilizing them as integrated YI chips.

The organization of this paper is as follows: In Section 2 we describe the sensor design and the sensing principle of integrated YIs. Section 3, Materials and setups, discusses the determination of the RIs of the used materials, optical setups, and sample solutions used in the sensing experiments as well as their actuation. In Section 4 the stamp fabrication and the R2R processing of PICs are described. Section 5 contains the experimental results and discussion of the single-modality of the waveguides, the waveguide attenuation measurements, and the ambient RI sensing experiments. Finally, our conclusions are given in Section 6.

2. Sensor design and sensing principle

A roll of PICs is shown in Fig. 1(a) and a sensor chip with PIC sensors cut from the roll is shown in Fig. 1(b). A schematic of the YI sensor chip layout used in this paper is shown in Fig. 1(c). The sensor chip input waveguide has three Y-junctions splitting the waveguide into four parallel waveguides forming two YIs, named YI1 and YI2, both consisting of a reference and a measurement waveguide. The distance between the measurement and reference waveguides is increased at the measurement window enabling the patterning of the necessary overcladding layer without lithographic precision. The exact sensor chip design used in this paper, is discussed in detail in Section 5.3.

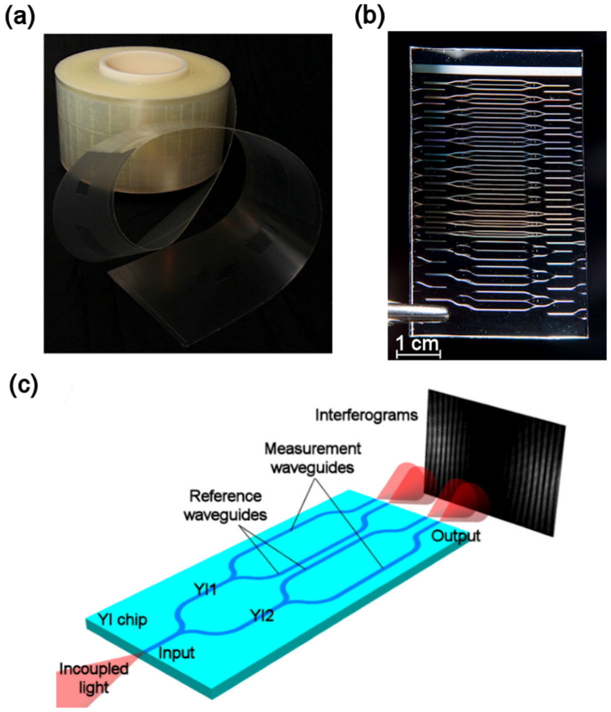

Fig. 1. (a) Roll of sensor PICs, (b) sensor chip cut from the roll, and (c) illustration of the YI sensor layout with a captured interferogram.

During YI experiments, laser light was end-fire coupled into the input waveguide. The outcoupled diverging light beams overlapped and interfered, and the interferogram was imaged onto a camera detector by using a microscope objective. Imaging was done sufficiently close to the end of the chip, and thus the beams interfered only with the nearest beam forming two, 2-beam interferograms. In addition, the separation between the microscope objective and the camera was chosen so that the interferograms were imaged simultaneously onto a single camera detector as shown in Fig. 1(c).

The sensing method is based on the analysis of the sample-induced shifts of the interferogram fringes. When RI in the measurement window on the measurement waveguide is changed by the sample, the effective RI of the waveguide is changed due to the interaction of the sample with the evanescent wave of the light propagating in the waveguide. Since the reference waveguide is passivated by an overcladding layer, the mutual optical path length difference between the measurement and reference waveguides changes that is seen as a shift of the interferogram fringes. More detailed discussion of the designing principles of integrated YIs and the measurement technique can be found in the literature [53,54].

3. Materials and setups

3.1 Determination of refractive indices

Refractive indices, n, of the used materials including undercladding (Nalax2, Nanocomp), core material (Epocore, Micro resist technology) and overcladding (OP-4-20632, Dymax) were determined by using the prism coupling method and applying the first order Sellmeir equation of

$$n(\lambda) = \sqrt{1 + \frac{A\lambda^2}{\lambda^2 - B}} \tag{1}$$

to interpolate the RIs for the wavelength of 975 nm, *i.e.* for the wavelength used in the experiments. In Eq. (1) λ is the wavelength of light, and A and B are the Sellmeir coefficients.

A prism coupler (2010, Metricon) was equipped with lasers of 633, 829, 1320 and 1552 nm wavelengths. The obtained Sellmeir coefficients for each material are listed in Table 1. The Sellmeir RI dispersion curves and measured RIs at discrete wavelengths are shown in Fig. 2. It is worth noting that the maximum observed deviation between the experimentally obtained RI value and the dispersion curve is 0.001. Calculated RIs at the wavelength of 975 nm are shown in Table 1.

Table 1. Obtained Sellmeier coefficients for the used materials and the RIs calculated at the wavelength of 975 nm.

Material	A	B (μm^2)	Refractive index @ 975 nm
Nalax2	1.256	0.01308	1.508
Epocore	1.481	0.01667	1.583
OP-4-20632	1.354	0.01500	1.541

#255397 Received 11 Dec 2015; revised 21 Jan 2016; accepted 23 Jan 2016; published 1 Feb 2016

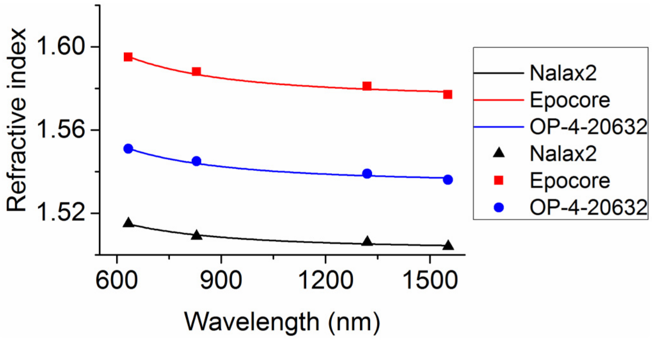

Fig. 2. Obtained Sellmeier dispersion curves and measured RIs at discrete wavelengths for the used materials.

3.2 Optical setups

The measurement setup for the attenuation measurements is illustrated in Fig. 3(a). Laser light from a source (QFBGLD-980-5, QPhotonics) emitting at 975 nm was coupled into the waveguides from a tapered polarization maintaining (PM) input fiber forming a spot about 2.8 µm in diameter. The operational wavelength of 975 nm was chosen in this work allowing the usage of silicon-based cameras and the single-modal waveguide operation that is discussed in Section 5.1. When investigating modal intensity distribution, the waveguide output facet was imaged onto a camera (UI-3240CP-NIR-GL, IDS Imaging Development Systems) through a 100× microscope objective. During intensity measurements, the transmitted light was collected with another tapered fiber. An autoalign station (Newport) was used during measurements to align the fibers into their optimal transmission positions.

A schematic of the measurement setup for YI experiments is shown in Fig. 3(b). The light source, the incoupling optics and the camera were the same as used for the attenuation measurements. TM polarized light was used in the YI experiments due to its higher sensitivity compared to TE polarization [51]. Polarization state was confirmed with an external polarizer prior to the measurements. The interference patterns were imaged onto the camera using a 40× microscope objective. The distance between the camera detector and the outcoupling end of the chip was about 17 cm. The interferograms were imaged at a distance of ~250 µm and the interval between the captured interferograms was 2 s.

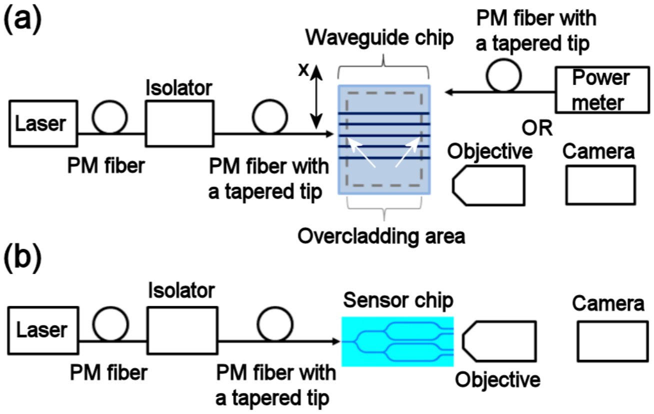

Fig. 3. (a) Setup for investigating the modal intensity distribution and for the measurement of attenuation values. The input fiber was moved in the x-direction in the intensity distribution experiments. The white arrows point to the edges of the overcladding area related to the modal mismatch loss discussed in Section 5.1. (b) Optical setup for ambient RI sensing experiments. PM = polarization maintaining.

#255397 Received 11 Dec 2015; revised 21 Jan 2016; accepted 23 Jan 2016; published 1 Feb 2016

Interferograms were analyzed by a two-dimensional fast-Fourier transform (FFT) algorithm yielding the phases of the fringes [53]. The areas of the interferograms for the FFT analysis were selected for each measurement and for both of the interferometers individually.

3.3 Sample solutions for ambient refractive index sensing experiments and their actuation

For ambient RI measurements, D-Glucose (Sigma-Aldrich) solutions were prepared in ultrapure water (MilliQ Academic, Merck Millipore) at the following concentrations: 0.006, 0.01, 0.03, 0.1 and 0.5 weight % (wt.%) with the following calculated RI differences to pure water: 8×10^{-6}, 1.4×10^{-5}, 4.2×10^{-5}, 1.4×10^{-4} and 7.0×10^{-4} RIU, respectively. The RI differences were calculated by using a polynomial [55] fitted to the tabulated RI values of aqueous glucose solutions [56]. Solutions were stored at room temperature to make sure that samples and measurement setup had the same temperature.

For the sample actuation during the sensing experiments, a flow cell was assembled on top of the interferometer chip, and sealed with a seal ring. The outlet of the flow cell was connected to a syringe pump (Nexus 3000, Chemyx) and the inlet to a sample vial by a tube. The syringe pump was operated in withdraw mode at a constant flow rate of 100 µl/min. To reduce the effect of water absorption into the waveguides during the experiments [50], the flow cell was filled with water at least a day before the measurements. During the experiments the sample and flushing solutions were sequentially pipetted into the sample vial.

4. Roll-to-roll fabrication

4.1 Nickel stamp fabrication

A nickel (Ni) stamp was used as a stamping tool to produce the waveguide grooves on the rolls. The fabrication and usage of the Ni tool is illustrated in Fig. 4(a). First, a contact lithography process with an aligner (MA6, Karl Suss) with an i-line filter was applied to fabricate original waveguide groove structures in a positive tone resist layer (Ultra-I 123, Dow) that was spin-coated on a silicon (Si) wafer. In order to ease the release of the nanoimprint mould from the cured structures, tilted sidewalls were produced into the grooves by applying an additional reflow step.

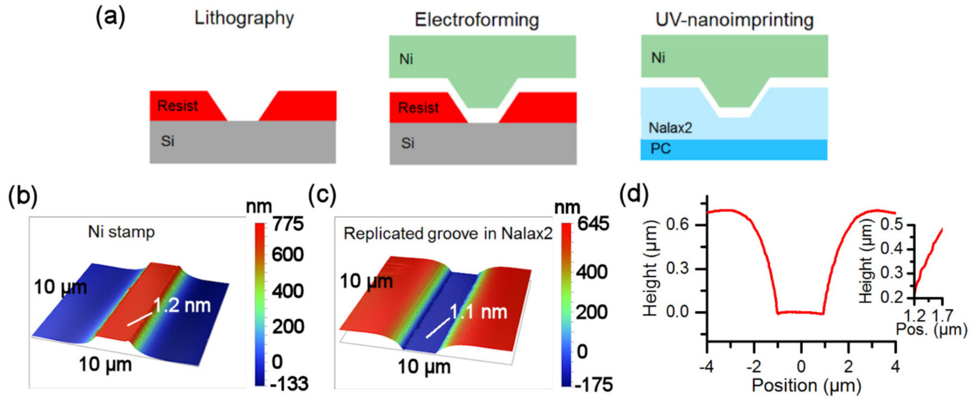

Fig. 4. (a) Fabrication of the Ni nanoimprint stamping tool and its usage to produce waveguide grooves into an acrylate layer. AFM scans from (b) the Ni stamp, and (c) the replicated waveguide groove. The numbers displayed in white lettering in figures b and c are the obtained RMS roughness values for the stamp and replica in the ridge and groove regions, respectively. d) Perpendicular scan from an AFM image of a waveguide groove. The inset shows slight ripple at the sidewall of the groove.

An actual UV-nanoimprint stamp with a ridge structure was fabricated by electroforming a Ni plate from the lithographically patterned grooves. Ni plates were then laser welded to an embossing reel. Atomic force microscopy (AFM) scans (Dimension 3100, Veeco) from the Ni-stamp and from an R2R produced waveguide groove in UV-cured Nalax2 (undercladding)

#255397 Received 11 Dec 2015; revised 21 Jan 2016; accepted 23 Jan 2016; published 1 Feb 2016

are shown in Fig. 4(b) and 4(c), respectively. Rather similar root-mean-square (RMS) surface roughness values of 1.1 nm and 1.2 nm were obtained for both the stamp and replicated structure, respectively, when 1.5 μm x 1.5 μm areas from the top of the imprint stamp and from the bottom of the waveguide grooves were analyzed. The values were obtained by averaging five AFM measurements from five different spots of the sample.

Figure 4(d) shows a single perpendicular scan from an AFM image. Depth of the replicated waveguide groove is about 700 nm. In the inset, slightly observable ripple at the sidewall of the groove is attributed to the lithography phase of the stamping tool fabrication, where interference effects during the UV-exposure results in sidewalls with waviness.

4.2 Roll-to-roll chip fabrication

The processing of the inverted ridge waveguides for the attenuation measurements and the sensor chips was done in two phases: in the first phase the waveguide grooves were fabricated, and in the second phase the grooves were filled. The length of the processed roll was about 200 m and the width 15 cm, while sensor chips about 3.5 cm long were used in the YI sensing experiments.

The R2R process to fabricate inverted ridge waveguides is depicted in Fig. 5(a) and 5(c). The continuous UV-nanoimprinting method was used to pattern waveguide grooves into the acrylate based under-cladding material (Nalax2). As illustrated in Fig. 5(a), the processing of the under-cladding layer was initiated by unwinding the blank polycarbonate (PC) web and removing a protective foil. During the processing, the web was run at the constant speed of 7 m/min. The gravure coating method was utilized to deposit the undercladding material [57]. The groove pattern was transferred by pressing a nickel stamp (temperature 30 °C) onto the uncured undercladding resin, and applying UV-light through the transparent PC web resulting in grooved surface structures whose shape and dimensions were defined by the stamp. The grooves were manufactured with strongly tilted sidewalls to facilitate the release of the stamp from the UV-cured waveguide grooves. The thickness of the replicated under-cladding material was about 6 μm being rather thick compared to the waveguide groove thickness of about 0.7 μm. Therefore, it is expected that modal field is well isolated from the PC web as illustrated in Fig. 6(a). An additional foil was applied on the structured surface before rewinding the roll to protect the waveguide grooves against mechanical defects. The top view image of the waveguide groove with a Y-junction structure is shown in Fig. 5(b).

The rolls with the waveguide grooves were then processed in another R2R unit to fill the grooves with an epoxy-based waveguide core material (Epocore). During the processing, the roll was running at a constant speed of 1 m/min. As illustrated in Fig. 5(c), the protective foil was removed after the unwinding of the roll. As in the coating of the undercladding layer, the gravure printing method was utilized to deposit the core material that was diluted in propylene glycol monomethyl ether acetate (PGMEA) with the weight ratio of 1:3.5. The printing was done at room temperature. The solvent was evaporated in three sequential ovens (length of each 1 m, temperature 80 °C) before UV-curing of the epoxy resin. It is worth noting that no replication stamp was applied in this step, because no surface pattern was required. Finally, the roll with the inverted ridge waveguide structures was protected with foil, and the processed roll was rewound. A cross-sectional image of the inverted ridge waveguide is shown in Fig. 5(d). Strongly tilted sidewalls are due to a reflow step applied during the stamp preparation in order to ease the release of the stamp from the UV-cured under-cladding layer.

The thickness variation of the waveguide groove processed in the under-cladding material was determined from AFM scans to be less than 40 nm. The groove filling with the core material using the gravure printing method resulted in bending of the surface as observable in Fig. 5(d). According to the AFM measurements, the variation in the bending was below 20 nm. This observation is consistent with the previously reported values for gravure printed layers showing thickness variations of few tens of nanometers [58]. In addition, the thickness variations were smooth when lossless adiabatic changes to the propagating modes are expected.

#255397 Received 11 Dec 2015; revised 21 Jan 2016; accepted 23 Jan 2016; published 1 Feb 2016

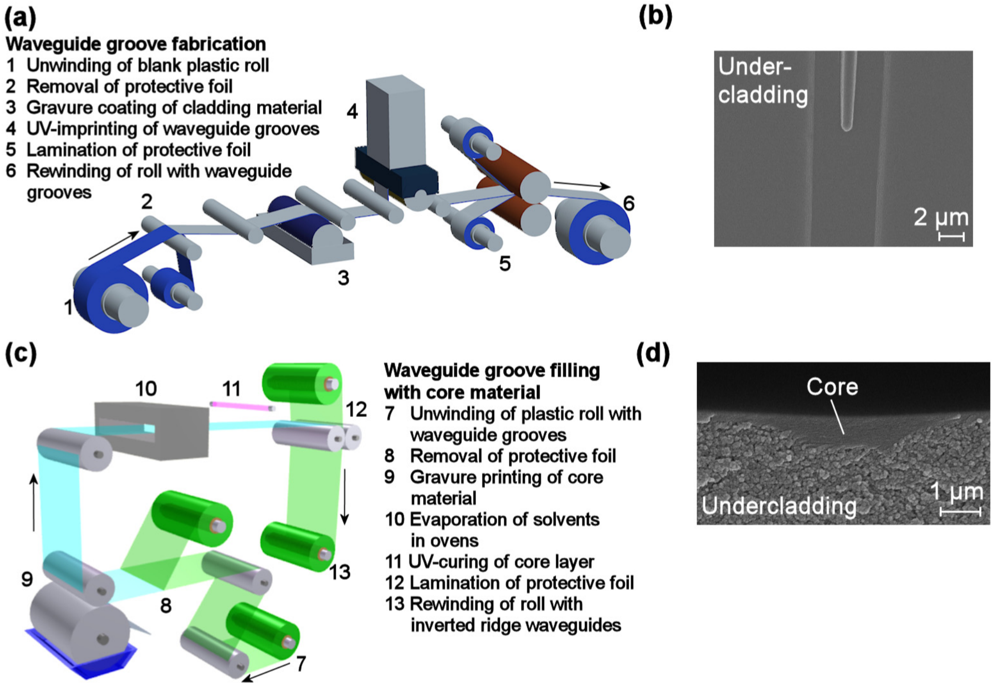

Fig. 5. a) R2R unit for waveguide groove fabrication, b) waveguide groove with a Y-junction, c) R2R unit for waveguide groove filling, and d) cross-sectional scanning electron microscope image of an inverted ridge waveguide.

The waveguide chips were cut from the roll by first pre-cutting the web with scissors leaving the waveguide facet areas intact. The waveguide facets were formed by cooling the plastic samples with liquid nitrogen and cleaving the intact areas. As it can be seen in Fig. 5(d), the facet of the cleaved core material is smooth while the surface of the undercladding material is granular. As the waveguide facet quality affects the results of attenuation measurements, a large number of samples (640) were characterized to obtain reliable data. The potential variation in the facet quality does not affect significantly the operation of interferometric sensor used in this work, since the operation is based on the phase difference occurring during the light propagation in the waveguides. In the sensor measurements, only the visibility of the interference pattern is decreased if the facet quality varies between the reference and measurement waveguides.

5. Experiments and discussion

5.1 Simulations and experiments of single-modality

The single-modality of the fabricated waveguides was first assessed by fully vectorial finite-element method (FEM) simulations and experiments. Theoretical mode field profiles of the waveguides were calculated with commercial waveguide simulation software (Fimmwave, Photon Design). The waveguide geometry for the simulation was delivered from the scanning electron microscope image of the cross-section of the fabricated waveguide shown in Fig. 5(d). In the simulations, RI values shown in Table 1 for the waveguide undercladding and core material were used.

According to simulations, the waveguides without the overcladding layer can support two TM-modes at the wavelength of 975 nm (*i.e.* at the polarization state and the wavelength used in sensor experiments). On the other hand, simulations suggested that by utilizing an overcladding with a RI of 1.541, only one propagating TM-mode is supported. The theoretical TM-mode field profiles are shown in Fig. 6(a). The simulations showed that besides the difference in the number of propagating modes, there is also a notable difference in the intensity location: while most of the intensity remains inside the waveguide core layer, when no overcladding is applied, modes are strongly pushed towards the overcladding layer in case one is present on the structure.

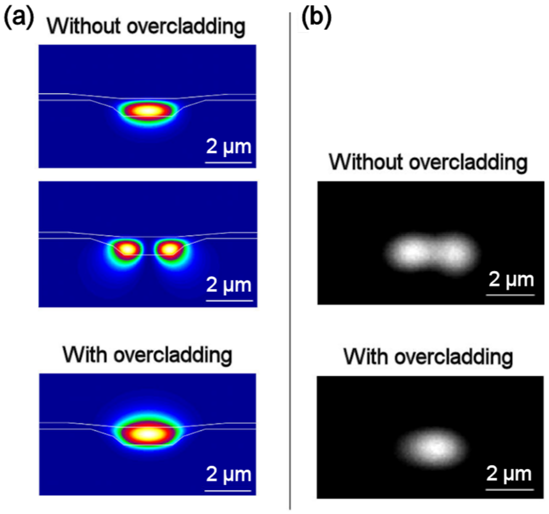

Fig. 6. (a) Theoretical TM-mode field profiles of the waveguides with and without the overcladding, and (b) imaged intensity distributions for TM-modes with and without the overcladding layer.

As illustrated in Fig. 3(a), area with the width of 2 mm was left uncoated with the overcladding layer at the edges of the chips to ensure intact waveguide facets and to facilitate the alignment of the input fiber and the input waveguide in the experiments. Thus every waveguide had two interfaces between areas with and without the overcladding as indicated by the white arrows in Fig. 3(a). It was simulated that a loss of about 2.2 dB occurs at each of these interfaces due to the modal mismatch.

The simulation results were confirmed by experiments: with the waveguides without the overcladding layer, it was possible to observe a double-peaked intensity distribution by moving the input fiber laterally, as shown in Fig. 6(b). However, such excitation of higher-order modes could not be confirmed with the waveguides with the overcladding layer being well in accordance with the simulation results of single-modality.

5.2 Waveguide attenuation measurements

The attenuation measurements were carried out for the waveguide samples with and without the overcladding layer. For attenuation measurements, chips lengths of 10, 18, 26 and 34 mm were cut from the roll at each of the four sampling areas that were about 10 m apart from one another. This resulted in 16 sample chips. Each chip contained 40 parallel straight waveguides, and thus a total of 640 individual waveguides were characterized.

The attenuation value histograms, each based on 160 measurements, and the line fitted to the median attenuation values are shown in Fig. 7 for the waveguides without and with the overcladding. Rather similar attenuation values of 1.7 and 1.5 dB/cm were obtained with and without the overcladding layer, respectively. It is worth noting that the attenuation values were comparably well localized in the vicinity of the median value. As can be seen from the histograms of Fig. 7, 80% of the samples had attenuation values at the maximum, about 1 dB higher than the related median value. The observations from attenuation measurements confirm that the R2R method can be applied to produce integrated optics with repeatable performance. The excess loss from 2.2 dB to 6.3 dB in the presence of an overcladding layer can mostly be explained by the theoretical modal mismatch loss of 2.2 dB at each of the overcladding interfaces near the waveguide input and output facets. The length of the waveguides in Fig. 7(b) is the area with the overcladding layer being 4 mm shorter than the overall length of waveguides.

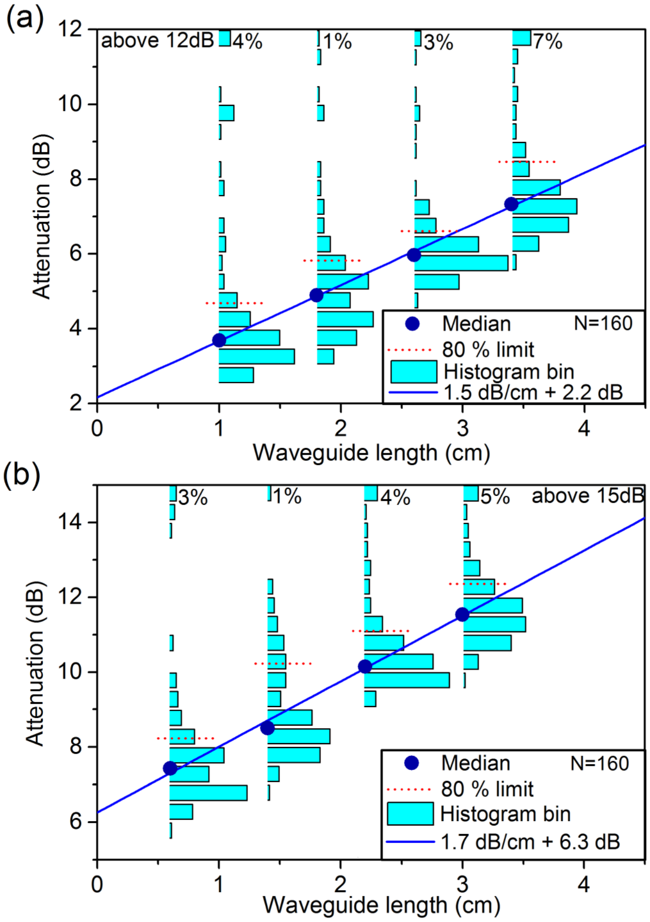

Fig. 7. Attenuation value histograms, each of which is based on measurements from 160 different waveguides a) without, and b) with an overcladding layer. Median attenuation values at different waveguide lengths are shown as well as line fitted to values. The red dashed lines show the attenuation values below which 80% of the measured values lie.

Obtained attenuation values are higher than the recently reported value of 0.19 dB/cm for polymeric single-mode waveguides produced on rigid silicon wafers with static nanoimprint processing [44]. However, since typical sensor chip lengths are in the centimeter range, the waveguides are suitable for sensors and applications that are not highly sensitive to power budget. For example, the waveguide length of 3.5 cm, corresponding to roughly the length of the sensor waveguides in this work, results in about 5.3 dB propagation loss that is acceptable in many applications.

The losses in optical waveguides can be generally associated with radiation, absorption and scattering [59]. Losses due to radiation are typically negligible in straight waveguides with well confined modes. The absorption is determined by the material properties, while scattering can be due to inhomogeneity of the material or surface roughness. In this work, the main selection criteria for the materials were their refractive indices, R2R processability and compatibility when layering different materials. Refractive index contrast between the core and cladding materials is obviously required to form waveguide structures. In the used R2R process, the requirement for the undercladding material (Nalax2) and the core material

(Epocore) was that they could be coated with a good wettability by gravure printing method. While the under-cladding material had to be UV-imprintable, the requirement for the core material was the formation of smooth surface during drying and UV-curing without applying a moulding tool. Furthermore, since solvent (PGMEA) was utilized to tune the viscosity of the core material, the underlying under-cladding with imprinted groove structures had to tolerate the used solvent. Enormous amount of research efforts has been made over the time to develop polymeric materials with low absorption and volume scattering for the optical waveguide applications [60]. Providing that new materials meeting the above mentioned criteria for processing and refractive indices are developed, the attenuation of R2R processed waveguides might be decreased. Furthermore, the optimization of the fabrication process to produce smoother waveguide surfaces might be another approach to decrease the attenuation value. This process optimization can cover both the mould tool processing with lithography and electroplating steps together with the actual R2R processing.

5.3 Ambient refractive index sensing experiments

To demonstrate the applicability of the waveguides for evanescent wave sensing, sensor responses to ambient RI changes were determined with two chips by using aqueous glucose solutions to modify the RI in the measurement window. The chips were first cut from the roll for post-processing. An optical adhesive (OP-4-20632) was used to pattern the overcladding layer leaving 10 mm of the measurement waveguide of YI2 uncoated to form a measurement window for the sample interaction. Illustration of the sensor structure with dimensions is shown in Fig. 8.

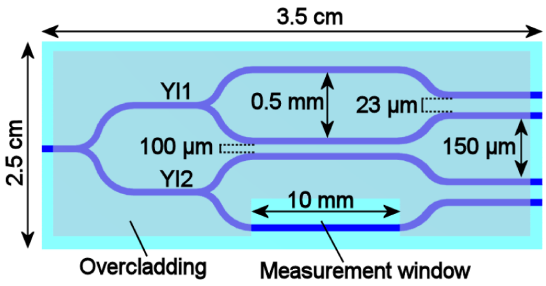

Fig. 8. Illustration of the sensor chip layout for ambient RI detection with dimensions.

Each concentration was measured four times by exposing the sensor surface to the respective glucose solution for five minutes leading to a 500 μl sample volume. This was followed by flushing with water until the end of the experiment. The timing of the glucose solutions and water in the flow cell are indicated in Fig. 9(a). The phase change curves were first calculated from the interferograms and were baseline corrected based on the values between 0 and 1.1 min. Phase change curves of YI2 are shown in Fig. 9(a). It can be seen that ambient RI changes were detected at the level of 10^{-6} RIU, thus showing comparable or better performance than reported earlier for polymeric YIs [51,52].

#255397 Received 11 Dec 2015; revised 21 Jan 2016; accepted 23 Jan 2016; published 1 Feb 2016

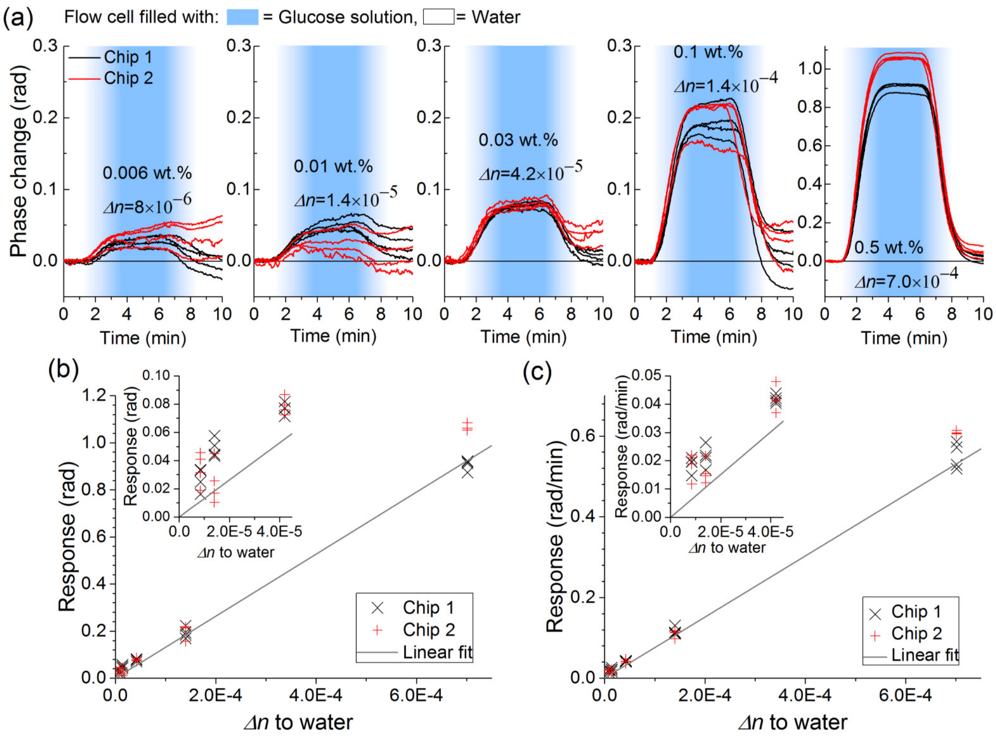

Fig. 9. (a) Phase change curves of YI2 of ambient RI experiments measured with various glucose concentrations. Two chips were used in the experiments and every concentration was measured four times with each of the chips. The RI difference of the glucose solution to water, Δn, and the glucose concentration are indicated next to the curves. Timing of the solutions in the flow cell is indicated by the background color. Calculated responses and lines fitted to the data points are based on (b) the phase change step height, and (c) the slope of the rising edge of the phase change curves. Responses of the three lowest concentrations are also shown in the inset figures.

Responses of YI2 were determined by 1) calculating the height of the phase change step by taking the average of the phase change values within 5.0-5.3 min, and 2) by determining the slope of the phase change curves within 2.0-2.8 min. Responses are shown Fig. 9(b) and 9(c) including lines fitted to the data points. It can be seen that, in general, the responses increase with increasing glucose concentration quantitatively. Thus, at the two lowest concentrations the measurement cannot be considered quantitative since the response values overlap significantly. The slope-based method enables faster signal quantification than the method based on the phase change step height representing an advantage for rapid diagnostics. The results of these experiments demonstrate that the YI sensor chips with R2R manufactured waveguides are capable of sensing ambient RI changes.

6. Conclusion

In conclusion, we demonstrated that disposable polymeric PICs can be produced by ultra-high volume, large-area, and low-cost fabrication methods in the roll format for sensor applications in lengths of hundreds of meters. The attenuation properties of hundreds of waveguides were investigated showing that the attenuation values were well localized in the vicinity of the median value indicating that waveguides with repeatable performance were produced. The attenuation of the single-mode waveguides was about 1.7 dB/cm that is high in comparison to requirements of telecommunication applications, but can be well suitable in sensor usage. We also demonstrated that the waveguides were suitable for evanescent wave sensing of ambient RI.

#255397 Received 11 Dec 2015; revised 21 Jan 2016; accepted 23 Jan 2016; published 1 Feb 2016

The fabrication of integrated photonic devices using ultra-high volume fabrication, in a similar manner as paper is produced, may inherently open up ways of manufacturing low-cost disposable photonic integrated circuits for a wide range of applications including point-of-care diagnostics, food safety applications and environmental monitoring.

Acknowledgments

The authors gratefully acknowledge financial support by the European Commission via the Seventh Framework Programme under the grant agreement No. 263382 "PHOTOSENS". M. Hiltunen, J. Hiltunen and P. Karioja gratefully acknowledge financial support by Academy of Finland grant No. 284907. The authors want to acknowledge J. Ollila, VTT, for his assistance in preparing the sensor chips.

#255397 Received 11 Dec 2015; revised 21 Jan 2016; accepted 23 Jan 2016; published 1 Feb 2016

PAPER IV

Disposable (bio)chemical integrated optical waveguide sensors implemented on roll-to-roll produced platforms

RSC Advances 6, 50414–50422.

RSC Advances

PAPER

Cite this: *RSC Adv.*, 2016, **6**, 50414

Disposable (bio)chemical integrated optical waveguide sensors implemented on roll-to-roll produced platforms

Sanna Aikio,*[a] Martin Zeilinger,[b] Jussi Hiltunen,[a] Leena Hakalahti,[a] Johanna Hiitola-Keinänen,[a] Marianne Hiltunen,[a] Ville Kontturi,[c] Samuli Siitonen,[c] Jarkko Puustinen,[d] Peter Lieberzeit[b] and Pentti Karioja[a]

Received 20th March 2016
Accepted 15th May 2016

DOI: 10.1039/c6ra07320d

www.rsc.org/advances

To enable wide spread dissemination of sensors in cost-critical applications and resource poor settings, methods to implement sensor chips using low-cost materials and mass-manufacturing methods are developed. In this paper we demonstrate that disposable polymeric integrated Young interferometer (YI) sensor chips, implemented on roll-to-roll mass-manufactured waveguides, are applicable for analyte specific sensing of small molecules and for multi-analyte detection of biomolecules. For the chemical sensing of small molecules, a sensor chip was functionalized with a molecularly imprinted polymer (MIP). We demonstrate that the MIP receptor layer is compatible with a polymer-based evanescent wave sensor for direct refractive index sensing. For multi-analyte detection of biomolecules, antibody-based receptor layers were patterned by inkjet printing onto the sensor surface demonstrating the applicability of the method with integrated YI chips. Demonstration of the analyte specific chemical- and biosensing with disposable polymeric YI sensor chips opens new possibilities to implement low-cost (bio)chemical sensors.

Introduction

Research on micro total analysis and optofluidic systems is advancing rapidly, developing sensor technologies for a wide range of applications including point-of-care diagnostics, environmental monitoring and food safety.[1,2] To enable wide spread dissemination of the sensors, also in resource poor settings, there is a need for sensor chips that are sensitive, robust, and reliable, and that can be implemented using low-cost fabrication methods and materials.

Waveguide based integrated interferometric sensors, such as integrated Young interferometers (YIs), show potential for low-cost sensor applications.[3] Integrated YI sensors utilize the evanescent wave field of the guided optical wave to directly sense the refractive index (RI) changes at or within a few hundred nanometres of the waveguide surface. The label-free sensing method enables simpler sample handling, and reduced complexity and cost of the sensor chip.[3] YI sensor chips are reported to detect RI differences 10^{-5} to 10^{-8} refractive index units (RIU) showing some of the lowest limit of detection values among integrated interferometric sensors.[3–6]

The fabrication of YI sensor chips has relied on batch-based manufacturing methods,[3] for example micromachining of silicon wafers, using inorganic[4,5,7–10] or low-cost polymeric[6,11–13] materials. Recently, the authors have demonstrated that single-mode waveguides for polymeric integrated YI sensor chips can be fabricated on flexible foils with length of hundreds of meters by using continuous ultra-high volume roll-to-roll (R2R) manufacturing methods making the chips inherently disposable.[14] Quality of the waveguides was assessed by measuring the attenuation properties of hundreds of samples showing that waveguides with repeatable performance were manufactured. It was also demonstrated that the unfunctionalized integrated YI sensor chips were capable to detect ambient unspecific RI changes in the level of 10^{-6} RIU and quantify them in the level of 10^{-5} RIU by using aqueous glucose solutions, showing thus rather comparable performance than reported earlier for polymeric YI sensors.[6,13]

For analyte specific sensing, YI sensor chips need to be functionalized with a receptor layer that binds analyte molecules selectively to the sensor surface. When analyte molecule binds to a receptor it replaces sample matrix that typically has lower RI, and induces a RI change. The magnitude of the RI change depends on the RIs of the chosen analyte molecule and sample matrix. Of biological receptors, antibodies have been used to functionalize inorganic and polymeric YI sensors for detection of proteins and viruses including demonstration of

---

[a] *VTT Technical Research Centre of Finland, Kaitoväylä 1, FI-90590, Oulu, Finland. E-mail: sanna.aikio@vtt.fi*

[b] *University of Vienna, Faculty for Chemistry, Department of Analytical Chemistry, Währinger Straße 38, 1010 Vienna, Austria*

[c] *Nanocomp Oy Ltd, Ensolantie 6, FI-80710 Lehmo, Finland*

[d] *University of Oulu, Faculty of Information Technology and Electrical Engineering, Department of Electrical Engineering, Microelectronics and Materials Physics Laboratories, Pentti Kaiteran katu 1, FI-90014 Oulu, Finland*

multi-analyte sensing.[6,8,9,15,16] Artificial receptor layers, such as molecularly imprinted polymers (MIPs), provide another route for sensor functionalization. MIP receptor layers may be advantageous for low-cost sensors due to their potential to be low-cost, robust, repeatable, and mass-manufacturable.[17] MIP receptor layers have been applied with silicon-based interferometric sensor chips to detect vapor phase trinitrotoluene and proteins.[18,19] In this work we study the applicability of MIP receptor layer with polymeric YI sensor chips.

The antibody receptor layers of integrated YI sensors are applied by either incubating antibody solution on the chip surface,[9] or by flowing the antibody solution through the flow-cell assembled on top of the sensor chip enabling the binding of the antibodies onto the sensor surface.[6,8,15,16] The MIP receptor layers are formed by either dip coating the YI sensor chip[18] or injecting the polymer solution onto the sensor surface, and performing the polymerization under glass plate resulting in a thin receptor layer.[19] Patterned functionalization by inkjet printing of antibodies has been demonstrated for multi-analyte functionalization of silicon-based ring resonator sensors,[20] however that method has not been utilized to functionalize YI sensor chips. Functionalization by inkjet printing is especially interesting for low-cost sensors since, as an additive method, it minimizes the consumption of potentially expensive receptor materials, and is also considered to be compatible with mass-production methods.[21]

In this paper, we demonstrate the applicability of the disposable polymeric multi-analyte YI sensor chips having R2R fabricated waveguides for analyte specific chemical- and biochemical sensing. Due to strict surface quality requirements of optical waveguides, it is not self-evident that receptor layers can be applied onto polymeric waveguides without deteriorating their capability to guide light and act as a sensor, for example due to increased scattering. We use melamine as a model analyte to demonstrate the chemical sensing of small molecules and the applicability of the MIP receptor layer with a polymeric evanescent wave sensor chip for direct RI sensing. The multi-analyte sensor design and patterning of the MIP and the reference non-imprinted polymer (NIP) layer onto a single sensor chip enables the simultaneous measurement of the analyte specific binding into the MIP layer and the non-specific sample matrix effects. The multi-analyte detection of biomolecules is demonstrated by using C-reactive protein (CRP) and human chorionic gonadotropin (hCG) as model analytes. We also demonstrate the applicability of the inkjet printed antibody-based receptor and reference layers with integrated YI sensor chips for multi-analyte detection. The chosen functionalization schema enables real-time detection of the specific binding of analytes and suppression of non-specific sample matrix effects.

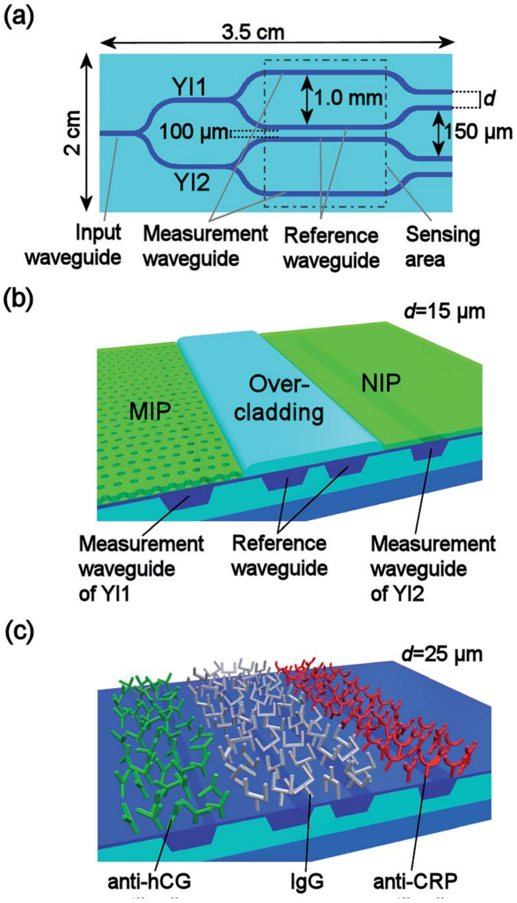

Fig. 1 (a) Top view illustration of the sensor chip with names of the parts and dimensions. (b) Illustration of the cross-cut structure of the MIP functionalized sensor chip within the sensing area showing the MIP and NIP coatings on the respective measurement waveguides, and the passivating overcladding layer on the reference waveguides. (c) Antibody functionalized chip having analyte specific anti-hCG and anti-CRP antibody coatings on the respective measurement waveguides and reference IgG coating on the reference waveguides. The separations of the measurement and the reference waveguides at the outcoupling end of the chip, *d*, are shown next to the sensor illustrations in (b) and (c).

Sensor chip embodiments and sensing principle

Illustration of the sensor chip is shown in Fig. 1(a). Sensor chip has an input waveguide that branches into four waveguides forming two parallel Young interferometers, named YI1 and YI2, integrated into one sensor chip. Both of the interferometers contain a reference and a measurement waveguide. The separation between the reference and measurement waveguides is increased at the sensing area enabling patterning of the measurement windows and receptor layers with loose positional tolerances. Measurement window is an opening in the passivating overcladding layer of the waveguides enabling the interaction of the sample with the evanescent wave field of the light propagating in the underlying waveguide.

Illustration of the cross-section of the sensor chip structure for the chemical sensing within the sensing area is shown in Fig. 1(b). The reference waveguides of both YIs were passivated by the overcladding layer and were thus not exposed to sample solutions. The measurement windows were formed by leaving a length of 10 mm of the measurement waveguides without the overcladding layer. The MIP receptor layer was applied into the measurement window of YI1, and the reference NIP layer into the measurement window of YI2.

Cross-section of the sensor chip for multi-analyte biosensing is illustrated in Fig. 1(c). In the sensing area, all the waveguides were left without the overcladding layer and they were sharing a single measurement window. Thus, all the waveguides were similarly exposed to sample solutions. Inkjet printing was used to pattern analyte specific antibody layers, *i.e.* anti-human CRP antibodies and anti-hCG antibodies, onto their respective measurement waveguides and the reference antibody layer, *i.e.* mouse immunoglobulin G (IgG), onto the reference waveguides. It is worth noticing that with this sensor embodiment the sensing length of the sensor is defined by the inkjet printed receptor layers, not by the measurement window patterned in the overcladding layer. The overcladding layer was applied onto the waveguides outside the sensing area as required by the single mode operation of the waveguides.[14]

In the measurements, laser light was end-fire coupled into the input waveguide and was divided into the measurement and reference waveguides. The four light beams emerging from the outcoupling end of the chip diverge, overlap and interfere forming a fringed interferogram that was imaged onto the camera by using a microscope objective as illustrated in Fig. 2(a). Since the imaging was done close to the chip outcoupling end, the beams emanating from the measurement and reference waveguide of YI1 interfered only with each other. Similarly, the beams of YI2 interfered mutually. This resulted in two separate 2-beam interferograms that were imaged simultaneously onto a single camera detector as shown in Fig. 2(b) and (c). Another approach to implement multi-analyte integrated YI sensors is to use sensor layouts that have multiple measurement waveguides and a single reference waveguide with unique waveguide pair separations at the outcoupling end, and letting all the emanating beams interfere to form a multibeam interferogram.[16,22,23]

Sensing method is based on the analysis of the sample induced changes in the interferogram fringe positions.[22,23] When RI on top of the waveguide is changed by the sample, the effective RI of the waveguide is changed due to the interaction of the sample with the evanescent wave field of the light propagating in the waveguide. The binding of the molecules changes the RI of the layer on top of the waveguides since water is replaced by a material having typically a higher RI. In the designed sensor layouts, sample induced effective RI change differs between the measurement and reference waveguides. This changes their mutual optical path length difference that again shifts the interferogram fringes. The sample induced phase change of the fringes, $\Delta\phi$, is[23]

$$\Delta\phi = 2\pi \frac{\ell(\Delta n_{\mathrm{eff,m}} - \Delta n_{\mathrm{eff,r}})}{\lambda}, \tag{1}$$

where ℓ is the sensing length of the sensor, $\Delta n_{\mathrm{eff,m}}$ and $\Delta n_{\mathrm{eff,r}}$ are the sample induced effective refractive index changes of the measurement and reference waveguides, respectively, and λ the wavelength of the light. As shown by eqn (1), the induced phase change is inversely proportional to the wavelength that also affects to the probing depth of the evanescent wave field and to the effective refractive index changes of the waveguides. Interferograms captured during the experiments were analyzed by using two dimensional fast Fourier transform (FFT) yielding the phases of the fringes and enabling the calculation of the sensor responses as phase changes.

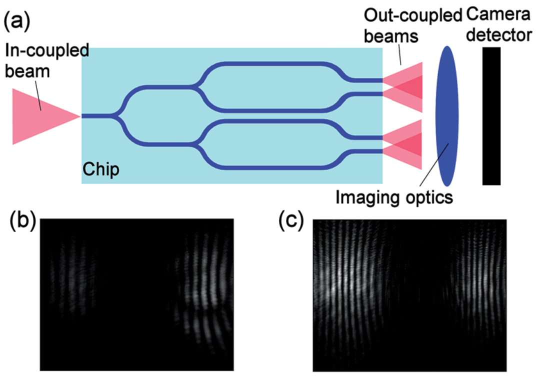

Fig. 2 (a) Schematic illustration of the experimental arrangement. Captured interferogram of (b) MIP functionalized, and (c) antibody functionalized sensor chip.

Materials and methods

Fabrication of sensor chips

Illustration of the cross-section of the inverted ridge waveguide structure used in the sensor chips is shown in Fig. 3(a). The waveguide fabrication is shortly outlined in this paper, and detailed description is given in the earlier paper by the authors.[14]

The fabrication of the waveguides was done in two phases using two R2R units. In the first phase, the waveguide grooves were patterned into the UV-curable acrylate based undercladding material (Nalax2, Nanocomp) using UV-imprinting method, and in the second phase the grooves were filled with the epoxy-based waveguide core material (Epocore, Micro resist technology). In the first phase, the undercladding material was gravure coated onto polycarbonate foil. The waveguide grooves were patterned by pressing a nickel stamp, having a ridge structure, into the uncured undercladding material and curing the material by applying UV-light through the transparent foil. In the second phase, gravure printing method was used to fill the waveguide grooves with the UV-curable waveguide core material followed by curing with UV-light. A roll of R2R produced sensor platforms is shown in Fig. 3(b).

The sensor platforms were cut from the roll for post-processing to sensor chips as shown in Fig. 3(c). The in- and outcoupling facets of the waveguides were formed by cleaving. The overcladding layer (OP-4-20632, Dymax) was patterned onto the chips as required by the different sensor embodiments.

Functionalisation with MIP layer

The MIP- and NIP-layers were applied into the measurement window of YI1 and YI2, respectively, by spin-coating the

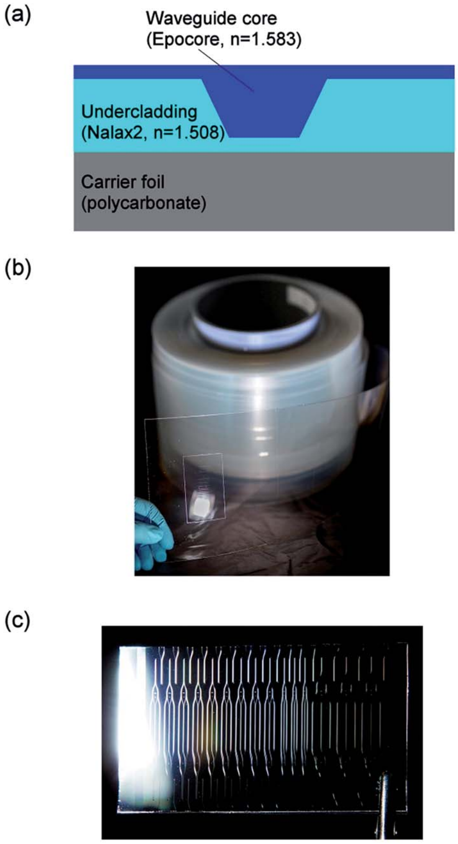

Fig. 3 (a) Schematic of the cross-section of the inverted ridge waveguide structure showing the materials and the refractive indices,[14] *n*, of the core and undercladding layers at the wavelength of 975 nm, *i.e.* at the wavelength used in the sensing experiments. (b) Roll of sensor waveguides. (c) Sensor platform cut from the roll.

respective oligomer solutions at 3000 rpm using custom-built spin coater. Oligomers leading to MIP were prepared by dissolving 17 mg dihydroxyethene bisacrylamide (DHEBA; cross-linker), 8 mg methacrylic acid (MAA; functional monomer) and 1.5 mg melamine (template) in 1 ml de-ionized water. Synthesis of NIP followed the same experimental protocol but for adding melamine. This solution was then heated to 55 °C followed by adding 5 mg sodium peroxodisulfate (PODS; radical initiator). Then, polymerization took place until the solution turned slightly turbid. The coated length of the waveguides was 10 mm defined by an opening in the overcladding layer. Prior to interferometric experiments, the melamine template molecules were removed from the MIP layer by immersing the sensor chip into water and shaking it overnight.

Functionalisation with antibodies

For multi-analyte biosensing, antibodies for hCG and human-CRP were inkjet patterned onto the measurement waveguides of YI1 and YI2, respectively, and mouse IgG, onto the reference waveguides. Bio-inks containing anti-human CRP antibodies (monoclonal antibody (Mab) 6404, Medix Biochemica), anti-hCG antibodies (Mab 5006, Medix Biochemica) or mouse IgG (ChromPure, Jackson ImmunoResearch Laboratories) were prepared. Each bio-ink contained 1.0 mg ml^{-1} of the respective antibody prepared in Na$_2$CO$_3$ buffer solution (50 mM, pH 9.6) containing 3% of isopropanol and 0.1% of Tween-20. Inks were filtered through a nylon membrane filter with 0.2 μm pore size to avoid clogging of the inkjet printhead nozzles. Before inkjet printing, the chips were oxygen plasma treated 1 min at 300 W to make surfaces more hydrophilic to improve the printing quality. The printing was done using a piezoelectric inkjet printer (Dimatix DMP-2800, Fujifilm Dimatix). Size of the printed rectangular patterns, shown in Fig. 8(b), was 0.6×10 mm^2.

After inkjet printing, the sensor surface was blocked to reduce unspecific binding during the experiments by applying 500 μl of 3% bovine serum albumin (BSA) (Sigma-Aldrich) in phosphate buffered saline (PBS) buffer (12 mM, pH 7.4) on top of the sensor chips. Chips were shaken for 10 min, after which they were aspirated. The unbound BSA was washed with 500 μl PBS with Tween-20 (PBST) applied on the sensor chips. Chips were shaken for 5 min, after which they were aspirated. During these steps the salts in the bio-inks that dry onto the chip surface during the inkjet printing were washed away.

Sample solutions and their actuation

For chemical sensor experiments, aqueous melamine solutions were prepared by dissolving melamine (Alfa Aesar) in ultrapure water at the following concentrations: 0.1, 0.25, 0.5 and 1.0 g l^{-1}. Melamine concentrations of the sample solutions were chosen to reflect the levels found in contaminated milk powders reported to contain melamine up to 2563 mg kg^{-1}.[24]

For biosensor experiments, sample solutions containing either 2.0 μg ml^{-1} of human-CRP antigen (BBI Solutions) or 0.9 μg ml^{-1} (corresponding 100 mIU ml^{-1}) of hCG antigen (Scripps Laboratories) were prepared in 1% bovine serum albumin (BSA) (Sigma-Aldrich) in phosphate buffered saline (PBS) buffer (12 mM, pH 7.4) as a sample matrix. To study the sensing of ambient RI changes, a sample solution was prepared containing 0.5 weight% (wt%) of D-glucose (Sigma-Aldrich) in 1% BSA in PBS buffer. The BSA content of the sample matrix increases its complexity compared to mere buffered saline solution. The concentrations of hCG and CRP in sample solutions were chosen to be physiologically relevant. For hCG, pregnancy tests typically have sensitivities ∼25 IU l^{-1}.[25] However, during pregnancy the concentration of hCG in serum can be >300 000 IU l^{-1} and in urine >2500 IU l^{-1} although the levels vary greatly.[25] For CRP, the normal concentration in human serum is <8 μg ml^{-1} but the levels can even 1000 fold in inflammation.[26] CRP concentration can also be used to estimate the risk of cardiovascular disease where levels <1 μg ml^{-1} indicate low, 1–3 μg ml^{-1} moderate, and >3 μg ml^{-1} high risk.[27]

Flow cell was assembled on top of the interferometer chips at least a day before the measurements, and it was filled with the sample matrix solution. The inlet and the outlet of the flow cell were connected to a sample vial and to a syringe pump (Nexus 3000, Chemyx), respectively, by a tube. Sample and flushing solutions were pipetted into the sample vial sequentially. The syringe pump was driven in withdraw mode at a flow rate of 100 μl min^{-1} during the chemical sensing experiments and at a flow rate of 20 μl min^{-1} during biosensing experiments. In the chemical- and biosensing experiments, the sensor response time was limited by the time it took for the sample to replace the preceding fluid within the flow cell, and by the mass transportation of the analyte molecules from the sample volume to the sensor surface. The response time was about 2 min in chemical sensing experiments, and about 5 min in biosensing experiments. The fluid replacement times were different for the chemical- and biosensing experiments due to different flow rates and different flow cell volumes.

Fluorescent staining

For the fluorescent staining of CRP analytes, 13.2 μg ml^{-1} of anti-CRP antibody (Mab 6405, Medix Biochemica) labelled with Alexa Fluor 546 (Thermo Fisher Scientific) fluorescent label was prepared in 1% BSA in 12 mM PBS buffer (pH 7.4). For the staining of hCG analytes, 6.6 μg ml^{-1} of anti-hCG antibody (Mab 5014, Medix Biochemica) labelled with Alexa Fluor 546 fluorescent label was prepared in 1% BSA in 12 mM PBS buffer (pH 7.4). For IgG staining, 4.0 μg ml^{-1} of goat anti-mouse IgG antibodies (Thermo Fisher Scientific) labelled with Alexa Fluor 647 (Thermo Fisher Scientific) fluorescent label was prepared in 1% BSA in 12 mM PBS buffer (pH 7.4).

Fluorescent staining was done by using the following procedure: 500 μl of staining solution was pipetted onto the sensor surface, and the chip was placed onto a shaker for 10 minutes. The staining solution was aspirated and 400 μl of PBST solution was pipetted onto the chip to wash the unbound labelled antibodies. The chip was placed onto a shaker for 10 minutes, and PBST solution was aspirated.

Optical setup and stability

Light from a laser source (QFBGLD-980-5, QPhotonics) emitting at the wavelength of 975 nm was end-fire coupled into the input waveguide of a sensor chip by using a tapered polarization maintaining fibre (spot size of ~2.8 μm). The chosen wavelength enabled the single-mode operation of the waveguides[14] as well as the use of a silicon-based camera. An optical isolator was used to prevent the disturbing reflections back to the laser. The sensor experiments were conducted using TM polarized light reported to have a higher sensitivity than TE polarization.[6]

Interferograms were imaged onto a camera detector (UI-3240CP-NIR-GL, IDS Imaging Development Systems) using a 40× microscope objective. The imaging was done at the distance of ~200 μm from the out-coupling end of the chip. The camera was located ~17 cm from the chip. The interval between the captured interferograms was 2 s during the chemical sensing experiments and 10 s during biosensing experiments.

Stability of the sensing system was studied by measuring phase changes while the sample matrix was flowing through the flow cell. Measured phase change curves for MIP and antibody functionalized chips are shown in Fig. 4 as well as lines fitted to the data points showing the trend of the system drift. In the curves, the noise of the system is seen as the small scale variation of the phase changes in the range of milliradians. The larger fluctuations and the overall drift of the phase change curves were attributed to the mechanical and thermal instabilities of the sensor chip and the experimental setup. The phase change fluctuations were less than 0.1 radians being thus much smaller than the analyte induced phase changes that were in the range of radians. It can be also seen that in all of the cases the trend of the drift was below 0.01 rad min^{-1} that is less than responses induced by the analytes in the sensing experiments.

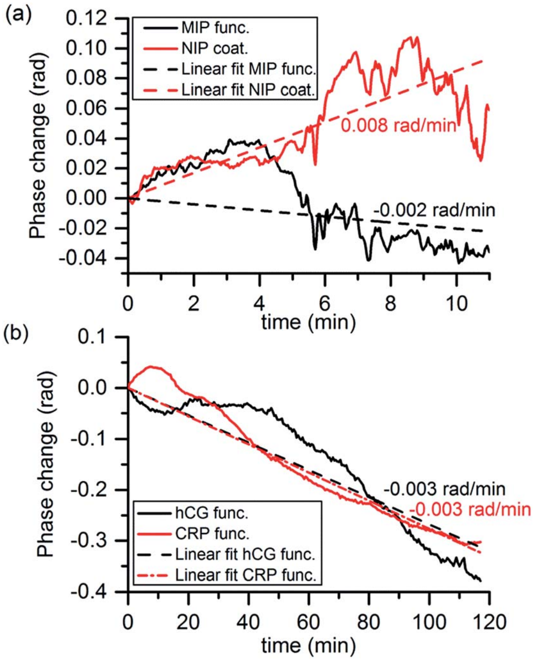

Fig. 4 Phase change curves measured while the sample matrix flowed in the flow cell, and lines fitted to the data points for (a) MIP functionalized chip (image interval 2 s), and (b) for antibody functionalized chip (image interval 30 s). The slope of the fitted lines is also shown indicating the trend of the system drift.

Results

Chemical sensor

To demonstrate the chemical sensing, a MIP-functionalized sensor chip was exposed to aqueous melamine solutions. Each concentration was measured three times by flowing 500 μl of the melamine solution through the flow cell followed by flushing with water until the end of the measurement leading to 5 min analyte exposure. Timing pattern of the solutions in the flow cell is indicated in Fig. 5.

Due to the patterned functionalization of the chip, the MIP functionalized interferometer was measuring the specific binding and the NIP coated interferometer the non-specific binding of melamine to the polymer layers. Both interferometers were also measuring the bulk effects of the sample solutions. The shift of the interference fringes during an experiment is shown in Fig. 6. The phase change curves of the MIP and NIP coated interferometers, *i.e.* $\Delta\phi_{\text{MIP}}$ and $\Delta\phi_{\text{NIP}}$, respectively, are shown in Fig. 5(a). The phase change curves were first analysed from the interferograms and were subsequently baseline

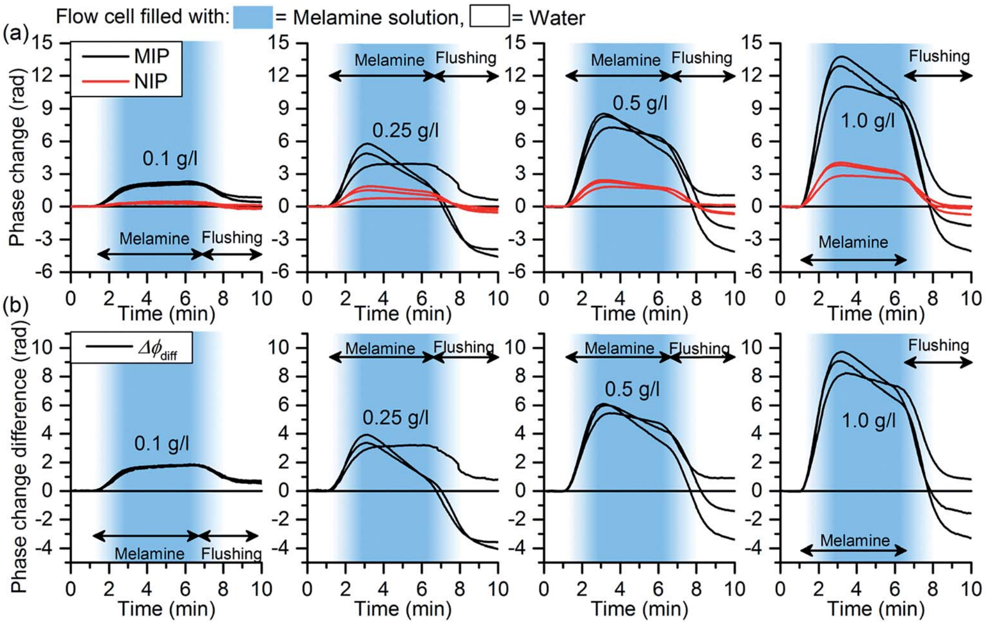

Fig. 5 (a) Phase change curves of MIP functionalized YI1 and NIP coated YI2 measured at various melamine concentrations. Each concentration (value shown next to the curves) was measured three times. (b) $\Delta\phi_{\text{diff}}$ curves showing the net difference of the phase change values between the MIP functionalized YI1 and NIP functionalized YI2 at different melamine concentrations. Timing of the solutions in the flow cell is indicated by the arrows and the background colour.

corrected based on the values between 0 and 1.1 min. The curves clearly show that the MIP coated interferometer undergoes significantly higher phase changes on exposure to melamine: they are exceeding those of the corresponding NIP by roughly a factor of four. This gives clear evidence that incorporation of the melamine into the cavities of the MIP leads to substantial measurable phase change.

The measured phase changes also clearly exceed the values that would be produced by the mere bulk refractive index differences of the melamine solutions to pure water. The phase change $\Delta\phi_{\text{bulk}}$ induced by the bulk RI difference of the sample solutions to pure water, Δn, was evaluated by using formula

$$\Delta\phi_{\text{bulk}} = S\Delta n = S\left[\underbrace{\frac{C}{\rho_{\text{m}}}n_{\text{m}} + \left(1-\frac{C}{\rho_{\text{m}}}\right)n_{\text{w}}}_{\text{RI of melamine solution}} - n_{\text{w}}\right], \qquad (2)$$

where S is the sensitivity of the sensor in radians per RIU, C the concentration of melamine in g cm^{-3}, ρ_{m} the density of melamine in g cm^{-3}, and n_{m} and n_{w} the RI values of melamine and water, respectively. The RI of melamine solution was evaluated using the volume fractions of solution components.[28] The ratio C/ρ_{m} gives the volume fraction of melamine in the solution. The volume fraction of water was calculated assuming that the volumes of the components are additive with the melamine concentrations used in the experiments. For the concentration of 1.0 g l^{-1}, $\Delta\phi_{\text{bulk}}$ was calculated to be 0.4 rad by using the RI value of 1.872 to melamine[29] and 1.333 to water[29] (RIs were measured at the wavelength of 589 nm and at the temperature of 20 °C), and the melamine density[29] 1.573 g cm^{-3} (measured at 16 °C). The sensor sensitivity[14] 1251 rad RIU^{-1} was obtained from the earlier paper by the authors defined for similarly manufactured non-functionalized YI sensor chips for bulk RI changes. The calculated value of $\Delta\phi_{\text{bulk}}$ is indicative of the magnitude of the phase change due to the uncertainty of the RI value of the melamine solution and the uncertainty of the sensor chip response to bulk RI changes through the MIP and NIP layers. Since the phase changes measured with the highest melamine concentration shown in Fig. 5(a) are roughly a magnitude larger than the calculated values of $\Delta\phi_{\text{bulk}}$, the phase changes are enhanced by interaction of the molecules with MIP and NIP layers.

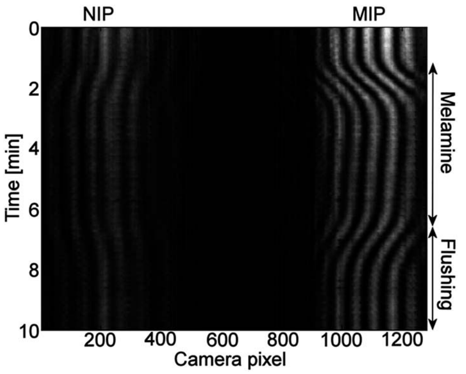

Fig. 6 Shift of the interferogram fringes during a chemical sensing experiment conducted with the melamine concentration of 1.0 g l^{-1}. Figure is constructed by first selecting the same narrow section (height 5 pixels) across each of the time laps images captured during the experiment, and then combining these sections.

The actual imprinting effect can be assessed by calculating the net difference of the phase change values, $\Delta\phi_{\text{diff}}$, between the MIP and NIP coated interferometers, *i.e.* $\Delta\phi_{\text{diff}} = \Delta\phi_{\text{MIP}} - \Delta\phi_{\text{NIP}}$, shown in Fig. 5(b). It is worth noticing that the calculation of the difference signal eliminates the phase changes related to internal changes at the chip that both YIs see similarly. These kinds of changes may be induced, for example, by temperature variations. However, the capability of the method to eliminate the chip internal changes was not separately assessed by experiments.

Responses were determined from $\Delta\phi_{\text{diff}}$, curves by (1) calculating the height of the phase change step by taking the average of the values within 5.0–5.3 min, and (2) by determining the slope of the phase change curves within 2.0–2.8 min. The responses and the second order polynomials fitted to the data points are shown in Fig. 7(a) and (b). In the fitting, the limit of detection was not taken into account since it was not assessed by the experiments. As can be seen, the sensor responses in overall increase with increasing melamine concentration demonstrating the capability of MIP functionalized chip to chemical sensing. The slope-based method was capable to differentiate between the two lowest concentrations whereas the step height-based method could not differentiate between these two. The results show beginning saturation for melamine concentrations above 0.5 g l^{-1}, which is in line with previous MIP studies aiming at detecting small molecules.[30] The reason for such saturation behavior can be found in the recognition mechanisms of MIP: analyte incorporation is the result of thermodynamic equilibrium between analyte molecules bound in recognition sites of the MIP and those in solution. Both the amount of binding sites within a MIP layer and accessibility of diffusion pathways within the matrix are limited hence limiting the dynamic range of the sensors. The slope-based method enables faster signal quantification than the method based on the step height that is an advantage for rapid diagnostics. The slight decrease in the sensor responses seen in the $\Delta\phi_{\text{MIP}}$ and $\Delta\phi_{\text{NIP}}$ curves of Fig. 5(a) with time can most probably be appointed loss of a few percent of the film as well as to minimal irreversible binding of melamine by the films. However, this does not affect the difference signal and hence can be neglected.

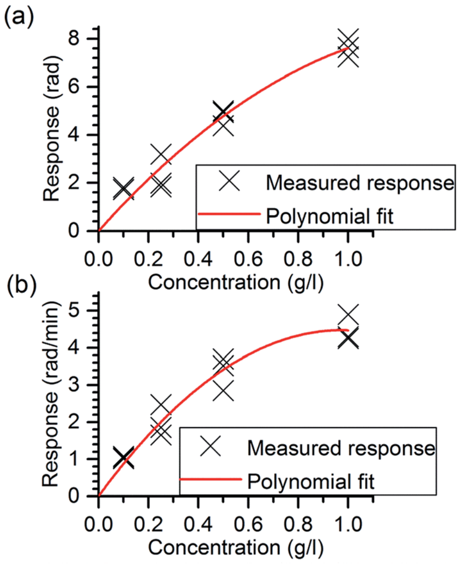

Fig. 7 Calculated responses and lines fitted to the data points based on (a) the phase change step height, and (b) the slope of the rising edge of $\Delta\phi_{\text{diff}}$ curves.

Multi-analyte biosensor

To demonstrate the multi-analyte biosensing, three antibody-functionalized chips were sequentially exposed to 400 μl of hCG and CRP sample solutions separated by a flushing step with 300 μl of the sample matrix leading to 20 min analyte exposure followed by 15 min sample matrix exposure. The timing of the solutions in the flow cell is indicated in Fig. 8(a).

With the chosen antibody functionalization schema, the antibody coating on the measurement waveguide makes it specifically bind its target analyte onto the sensor surface whereas the IgG-coated reference waveguide takes into account unspecific binding. Since all the sensor waveguides are exposed similarly to the solutions in the measurement window, in theory, the ambient RI change should not induce any phase difference between the measurement and the reference waveguides, and thus also not lead to measurable signal. Therefore, the measured phase change signal can be assumed to directly show the difference between the binding of the analytes on the measurement and the reference waveguides in real-time. In addition, the similarity of the measurement and reference waveguide structures makes them react similarly to temperature changes reducing the temperature sensitivity of the sensor.

The phase change graphs, shown in Fig. 8(a), were analysed from the captured interferograms and were subsequently baseline corrected based on the values between 0 and 5.7 min following the same procedure with melamine measurements. In each of the three experiments, YI1 shows a clear phase change signal when the sensor was exposed to hCG sample, whereas the curve of YI2 remains nearly unchanged. Similarly, when the sensor was exposed to CRP sample, the phase change curve of YI2 shows a clear phase change signal whereas the curve of YI1 remains unchanged. This indicates that analytes were selectively binding to the receptor layers on the measurement waveguides. During the following flushing steps, the phase change curves level off, indicating that no more analyte molecules were binding onto the surface.

Sensor responses to the hCG and CRP samples were determined from the phase change curves by calculating the average value within 35–38 min for YI1, and within 68–71 min for YI2, *i.e.* during the flushing step following the analyte exposure. The average response of the three measurements of YI1 to hCG samples was 1.0 rad and the range of the response values was 0.6 rad. Similarly the average response of YI2 to CRP samples was 2.5 rad and the range 1.7 rad. The responses to both analytes varied substantially from chip to chip. This was attributed to variations in the inkjet printed functionalization layers on the waveguides, such as the layer thickness and the amount of

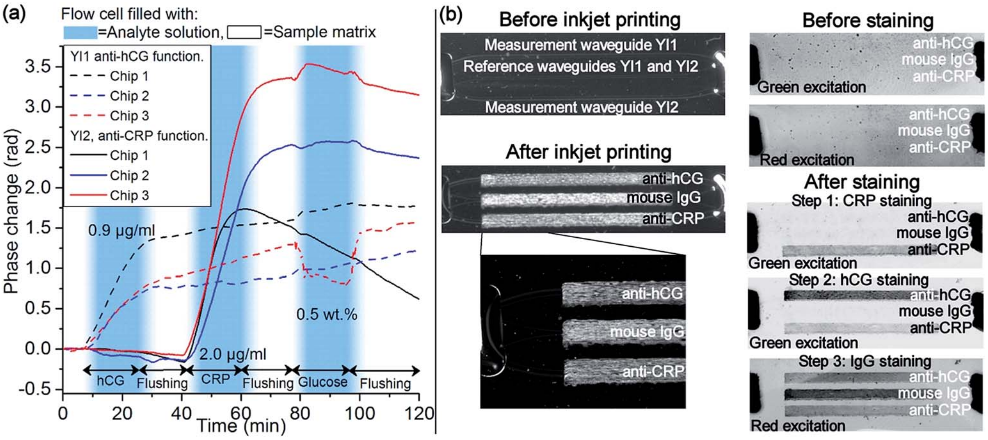

Fig. 8 (a) Phase change curves showing the specific responses of YI1 (dashed lines) and YI2 (solid lines) to hCG and human CRP samples, respectively. Responses to glucose solution demonstrate the sensor sensitivity to ambient RI changes. (b) Left: Microscope images of the YI chip before and after the antibody functionalization by inkjet printing showing the printed areas on top of the waveguides. Printed areas are visible due to the salts in the bio-inks that dry onto the chip surface. Right: Verification of specific binding of analytes onto the inkjet printed areas by fluorescent staining and imaging. The fluorescence images (the darker the colour the higher the fluorescence intensity) taken before staining show no fluorescence from the printed areas. After each staining step, the corresponding inkjet printed area became fluorescent verifying the localized presence of the analytes and the reference IgG coating.

capture antibodies, causing also variation in intensity of the fluorescence signal in Fig. 8(b).

As discussed above, the chosen antibody functionalization schema should desensitize the sensor to ambient RI changes. To study sensitivity to ambient RI changes, chips were exposed to 400 μl of 0.5 wt% glucose solution followed by flushing with the sample matrix. Timing of the solutions is shown in Fig. 8(a). It can be seen that in all but one of the phase change curves, the response to the ambient RI change is significantly smaller than the value of ~1 rad reported earlier by the authors for polymeric R2R fabricated non-functionalized YI sensor chips for aqueous glucose solution having the same concentration. The larger phase change signal of one of the curves, ~0.5 rad, is most likely caused by the different thicknesses of the inkjet-printed antibody layers on the measurement and reference waveguides causing a different penetration of the evanescent wave fields into the sample volume and thus different change of the effective RIs. Although the chosen functionalization schema could not render the sensors completely insensitive to the ambient RI changes, the effect was nonetheless suppressed.

After the interferometric measurements, fluorescent staining and imaging was used to verify the specific binding of the analytes to the correspondingly functionalized areas, as well as the presence of IgG on the reference waveguides. Fluorescently labelled antibodies were used to stain CRP and hCG analytes (green fluorescence excitation) and IgG (red fluorescence excitation) in three sequential steps. The fluorescence images of Fig. 8(b) show no fluorescence signal from the printed areas before staining. During each staining step, the corresponding inkjet functionalized area became fluorescent, as shown in Fig. 8(b), proving the presence of CRP, hCG and IgG at these areas, and confirming the results of interferometric measurements. However, when investigating the fluorescent areas in detail, it can be observed that fluorescent intensity is not uniform. This indicates that the variations in the inkjet printed functionalization layers lead to fluctuating amounts of bound analyte molecules resulting in variation of the response values of biosensor experiments.

Discussion

In this paper we reported for the first time analyte specific sensing using integrated YI sensor chips having R2R mass-fabricated polymeric single-mode waveguides. We demonstrated proof-of-concept for chemical sensing of small molecules using MIP receptor layer, and for multi-analyte detection of biomolecules using inkjet printed antibody-based receptor layers. The model analytes chosen for the demonstrations have substantial interest: melamine has become an important analyte in food adulteration, whereas both hCG and CRP are important clinical parameters: the former is an early stage pregnancy marker, the latter an unspecific inflammation marker and an indicator for the assessment of the risk of cardiovascular disease.

The MIP functionalized chip was shown to be capable to measure melamine concentrations quantitatively having linear responses below the concentration of 0.5 g l^{-1} and beginning saturation at the higher concentrations. In the case of the antibody functionalized chip, the responses to both analytes varied substantially from chip to chip. Thus the sensor responses at the moment only qualitatively indicate the presence or absence of the analytes and no quantitative responses were obtained. Deviating responses with the antibody-functionalized chips were attributed to variations in the inkjet printed functionalization layers on the waveguides. These are related to reproducibility of layer thickness and the amount of active capture antibodies. The repeatability of the sensor responses is most likely improved if the capture antibodies are bound to waveguide surface oriented and are forming mono layers.

To further characterize the sensor chip properties, the limit of detection, limit of quantification and repeatability of the sensor responses need to be studied by conducting experiments with large number of sensor chips. In addition, to assess the applicability of the sensors for real-life applications, experiments need to be conducted with real samples in realistic experimental conditions.

Conclusions

In conclusion, we demonstrated that disposable polymeric YI sensor chips are applicable for analyte specific chemical sensing of small molecules, and for multi-analyte detection of biomolecules. The MIP functionalized sensor chip indeed revealed responses depending on melamine concentration, which is the first demonstration of MIP on a low-cost, polymer-based sensor device for direct RI sensing. The antibody-functionalized YI sensor chips demonstrated the applicability of patterned, inkjet printed receptor layers for specific multi-analyte detection showing qualitative indication of the presence or absence of the analytes.

Proving the concept of disposable, low-cost sensor systems thus inherently opens up scientifically and economically interesting strategies for portable sensing and analysis. This ranges from determining the quality of food at home or providing low-cost diagnostic tests for rapid evaluation of important clinical parameters directly at the point-of-care.

Development of low-cost sensor solutions is one of the main challenges in the sensor field. Demonstration of the analyte specific chemical- and biosensing with disposable polymeric YI sensor chips using artificial and biological receptor layers opens new avenues for sensor implementation.

Acknowledgements

Authors acknowledge financial support by the European Commission *via* the Seventh Framework Programme under the grant agreement No. 263382 "PHOTOSENS", and by Academy of Finland grant No. 284907. Authors also acknowledge the assistance of J. Ollila, VTT, in preparing the sensor chips.

Notes and references

1 D. E. W. Patabadige, S. Jia, J. Sibbitts, J. Sadeghi, K. Sellens and C. T. Culbertson, *Anal. Chem.*, 2016, **88**, 320.

2 Y. Chen, L. Jiang, M. Mancuso, A. Jain, V. Oncescu and D. Erickson, *Nanoscale*, 2012, **4**, 4839.

3 P. Kozma, F. Kehl, E. Ehrentreich-Förster, C. Stamm and F. F. Bier, *Biosens. Bioelectron.*, 2014, **58**, 287.

4 A. Ymeti, J. S. Kanger, R. Wijn, P. V. Lambeck and J. Greve, *Sens. Actuators, B*, 2002, **83**, 1.

5 K. Schmitt, B. Schirmer, C. Hoffmann, A. Brandenburg and P. Meyrueis, *Biosens. Bioelectron.*, 2007, **22**, 2591.

6 M. Wang, J. Hiltunen, C. Liedert, L. Hakalahti and R. Myllylä, *J. Eur. Opt. Soc., Rapid Publ.*, 2012, **7**, 12019.

7 A. Brandenburg and R. Henninger, *Appl. Opt.*, 1994, **33**, 5941.

8 G. H. Cross, A. A. Reeves, S. Brand, J. F. Popplewell, L. L. Peel, M. J. Swann and N. J. Freeman, *Biosens. Bioelectron.*, 2003, **19**, 383.

9 J. Xu, D. Suarez and D. S. Gottfried, *Anal. Bioanal. Chem.*, 2007, **389**, 1193.

10 A. Schimpf, D. Bucci, M. Nannini, A. Magnaldo, L. Couston and J.-E. Broquin, *Sens. Actuators, B*, 2012, **163**, 29.

11 G. H. Cross and Y. Ren, *J. Appl. Phys.*, 1999, **86**, 6483.

12 M. Wang, S. Uusitalo, C. Liedert, J. Hiltunen, L. Hakalahti and R. Myllylä, *Appl. Opt.*, 2012, **51**, 1886.

13 M. Hiltunen, J. Hiltunen, P. Stenberg, S. Aikio, L. Kurki, P. Vahimaa and P. Karioja, *Opt. Express*, 2014, **22**, 7229.

14 S. Aikio, J. Hiltunen, J. Hiitola-Keinänen, M. Hiltunen, V. Kontturi, S. Siitonen, J. Puustinen and P. Karioja, *Opt. Express*, 2016, **24**, 2527.

15 A. Ymeti, J. S. Kanger, J. Greve, G. A. J. Besselink, P. V. Lambeck, R. Wijn and R. G. Heideman, *Biosens. Bioelectron.*, 2005, **20**, 1417.

16 A. Ymeti, J. Greve, P. V. Lambeck, T. Wink, S. W. F. M. van Hövell, T. A. M. Beumer, R. R. Wijn, R. G. Heideman, V. Subramaniam and J. S. Kanger, *Nano Lett.*, 2007, **7**, 394.

17 L. Uzun and A. P. F. Turner, *Biosens. Bioelectron.*, 2016, **76**, 131.

18 P. L. Edmiston, D. P. Campbell, D. S. Gottfried, J. Baughman and M. M. Timmers, *Sens. Actuators, B*, 2010, **143**, 574.

19 S. M. Reddy, D. M. Hawkins, Q. T. Phan, D. Stevenson and K. Warriner, *Sens. Actuators, B*, 2013, **176**, 190.

20 J. T. Kirk, G. E. Fridley, J. W. Chamberlain, E. D. Christensen, M. Hochberg and D. M. Ratner, *Lab Chip*, 2011, **11**, 1372.

21 N. Komuro, S. Takaki, K. Suzuki and D. Citterio, *Anal. Bioanal. Chem.*, 2013, **405**, 5785.

22 A. Ymeti, J. S. Kanger, J. Greve, P. V. Lambeck, R. Wijn and R. G. Heideman, *Appl. Opt.*, 2003, **42**, 5649.

23 J. S. Kanger, V. Subramaniam, P. H. J. Nederkoorn and A. Ymeti, in *Advanced Photonic Structures for Biological and Chemical Detection*, ed. X. Fan, Springer, Dordrecht, Heidelberg, London, New York, 2009, ch. 10, pp. 265–295.

24 J. Liu, A. Ren, L. Yang, J. Gao, L. Pei, R. Ye, Q. Qu and X. Zheng, *Can. Med. Assoc. J.*, 2010, **182**, 439.

25 M. Montagnana, T. Trenti, R. Aloe, G. Cervellin and G. Lippi, *Clin. Chim. Acta*, 2011, **412**, 1515.

26 K. D. McClatchey, S. Alkan and E. Hackel, *Clinical Laboratory Medicine*, LWW, Philadelphia, PA, 2nd edn, 2001.

27 P. M. Ridker, *Texas Heart Institute Journal*, 2005, **32**, 384.

28 W. Heller, *J. Phys. Chem.*, 1965, **69**, 1123–1129.

29 D. R. Lide, *CRC Handbook of Chemistry and Physics*, CRC, Boca Raton, FL, 83rd edn, 2002.

30 R. Suedee, W. Intakong, P. A. Lieberzeit, P. Wanichapichart, P. Chooto and F. L. Dickert, *J. Appl. Polym. Sci.*, 2007, **106**, 3861.

Series title and number

VTT Science 136

Title	**Improving robustness and disposability of integrated Young interferometer sensors for portable diagnostics**
Author(s)	Sanna Aikio
Abstract	Integrated Young interferometers (YIs) are label-free photonic sensors having many desirable features for point-of-need diagnostics. They have been shown to be sensitive, they are capable of multi-analyte detection, and they can be implemented using low-cost polymeric materials. However, there are also some disadvantages from the low-cost portable diagnostics point of view: sensor readout is easily disrupted by mechanical disturbances, and the realization of disposable photonic sensor chips for cost-critical applications using established batch-based processes is difficult. The objective of the work discussed in this thesis was to improve the applicability of integrated Young interferometer sensors for low-cost portable diagnostics by means of two themes: improving the robustness of the sensing method against mechanical disturbances and improving the disposability of the sensor chips. To improve the robustness, a drift compensation method was derived. The method was shown to be able to extract sample-induced phase change responses from up to 161 times larger phase changes measured with a deliberately mechanically disturbed setup. Disposability was improved by demonstrating that YI sensor chips can be implemented using polymeric waveguides manufactured by ultra-high volume roll-to-roll (R2R) methods. Three sensor embodiments were designed: one for ambient refractive index sensing, one for sensing of small molecules, and one for multi-analyte detection of biomolecules. In the experiments, ambient refractive index changes were detected at a level of 10^{-6} refractive index units. Analyte-specific sensing of small molecules was demonstrated using a sensor chip functionalized with a molecularly imprinted polymer. For multi-analyte detection of biomolecules, sensor chips were functionalized with inkjet-printed antibody layers. Improving the robustness of the sensing method and proving the concept of disposable photonic sensor chips opens up new possibilities to implement low-cost portable sensor systems.
ISBN, ISSN, URN	ISBN 978-951-38-8462-8 (Soft back ed.) ISBN 978-951-38-8461-1 (URL: http://www.vttresearch.com/impact/publications) ISSN-L 2242-119X ISSN 2242-119X (Print) ISSN 2242-1203 (Online) http://urn.fi/URN:ISBN:978-951-38-8461-1
Date	September 2016
Language	English, Finnish abstract
Pages	112 p. + app. 51 p.
Name of the project	
Commissioned by	
Keywords	compensation, diagnostics, disposable sensor, interferometry, waveguide, Young interferometer
Publisher	VTT Technical Research Centre of Finland Ltd P.O. Box 1000, FI-02044 VTT, Finland, Tel. 020 722 111

Julkaisun sarja ja numero

VTT Science 136

Nimeke	**Integroitujen Youngin interferometrisensoreiden häiriöiden siedon ja kertakäyttöisyyden parantaminen – kohti kannettavaa diagnostiikkaa**
Tekijä(t)	Sanna Aikio
Tiivistelmä	Integroidut Youngin interferometrit (YI) ovat leimattomia fotoniikkaan perustuvia sensoreita. On osoitettu, että niillä on monia hyödyllisiä pikadiagnostiikkaan liittyviä ominaisuuksia, kuten mittausmenetelmän herkkyys sekä mahdollisuus toteuttaa sensoriliuskat käyttäen edullisia polymeerimateriaaleja. Mittausmenetelmällä on myös epäedullisia ominaisuuksia edullisen kannettavan diagnostiikan kannalta: menetelmä on herkkä ulkoisille mekaanisille häiriöille, ja kertakäyttöisten mittaliuskojen toteuttaminen edullisiin pikadiagnostiikkasovelluksiin on vaikeaa vakiintuneilla mikrovalmistustekniikoilla, jotka perustuvat liuskojen prosessointiin erissä. Työn tavoitteena oli parantaa integroitujen YI-sensoreiden soveltuvuutta edulliseen kannettavaan diagnostiikkaan kehittämällä mittausmenetelmän mekaanisten häiriöiden sietokykyä sekä mittaliuskojen kertakäyttöisyyttä. Mekaanisten häiriöiden kompensoimiseen kehitettiin menetelmä, jonka osoitettiin kykenevän erottamaan näytteen aiheuttama vaihesiirto 161 kertaa suuremmasta häiriöstä. Mittaliuskojen kertakäyttöisyyttä parannettiin osoittamalla, että sensoriliuskat voidaan toteuttaa käyttäen polymeerisiä valokanavia, jotka on valmistettu jatkuvalla rullalta rullalle -menetelmällä. Se soveltuu erittäin suurien tuotantomäärien valmistamiseen. Kokeellista työtä varten suunniteltiin mittaliuskat ympäröivän taitekertoimen, pienmolekyylien ja biomolekyylien mittauksiin. Kokeiden perusteella mittaliuskoilla voidaan havaita 10^{-6} taitekerroinyksikön muutoksia ympäröivän materiaalin taitekertoimessa. Pienmolekyylien mittaaminen toteutettiin mittaliuskalla, joka oli funktionalisoitu molekyyli-imprintatulla polymeerillä. Biomolekyylien monianalyyttimittaus toteutettiin mittaliuskalla, joka oli funktionalisoitu liuskan pintaan muistesuihkutulostetuilla vasta-aineilla. Mittausmenetelmän parempi häiriönsietokyky ja rullalta rullalle valmistetun polymeerisen valokanavan soveltuvuuden osoittaminen sensorikäyttöön avaavat uusia mahdollisuuksia kannettavan diagnostiikan toteutukseen.
ISBN, ISSN, URN	ISBN 978-951-38-8462-8 (nid.) ISBN 978-951-38-8461-1 (URL: http://www.vtt.fi/julkaisut) ISSN-L 2242-119X ISSN 2242-119X (Painettu) ISSN 2242-1203 (Verkkojulkaisu) http://urn.fi/URN:ISBN:978-951-38-8461-1
Julkaisuaika	Syyskuu 2016
Kieli	Englanti, suomenkielinen tiivistelmä
Sivumäärä	112 s. + liitt. 51 s.
Projektin nimi	
Rahoittajat	
Avainsanat	diagnostiikka, interferometria, kertakäyttöinen sensori, kompensointi, valokanava, Youngin interferometri
Julkaisija	Teknologian tutkimuskeskus VTT Oy PL 1000, 02044 VTT, puh. 020 722 111

Improving robustness and disposability of integrated Young interferometer sensors for portable diagnostics

Integrated Young interferometers (YIs) are photonic sensors having desirable features for point-of-need diagnostics such as sensitivity, capability to multi-analyte detection and compatibility with low-cost polymeric materials. However, they have also some disadvantages: sensor readout is easily disrupted by mechanical disturbances, and the realization of disposable photonic sensor chips for cost-critical applications using established batch-based processes is difficult.

The objective of the work discussed in this thesis was to improve the applicability of integrated YI sensors for low-cost portable diagnostics by means of two themes: improving the robustness of the sensing method against mechanical disturbances and improving the disposability of the sensor chips. To improve the robustness, a drift compensation method was derived. It was shown to be able to extract sample-induced phase change responses from up to 161 times larger phase changes measured with a mechanically disturbed setup. Disposability was improved by demonstrating that YI sensor chips can be implemented using polymeric waveguides manufactured by ultra-high volume roll-to-roll methods. In the experiments, ambient refractive index changes were detected at a level of 10^{-6} refractive index units. Analyte-specific sensing of small molecules and multi-analyte detection of biomolecules was also demonstrated.

Improving the robustness and proving the concept of disposable photonic sensor chips open up scientifically and economically interesting opportunities for exploiting portable low-cost diagnostics in various application areas.

ISBN 978-951-38-8463-5 (Soft back ed.)
ISBN 978-951-38-8461-1 (URL: http://www.vttresearch.com/impact/publications)
ISSN-L 2242-119X
ISSN 2242-119X (Print)
ISSN 2242-1203 (Online)
http://urn.fi/URN:ISBN:978-951-38-8461-1

VTT SCIENCE 136
Improving robustness and disposability of integrated...